Stony Brook University

Chemical Aging and Cloud Condensation Nuclei Activity of Biomass Burning Aerosol Proxies in the Presence of OH Radicals

A Dissertation presented

by

Jonathan H. Slade Jr.

to

The Graduate School

in Partial Fulfillment of the

Requirements

for the Degree of

Doctor of Philosophy

in

Marine and Atmospheric Sciences

Stony Brook University

May 2015

Stony Brook University

The Graduate School

Jonathan H. Slade Jr.

We, the dissertation committe for the above candidate for the
Doctor of Philosophy degree, hereby recommend
acceptance of this dissertation

Daniel A. Knopf - Dissertation Advisor
Associate Professor, School of Marine and Atmospheric Sciences/
Institute for Terrestrial and Planetary Atmospheres

John E. Mak - Chairperson of Defense
Associate Professor, School of Marine and Atmospheric Sciences/
Institute for Terrestrial and Planetary Atmospheres

Sultan Hameed
Professor, School of Marine and Atmospheric Sciences/
Institute for Terrestrial and Planetary Atmospheres

Jian Wang
Tenured Scientist, Brookhaven National Laboratory
Department of Environmental and Climate Sciences

Jonathan Abbatt
Professor, University of Toronto
Department of Chemistry

This dissertation is accepted by the Graduate School

Charles Taber
Dean of the Graduate School

Abstract of the Dissertation

Chemical Aging and Cloud Condensation Nuclei Activity of Biomass Burning Aerosol Proxies in the Presence of OH Radicals

by

Jonathan H. Slade Jr.

Doctor of Philosophy

in

Marine and Atmospheric Sciences

Stony Brook University

2015

Biomass burning aerosol (BBA) can adversely impact regional and global air quality and represents a significant source of organic aerosol (OA) to the atmosphere that can affect climate. Aerosol particles can alter the transfer of radiation in Earth's atmosphere directly by scattering and absorbing radiation or indirectly via cloud formation. Gas-to-particle, also termed heterogeneous, oxidation reactions can significantly alter the particle's physical and chemical properties. In turn, this can lead to the degradation of biomolecular markers for air quality-related aerosol source apportionment studies, the particles lifetime, and modify the particles abilities to serve as cloud condensation nuclei (CCN). However, the rates, mechanisms, and conditions by which these multiphase oxidation reactions occur and influence the CCN activity of OA is not well understood. The work presented here aims to determine the reactivity and products from the interaction of BBA surrogate-particles and trace gas-phase oxidants and to link the effects of OA chemical aging on the particles ability to nucleate clouds.

The reactive uptake of OH by BBA surrogate-substrates and particles, including levoglucosan, nitroguaiacol, abietic acid, and methyl-nitrocatechol,

was determined as a function of both OH concentration and relative humidity (RH) using chemical ionization mass spectrometry coupled to various flow reactors. OH reactive uptake decreased with increasing OH concentration, indicative of OH adsorption followed by reaction. OH oxidation led to significant volatilization, i.e. mass loss of the organic material, as determined by application of high resolution proton transfer reaction time-of-flight mass spectrometry. Volatilized reaction products were identified, providing mechanistic insight of the chemical pathways in the heterogeneous OH oxidation of BBA. The reactive uptake of OH by levoglucosan particles increased with RH due to enhanced OH and organic bulk diffusivity. In contrast, OH uptake by methyl nitrocatechol decreased with increasing RH, attributed to the adsorption of water molecules on the particle surface, which blocks surface reactive sites. The CCN activity of single-component BBA surrogate-particles can be enhanced following OH exposure; however, when mixed with more water-soluble organic or inorganic compounds, OH oxidation showed no impact on the particles CCN activity. Ambient temperature has been shown to impact the extent of particle oxidation and CCN activity of Suwannee River Fulvic Acid particles, a surrogate Humic-Like Substance of BBA. The atmospheric implications of the results on the understanding of the OH oxidative aging of OA and their cloud formation potential are discussed.

Dedication Page

For my daughters, Anjali and Neha.

Table of Contents

Contents

List of Figures

List of Tables

Acknowledgements

"Necessity, which is the mother of invention."-from *Republic* by Plato

As I reminisce on the time and dedication of many spent toward developing, testing, and finalizing the research presented in this thesis, I am reminded of the above sentiment by the Greek philospher Plato, that necessity is a cause for vigilance, for progress and invention. I am proud of this work, but I am more proud to have *worked* alongside passionate and caring individuals who share a common goal of advancing scientific thought out of the necessity of intellect. I am indebted to many colleagues, friends, and family for their unwavering support over the course of my doctoral studies.

I want to offer a special thanks to my advisor, my mentor, my friend, Daniel Knopf. I am grateful that you accepted me into your group. You are a model scientist and mentor. Under your tutelage, I feel I have developed confidence and skill as a young scientist and mentor. I hope to instill in others the same rigor and passion for teaching and research as I have received from you. Thank you for your patience and for always being there to listen and offer advice, whether it was about family or work. I could not imagine a better advisor for me during this period of my life.

I am grateful for my collaborators Jian Wang and Ryan Thalman from Brookhaven National Laboratory for providing the necessary resources, help and mentorship while working on the CCN activity studies. I want to thank Manabu Shiraiwa and colleagues at the Max Planck Institute for Chemistry for giving me the opportunity to collaborate on the kinetic flux modeling study of OH uptake, and also Robert de Zafra and the folks from the Physics machine shop at Stony Brook University for their guidance and support in developing a microwave cavity for generating OH.

I wish to thank the members of my Ph.D. committee including Jonathan Abbatt, Jian Wang, Sultan Hameed, John Mak, and Daniel Knopf for their encouragement, advice, and comments regarding research and life in general.

I want to especially thank the members of the Knopf, Mak, and Aller groups including Peter Alpert, Seanna Forrester, Bingbing Wang, Yannick Rigg,

Joseph Charnawskas, Alicia Mullaley, Tracey Evans, Luping Su, Joann Radway, Wendy Kilthau, and Dylan Bothe. You all are what makes a good working environment possible. I especially want to thank Peter and his wife Sierra for being "my home away from my home" during my final year. I am grateful for your friendship.

Most importantly, this work would not have been possible without the love, encouragement, and support of my family, my wife Michelle Slade, and my two amazing children, Anjali and Neha Slade. Thank you, Michelle, for your sacrifices as my wife and as the mother of our two girls, you are my hero.

Publications

Slade, J.H., Thalman, R., Wang, J., and Knopf, D.A. "Chemical aging of single and multicomponent biomass burning aerosol surrogate-particles by OH: Implications for cloud condensation nucleus activity", in preparation for submission to *Atmos. Chem. Phys. Discuss.*

Arangio, A., **Slade, J.H.**, Berkemeier, T., Pöschl, U., Knopf, D.A., and Shiraiwa, M. "Multiphase chemical kinetics of OH radical uptake by molecular organic markers of biomass burning aerosols: humidity and temperature dependence, surface reaction and bulk diffusion", in review for *J. Phys. Chem. A*, 2015.

Slade, J.H. and Knopf, D.A. "Multiphase OH oxidation kinetics of organic aerosol: the role of particle phase state and relative humidity", *Geophys. Res. Lett.*, 2014, **41**, doi:10.1002/2014GL060582.

Slade, J.H. and Knopf, D.A. "Heterogeneous OH oxidation of biomass burning organic aerosol surrogate compounds: assessment of volatilisation products and the role of OH concentration on the reactive uptake kinetics", *Phys. Chem. Chem. Phys.*, 2013, **15**, 5898-5915, doi:10.1039/c3cp44695f.

Knopf, D.A., Forrester, S.M., and **Slade, J.H.** "Heterogeneous oxidation kinetics of organic biomass burning aerosol surrogates by O_3, NO_2, N_2O_5, and NO_3", *Phys. Chem. Chem. Phys.*, 2011, **47**, 21050-21062, doi:10.1039/c1cp22478f.

Slade, J.H., VanReken, T.M., Mwankiki, G.R., Bertman, S., Stirm, B., and Shepson, P.B. "Aerosol production from the surface of the Great Lakes", *Geophys. Res. Lett*, 2010, **37**, L18807, doi:10.1029/2010GL043852.

Chapter 1

Chemical Aging and Cloud Condensation Nuclei Activity of Biomass Burning Aerosol Proxies in the Presence of OH Radicals

February 7, 2015

1 Introduction

Aerosol particles are ubiquitous in the atmosphere and have the ability to affect the global radiative budget and thus Earth's climate directly by scattering and absorbing solar and terrestrial radiation[1–3] or indirectly by acting as cloud condensation nuclei (CCN) and ice nuclei (IN).[4,5] Quantifying the impact of aerosol particles on cloud formation and subsequently their radiative effects has proven highly uncertain.[5,6] Inherent in this uncertainty is the difficulty in evaluating the chemical transformations, also termed chemical aging, of aerosol particles during atmospheric transport.[7–9] Chemical aging of aerosol through heterogeneous oxidation by reactive trace gas species including OH, O_3 and NO_3 can significantly influence aerosol lifetime, composition, and physicochemical properties,[8,10–15] and thus its climate potential.[16,17]

A considerable mass fraction (up to 95%) of aerosol particles in Earth's lower atmosphere is composed of organic material.[18,19] A significant portion of organic aerosol (OA) is derived from primary emissions, including biomass burning.[20,21] Biomass burning aerosol (BBA) constitutes the largest source of primary organic aerosol (POA) and black carbon (BC) and has a direct impact on climate.[6] Studies have repeatedly confirmed that water-soluble organic particles can efficiently act as CCN.[9,22,23] However, its CCN efficiency is strongly dependent on size[24] and chemical composition, and thus its hygroscopicity.[25–27] Chemical aging can result in various degrees of particle

oxidation and impact particle size, thereby affecting its hygroscopicity and thus increase or decrease the aerosol particle population's CCN efficiency by modification of its chemical and physical properties.[16,17,28–30]

The degree of particle oxidation is, in part, dictated by oxidant concentration and the rate at which an oxidant is taken up and reacts with the particle.[8,9,12,31–33] For instance, while OH radicals react more efficiently than O_3 with organic aerosol on a per molecule basis, O_3 can have similar atmospheric oxidizing potential as OH because its atmospheric concentration is significantly higher.[13,15] However, the efficiency at which an oxidant is taken up by a particle can also be kinetically limited by oxidant concentration, particle composition, and particle phase, which is influenced by temperature and relative humidity (RH).[15,32–35] Furthermore, chemical aging of organic aerosol by OH can enhance particle volatility, leading to a loss in particle mass through volatilization reactions, directly impacting particle lifetime,[15,32,36] the gas-phase budget of volatile organic compounds (VOCs)[37], and secondary organic aerosol (SOA) formation[38]. This not only changes the distribution of aerosol mass, but also particle number density, potentially impacting the available CCN[39] and IN[40–42] for the formation of clouds.

Here, I present a detailed investigation of the heterogeneous oxidation kinetics and CCN ability of laboratory-generated organic aerosol particles and substrates closely representative of BBA in presence of OH radicals and its dependence on oxidant concentration and particle phase. Within this dissertation I report on the reactive uptake efficiency of OH radicals by BBA particle proxies at different relative humidities to assess the role of water vapor on particle phase and heterogeneous kinetics, and consequently particle lifetime. In particular, the material presented in this dissertation will help to better constrain kinetic parameters in BBA source apportionment models. The effect of chemical aging by OH on reaction products and cloud nucleation ability of laboratory generated BBA type particles is also investigated. Overall, the results presented in this dissertation will improve our understanding of how organic aerosol particles chemically transform and take up water vapor in the atmosphere in the presence of trace gases.

1.1 Atmospheric aerosol particles and their impacts on air quality and climate

Aerosol is broadly defined as a suspension of particulate matter in a gas. Aerosol particles are small and their diameters can vary from 10^{-9} m to 10^{-4} m as shown in Fig. 1.1, and thus are not typically visible to the naked eye. Aerosol particles are ubiquitous in Earth's atmosphere, yet aerosol number concentrations, quantified as the total number of particles that occupy a volume of air (e.g. cm^{-3}), are spatially and temporally variable and range from <100 cm^{-3} in rural continental free troposphere (clean) air, to $>10^5$ cm^{-3} in polluted urban environments.[43] This is in part due to the complex array of aerosol sources and their source strengths.

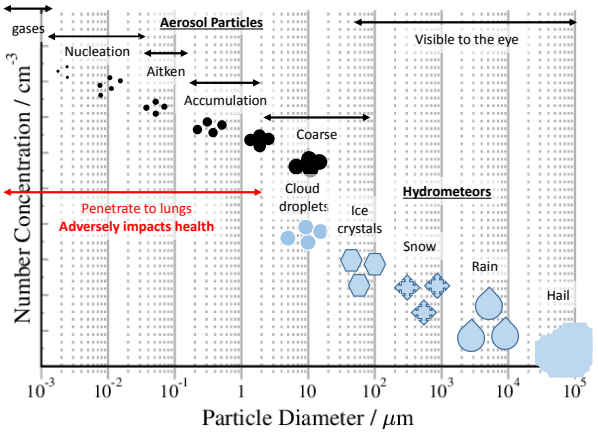

Figure 1.1: Typical aerosol particle and hydrometeor sizes and their relative (arbitrary) number concentrations.

Atmospheric aerosols are comprised of a complex mixture of inorganic and carbonaceous or organic material and are produced directly or indirectly depending on their source. Aerosols are emitted directly as salt and biological particles from wave-breaking activity over oceans, wind-transported pollen and dust particles, and ash and smoke particles from incomplete combustion, referred to collectively as primary aerosol particles[43]. Aerosol particles are also produced indirectly from chemical reactions in the atmosphere between trace gas-phase oxidants and volatile organic compounds (VOCs) from fossil fuel emissions and forests, referred to as secondary aerosol particles[43].

Aerosol particles are largely comprised of water, sulfate, ammonium, nitrate, and organic or elemental carbon. A major mass fraction of atmospheric aerosol (up to 90%) is comprised of organic material[18,19].

Aerosol particles play an important role in the atmosphere and the environment[44], impacting the transfer of radiation and affecting air quality. High aerosol concentrations have been directly correlated with respiratory issues[45]. Ultrafine aerosol particles, typically smaller than 2.5 μm, can penetrate deep into our lungs and depending on the particles' chemical composition, can be toxic to humans[46]. Aerosol particles impact atmospheric temperatures and climate by directly absorbing or deflecting incoming solar radiation and outgoing longwave radiation from Earth's surface and indirectly by the modification of the radiative properties of clouds.

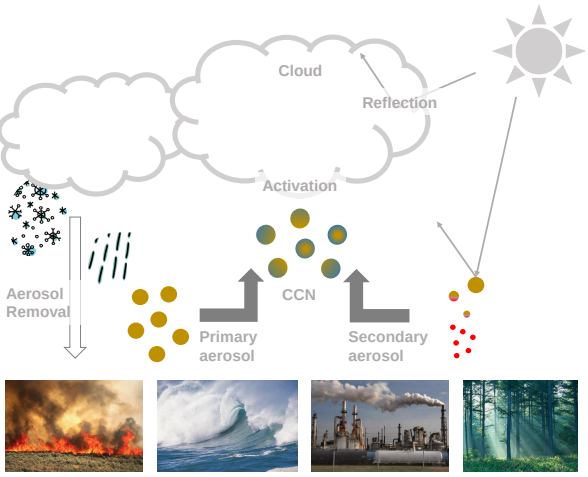

Figure 1.2: Overview of atmospheric aerosol life cycle including production, cloud formation, and sinks. Atmospheric aerosol particles are generated from both natural and anthropogenic sources, e.g. biomass burning, wave-breaking, fossil-fuel emissions, and forests. Primary aerosol particles are formed directly at the source. Secondary aerosol particles are formed via chemical reactions in the atmosphere. Aerosol particles increase the available cloud condensation nuclei (CCN) in cloud formation. Aerosol particles are removed by deposition.

Aerosol particle concentrations can vary widely depending on their susceptibility to different removal processes, which include dry and wet depo-

sition, and chemical reaction. Our ability to quantify the impacts aerosol particles have on air quality and the environment depends crucially on our understanding of their source and source strengths and the chemical and physical transformations that aerosol particles undergo during atmospheric transport. Figure 1.2 illustrates the general atmospheric aerosol life cycle including particle production, incorporation into and formation of clouds, particle removal processes, and their general influence on the transfer of radiation in the atmosphere.

1.2 Aerosol particle interactions with water vapor and cloud formation

The extent to which aerosol particles influence visibility and climate is partially due to size[24] and chemical composition, and hygroscopic particle properties[25]. Aerosol particles interact with water vapor in Earth's atmosphere to form hydrometeors in the form of liquid droplets or ice depending on the thermodynamic conditions of temperature and the partial pressure of water, $p_{\mathrm{H_2O}}$, defined as the amount of water in air. From emission, aerosol particles are vertically transported due to rising, bouyant air. During their ascent the surrounding air cools due to adiabatic expansion. A rise in the atmosphere is characterized by decreasing temperature. As temperature decreases, the water vapor pressure, $p^{\circ}_{H_2O}$, also decreases. Assuming the amount of water in air does not change significantly, the relative humidity, RH=$p_{\mathrm{H_2O}}/p^{\circ}_{H_2O}$, increases as the air rises. Aerosol particles will remain dry until the RH of the environment is at the particle deliquescence relative humidity (DRH), defined as the point at which particles spontaneously take up water and liquefy. The particles will remain as haze droplets or interstitial aerosol until supersaturation (i.e. when RH exceeds 100%) is reached, defined as the point at which the particles grow spontaneously to cloud droplets.[43] The particles that form cloud droplets are referred to as cloud condensation nuclei (CCN).

1.3 Aerosol influence on radiative transfer

Aerosol particles, clouds, and ice crystals can alter the balance of radiation transferred between Earth and sun. Assuming conservation of energy, the incoming energy of the sun in the form of solar radiation (shortwave) must balance the amount of radiation leaving Earth, including reflected shortwave and Earth's longwave radiation. Understanding current and future climate

depends on our ability to quantify changes in temperature due to perturbations in the balance of radiation, which is affected by changes in greenhouse gas concentrations, particles, and clouds. Figure 1.3 shows the different radiative forcing components, extent of forcing, and level of certainty or understanding associated with each atmospheric constituent, relative to pre-industrial conditions.[6] Radiative forcing is defined in Stocker *et al.*[6] as the net change in irradiance from short and longwave radiation at the tropopause allowing for stratospheric temperatures to readjust keeping tropospheric and surface temperatures fixed. The radiative forcing can be directly related to the global mean surface temperature change at equilibrium. A positive radiative forcing indicates a global rise in temperatures, while a negative radiative forcing indicates cooling.

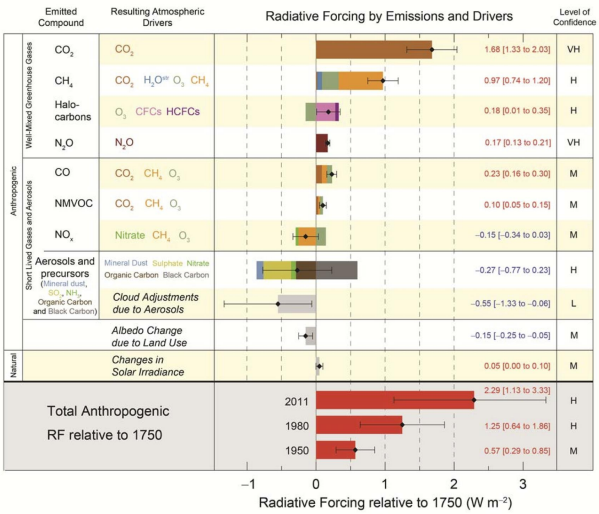

Figure 1.3: The difference in the globally averaged radiative forcing estimates due to greenhouse gases, aerosols, and clouds for 2011 relative to pre-industrial conditions defined at 1750. The change in radiative forcing is defined as the change in net (downward minus upward energy flux) irradiance (incoming solar radiation plus outgoing long-wave radiation in units of energy in Watts per square meter of Earth's surface, W m^{-2}). Adapted from Stocker *et al.*[6].

Aerosol particles ultimately cool Earth's surface as indicated by its overall

negative contribution to the radiative flux as shown in Fig. 1.3[6]. Aerosol particles cool Earth's surface by producing brighter, i.e. more reflected, and less efficient precipitating clouds[47]; however, aerosol particles containing black carbon and so-called "brown" clouds, which are associated with urban haze, can enhance surface and atmospheric temperatures by absorbing incoming solar radiation or outgoing longwave radiation due to their low reflectivity (i.e. albedo)[5,48]. There are two mechanisms by which aerosol particles can influence radiative forcing and thus climate: (1) *the direct effect*, whereby aerosol particles directly scatter incoming shortwave radiation back to space, which reduces solar insolation and cools the surface of Earth or (2) *the indirect effect*, whereby aerosol particles acting as CCN or IN modify the radiative properties of clouds.

Despite this effort, our level of understanding of the radiative forcing component of the aerosol indirect effect remains poor. This is attributed, in part, to the complex transformation pathways that aerosol particles undergo during transport in the atmosphere, including chemical aging[8,9,12]. In other words, our ability to predict how aerosol particles will impact cloud formation and thus indirectly radiative transfer, depends on our understanding of the particles' physical and chemical nature at the onset of cloud formation, which is influenced by atmospheric aging processes.

1.4 Atmospheric organic aerosol sources

Organic aerosol particles are the most dynamic class of atmospheric aerosol and are continuously modified during atmospheric particle transport due to interactions with different atmospheric constituents including trace gas-phase oxidants and VOCs. In this section, the different organic aerosol sources are outlined and discussed in some detail.

1.4.1 Primary organic aerosol

Organic or carbonaceous aerosol particles are the most complex aerosol in the atmosphere since they can contain thousands of different organic compounds[49]. They are also the least stable due to their relatively high susceptibility to reaction with gas-phase atmospheric constituents[8,12,32]. Much of its complexity is owed to the many different sources from which organic aerosol is derived. Organic aerosol particles can be emitted directly to the atmosphere in particulate form from the burning of biomass (e.g. wood

burning and cooking) and fossil fuels (e.g. motor vehicles). These particles are referred to as primary organic aerosol (POA). POA emitted from combustion processes typically include elemental or black carbon (EC/BC) and hydrocarbon-containing organic material, including polycyclic aromatic hydrocarbons (PAHs), anhydrosugars, and unburnt motor fuel. Other major sources of POA are derived from wind-driven processes, including the suspension of pollen grains and waxes from plants, and the aerosolization of dissolved organic carbon and biological material from sea spray or wave breaking activity. For example, the production of organic aerosol over the oceans is strongly correlated with high biologically active periods.[50] POA particles can be several hundreds of nanometers in diameter and thus can persist in the atmosphere up to several days to weeks, depending on the conditions of the ambient environment.

1.4.2 Secondary organic aerosol

In addition to the emitted POA, a significant source of atmospheric OA is formed in the atmosphere in situ through oxidation reactions between gas-phase oxidants such as OH, O_3, and NO_3 and volatile organic compounds (VOCs) emitted from both biogenic and anthropogenic sources.[43] The resulting reaction products are typically oxidized, low-volatility organics that can partition to the aerosol phase[10]. The partitioning process can occur both homogeneously through nucleation of low-volatility vapors or heterogeneously through condensation of low-volatility vapors onto pre-existing aerosol particles. Globally, the largest source of SOA comes from biogenic emissions from forest environments[51]. Daytime SOA production in forested environments is largely attributed to reactions between monoterpenes emitted from trees and OH and O_3[52,53]. At nighttime, NO_3 radicals can contribute to the overall organic aerosol burden through VOC oxidation[54]. A key issue in the production of SOA is the availability of trace gas-phase oxidants and VOCs, which depend on the prevalence and strength of different emission sources. In general, SOA production is more prevalent in polluted environments, but the extent of production depends on many factors, including relative humidity, initial oxidant concentration, temperature, particle acidity and phase, molecular structure, and pre-existing aerosol mass loading[38,55,56].

Despite our understanding and ability to identify some key SOA sources and precursors, model estimates of atmospheric SOA concentrations based on experimental data largely underpredicts SOA mass[57–59]. A potentially

important source of this discrepancy is that there is a large source of unaccounted "missing" SOA mass or SOA precursors. Recent studies have highlighted the importance of an unclassified set of compounds derived from semi-volatile POA that may be a possible missing SOA source[60]. Similarly, reaction products formed from POA oxidation are known to contribute to the overall VOC burden[37]. These products exhibit a range in volatility and thus may represent a missing source of SOA. However, the mechanisms, pathways, and sources from which these missing SOA precursors are derived, has not been explored in detail.

1.5 Atmospheric trace gases

The Earth's atmosphere consists of both reactive and non-reactive gases, which are essential for life and in driving atmospheric temperatures and other meteorological processes. The most abundant gases in Earth's atmosphere are nitrogen (N_2), oxygen (O_2) and the noble gases (e.g. Ar and He). N_2 and O_2 are derived from biological and microbiological processes including anaerobic respiration and photosynthesis, and together make up ∼99% of Earth's atmosphere (∼78% N_2 and 21% O_2). The noble gases are produced from the radioactive decay of rocks. The remaining gases, considered "trace" gases because they constitute collectively <1% of gases in the atmosphere, are comprised of the greenhouse gases, which include water vapor (H_2O), CO_2, CH_4, and CO, H_2, OH radicals, ozone (O_3), nitrogen oxides (e.g. NO_x), and volatile organic compounds (VOCs). Their atmospheric concentrations depend on their source strengths and decay rates. Gases are removed from the atmosphere by chemical reactions, biological activity, physical and chemical interactions with aerosol particles, and by deposition to the oceans and Earth's surface[43].

While radicals such as OH, Cl and NO_3 constitute a small percentage by volume of gas in the atmosphere, they play important roles in atmospheric chemistry and air quality. The oxidation potential of the atmosphere is primarily driven by OH radicals, which are formed through photodissociation of O_3 by ultra-violet (UV) radiation, producing $O(^1D)$ atoms followed by OH via

$$O_3 + h\nu\ (\lambda \leq 320 \text{ or } 410 \text{ nm}) \rightarrow O(^1D) + O_2 \qquad \text{R1}$$
$$O(^1D) + H_2O \rightarrow 2\ OH \qquad \text{R2}$$

Globally and diurnally averaged tropospheric OH radical concentrations are

on the order of 10^6 molecule cm^{-3}, which corresponds to a tropospheric mixing ratio of only about 0.04×10^{-12} or 0.04 parts per trillion (ppt). However, reaction with OH is the major sink for most trace gases, and thus their atmospheric lifetimes and concentrations are largely determined by their reactivity with OH. For example, the simplest hydrocarbon, methane (CH_4), reacts slowly with OH, resulting in a residence time in the atmosphere of about 8 years. The oxidation lifetimes of other hydrocarbons are typically shorter and depend on the hydrocarbon's structure[43,61]. For example, relatively larger organic gas molecules including isoprene (C_5H_8) have a residence time in the atmosphere of less than an hour due to reaction with OH, and thus its concentration is highly variable in space and time.

Essential for OH is the presence of O_3. Tropospheric O_3 is derived from the photodissociation of NO_2, and thus O_3 is directly linked to human activities. O_3 is removed and produced in the troposphere by chemical reactions involving the CO, CH_4, and non-methane hydrocarbon (NMHC) oxidation cycles.[62] O_3 concentrations have increased over the years due to enhanced emissions of NO, CO, CH_4, and NMHC by anthropogenic activity. O_3 can be removed by chemical reaction with hydrocarbons, most efficiently with unsaturated (double bond) hydrocarbons[43]. O_3 mixing ratios in background tropospheric air range from about 20-30 ppb, but can reach as high as several hundred ppb under highly polluted conditions[43]. As a result, OH concentrations can reach as high as 10^7 molecule cm^{-3} in polluted air[63]. OH concentrations are generally highest in the tropics due to its high water vapor content; however, some of the largest concentrations of OH in the atmosphere have been measured in biomass burning plumes[63,64].

1.6 Biomass burning particulate and gaseous emissions

From its origins, the burning of biomass, i.e. wood, land, and crops, has been a cheap and effective method in e.g. land-clearing and agricultural processes, providing a source of heat for cooking and in warming households, and a source of energy for mechanical means, including the steam engine. Biomass burning is an important source of greenhouse gases, VOCs, and fine particulate matter to the atmosphere. Fires from deforestation, for example, have contributed an estimated 19% of global CO_2 radiative forcing since the dawn of the industrial revolution[65]. While only a small portion of global biomass burning emissions come from North America, it can play an important role in contributing to poor regional air quality in the US. In

the US, an estimated 50% of the annual mean particulate carbon concentrations is attributed to biomass burning.[66] Globally, biomass burning accounts for an estimated 2.5 $PgCyr^{-1}$, most of which come from the tropics[67]. Reflectance data from satellite retrievals indicate that globally, biomass burning accounts for a footprint of 464 Mha yr^{-1}, or equivalent to ∼36% of cropland on Earth.[68] With an expected increase in the world's population by another billion by 2020,[69] evaluating the effects of land-use change such as biomass burning on Earth's climate will become increasingly important.[70,71]

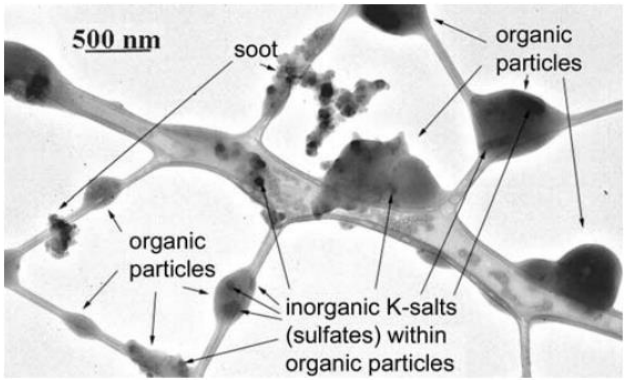

Figure 1.4: Scanning electron microscope (SEM) image of a portion of a sample of young smoke particles from a smoldering and flaming fire. The particles are attached to a lacey support film; most particles are carbonaceous (organic) with inorganic K-sulfate inclusions. This image was adapted from Posfai *et al.*[72]

Biomass burning aerosol (BBA) constitutes the largest source of POA to the atmosphere, representing an estimated 90% of POA and 40% of black carbon[20], and has a source strength similar to fossil-fuel burning.[73] BBA is a complex mixture of inorganic and organic compounds as determined in both field[74–82] and in controlled laboratory settings,[83,84] but are composed largely (∼80%) of organic carbon.[82] Black or elemental carbon, soot, and tarballs are also common materials found in BBA as a result of incomplete combustion. An example BBA particle is shown in Fig. 1.4 and indicates potassium sulfate rich particles encased in organic coatings. Humic like substances (HULIS) including fulvic and humic acids are surrogate biomass burning compounds, which represent multifunctional organic ma-

terial with high molecular weight typical of BBA.[85–89] While BBA composition can vary depending on vegetation-type[82], a major mass fraction of biomass burning organic aerosol (BBOA) consists of pyrolyzed cellulose and hemicellulose such as levoglucosan (1,6-anhydro-β-glucopyranose, $C_6H_{10}O_5$), resin acids such as abietic acid (1-phenanthrenecarboxylic acid, $C_{20}H_{10}O_5$), and substituted phenols from lignin decomposition such as 5-nitroguaiacol (2-methoxy-5-nitrophenol, $C_7H_7NO_4$).[90–93] Levoglucosan is a commonly applied molecular marker in biomass burning source apportionment studies,[94] but has recently been shown, along with abietic acid and nitroguaiacol, to be photochemically unstable with respect to heterogeneous reactions with trace gas species such as OH, O_3, and NO_3.[13,15,83,95]

Biomass burning is a major precursor to a number of long-lived greenhouse gases including CO, NO, H_2O, and CO_2 and relatively short-lived reactive trace gases such as O_3, OH, and NO_2.[71,73,96] Non-methane VOC composition in biomass burning plumes is complex due to the many diverse biomass fuels, but consist mostly of C_2-C_{11} hydrocarbons composed of alcohols, aldehydes, ketones, carboxylic acids, esters, ethers, and furanes.[80,97] The production and consumption of these VOCs can depend, to a large extent on heterogeneous and gas-phase reactions by OH.[15,37,80,83,98] Next to SOA production from forest VOC emissions, a significant source of SOA is generated during oxidative aging of VOCs emitted during biomass burning.[51,84] Recently, methyl-nitrocatechols (e.g. 4-methyl-5-nitrocatechol, $C_7H_7NO_4$) have been identified as a tracer species for biomass burning SOA[99] generated during the OH oxidation of cresol in the presence of NO_x.[99,100] A key point here is that these VOCs, whether emitted directly or volatilized from pre-existing particle surfaces present possible missing SOA precursors that require further study.

1.7 Atmospheric aerosol particle removal mechanisms

Our ability to quantify the climatic and air quality effects of aerosol particles depends on how well the particles' lifetime can be predicted during atmospheric particle transport. Aerosol particle lifetimes will depend on how efficiently they are removed from the atmosphere. In this section, the different aerosol removal processes are discussed in more detail.

Sinks of atmospheric aerosol particles include dry and wet deposition, and chemical reaction. Dry deposition is a continuous process and refers to the removal of particles from the atmosphere onto surfaces in the absence

of precipitation. Its effectiveness will depend on particle size and density. For example, smaller particles, having in general less mass than larger particles of the same density, can more efficiently be transported vertically in the atmosphere through turbulent motions and updrafts, and thus can persist at higher altitudes away from surfaces near the ground. More dense aerosol particles settle faster than less dense particles because they exhibit less bouyancy. Very small particles (i.e. $<0.1\mu$m) behave similar to gases and are effectively removed by dry deposition due to turbulent transport and Brownian diffusion[43]. Particles in the coarse mode (>1 μm) are efficiently removed by gravitational settling because of their large settling velocities. Particles having sizes in the accumulation mode ($0.1\mu\text{m} \leq \text{x} \leq 1\mu\text{m}$) are not easily removed via dry deposition and thus its major removal pathway is through wet deposition processes.

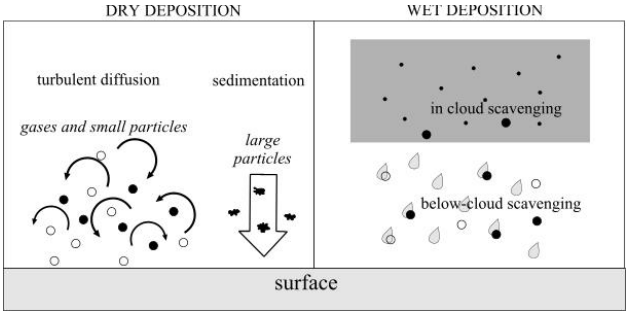

Figure 1.5: Major processes associated with dry and wet deposition of aerosol particles[101].

Wet deposition is a sporadic event and removal pathways can be categorized as in-cloud and below-cloud scavenging as illustrated in Fig. 1.5. Below-cloud scavenging refers to particle scavenging by precipitation (rain-out/washout) and in-cloud scavenging refers to removal processes that occur when particles are removed at cloud level such as nucleation scavenging during cloud formation (i.e. coagulation) and dissolution into aqueous droplets. Aerosol particles in the accumulation mode are removed via wet deposition over a period of a few days up to a couple of weeks, and hence accumulation mode particles typically remain in the atmosphere for about a week. Wet deposition accounts for $\sim$85% of the removal of organic aerosol in the troposphere[10], the most important of which is cloud formation. Globally, up to

~60% of Earth is covered by clouds, but only 10% produce rain[10].

Chemical reactions between organic aerosol particles and radical species, including Cl and OH radicals, is thought to be another important sink for organic aerosol[32]. OH or Cl radical reactions with organic compounds can lead to the formation of smaller, low molecular weight, or fragmented reaction products. These reaction products possess a higher vapor pressure than their parent compound and are lost to the gas phase, a process referred to as "volatilization" since the reaction products are volatile. Long term exposure to OH radicals has been shown to completely evaporate thin organic films[32] and significantly reduce particle mass[95]. Volatilization does not only reduce the mass of organic aerosol particles, but also alters the budget of VOCs[37] and provides a source of condensable organic vapors in the nucleation process or growth of new or pre-existing particles.

1.8 Atmospheric aerosol aging

Broadly defined, aerosol particle "aging" refers to the physical and chemical transformations that aerosol particles undergo when residing in the atmosphere. Aging is a major process governing aerosol particle chemical composition, lifetime, and its role in air quality and climate change[7–9]. Source-specific condensed-phase organic compounds, which include oleic acid for meat cooking, hopanes for gasoline engines, and levoglucosan for wood burning are commonly employed molecular markers used for apportioning their specific emission sources[102–104]. However, chemical and physical transformations to the particles during particle transport can significantly alter their chemical and physical makeup. Thus, quantifying the rate of chemical transformation and aging of aerosol particles is vital to the integrity of using molecular markers for identifying aerosol sources, the age of aerosols, and in understanding the aerosol's role in air quality and climate change.

Figure 1.6 gives a general overview of the different atmospheric aerosol aging processes. Aerosol particles transform chemically and physically following emission. Chemical transformations to aerosol particles can occur from interactions with water vapor and other chemically reactive gases including OH, O_3, and NO_3. Physical transformations to aerosol particles, such as changes to particle size and mass, can occur via condensation and coagulation[43]. In general, atmospheric aerosol aging can significantly alter the particles' efficiency to take up water vapor and serve as CCN or IN[7–9,16]. Physical changes to particle phase due to e.g. water uptake during atmo-

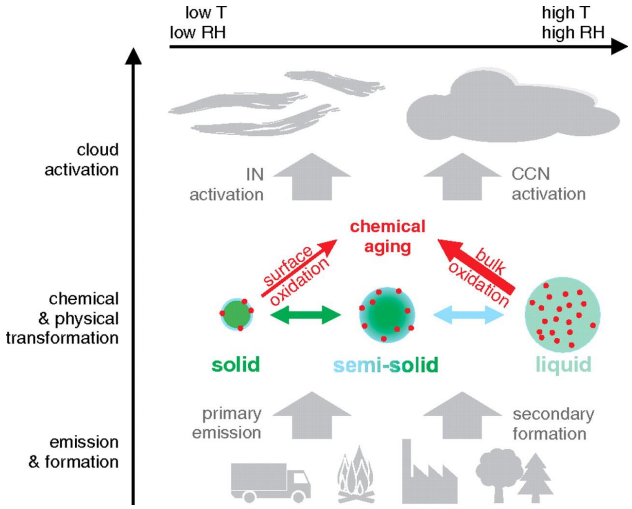

Figure 1.6: Major processes associated with aerosol aging. The red circles symbolize gas-phase molecules. This figure is adapted from Shiraiwa *et al.*[33].

spheric transport can alter the degree that the particles interact with trace gas-phase species as illustrated in Fig. 1.6. Particle phase can alter the extent that aerosol particles age by gas-to-particle, so-called "heterogeneous" reactions. Heterogeneous reactions can be limited to the particle surface under dry atmospheric conditions when the particles exhibit a solid phase, than at higher RH when the particles are more likely to exist as a semi-solid or liquid[33]. Aging can impact the aerosol particles' chemical composition and potency in the environment, e.g. toxicity and solubility in water, thus impacting the carbon and hydrological cycles[10]. Consequently, the aging process of atmospheric aerosol is important in assessing how e.g. advected (aged) air masses influence cloud formation and the environment. In this section, major physical and chemical aging mechanisms are discussed, which will lead to a more refined discussion of the current status of our understanding of BBA aging and its environmental significance.

1.8.1 Physical aging mechanisms

Aerosol particles can age physically, e.g. change in size and mass, through processes such as coagulation, condensation, and evaporation[43]. Coagulation refers to the growth in particle size when one particle comes in contact

with another particle (of same or varying size). Coagulation reduces the total number concentration of particles in air and increases particle size[43]. Physical aging through condensation refers to the growth of particles due to uptake of condensable atmospheric constituents, e.g. low-volatility organic compounds or water vapor. The condensation of water vapor onto aerosol particles is the first step in cloud formation. Condensation enhances particle size, but does not increase the total number concentration of particles in air[43]. Particle evaporation due to the particles' exposure to high temperatures or evaporation following chemical reaction[32] can lead to a reduction in particle size and mass.

The particles' physical properties including particle phase (solid, semisolid, or liquid) depend strongly on temperature and water vapor (i.e. RH)[33,105,106]. In general, high temperatures or RH can induce a physical transformation of the particle from a highly viscous state to a less viscous one[105], since water acts as a plasticizer. An example of such a physical transformation is the phase change from solid to liquid upon melting. Particle deliquescence (i.e. transformation from solid to liquid due to water uptake) is another example of physical aging. Particle phase is an important determinant in the rate at which aerosol particles interact with gas-phase material, for example the uptake of O_3 or OH by condensed-phase organics at different RH[33,107].

1.8.2 Chemical aging mechanisms

Chemical aging refers to the changes in particle chemical composition due to aqueous-phase, multiphase, or heterogeneous reactions with adsorbed trace gas species, including oxidants such as OH, O_3, and NO_3[8,9,12,33]. Heterogeneous oxidation can alter the particles' hydrophilicity, or ability to take up water vapor, which influences particle wet depositional losses and cloud formation[10,16,17]. In addition to an increase in particle size and mass, condensation and coagulation of chemically different components can change the particle's chemical composition[10]. Important examples of heterogeneous reactions that impact atmospheric chemistry and other atmospheric phenomena include the heterogeneous hydrolysis of N_2O_5, known directly to impact the concentrations of nitrogen oxides, which drive much of the important chemical reactions related to photochemical smog and ozone formation, and nighttime removal of NO_x[108], and the formation of Cl reservoir species from heterogeneous reactions on polar stratospheric ice clouds, which leads to stratospheric ozone depletion in the polar spring[109]. Oxidation of gas-phase

precursors can generate low vapor pressure products that contribute to the atmospheric OA burden by producing SOA. Many of the products resulting from oxidation of OA and gas-phase precursors are semi-volatile, thus atmospheric chemical aging can influence the mass transport of organics to and from the particulate phase.

The extent that particles age chemically during particle transport depends on particle and gas-phase composition, oxidant concentration, particle phase, and lifetime. For example, the uptake of O_3 and NO_3 and the subsequent oxidative aging of representative organic aerosol surfaces, although relatively slow, can compete with the oxidizing potential of OH due to their relatively higher atmospheric concentrations[7,13]. Furthermore, the heterogeneous oxidation of model OA surfaces and particles shows a strong dependency on RH and particle phase[33,34,107], which in turn affects the lifetime of organics in the aerosol phase[95,107] and OA particle lifetime[32,35,107,110]. During particle transport, aerosol particles experience different RH and temperature, which may impact the chemical aging process and lifetime of OA. However, the effects of varying RH and temperature on the chemical aging and lifetime of OA, and its role in air quality and climate is not well-characterized.

1.8.3 The effect of aging on particle hygroscopicity

Chemical aging of aerosol particles can lead to an increase in the particles' hygroscopicity by forming for instance more polar, hygroscopic products than its predecessor, and thus is a key process determining the wet deposition and hence residence time and atmospheric burden of organic particles in the atmosphere[8,9,111]. For example, the OH oxidative aging of stearic acid and bis-ethyl sebecate (BES) particles, representing single-component unsaturated and saturated atmospheric OA, respectively, become more hygroscopic with exposure to OH[17]. Additionally, aging of oleic acid particles by O_3 has been shown to increase the particles' hygroscopicity and ability to nucleate clouds[112,113]. The CCN activity of model unsaturated and saturated OA is shown to increase following oxidation by OH and NO_3[16]. The hygroscopicity of OH oxidized biogenic SOA has been shown to increase with greater exposure to OH as a result of increasing oxygen-to-carbon (O:C) ratio[114]. Studies of diesel soot particles coated by benzo(α)pyrene (BaP) demonstrate that the particles become more hydrophilic with O_3 exposure[115]. Conversely, chemical aging may reduce the ability of an aerosol particle population to act as CCN by reducing particle size through volatilization reactions[30]. Conse-

quently, understanding the aging process of atmospheric aerosol is important in assessing its role in cloud formation and thus climate.

1.9 Chemical and physical aging of biomass burning aerosol

BBA has a significant, yet poorly quantified impact on air quality and climate[73,116–119]. This uncertainty is due in part to the temporal and spatial variability of biomass burning smoke and its optical properties.[6] Biomass burning aerosol particles can change chemically, physically, and optically during atmospheric particle transport[21,83,120–125] thereby, in some cases, reach the upper troposphere (UT) and lower stratosphere (LS)[126–128]. As BBA particles are advected and transported vertically, they experience a wide range of temperatures and RH, which can influence particle phase. Chemical aging by heterogeneous OH and O_3 oxidation can influence the oxidation state of BBA and thus its ability to act as CCN. Evidence from in-situ mass spectrometric analysis of the organic component of biomass burning aerosol indicates a shift in oxidation state from less oxidized to more oxidized over the course of a day, likely due to a combination of heterogeneous reactions with trace gas-phase oxidants and scavenging of other, more oxidized, low-volatility organic species[124]. An increase in the organic aerosol mass, total aerosol concentration, and modal particle diameter also accompany the aging process of BBA[124]. Measurements of single scattering albedo of smoke plumes near its emission source and aged biomass burning haze show a shift from low to high single scattering albedo as the aerosol ages[120,129]. Abel *et al.*[120] suggests that the condensation of scattering material from the gas phase was the dominant mechanism leading to higher albedo. Heterogeneous OH oxidation of model organic aerosols squalane and azelaic acid have been shown to enhance the aerosol extinction cross-section with increasing exposure to OH radicals, which corresponds to an increase in both oxygen to carbon (O:C) atomic ratio and particle density.[130] Unfortunately, the mechanisms and kinetics of heterogeneous oxidation of biomass burning organic aerosol and its effects on BBA-atmosphere interactions are poorly characterized. This is an outstanding issue as our ability to predict the particles climatic and air quality impacts depends crucially on our ability to predict how the particles age during particle transport.

1.10 Dissertation objectives

The overall objective of the results presented in this dissertation is to advance our understanding of heterogeneous chemical kinetics and processes that occur between reactive trace gas species and organic aerosol particles. This work focuses on the heterogeneous OH oxidation of BBA. Specific objectives include measuring the rate that OH is taken up or reacts with BBA surrogate-particles and substrates, the formation of volatile reaction products, exploring potential physical and chemical mechanisms that limit OH uptake, and the role OH-initiated oxidative aging of BBA plays in the particles' CCN activity and lifetime. To achieve this, several well-controlled experiments employing state-of-the-art chemical instrumentation and particle analysis techniques were used to quantify and identify gas-phase reactants and products in the presence of different substrate and aerosolized forms of BBA, and to measure the particles' CCN activity.

2 Background and Theory

2.1 Water vapor

Water vapor plays an important role in regulating the temperature of the atmosphere, cloud formation, particle phase, aqueous-phase chemical reactions, and thus radiative transfer and climate. Relative humidity is defined as the ratio of the water partial pressure (p_{H_2O}) to the pressure exerted over a plane surface of pure water, referred to as its equilibrium vapor pressure, ($p^{\circ}_{H_2O}$), which is dependent on temperature. Figure 2.1 shows the temperature-dependence of $p^{\circ}_{H_2O}$ [131].

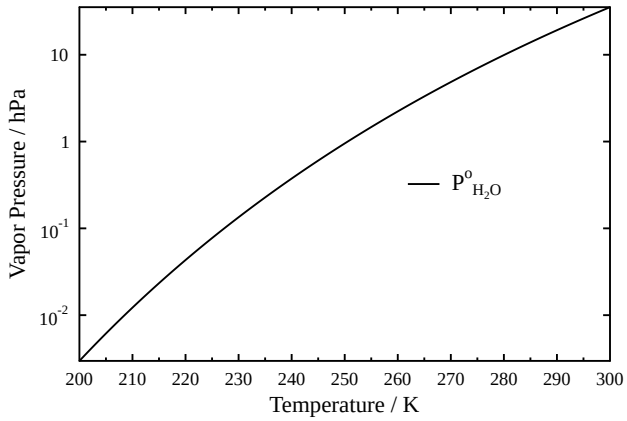

Figure 2.1: Water vapor pressure with respect to a plane surface of pure water, $p^{\circ}_{H_2O}$, as a function of temperature [131].

The vapor pressure of water over a flat surface of pure water is described by the water activity, a_w, where

$$a_w = \frac{p_{H_2O}}{p^{\circ}_{H_2O}}. \quad (1)$$

The water activity over pure water is equivalent to the relative humidity of the environment when the water vapor pressure is equal to the ambient partial pressure. In cases where the water is mixed with soluble material, the activity of water in the aqeuous solution is lowered, referred to as the Raoult effect; in the complete absence of water, a_w=0. The suppression of the water

activity over an aqueous solution droplet containing soluble material at a given droplet size is described as[132]

$$a_{\mathrm{w}} = 1 - \frac{6 n_{\mathrm{s}} M_{\mathrm{w}}}{\pi \rho_{\mathrm{sol}} D^3}, \tag{2}$$

where n_s is the number of moles of solute in solution, which depends on the number of ions dissociated, i.e. van't Hoff factor (ν). Thus, aerosol particles containing water-soluble material can lower the water activity over solution. As an aqueous droplet comes into equilibrium with the surrounding water partial pressure, water will either condense onto or evaporate from the droplet, thus increasing or decreasing its water vapor pressure, respectively, until the vapor pressure of the aqueous solution droplet is in equilibrium with the partial pressure of the environment. At this point, a_{w}=RH.

2.2 Particle phase and diffusivity

Phase refers to a solid, liquid, or gas state. A change in phase is usually a consequence of a change in temperature or pressure. Examples of a change in phase include melting of ice, a solid-liquid phase transition, evaporation of water, a liquid-gas phase transition, and water condensation, a gas-liquid phase transition. Both temperature and water activity affect the motions of molecules in solution. An increase or decrease in temperature will increase or decrease molecular motions, respectively. An increase in water activity due to the condensation of water vapor can promote liquefaction. Thus, it follows that aerosol particle phase, size, and water content will vary with respect to changes in ambient RH and temperature. This section briefly describes the different phase states and changes to particle phase in response to water uptake and evaporation, and the glass transition of organic aerosol particles.

2.2.1 Particle deliquescence and efflorescence

This section briefly discusses how aerosol particles grow, shrink, and undergo phase transitions in response to water uptake at different RH. Figure 2.2 demonstrates the effect of varying RH on the size changes to liquid and crystalline aerosol particles as described in Koop *et al.*[105].

In Fig. 2.2a and Fig. 2.2b, water uptake by a pure liquid particle is shown as a function of RH. At low RH, the particle is comprised only of the pure

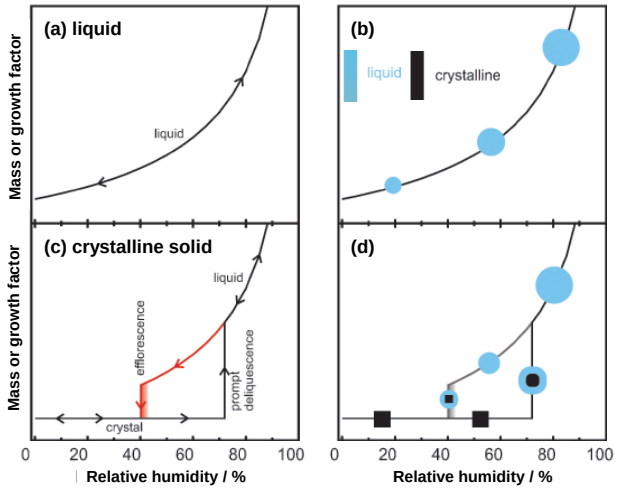

Figure 2.2: (a,b) water uptake and release by a liquid particle with negligible water vapor pressure; (c,d) water uptake by a crystalline solid particle and water evaporation by an aqueous droplet until reaching its original crystalline state. This figure was adapted from Koop *et al.*[105]

liquid solute. Upon increasing RH, the particle continuously takes up water since thermodynamic equilibrium exists between the partial pressure of water in the gas-phase and the equilibrium vapor pressure of the liquid droplet. Upon drying, the particle shrinks, but follows the same growth pathway as a function of RH since thermodynamic equilibrium exists at all RH[105].

In Fig. 2.2c and Fig. 2.2d, water uptake by a water-soluble crystalline solid particle is shown as a function of RH. Under dry conditions, the crystal is in a stable state and remains stable with increasing RH until the particle's deliquescence RH (DRH) is reached, at which point the liquid phase is thermodynamically favored and the crystal grows instantaneously to an aqueous solution droplet. With increasing RH, the aqueous solution droplet behaves similar to pure liquid water uptake as described in Figs. 2.2a,b. Upon drying (Fig. 2.2d), water in the aqeuous droplet evaporates and above the DRH, the droplet and gas phase are in thermodynamic equilibrium. Below the DRH, water does not completely evaporate from the particle and the particle remains in a metastable liquid state since crystallization is kinetically hindered until the occurrence of an initial nucleation step. The RH at which the par-

ticles crystallize is referred to as the efflorescence RH (ERH) at which point the stable state is crystalline.

2.2.2 Amorphous phase state

Aerosol particles can exhibit many different phases and morphologies (solid (glassy), semisolid, or liquid) depending on conditions of the ambient environment such as RH and temperature. Most organic aerosol exhibit an intermediate, amorphous semisolid or glassy phase state that transitions between more and less-viscous phases depending on conditions of temperature and RH[105]. Recent studies have shown that SOA derived from several different biogenic and anthropogenic precursors exhibit amorphous solid or semi-solid phases[105,133–135]. Conversely, inorganic salts such as NaCl and mineral dust exhibit a solid crystalline structure. Figure 2.3 is a phase diagram of aqueous levoglucosan, indicating the different phase states of levoglucosan depending on temperature and mass fraction of the solute[136]. The diagram indicates that an increase in mass fraction of solute corresponding to a decrease in a_{w}, decreases the temperature required to melt or freeze the solution, while raising the temperature at which levoglucosan transitions from a solid (glassy) phase to a semi-solid or liquid phase state.

Particle phase can be characterized based on viscosity (η, in units Pa·s) or self-diffusion of the bulk condensed-phase material. Viscosity is a measure of rigidity, such that the larger the viscosity the more solid the material. For example, a marble has a viscosity on the order of 10^{12} Pa·s, while water has a viscosity on the order of 10^{-3} Pa·s. To a first approximation, the Stokes-Einstein equation shown in Eq. 3 relates viscosity to bulk diffusivity (D_{bulk}, in units cm^2 s^{-1})[105].

$$D_{\mathrm{bulk}} = \frac{kT}{6\pi\eta r}, \tag{3}$$

where k is the Boltzmann constant, T is the absolute temperature, and r is the radius of the molecule assumed to be spherical. The Stokes-Einstein equation works well for most liquids at relatively high temperatures, but breaks down for supercooled liquids and near the glass transition temperature due to the formation of highly mobile and cooperative molecular clusters, referred to as "dynamic heterogeneities", which facilitates molecular diffusion, but not the relaxation time of the system (τ_{D}, defined in Eq. 4)[137]. The bulk self diffusion coefficient and viscosity are important particle physical parameters that can be related to particle phase. For example, aerosol particles exhibiting

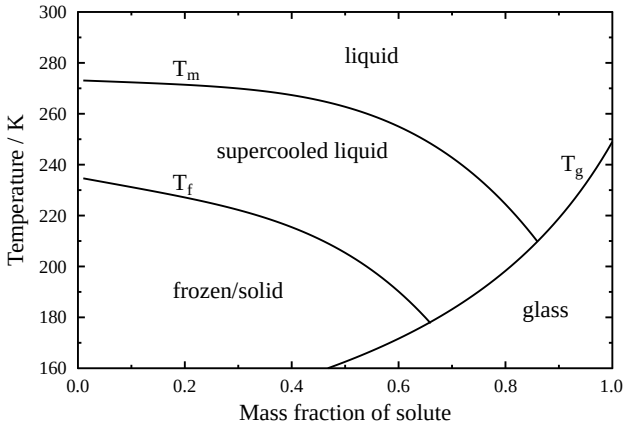

Figure 2.3: Phase diagram of levoglucosan. The labels T_{m}, T_{f}, and T_{g} refer to the melting temperature, homogeneous freezing temperature, and glass transition temperature of levoglucosan, respectively. Below each curve is given the corresponding phase state of the particle (i.e. liquid, supercooled liquid, frozen solid, or glass). The curves were generated from the parameterizations presented in Lienhard *et al.*[136].

intermediate viscosities from 10^2-10^{12} Pa·s have semisolid features and physical properties similar to ketchup, peanut butter, or pitch[105]. Low-viscosity liquid aerosol particles may exhibit similar physical features as honey or olive oil[105]. Cloud droplets, which constitute highly dilute aqueous solutions have viscosities close to that of water and thus relatively larger bulk diffusion coefficients. The time required for self-diffusion to reach a stable, homogeneously mixed state is given by:

$$\tau_{\mathrm{D}} = \frac{r^2}{\pi^2 D_{\mathrm{bulk}}}, \tag{4}$$

where r is the particle radius and D is the condensed phase diffusion coefficient. For non-viscous liquids, D can be as large as 10^{-5} cm^2 s^{-1}, which for a particle diameter of 100 nm corresponds to a diffusive mixing timescale on the order of 10 μs. Conversely, viscous particles such as organic glasses and solid particles have much longer diffusive mixing timescales that can take several years[33,105,138]. This timescale for self-diffusion is paramount for heterogeneous reactions as it also dictates diffusion timescales of bulk transport of gases into particles, and thus the extent of multiphase reaction.

In Fig. 2.4a and Fig. 2.4b, water uptake by an amorphous (semisolid) particle is shown as a function of RH. Upon increasing RH, the particles take up some water, but because the diffusion of water into glassy matrices can be small, typically less than 10^{-10} cm^2 s^{-1} at room temperature[105], and significantly lower below the freezing temperature of pure liquid water, timescales for equilibrium can be slow and take as long as several years depending on the size of the particle.

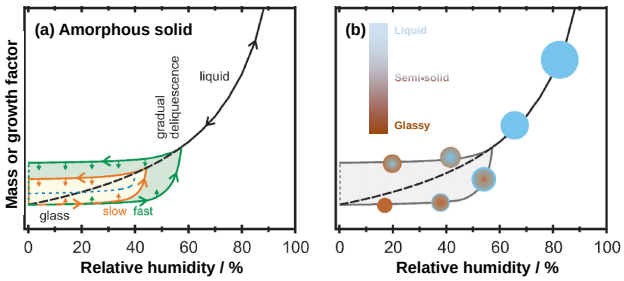

Figure 2.4: Water uptake and release by an amorphous particle showing the humidity-induced glass transition[105].

Water uptake occurs at first only near the particle surface. A self-accelerating water uptake process is established since further increases in RH softens the particle, which decreases the particle's viscosity and increases water diffusivity. Thus, deliquescence is gradual for amorphous particles and the particles can transiton from a highly viscous glassy state to a viscous liquid state, referred to as the humidity-induced glass transition[105,133]. This non-ideal water uptake behavior has been observed experimentally for different carbohydrates, anhydrosugars, polymeric materials, and glass forming inorganics[105,106,139]. Upon drying, the solute concentration increases and the particles become more viscous as water diffusivity is reduced. Water-diffusion limitations in the particle bulk limits water transport from the particle core to surface, while water evaporates from the surface. This process may lead to the formation of a highly viscous or solid shell at lower RH that encapsulates a liquid core. Thus, even near RH=0%, amorphous particles can still retain significant amounts of liquid water[105,106,140]. While the particle's water content will gradually approach the equilibrium conditions of the dashed black line in Fig. 2.4a, the exact kinetics and timescales for diffusion can vary, and thus the shaded region in Fig. 2.4b represents the water content range

accounting for this effect.

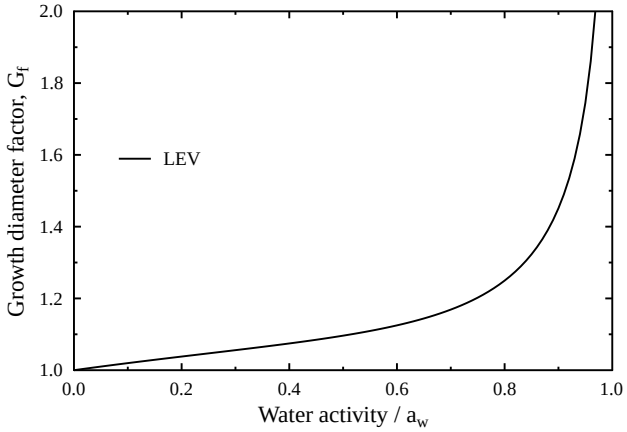

Figure 2.5: The growth factor, G_f, of levoglucosan plotted as a function of its water activity, a_w applying a fit to experimental data in Mikhailov *et al.*[106]

Levoglucosan has amorphous properties, exhibiting gradual deliquescence[106] and retaining significant amounts of water even at low RH near 0%[140]. Knowledge of the particle's initial dry size and size change following water uptake can be used to determine the particle's growth factor at a given RH. The growth factor is determined as a function of the solution's a_w, which parameterizes water uptake for that individual material over a range of RH. Levoglucosan has a known growth factor of ∼1.33 at RH=85%[106,140], which varies as a function of a_w using the approximation in Kreidenweis *et al.*[141]

$$G_f = (1 + [k_1 + k_2 \cdot a_w + k_3 \cdot a_w^2] \times \frac{a_w}{1 - a_w})^{1/3}, \quad (5)$$

where the parameters $k_{1,2,3}$ are fitting parameters applied to experimental data. Figure 2.5 shows the change in G_f for levoglucosan as a function of its a_w applying the fitting parameters in Mikhailov *et al.*[106].

2.2.3 Glass transition temperature

In general, the molecular viscosity decreases with increasing temperature and RH, and vice versa. Higher temperature or RH increases molecular translational motions[105,142,143]. The reason for this temperature dependence is

that molecules exhibit Arrhenius behavior during activation for a translational molecular jump, leading to faster diffusion at higher temperatures[105]. The temperature at which a transition between liquid/semi-solid and solid states occurs is defined as the glass transition temperature (T_g)[105,142–144]. T_g describes the temperature below which amorphous organic aerosol have solid-like properties and above which exhibit properties of semi-solids or liquids. However, T_g can depend on several factors including the oxygen-to-carbon ratio and mixing state of the particles, and the rate of change in temperature and RH[105].

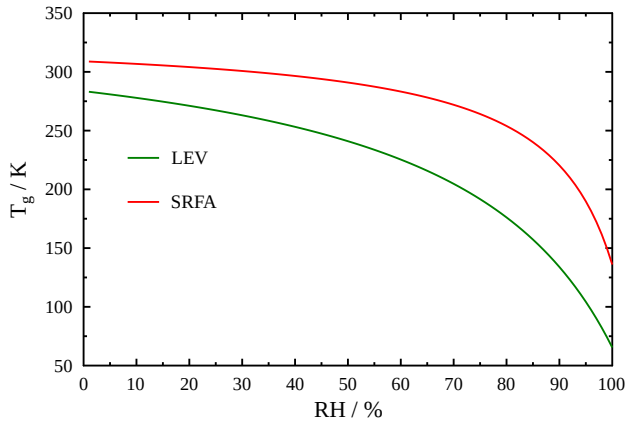

Figure 2.6: Glass transition, T_g, as a function of RH for levoglucosan (green) and Suwannee River fulvic acid (red). κ_{LEV} is assumed to be 0.17[27,145] and κ_{SRFA} is assumed to be 0.07, representing a lower limit to SRFA T_g.

T_g as a function of RH, $T_g(\mathrm{RH})$, can be expressed as[42,105]

$$T_g = \frac{T_{g,w} k_{GT} + f(\mathrm{RH}) T_g(\mathrm{RH} = 0\%)}{k_{GT} + f(\mathrm{RH})}, \tag{6}$$

where

$$f(\mathrm{RH}) = \frac{w_{org}}{w_w} = \frac{100 - \mathrm{RH}}{\mathrm{RH}} \frac{1}{k_{org}} \frac{\rho_{org}}{\rho_w}. \tag{7}$$

w_w and w_{org} are the mass fractions of water and organic matter, respectively, $T_{g,w}$ is the glass transition of pure water of 136 K, k_{GT} is the Gordon-Taylor constant for the specific water/organic system representing the interaction

between water and the organic solute, and κ_{org} is the CCN-derived hygroscopicity parameter of the organic fraction. T_g curves as a function of RH are given in Fig. 2.6, showing the T_g of levoglucosan and Suwannee river fulvic acid, representative BBA compounds.

2.3 Hygroscopicity and cloud droplet activation

The thermodynamic conditions of the environment necessary for cloud formation is such that the partial pressure of water at equilibrium with a given droplet size exceed the vapor pressure of water at a given temperature, and thus is represented by a supersaturation ratio, S (S>1). The required supersaturation ratio for pure water to nucleate cloud droplets is ∼400%, however supersaturations of up to only ∼2% are achieved in the atmosphere[43]. Aerosol particles lower the required supersaturation ratio for pure water cloud activation. The ability for aerosol particles to activate to cloud condensation nuclei (CCN) depends on both size and chemistry of the particle. Larger particles have more surface area to scavenge water molecules and smaller surface area-to-volume ratios that suppresses the Kelvin effect. The CCN activity of atmospheric aerosol particles can be described by the Köhler equation, which relates the saturation ratio over the solution droplet, *S(D)*, to the aqeuous solution droplet particle diameter *D*.

$$S(D) = \frac{p_{w,D}}{p_w^\circ} = a_w \exp\left(\frac{4\sigma M_w}{RT\rho_w D}\right), \tag{8}$$

where σ is droplet surface tension, M_w is the molecular weight of water, R is the universal gas constant, T is temperature, and ρ_w is the density of water. The Köhler equation can be used to predict the minimum supersaturation required for a particle to become CCN active.

Equation 8 can be expressed alternatively by the κ-Köhler equation,[27] which relates dry and wet particle diameter to supersaturation based on a single hygroscopicity parameter, κ as given in Eq. 9:[27]

$$S(D) = \frac{D^3 - D_d^3}{D^3 - D_d^3(1-\kappa)} \exp\left(\frac{4\sigma M_w}{RT\rho_w D}\right), \tag{9}$$

where *S(D)* is supersaturation, D is wet particle diameter, and D_d is dry particle diameter. κ or hygroscopicity is defined as the amount of water per unit volume of dissolved solute and ranges from ∼0.5-1.4 for hygroscopic

inorganic species and from ∼0.01-0.5 for less-hygroscopic organic species; κ=0 represents an insoluble but wettable particle and thus Eq. 9 reduces to the Kelvin equation.[27]

For a given particle diameter, the supersaturation at which the particle is activated to a cloud droplet is referred to as the critical supersaturation, S_{c}. If the diameter of the dry particle size is known at the S_{c}, κ can be determined from the following:[27]

$$\kappa = \frac{4A^3}{27D_{\mathrm{d}}^3 ln^2 S_{\mathrm{c}}}, \tag{10}$$

where

$$A = \frac{4\sigma_{s/a} M_{\mathrm{w}}}{RT\rho_w}. \tag{11}$$

Hygroscopic growth of compounds exhibiting moderate to weak solubility in water can be limited by their low water-solubility[146], and thus cannot be treated as either fully dissolvable or insoluble substances. A theoretical treatment of κ, which includes solubility limitations has been detailed in Petters and Kreidenweis[146]. Here,

$$\kappa = \varepsilon_i \kappa_i H(x_i) \tag{12}$$

$$H(x_i) = \left\{ \begin{array}{ll} 1 & \text{if } x_i \geq 1; \\ x_i & \text{if } x_i < 1. \end{array} \right\},$$

where ε is the volume fraction of the solute i in the dry particle. κ_i is the theoretical κ of solute i in the absence of solubility limitations and given by

$$\kappa_i = \frac{\nu \rho_i m_{\mathrm{w}}}{\rho_{\mathrm{w}} m_i}, \tag{14}$$

where ν is the Van't Hoff factor, ρ_i is the density of solute, ρ_{w} is the density of water, m_i is the molar mass of the solute, and m_{w} is the molar mass of water. x_{i} is defined as the dissolved volume fraction of the solute[146] and given as

$$x_i = C_i \frac{V_{\mathrm{w}}}{V_i}, \tag{15}$$

where C_i is the water solubility of the solute i, expressed as the solute volume per unit water volume at equilibrium with saturation, and V_i and V_{w} are the volumes of the solute i and water, respectively. For complete dissociation, x_i is equal to unity.

2.4 Resistor model for mass transport and gas uptake

The importance of multiphase chemical reactions between trace gas species and aerosol particles and cloud droplets has been recognized since e.g. the discovery that heterogeneous reactions on polar stratospheric clouds lead to the formation of reactive species responsible for strong ozone depletion during polar spring[109,147]. In addition, Schwartz and Freiberg[148] characterized key physical and kinetic mechanisms by which SO_2 is taken up by cloud droplets and aerosol particles that lead to acid rain, and provided one of the first comprehensive model frameworks for multiphase chemical processes. Current studies of heterogeneous reactions of aerosol particles are directed toward understanding the aging/atmospheric evolution of aerosol particles by reactive trace gas species, in particular the efficiency of gas uptake and corresponding chemical and physical transformations of the particle, which may affect a particle's ability to act as CCN or IN.[9,12,16,32,33,88,138,149] An accurate description of the overall gas uptake thus requires an understanding of the rate of transfer of gas-phase reactants from the gas phase to the condensed phase. The efficiency at which gas molecules are taken up by a particle is typically expressed in terms of an uptake coefficient (γ). γ is a kinetic parameter to describe heterogeneous kinetic reaction rates and is physically defined as the ratio of the number of gas-to-particle collisions that result in a loss of the gas molecules to the total number of gas-to-particle collisions, or alternatively as the difference in the adsorpion (J_{ads}) and desorption (J_{des}) fluxes of gas molecules divided by the collisional flux (J_{coll}) as shown in Eq. 16, ranging from 0 (no reactive collisions) to 1 (unity reactive uptake)

$$\gamma = \frac{J_{\mathrm{ads}} - J_{\mathrm{des}}}{J_{\mathrm{coll}}} \, . \tag{16}$$

The total flux (J, in units molecule cm^{-2} s^{-1}) of the reactant gas into the condensed material is expressed in terms of γ as follows[150]:

$$J = \frac{[\mathrm{X}]_{\mathrm{g}} \mathrm{c}_{\mathrm{avg}} \gamma}{4}, \tag{17}$$

where $[\mathrm{X}]_{\mathrm{g}}$ (molecule cm^{-3}) is the concentration of gas molecules in the bulk gas and c_{avg} (cm s^{-1}) is the thermal velocity of the gas molecules defined as

$$c_{\mathrm{avg}} = \sqrt{\frac{8RT}{\pi M}}, \tag{18}$$

where R is the gas constant, T is temperature, and M is the molecular weight of the reacting gas. The term $[\mathrm{X}]_\mathrm{g} c_\mathrm{avg}/4$ is the Maxwellian-Boltzmann collision rate.

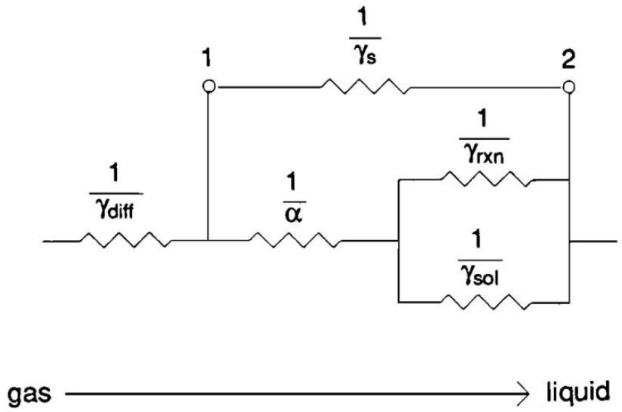

Figure 2.7: Resistor model of the major processes dictating gaseous uptake by condensed-phase liquid material. This figure was adapted from Davidovits *et al.*[150].

In quantifying these heterogeneous reactions it is useful to relate mass transport to a resistor model as shown in Fig. 2.7.[9,12,111,138,148–151] Here, the net uptake γ is the sum of decoupled resistances in the gas phase, at the particle surface, and within the particle bulk. Resistances in the gas-phase such as gaseous diffusion (γ_diff) dictate surface collisional fluxes (J_coll) and is defined as[150]

$$\frac{1}{\gamma_\mathrm{diff}} = \frac{cD_p}{8D_\mathrm{g}} - \frac{1}{2}, \tag{19}$$

where D_p is the particle diameter and D_g is the gas-phase diffusion coefficient of the reactant gas ($\mathrm{cm}^2\ \mathrm{s}^{-1}$). The term -1/2 in Eq. 19 accounts for distortion of the Maxwellian-Boltzmann collision rate when there is net gas uptake at the surface[150]. Alternatively, the gas-phase diffusive resistance term can be related to the Knudsen number (Kn) defined as $Kn{=}\lambda/\mathrm{r}$ given in Eq. 20, where the mean free path of the gas (λ) is defined by Eq. 21.

$$\frac{1}{\gamma_\mathrm{diff}} = \frac{0.75 + 0.283Kn}{Kn(1+Kn)} \tag{20}$$

$$\lambda = \frac{3D_{\mathrm{g}}}{c_{\mathrm{avg}}} \tag{21}$$

As gas molecules collide with the surface, a fraction of the collisions may not be immediately reflected and gas molecules reside at the surface longer than the timescale for direct scattering ($>10^{-12}$ s)[149]. The adsorbed gas molecules are bound to the surface by relatively weak forces including van der Waals forces or hydrogen bonds[149]. The number of gas molecules accommodated at the surface normalized to the total number of gas-to-surface collisions is referred to as the accommodation coefficient (α) or sticking efficiency defined in Eq. 22[152].

$$\frac{1}{\alpha} = \frac{1}{S} + \frac{k_{\mathrm{des}}}{Sk_{\mathrm{sol}}}, \tag{22}$$

where S is the adsorption coefficient and k_{des} (cm s^{-1}) and k_{sol} (s^{-1}) are the rates of desorption and transfer of molecules from the surface into the bulk liquid (solvation), respectively[152].

After surface accommodation gas molecules may be incorporated into the bulk of the condensed-phase due to interfacial mass transport. Absorption and transport into the particle bulk are dependent on Henry's law and bulk diffusion rates as shown in the Henry's law saturation resistance (γ_{sol}) in Eq. 23

$$\frac{1}{\gamma_{\mathrm{sol}}} = \frac{\sqrt{\pi}c_{\mathrm{avg}}}{8RTH}\sqrt{\frac{t}{D_{\mathrm{l}}}}, \tag{23}$$

where D_l is the liquid-phase diffusion coefficient of the reactant gas, H is the Henry's law coefficient, and t is the gas-liquid interaction time. Note that t is proportional to $1/\gamma_{\mathrm{sol}}$, reflecting the increasing rate of evaporation of the reactant gas molecules as the surface becomes saturated and approaches equilibrium with the gas-phase concentration, and as a result net uptake decreases with increasing exposure time. Reactions between the trace gas reactant and the liquid can take place either at the particle surface or (after diffusion) within the particle bulk. Chemical reaction provides a sink for the trace species and, in turn, reduces saturation. The resistance term to chemical reaction at the particle surface (γ_{surf}) is defined as:[152]

$$\frac{1}{\gamma_{\mathrm{surf}}} = \frac{c_{\mathrm{avg}}}{4k_{\mathrm{surf}}}b', \tag{24}$$

where b' (in units of cm) is a surface adsorption equilibrium constant that describes the proportionality in the surface and gas-phase concentration of

the reactant gas molecules in the absence of reaction[152]. k_{surf} is the surface reaction rate constant. Liquid or bulk-phase reactions exhibit a square-root dependence on the bulk-phase reactant concentration and thus the resistance term to chemical reaction in the particle bulk (γ_{rxn}) is defined as:[150]

$$\frac{1}{\gamma_{\mathrm{rxn}}} = \frac{c_{\mathrm{avg}}}{4RTH}\sqrt{\frac{t}{D_{\mathrm{l}}k}}, \tag{25}$$

where k is the pseudo-first order reaction rate constant for condensed phase reaction, i.e. $k{=}k_2[\mathrm{Y}]$. Here, k_2 is the bimolecular reaction rate constant for the trace gas species with the condensed phase species Y. The overall measured uptake coefficient expressed as the sum of decoupled resistances including both surface and bulk reaction is given as[150]

$$\frac{1}{\gamma_{\mathrm{meas}}} = \frac{1}{\gamma_{\mathrm{diff}}} + \frac{1}{\alpha} + \frac{1}{\frac{1}{S\frac{k_{\mathrm{sol}}}{k_{\mathrm{des}}}+\frac{1}{\gamma_{\mathrm{rxn}}+\gamma_{\mathrm{sol}}}} + \frac{1}{\gamma_{\mathrm{surf}}}}. \tag{26}$$

The diffusive resistance term plays an important role for larger particle sizes and fast reactions. In the free molecule, kinetic limit where the mean free path is much larger than the particle diameter, i.e. $\mathrm{Kn}{\gg}1$, γ_{diff} is large, and the term $1/\gamma_{\mathrm{diff}}$ goes to zero. In this regime, other resistances in Eq. 26 govern the overall gas uptake. Conversely, for $\mathrm{Kn}{\ll}1$, in the case of large particles and slow gas diffusion, the overall uptake can be diffusion-limited. Since OH radical uptakes can proceed rapidly, the overall uptake depends strongly on the rate of transfer of OH to the condensed-phase surface and thus OH uptakes can be diffusion-limited. On the other hand, for slower reactive uptakes, which is generally the case for O_3 or NO_2 uptakes where $\gamma{<}10^{-3}$ or lower[138], the gas-phase diffusion limitation is generally much smaller or insignificant.

2.4.1 Langmuir-Hinshelwood and Eley-Rideal uptake mechanisms

The underlying kinetic process by which trace gas species are taken up by a particle or substrate surface will dictate equilibrium timescales of heterogeneous reaction and thus the uptake efficiency over extended time periods. These mechanisms are categorized as either Eley-Rideal[153] (direct reaction upon gas-to-surface collision) or Langmuir-Hinshelwood (L-H)[154] (gas adsorption followed by reaction).[155,156] These two mechanisms are illustrated

in Fig. 2.8. In its simplest form, an Eley-Rideal mechanism occurs when an adsorbed molecule (X) on a surface (S), XS (in units of molecule cm^{-2}), reacts directly with a colliding gas-phase molecule (Y_g) as expressed in the following reaction mechanisms:

$$X(g) + S \rightarrow XS \quad \text{R3}$$
$$XS + Y(g) \rightarrow \text{Products} \quad \text{R4}$$

An example of an Eley-Rideal mechanism is the heterogeneous catalytic conversion of $CO_2(g)$ to CO(g) in the presence of adsorbed H_2[157]. The Eley-Rideal mechanism implies that heterogeneous reaction occurs instantaneously upon collision of a gas molecule with a surface, i.e. a first-order reaction, and that γ is independent of reactant concentration, assuming the number of reactive surface sites (surface concentration) is significantly larger than the reactant concentration.[156]

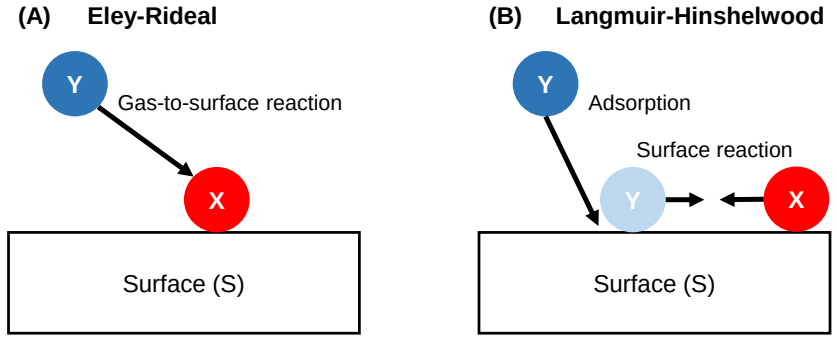

Figure 2.8: (A) Eley-Rideal reaction mechanism. Surface species X reacts directly with gas phase species Y. (B) Langmuir-Hinshelwood reaction mechanism. Gas Y adsorbs to surface followed by reaction with surface species X.

Conversely, if the adsorbed gas resides on the surface for an extended period of time before reacting, as it can be the case for O_3 or NO_2 uptake[158,159], the adsorbed gas species can saturate the surface and block surface reactive sites[138]. In this regime, referred to as L-H uptake, the gas uptake coefficient decreases with increasing gas-phase concentration. The derivation of L-H kinetics can be expressed in the following example. Assume a gas molecule

Y comes into contact with a surface, but instead of directly reacting with an adsorbed reactant XS, Y undergoes an initial adsorption step to a vacant surface site S_v and then reacts with XS as shown in the mechanism below.

$$Y(g) + S_v \rightarrow YS \quad \text{R5}$$
$$XS + YS \rightarrow \text{products} \quad \text{R6}$$

The rate of formation of products (or loss of surface bound Y, in units molecule cm^{-2} s^{-1}) is given as

$$\frac{d[YS]}{dt} = k_s[YS][XS], \tag{27}$$

where k_s is the surface reaction rate constant (cm^2 $molecule^{-1}$ s^{-1}), and both [YS] and [XS] have units of molecule cm^{-2}. The equilibrium adsorption/desorption constant, K_Y (in units of cm^3 $molecule^{-1}$) is given as

$$K_Y = \frac{[YS]}{[Y]S_v}. \tag{28}$$

The total number of surface sites (S_T) is the sum of the vacant sites and those occupied by the adsorbed gas Y as shown in Eq. 29.

$$S_T = S_v(1 + K_Y[Y]). \tag{29}$$

Re-arranging Eq. 28 to isolate [YS] and substituting in Eq. 27 leads to the following loss rate based on Langmuir-Hinshelwood kinetics.

$$\frac{d[YS]}{dt}(\text{molecule} \cdot \text{cm}^{-2} \cdot \text{s}^{-1}) = \frac{k_s[XS]K_Y[Y]S_T}{1 + K_Y[Y]}. \tag{30}$$

The pseudo first-order loss rate of the adsorbed species, XS (or YS), in units of s^{-1}, which follows a Langmuir isotherm, is expressed in Eq. 31 as

$$k_{obs-X}(s^{-1}) = \frac{k_s[XS]K_Y[Y]}{1 + K_Y[Y]}. \tag{31}$$

Alternatively, the Langmuir-isotherm can be expressed in terms of the observed loss rate of the gas-phase molecules Y_g (in units s^{-1}), k_{obs-Y_g}, if

assuming equilibrium and a bimolecular reaction rate constant[15] as shown in Eq. 32:

$$k_{\mathrm{obs-Y_g}}(\mathrm{s}^{-1}) = \frac{k_\mathrm{s}[\mathrm{XS}]K_\mathrm{Y}[\mathrm{Y}]}{1+K_\mathrm{Y}[\mathrm{Y}]}\frac{[\mathrm{XS}]}{[\mathrm{YS}]}, \tag{32}$$

where [YS] is determined by the product [Y](V/S) assuming unity surface accommodation of Y, where V/S is the volume-to-surface area ratio of the reactive surface.

γ has been formulated based on L-H kinetics as shown in Eq. 33[155]:

$$\gamma = \frac{4k_\mathrm{s}[\mathrm{XS}]K_\mathrm{Y}}{\sigma_\mathrm{Y}\omega_\mathrm{Y}(1+K_\mathrm{Y}[\mathrm{Y}])}, \tag{33}$$

where σ_ox is the surface area occupied by one adsorbed oxidant molecule.

2.4.2 Particle phase impacts on gas uptake

The balance of diffusion and reaction is important as it describes where heterogeneous reactions will occur within a particle. In general, the timescale for reaction is expressed as[138]

$$\tau_\mathrm{R} = \frac{1}{k^\mathrm{I}} = \frac{1}{k^\mathrm{II}[Y]}, \tag{34}$$

where k^I is the pseudo-first order reaction rate constant and k^II is the second order reaction rate constant for the bulk phase reaction with species Y. The distance a molecule diffuses in a particle over the course of a reaction is given by the reacto-diffusive length, l

$$l = \sqrt{\frac{D_\mathrm{bulk}}{k^\mathrm{I}}}. \tag{35}$$

Reactions occur near the particle surface for either slow diffusion or fast reaction, whereas under fast diffusion or slow reactions, the reaction can occur throughout the particle bulk. Gas-phase oxidants such as OH, O_3, NO_2, and NO_3, because they have relatively smaller molecular sizes than most low-volatility, condensed-phase organics, can diffuse quickly throughout the particle bulk. However, OH and NO_3 can react quickly with organic compounds and thus reaction typically occurs near the gas-surface interface[138]. On the other hand, O_3 and NO_2 generally react less efficiently than OH and NO_3, and thus their reacto-diffusive lengths can be much longer compared

to OH and NO_3. Heterogeneous reactions can be particularly sensitive to changes in particle viscosity, such that the increased translational motions of the molecules in the condensed phase results in a more efficient mix of the reactants, thus increasing the probability that the molecules interact with each other[160].

2.5 Kinetic flux model

Recent advancements in computational and modeling capabilities has enabled a more detailed and accurate representation of mass transport and gas-to-particle partitioning. Alternative to the resistor model, kinetic flux models couple differential rate equations of mass transport and chemical reactions using gas kinetic formulations to describe gas uptake and partitioning[111,156]. Here, the kinetic multi-layer model of gas-particle interactions (KM-GAP)[161], which is based upon the Pöschl-Rudich-Ammann (PRA) framework[155], is applied to experimental OH exposure data of levoglucosan and abietic acid, which serve as surrogate compounds and molecular markers of BBA. The purpose of applying KM-GAP to the experimental OH exposures is to develop a more detailed understanding of the importance of the different chemical and physical processes that govern reactive OH uptake, not easily accessible in the laboratory. KM-GAP can be used to derive different kinetic parameters including surface accommodation coefficient, desorption time, reaction rate constants, bulk diffusion coefficients of both the oxidant and organic, and the Henry's law coefficient of the oxidant in the organic phase. Figure 2.9 shows a schematic of the different compartments and layers of KM-GAP, which include gas phase, near-surface gas phase, sorption layer, surface layer, and several bulk layers. Mass transport and chemical reactions are treated explicitly in KM-GAP and include gas diffusion, surface adsorption/desorption, surface-bulk exchange, bulk diffusion, and chemical reactions at the surface and in the bulk.

Transport of the bulk and gas-phase species can be evaluated from the following differential equations, where here Z_i represents a reactant molecule (Z) and type (i) from the gas phase. These equations were first presented in Shiraiwa *et al.*[161]. The transport equation of Z_i from the gas-to-particle surface and between the sorption layer and surface is given in Eq. 36

$$\frac{d\mathrm{N}_{\mathrm{Z_i}}}{dt} = (J_{\mathrm{ads,Z_i}} - J_{\mathrm{des,Z_i}} + P_{\mathrm{s,Z_i}} - L_{\mathrm{s,Z_i}} - J_{\mathrm{s,ss,Z_i}} + J_{\mathrm{ss,s,Z_i}})A_{\mathrm{ss}}, \qquad (36)$$

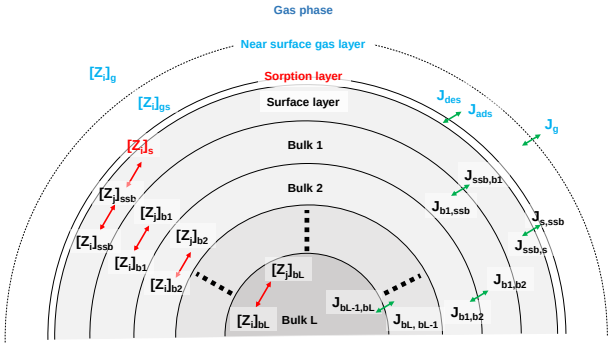

Figure 2.9: Schematic of the different compartments and flux terms of the kinetic multi-layer model of gas-particle interaction in aerosols and clouds (KM-GAP)[161]. Concentrations of species Z_i and Z_j in the gas (g) and near-surface gas phase, at the sorption layer (s), and in the surface (ssb) and in the bulk (b) layers are altered due to chemical reactions between each other as indicated by the red arrows. J represents the transport fluxes between each layer and is indicated with green arrows, including the gas-phase diffusion flux (J_g), the adsorption (J_ads) and desorption (J_des) fluxes, surface-bulk exchange fluxes ($J_\mathrm{s,ssb}$, $J_\mathrm{ssb,s}$) and bulk diffusion fluxes (J_b). Figure adapted from Arangio *et al.*[35].

where $N_{\mathrm{Z_i,s}}$ represents the absolute number of Z_i molecules at the surface and A_ss is the surface area of the outer layer. The different mass transport fluxes (J) and rates of chemical production and loss (P, L) are defined in Shiraiwa *et al.*[161]. Mass transport between the sorption layer, near surface layer and the first bulk layer $b(1)$ is expressed as

$$\frac{d\mathrm{N_{Z_i,ss}}}{dt} = (J_{\mathrm{s,ss,Z_i}} - J_{\mathrm{ss,s,Z_i}} + P_{\mathrm{ss,Z_i}} - L_{\mathrm{ss,Z_i}} - J_{\mathrm{ss,b1,Z_i}} + J_{\mathrm{b1,ss,Z_i}})A(1). \quad (37)$$

Mass transport between the surface layer, first bulk layer, and second bulk layer is shown in Eq. 38.

$$\frac{d\mathrm{N_{Z_i,b1}}}{dt} = (J_{\mathrm{ss,bl,Z_i}} - J_{\mathrm{bl,ss,Z_i}})A(1) + (J_{\mathrm{b2,bl,Z_i}} - J_{\mathrm{b1,b2,Z_i}})A(2) + (P_{\mathrm{b1,Z_i}} - L_{\mathrm{b1,Z_i}})V(1), \quad (38)$$

where V is the volume of the bulk layer. Mass transport between subsequent

bulk layers is shown in Eq. 39.

$$\frac{d\mathrm{N_{Z_i,bk}}}{dt} = (J_{\mathrm{bk-1,bk,Z_i}} - J_{\mathrm{bk,bk-1,Z_i}})A(k+1) + (J_{\mathrm{bk+1,bk,Z_i}} - J_{\mathrm{bk,bk+1,Z_i}})A(k+1) + (P_{\mathrm{bk,Z_i}} - L_{\mathrm{bk,Z_i}})V(k)(k = 2, ..., n-1) \tag{39}$$

Mass transport and chemical reactions within the bulk layer L is given by Eq. 40.

$$\frac{d\mathrm{N_{Z_i,bn}}}{dt} = (J_{\mathrm{bn-1,bn,Z_i}} - J_{\mathrm{bn,bn-1,Z_i}})A(n) + (P_{\mathrm{bn,Z_i}} - L_{\mathrm{bn,Z_i}})V(n) \tag{40}$$

The volume of each layer $V(\mathrm{k})$ is calculated using $N_{\mathrm{Z_i,bk}}$ and the molecular volume $V_{\mathrm{Z_i}}$ assuming volume additivity, i.e.

$$V(k) = \sum_i N_{\mathrm{Z_i,bk}} V_{\mathrm{Z_i}}. \tag{41}$$

The radius position $r(\mathrm{k})$, the outer surface area $A(\mathrm{k})$ and the layer thickness $\delta(\mathrm{k})$ of the bulk layer k and particle diameter d_{p} are calculated for spherical particles as described in Shiraiwa *et al.*[161], allowing each layer to either shrink or grow in response to mass transport and chemical reactions.

The surface and bulk number concentrations of Z_{i} are calculated as follows:

$$[\mathrm{Z_i}]_{\mathrm{s}} = \frac{\mathrm{N_{Z_i,s}}}{\mathrm{A_{ss}}} \tag{42}$$

$$[\mathrm{Z_i}]_{\mathrm{ss}} = \frac{\mathrm{N_{Z_i,ss}}}{\mathrm{A(1)}} \tag{43}$$

$$[\mathrm{Z_i}]_{\mathrm{bk}} = \frac{\mathrm{N_{Z_i,bk}}}{\mathrm{V(k)}} \tag{44}$$

The uptake coefficient of the gas phase species Z_{i} is handled as discussed above as the ratio of the net flux $J_{\mathrm{net,Z_i}}$ and the collision flux $J_{\mathrm{coll,Z_i}}$

$$\gamma_{\mathrm{Z_i}} = \frac{J_{\mathrm{net,Z_i}}}{J_{\mathrm{coll,Z_i}}}. \tag{45}$$

When the gas-phase molecules are adsorbing or condensing onto the surface γ is positive and ranges between 0 and 1. γ is treated as negative when the molecules are evaporating from the surface.

KM-GAP has been used to fully describe the growth of aerosol particles by water condensation, the evaporation of dioctyl phthalate, a widely used plasticizer in the production of PVC, from organic particles, and the oxidation and subsequent volatilization of oleic acid[161]. KM-GAP has also been used to describe the physicochemical interactions between organic BBA substrates and NO_3[14]. In addition, the effects of physical state, non-ideal mixing, and morphology on gas-to-particle partitioning and growth of atmospheric aerosols have been determined applying KM-GAP[162]. KM-GAP is applied here to describe the change in the reactive uptake of OH with organic substrates related to BBA as a function of exposure time and initial gas-phase concentration.

2.6 Radical-initiated heterogeneous chemical reaction mechanisms

Compositional changes to aerosol particles by heterogeneous reactions with gas-phase reactants are important, in part for dictating particle size and mass growth through e.g. formation of additional oxygenated functional groups (functionalization) that stay partitioned to the condensed phase or mass loss through e.g. formation of higher volatility species (fragmentation) that evaporate from the particle surface[12,15,32,95,110,163]. The reaction pathways leading to particle functionalization or fragmentation can be difficult to assess, but are important for predicting reaction products and their yields. Due to the difficulty in identifying condensed phase intermediate reaction products and pathways, often only the starting material and final reaction products are known. Thus, generally it is acceptable to relate multiphase chemical reactions involving gas-phase oxidants with gas-phase reaction mechanisms. The reaction mechanism by which OH radicals oxidize alkane (RH) organic aerosol was first presented in Molina *et al.*[32]. Adaptations of this mechanism have been developed to include its impacts on molecular weight, volatility, and "molecular corridors" (i.e. O:C, categorized as low, intermediate and high O:C) as shown in Fig. 2.10[164]. SOA precursor VOCs with high volatility and low molar mass are located in the lower right corner of the molecular corridor in Fig. 2.10. The initial reaction step involving OH and alkanes is the abstraction of hydrogen. In the presence of O_2, the alkyl radical ($R\cdot$) will rapidly form an alkyl peroxy radical ($RO_2\cdot$). The $RO_2\cdot$ radical reacts with NO or another $RO_2\cdot$ radical to form an alkoxy radical ($RO\cdot$) or an or-

ganic nitrate ($RONO_2$). Molina *et al.*[32] found that the $RO_2\cdot$ self reaction dominates and proceeds via the Russell mechanism forming a carbonyl and alcohol, or the formation of carbonyls via the Bennett-Summers reaction. In the absence of NO_2, the $RO\cdot$ radical may further react with O_2 producing a carbonyl and hydroperoxy radical (HO_2) or undergo decomposition (fragmentation) and/or isomerization.

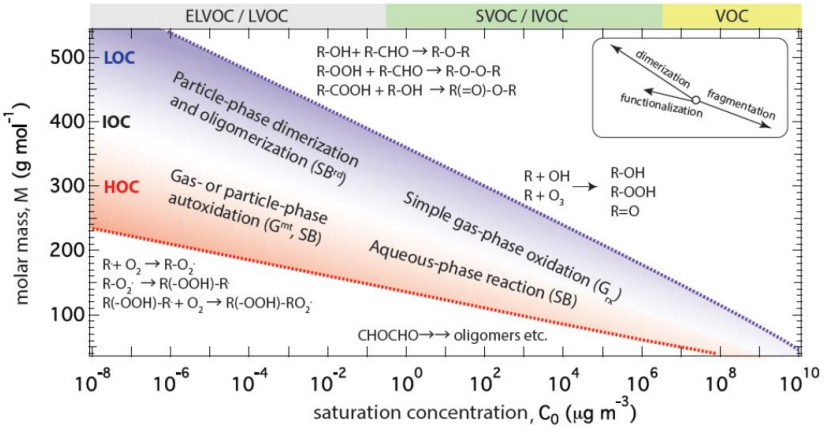

Figure 2.10: Evolution of volatility and molar mass of organic aerosol related to different multiphase reaction mechanisms. Shown is molar mass as a function of volatility, where the organic aerosol volatility is categorized as volatile (VOC), semivolatile and intermediate volatility (SVOC/IVOC) or extremely low and low volatility (ELVOC/LVOC). The level of oxidation, given by O:C, is shown in the blue and red shaded area, where the dotted lines represent linear alkanes C_nH_{2n+2} (purple with O:C=0) and sugar alcohols $C_nH_{2n+2}O_n$, and consists of high, intermediate and low O:C (HOC, red shaded area; IOC, white area; LOC, blue shaded area). Organic aerosol products evolve by three key reaction types of functionalization, oligomerization, and fragmentation, as illustrated in the insert. Note that the different arrow lengths indicate the different levels of intensity of the reactions' impacts on volatility. This figure was adapted from Shiraiwa *et al.*[164].

The decomposition reaction pathway can produce smaller molecular weight, higher volatility reaction products through scission of the C-C bond, yielding an aldehyde and alkyl radical. The decomposition reaction products are normally confined to the lower right area of Fig. 2.10. The other reaction

pathways lead to the production of relatively higher molecular weight, low-volatility oxygenated molecules that are confined in the uppler left-hand side of Fig. 2.10. As illustrated in Fig. 2.10, functionalization typically leads to an incremental increase in molar mass, which corresponds to one order of magnitude decrease in volatility, while oligomerization can lead to more significant decreases in particle volatility[164]. Similar reaction schemes will apply involving other radical species such as Cl radical and NO_3, although NO_3 oxidation of alkenes (R=RH) will result in addition of NO_3, and thus contribute to the increase in molecular weight of the organic material. It is still unclear which pathway (fragmentation, functionalization, or oligomerization) dominates, but recent studies have indicated that the efficacy of a given pathway will depend on the particle composition and molecular geometry.[12,15,32,36,81,95,110,164] The dotted lines in Fig. 2.10 indicate that the decrease in volatility with increasing molar mass is more pronounced for polar (higher O:C) compounds[164]. The extent of volatilization depends, in part, on the degree of branching and cyclization of the host molecule, whereby branched alkanes are more likely to lead to volatilization compared to cyclical compounds due to the additional ring-opening step necessary for fragmentation of cyclic compounds.[95,165] However, volatilization reactions reduce particle lifetime[32] and alter the gas-phase budget of VOCs.[37] For instance, Molina *et al.*[32] observed depletion of paraffin and pyrene substrates and production of VOCs such as formic acid (HCOOH) and formaldehyde (CH_2O) after extensive OH oxidation, and estimated a particle lifetime due to volatilization on the order of a week, comparable to atmospheric particle wet depositional lifetimes. McNeill *et al.*[166] measured significant production of formic acid from OH oxidation of palmitic acid particles. Vlasenko *et al.*[110] measured a suite of volatilized products related to scission of a -CH_2- group upon heterogeneous OH oxidation, resulting in the release of formic acid and formaldehyde from pyrene and *n*-hexane soot, ethylhexanal from BES bis(ethylhexyl)sebacate, and a series of carboxylic acids, aldehydic carboxylic acids, and alcohols from OH oxidation of stearic acid. Volatilization not only impacts the concentration and composition of VOCs in the real atmosphere[37], it increases the availability of condensable organics for SOA formation and aerosol mass growth[38], influencing particle size distributions and potentially CCN.

3 Experimental methods

3.1 Preparation and analysis of gas-phase oxidants and VOCs

3.1.1 OH generation under vacuum

OH radicals were produced under vacuum (pressure $\leq$ 30 hPa) via the microwave discharge and subsequent dissociation of hydrogen (H_2) in an inert background gas of either helium (He) or argon (Ar) in the presence of O_2 or NO_2, so-called "dark" reactions because they avoid the presence of ultraviolet (UV) light and a reactive precursor gas such as O_3 in order to produce OH, which might otherwise effect the analysis[31,32,34,167]. A dilute 0.1-5% by mass of ultra-high purity (UHP) H_2/He or H_2/Ar flow at 40-300 standard cm^3 min^{-1} (sccm, standard temperature and pressure, STP) is introduced to a 2.45 GHz microwave resonant cavity through a 1/4" outter diameter (o.d.) air-cooled Pyrex tube as indicated in Fig. 3.1. Powered by an 85 Watt Raytheon microwave generator, a custom-built Beenakker microwave cavity[168], shown in Fig. 3.1, was employed to initiate excitation/dissociation of H_2 in a mixed Ar/H_2 plasma. H_2 dissociates to form individual H-atoms as shown in reactions 7-12, which follows the well-known Penning ionization reaction[169]. The superscipts m, +, ++, and * signify metastable, ionized, doubly ionized, and excited states, respectively. The O_2 flow was first conditioned in an ethanol/dry ice trap to remove organics.

$$Ar^m + H_2 \rightarrow Ar + H_2^+ \quad \text{R7}$$
$$Ar^m + H_2^+ \rightarrow Ar + H_2^{++*} + e \quad \text{R8}$$
$$H_2^{++*} \rightarrow H + H \quad \text{R9}$$
$$H + O_2 \rightarrow HO_2 \quad \text{R10}$$
$$HO_2 + H \rightarrow 2OH \quad \text{R11}$$
$$H + NO_2 \rightarrow OH + NO \quad \text{R12}$$

The H atoms are generated in a 1/4" o.d. Pyrex tube that passes through the center of the microwave cavity, the region of greatest electric field strength[168]. The H atoms then pass through a 1/8" o.d. Pyrex tube directed down the center of a separate 1/4" o.d. Pyrex injector where OH production occurs as shown in Fig. 3.1. Residence times in the reaction region of the glass injector (i.e. where OH is formed) was sufficient for maximizing [OH] and minimizing

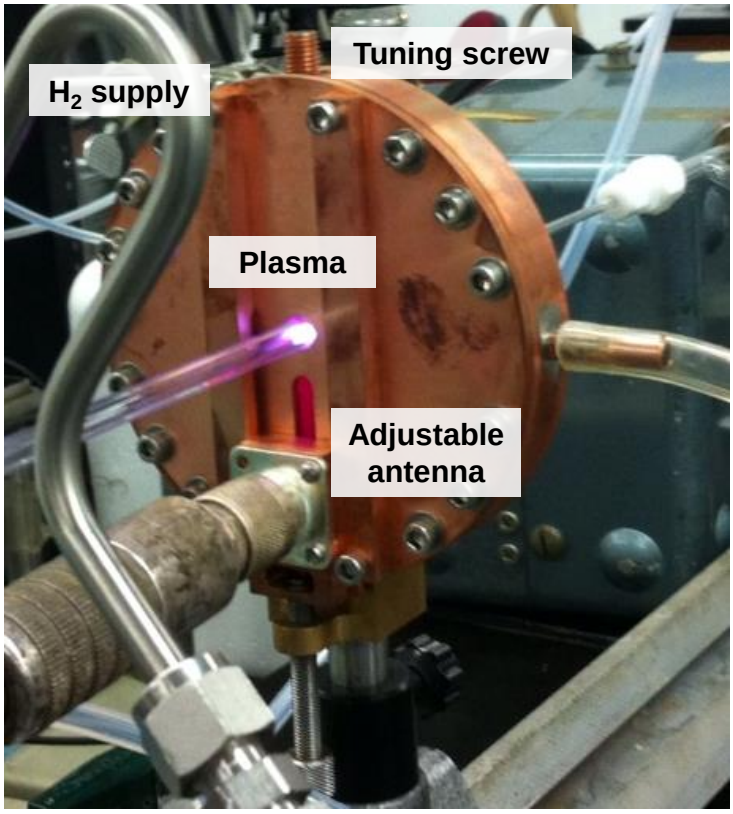

Figure 3.1: Schematic of Beenakker microwave cavity showing the glow of the Ar/H_2 plasma. The gases enter the center of the cavity, the region of greatest electrical field strength, through a Pyrex glass tube, and H_2 proceeds to dissociate. The plasma strength can be adjusted using the moveable antenna and tuning screw.

reactive gaseous byproducts, including HO_2, produced in reaction R10. The limiting step in the production of OH using this method is the dissociation of H_2. While no direct measurements of H_2 were made, the concentration of OH could be adjusted between $\sim 10^7$–10^{11} molecule cm^{-3} by varying the individual flows of H_2 and O_2 or NO_2 in the bulk gas, i.e. varying the dilution flow. Relatively higher [OH] was achieved by introducing a greater fraction of H_2 to the bulk gas flow. To achieve near atmospherically relevant [OH]$\sim 10^6$-10^7 molecule cm^{-3}, H_2 was first diluted by introducing trace quantities of

H_2 in a He-filled glass bulb before entering the plasma region. Flows were considered laminar with Reynold's numbers $Re \leq 27$. Flow velocities in the flow reactor ranged from 1800-3100 cm sec^{-1}. Temperature in the flow reactor was held between 293-295 K using a circulating bath chiller.

3.1.2 OH detection by chemical ionization mass spectrometry

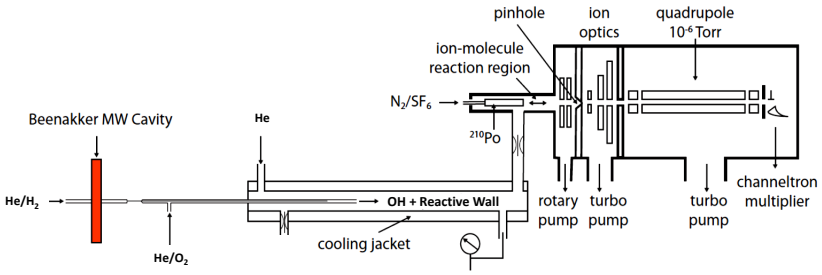

Figure 3.2: Schematic representation of the coated-wall flow tube reactor coupled to a chemical ionization mass spectrometer. The flow tube reactor incorporates a long Pyrex glass injector through which OH radicals are generated. The OH precursor gas molecules are introduced through either a sidearm to the injector or through the back of the injector after first passing through the microwave resonant cavity. The gas analyte molecules then undergo reaction with SF_6^- in a cylindrical glass tube coated with halocarbon wax and lined with a stainless steel rod or aluminum foil to generate a floating charge across the tube. A fraction of the sample flow is then passed through a critical orifice (pinhole) into the differentially pumped stainless steel chamber, where the ionized analyte experiences an electromagnetic field for guidance, filtration and detection. See text for more details.

A custom-built chemical ionization mass spectrometer (CIMS) was used for analysis and detection of gas-phase oxidant species[13] as shown in Fig. 3.2 for the coated-wall flow tube and aerosol flow reactor studies. CIMS operates on the principle of ion-molecule reactions that occur between the analyte, e.g. OH, and a reagent ion, e.g. SF_6^-. The reaction between the analyte and reagent ion is exothermic (favorable) as long as the electron affinity of the analyte is greater than that of the reagent ion. The charged analyte is then detected utilizing a quadrupole mass filter that creates an electromagnetic

field in which ions are accelerated and separated for detection based on their mass-to-charge ratio (m/z). CIMS has been succesfully employed in a number of heterogeneous kinetics studies due to its sensitivity and rapid scanning time.[13,15,32,34,170] Reagent SF_6^- ions are produced by flowing trace amounts of SF_6 in a UHP N_2 carrier flow through an α-emitting Po^{210} radioactive source. SF_6^- then undergoes ion-molecular reactions with the analyte species such as OH and NO_2, forming OH^- (m/z=17) and NO_2^- (m/z=46), respectively, as shown in reactions 15-16.

$$OH + SF_6^- \rightarrow OH^- + SF_6 \quad \text{R15}$$
$$NO_2 + SF_6^- \rightarrow NO_2^- + SF_6 \quad \text{R16}$$

The rate constant for reaction 15 is 2×10^{-9} cm^3 molecule^{-1} s^{-1} [171] and the rate constant for reaction 16 is 1.4×10^{-10} cm^3 molecule^{-1} s^{-1} [172]. HO_2 is detected as $SF_4O_2^-$ (m/z = 140 Th), presumably following a multi-step reaction with SF_6^-, however there is no measured rate constant of HO_2 reaction with SF_6^- [31,173]. Pressures in the chemical ionization (CI) region were maintained between 2-6 hPa. Concentration estimates were based on the reaction rates between SF_6^- and OH or SF_6^- and NO_2, and the residence time in the CI region as given in Eqs. 46-48 for [OH]. Starting from R15, [OH] can be inferred from the normalized $[SF_6^-]$, i.e. $[SF_6^-]_t/[SF_6^-]_0$:

$$\frac{[SF_6^-]_t}{[SF_6^-]_0} = e^{-k[OH]t}. \quad (46)$$

If the stoichiometric loss of SF_6^- to OH^- is assumed, then:

$$[SF_6^-]_t = [SF_6^-]_0 - [OH^-]_t \quad (47)$$

after substitution of Eq. 47 into Eq. 46 and rearranging,

$$\frac{[OH^-]_t}{[SF_6^-]_0} = 1 - \frac{1}{e^{k[OH]t}}. \quad (48)$$

The error in this estimate is 50% based on the uncertainty in the reaction rate constants between SF_6^- and OH or SF_6^- and NO_2.[171,172] The OH detection limit of our CIMS was determined based on a linear extrapolation of the calculated [OH] using Eq. 48 as a function of the signal output of the mass spectrometer, in counts per second (cps), using the Merlin Automation software version 0.9.4. Here, the OH signal (i.e. concentration) was varied

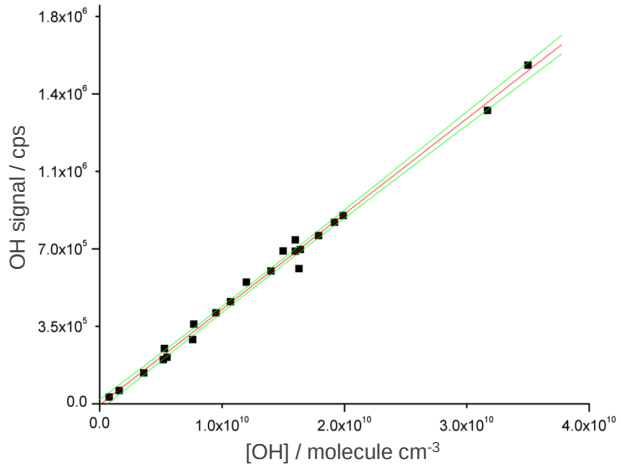

Figure 3.3: Calibration curve for OH showing the measured OH signal as a function of OH concentration calculated using Eq. 27. The measured data points are shown in black circles. The red line represents the linear fit to the data and the green lines show the upper and lower 95% confidence intervals in the measured data points.

pseudo-randomly and recorded along with the SF_6^- signal with the microwave plasma on. An example of such a calibration curve for OH is shown in Fig. 3.3. Based on the instrument noise, taken as the OH signal at 1 s integration time with the microwave plasma off, the detection limit is determined from the calibration curve by calculating the concentration of OH required to output a signal of 8 cps. Our detection limit for OH at 1 s integration time is $\sim 10^6$ cm^{-3} and comparable to the OH detection limit determined in previous studies[31].

CIMS was also used for analysis and detection of gas-phase oxidant species in the presence of H_2O vapor and lab-generated aerosol particles. At high relative humidities, it was shown that water clustering with SF_6^- can result in several interferences, largely $SOF_4^- \cdot (H_2O)_m$ and $F^- \cdot (HF)_2 \cdot (H_2O)_n$. Water clustering with OH^- forms $OH^- \cdot (H_2O)_k$, which influenced the detection limit for OH by reducing the intensity of both OH^- and SF_6^- [34,174]. The subscripts m, n, and k stand for the number of molecular water clusters. To prevent errors in calculated [OH] due to water clustering, the concentration of OH was determined under dry conditions in the flow reactor and then the OH signal

was allowed to equilibrate to the specified relative humidity. A previous study by Park *et al.*[34] showed that only the OH detection sensitivity was affected by water vapor and not the OH concentration in the flow reactor.

3.1.3 OH generation at atmospheric pressure

OH radicals were produced at atmospheric pressure by photolyzing O_3 in the presence of H_2O vapor via reactions R13–R14[17,95,110,175]. O_3 was generated by photolytically dissociating O_2 with a UV lamp (Jelight model 600, λ=185 nm). The concentration of O_3 was quantified using a photometric O_3 monitor (2B Technologis model 202) that sampled from the flow stream and varied from ∼250 ppb to 40 ppm by adjusting the O_2 mass flow and dilution flows of either N_2 or He.

$$O_3 + h\nu\ (\lambda \geq 220\text{ nm}) \rightarrow O(^1D) + O_2 \qquad \text{R13}$$
$$O(^1D) + H_2O \rightarrow 2OH \qquad \text{R14}$$

Water vapor was generated at atmospheric pressure by passing a UHP N_2 flow through a denuder filled with double deionized water held at room temperature. A 4.5 L glass vessel purged with a ∼400 sccm flow of dry N_2 was used to sufficiently mix O_3 and humidified N_2. A carbon trap and liquid N_2 cold trap was placed in-line with N_2 to remove organics. The head space in the vessel was saturated as determined by RH measurements using an RH probe (Vaisala model HM70). RH was varied from ∼15% to 60% by adjusting the fractional flow rates of the humidified and dried gas flows. A 22.9 cm or 60 cm-long Hg pen-ray O_3-free lamp emitting wavelengths >220 nm was located along the centerline of a temperature-controlled cylindrical flow reactor to photolyze O_3, which in the presence of H_2O, generates OH[17,28,95].

OH concentrations were quantified for the atmospheric pressure experiments applying a photochemical box model using the reactions presented in Table 4.4, which were validated based on in-situ measurements of isoprene loss in the presence of OH. The box model includes 24 O_x and HO_x reactions[176] and the photolysis of O_3. This model assumes gases are lost to the halocarbon wax-coated walls for several of the reactive species including OH, O, and HO_2.[31] The photolysis rate (j, in units s^{-1}) of O_3 was approximated based on the change in $[O_3]$ with the UV lamp on or off as shown in Eq. 49.

$$j = \frac{\ln \frac{[O_3]_f}{[O_3]_i}}{t}, \qquad (49)$$

where t is the residence time of the gas in the flow reactor. Based on these loss measurements over a range of initial [O_3], an average photolysis rate of $\sim$0.042 s^{-1} was determined for the smaller flow reactor and $\sim$0.008 s^{-1} for the larger flow reactor.

3.1.4 Proton transfer reaction time-of-flight mass spectrometry for VOC detection

Measurements of isoprene during calibration experiments and VOCs during volatilisation experiments were carried out by a high resolution PTR-MS utilizing a time-of-flight (ToF) mass analyzer.[177] VOCs were ionized via proton transfer with H_3O^+ ions[178] as long as their proton affinities are higher than that of H_2O, as shown in R17.

$$VOC + H_3O^+ \rightarrow VOC(H^+) + H_2O. \qquad \text{R17}$$

The advantage of using PTR-MS for detection of VOCs is the limited fragmentation during the ionization process[178]. Fragmentation can complicate mass spectra making the analysis and identification of unique reaction products ambiguous. The ToF mass analyzer[177] ($m/\Delta m \geq 6000$) allows for unique identification of the VOCs studied including distinguishing isobaric species or species of similar m/z.[177]

The electric field (E) to number density of air (N) ratio (E/N) in the drift tube was kept constant $\sim$130 Td with a drift tube voltage, pressure, and temperature of 600 V, 2.27 mbar, and 333.13 K, respectively. Due to the high RH in the flow reactor, there was considerable clustering of the reagent ion with water, i.e. $H_3O^+(H_2O)$. Unfortunately, clustering can significantly impact quantitative determination of VOC concentrations,[179] in particular formaldehyde (HCHO),[180] a common volatilization product.[32,110] As a result, in combination of not having gas standards for many of the detected VOCs, absolute VOC yields were not determined. Instead, VOC changes are interpreted based on relative differences in the intensities accounting for the measured background. The signal output follows a Gaussian distribution centered around a given m/z as shown in Fig. 3.4. The area underneath the curve is determined using the PTR-MS data automation software. The difference in the area underneath the curve at a given m/z in the absence and presence of OH is used to evaluate the differences in VOC intensities following OH oxidation. The most significant peaks were identified as those

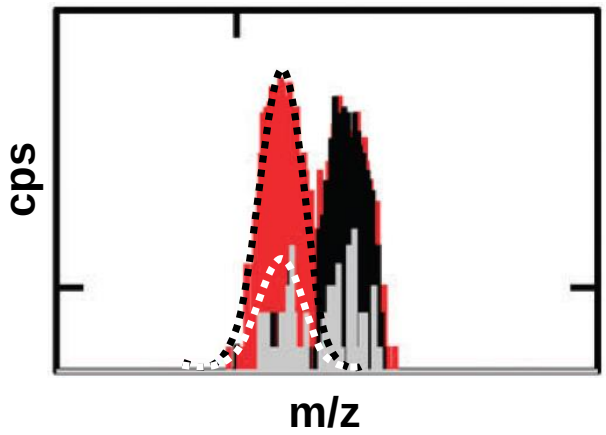

Figure 3.4: HR-PTR-ToF-MS spectra indicating the signal output of VOCs in the presence of OH (red), absence of OH (gray), and in the presence of UV light in the absence of OH (black). The dotted black and white curves indicate the position of the Gaussian peak used for analyzing the integrated VOC signal intensity.

exhibiting a peak amplitude of >1 cps, about a factor of 10 greater than the signal noise.

3.2 Preparation and analysis of substrates and aerosol particles

3.2.1 BBA surrogate substrates

Substrate preparation consisted of evenly distributing 1-2 mL of 1 wt% solutions of levoglucosan in H_2O, abietic acid in methanol, and 5-nitroguaiacol in methanol to glass flow tubes, placed in a temperature-controlled and inert atmosphere. When bringing the coated-wall flow tubes to low pressures, the substrates rapidly solidified due to outgassing of the solvent. However, it is likely that levoglucosan/H_2O mixtures remained in an amorphous highly viscous or solid state.[13,14,106] Both palmitic acid and halocarbon wax were applied to the flow tubes by melting the substance with a heat gun. Care was taken to ensure surface uniformity, however, inhomogeneities may exist, which are likely reflected in the measurement uncertainties. Before inserting

the heated tubes in the flow reactor, each tube was wrapped in aluminum foil and placed in a particle-free clean bench to cool to room temperature.

Prior to the volatilization experiments, the coated flow tubes were conditioned with dry N_2/O_2 flow, humidified N_2/O_2 flow, humidified N_2 flow in the presence of O_3/O_2, and humidified N_2/O_2 flow in the presence of UV light. Maximum substrate temperatures in the presence of UV were $\sim$303 K maintained by a cooling jacket.

3.2.2 BBA surrogate aerosol

Aerosol particles were generated via atomization of aqueous solutions of pure Suwannee River Fulvic Acid (SRFA), levoglucosan (LEV), 4-methyl-5-nitrocatechol (MNC), and potassium sulfate (KS), and mixtures in the following mass ratios of LEV:MNC:KS (1:0:1, 0:1:1, 1:1:0, 1:1:1, and 1:0.03:0.3) employing a commercially available constant output atomizer (TSI, Inc. model 3076). KS was also coated with MNC by passing a flow of atomized KS through a glass oven containing volatilized MNC, which condenses onto KS in a cooler region downstream. A flow of UHP N_2 carries the atomized particles. For the CCN activity measurements, the atomized particles first enter a dilution stage and are then passed through two diffusion dryers followed by a humidifier. A similar conditioning mechanism was employed for the humidified uptake experiments, whereby the atomized particles, instead of passing through the dilution stage, first entered a diffusion dryer and/or H_2SO_4 drying stage, where the RH of the atomized flow can be reduced to below RH=5%. The particles are then sampled by a Scanning Mobility Particle Sizer (SMPS) through a tee for determination of particle size and number concentration. Particle dilution and wall losses were accounted for to correct the number concentration of particles in the flow reactor. Particle wall losses in the tubes were determined by taking the difference in the measured number concentration at the inlet and outlet of the tubes.

3.2.3 Particle size distribution measurements

An SMPS was employed to measure the number concentration of particles as a function of particle size. In this technique, particles in the sample flow are first given an equilibrium charge distribution (i.e. the particles are neutralized having both positive and negative charges) after passing through a Kr-85 radioactive source. The particles are then transferred to a differential mobility

analyzer (DMA, TSI Inc. model 3081). Along the centerline of the DMA is a negatively charged stainless steel rod to which positively-charged particles are attracted. Depending on the electrical potential applied to the rod, the particles can be segragated (i.e. filtered) and counted as a function of their electrical mobility. There are three trajectories the polydisperse particles can take when flowing along the DMA, (1) collision with the charged rod, (2) recirculation with the bulk sample flow, or (3) exit with the monodisperse flow through a small slit located at the bottom of the charged collector rod. In the first case, if the particles acquire a high electrical mobility, then they collide with the upper portion of the rod. Particles that aren't collected on the rod have either the narrow range of electrical mobility necessary to exit the DMA and get counted or insufficient electrical mobility to be collected or exit the DMA. The electrical mobility of the particle, Z_{p}, can be related to particle diameter as defined in Eq. 50.

$$Z_p = \frac{neC}{3\pi\mu D_p}, \tag{50}$$

where n is the number of elementary charges on the particle, e is the elementary charge (1.6×10^{-19} Coulomb), C is the Cunningham slip correction factor, and μ is the gas viscosity. Thus, a specific particle size may be sampled simply by scanning the voltage applied to the collector rod. Smaller particles are sampled at lower applied voltages and larger particles require higher voltages because of their slower electrical mobility. The resolving power of the DMA depends on the voltage scanning time, i.e. the time it takes to adjust from one voltage to the next. Since the particles are continuously sampled as the voltage is adjusted, a range of particle sizes are sampled and binned. The number of size bins to be sampled can be adjusted in the software. Thus, to achieve a greater size resolution, the number of size bins to be sampled should be maximized. For the experiments discussed in this dissertation, the particle concentrations and timescales of collection were sufficiently high so that these errors in the counting efficiency are negligible.

When the particles are separated based on their electrical mobility, they are counted in a condensation particle counter (CPC, TSI Inc. model 3775). Here, the particles exiting the DMA are grown to sufficiently large droplet sizes that can be optically detected. Particle growth to detectable sizes occurs via condensational growth in a cooled condensor saturated with n-butanol vapor. Particle number concentrations can be detected from 0 to 10^7 cm^{-3}. For all of the particle uptake experiments, a sample flow rate of 0.3 lpm was

applied for the CPC with a 3 lpm sheath flow in the DMA, and thus 10:1 sheath-to-sample flow.

3.3 Cloud condensation nuclei activity measurements

Figure 3.5 shows the experimental setup, adapted from an earlier study [17], for conducting CCN activity and hygroscopicity measurements of OH-exposed BBA surrogate-particles.

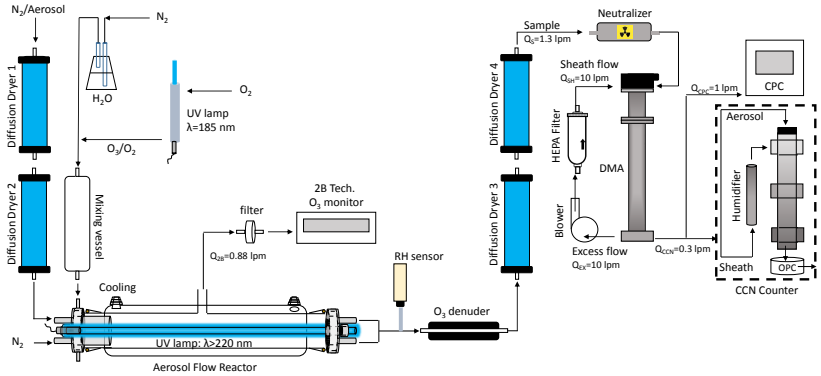

Figure 3.5: Schematic illustration of the experimental setup showing from top left to bottom right: aerosol generation and drying stage, O_3 production and humidification (mixing vessel), the aerosol flow reactor, O_3-free ultra-violet lamp and O_3 monitor, relative humidity probe (RH sensor), O_3 denuder, second drying stages, aerosol sizing by the DMA and particle counting by the CPC, and determination of the CCN activity by the CCNc.

The production of OH at atmospheric pressure is described in more detail in sec. 3.1.3. Briefly, OH was generated by photolyzing O_3 in the presence of water vapor (RH$\sim$40%). The flow reactor is a 60 cm in length, 5 cm i.d. Pyrex reactor having 4 ports at the inlet, two of which can be used to mix particles and O_3/H_2O, and the other two can be used as a sheath flow along the walls to reduce particle losses to the reactor walls. Three additional ports are situated along the length of the flow reactor for extra sampling or flow. The flow reactor is regulated using a water jacket. The UV lamp is placed

in a glass sheath tube along the centerline of the flow reactor and cooled with a flow of room air. The reacted particles are then analyzed for size and number concentration using a DMA and CPC, respectively, and for CCN activity using a commercial CCN counter (CCNc).

The CCNc and operating conditions are described in more detail in Mei *et al.*[181]. CCN activity data were acquired following procedures similar to previous studies[27,182], whereby the dry particle diameter is scanned while keeping the CCN chamber supersaturation fixed. A more detailed description of this approach is given in Petters *et al.*[182]. Briefly, particles first traverse through a Kr-85 aerosol neutralizer (TSI 3077A) and are then size-selected using a DMA (TSI 3081) and processed in a CCNc (DMT, single column CCNc)[183–185], while in tandem the total particle concentration is measured with a CPC. The CCNc is operated at 0.3 lpm total flow rate and 10:1 sheath-to-sample flow rate ratio. The total sample flow rate, which includes a 1 lpm CPC flow rate is 1.3 lpm and 10:1.3 sheath-to-sample flow rate ratio is applied for the DMA. The temperature gradient in the CCNc column is set by custom-programmed Labview software and operated at ΔT=6.5, 8, 10, and 12 K, corresponding to chamber supersaturations S=0.2, 0.27, 0.35, and 0.425% based on routine calibrations applying atomized ammonium sulfate particles. The temperature gradient was stepped successively, from 6.5-12 K and in reverse. Each temperature gradient was maintained for a total of 14 min to allow an up and down scan of the particle size distribution by the DMA. The aerosol size distributions and size-resolved CCN concentrations were acquired applying an inversion method described in Collins *et al.*[186], which implicitly accounts for multiple charged particles. The ratio of the aerosol size distribution and CCN size distribution provided size-resolved CCN activated fractions (i.e. fraction of dry particles that become CCN at a given supersaturation and particle size).

The hygroscopicity and CCN activity is described by κ-Köhler theory[16] as discussed in Sec. 2.3, where the κ-Köhler equation is given by Eq. 9. In determining κ from the CCNc measurements, the input variables based on the experiments are supersaturation (S, note that S_c=S-1) and critical dry diameter ($D_{p,c}$) applying Eq. 10. S is controlled by the CCNc and D_d is controlled by the DMA. However, determining $D_{p,c}$ is not straightforward due to partial activation at different D_p and limitations in droplet diameter size resolution. Instead, $D_{p,c}$ is determined by plotting CCN activated fractions (CCN/CN) with D_p and fitting using a sigmoidal, cumulative Gaussian distribution function (f(x)) as indicated in Eq. 51 using a non-linear least-

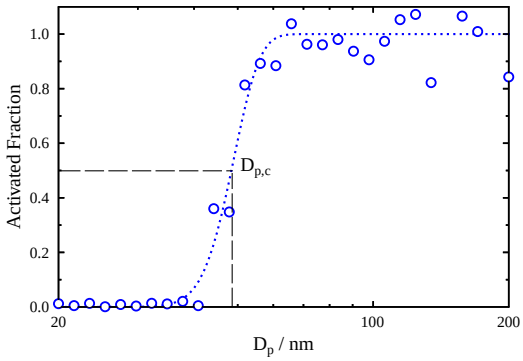

Figure 3.6: An example activated fraction curve showing the fraction of dry KS particles activated at a given particle size bin at S=0.425%. The dashed lines show the location of the 50% activated fraction point, which corresponds to $D_{p,c}$.

squares fitting routine.[17,28,29,181,182,185] CCN activation curves are generated by fixing S while systematically varying D_p until 100% become activated (i.e. when CCN/CN=1).

$$f(x) = \frac{1}{2}\mathrm{erfc}(\frac{x}{\sqrt{2}}), \tag{51}$$

where $x = (D_d\text{-}D_{d,50})/\sigma_D$. In the fitting procedure, D_d is the dependent variable and $D_{d,50}$ and σ_D are adjustable parameters to minimize the root mean square error between *f(x)* and the data. $D_{d,50}$ is the dry diameter interpreted as where 50% of the dry particles have activated into cloud droplets, also referred to as the critical particle diameter, $D_{p,c}$. An example of a measured activated fraction curve is shown in Fig. 3.6, showing the activated fractions of dry KS particles at S=0.425%. The dashed lines show the 50% activation point, which corresponds to $D_{p,c}$.

3.4 Heterogeneous kinetics measurements

Since γ describes the net gaseous uptake efficiency, it is derived experimentally by monitoring the concentration changes of one reactant in response to a second reactant[149]. In this section, a detailed description is given of the heterogeneous kinetics experiments and derivation of γ due to OH reactive uptake by (i) a reactive coated-wall flow tube and (ii) aerosol particles.

3.4.1 Coated-wall flow reactor uptakes and derivation of γ

One approach to derive heterogeneous kinetics is the use of a flow tube, which is coated along its inner walls with the substrates of interest. In this version, the flow tube is situated horizontal[170,187,188]. The flow tube apparatus is made of Pyrex glass with dimensions 20 cm in length and 2 cm i.d. containing a cooling jacket to regulate temperature as shown in Fig. 3.7. Inside the flow

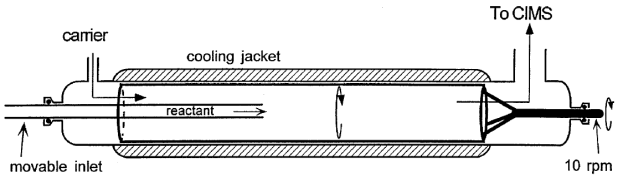

Figure 3.7: A schematic of the rotating coated-wall flow tube used for heterogeneous kinetics experiments. Figure adapted from Davidovits *et al.*[152].

tube along the centerline was a 15 cm in length and 1.77 cm i.d. sandblasted glass tube in which the inner walls were coated with the organic substrates of interest. The tubes were rotated during application to ensure coating uniformity when investigating liquid substrates.

Flow tube reactors are widely used for conducting both gas-phase and heterogeneous reaction kinetics studies[31,32,170,189–193]. The premise in determining heterogeneous reaction kinetics using cylindrical flow tubes is straightforward: first, a gas-phase reactant is introduced to the flow tube via a movable injector at an initial position (z_i) and its concentration is measured with a detector. The injector is moved to a second position (z_f) and the corresponding loss of the gas-phase reactant species is monitored as a function of the reaction time over the substrate length (i.e. time traversed over the distance dz) and quantified assuming a pseudo first-order reactive loss of OH applying Eq. 52.

$$\frac{d[\mathrm{OH}]}{dt} = -k[\mathrm{OH}], \tag{52}$$

where k is the pseudo-first order reaction rate constant to the walls (s^{-1}).

k is derived from measurements of [OH] at several different positions while the reactant flow rate is held constant. These data are plotted as the natural lorgarithm of [OH] as a function of reaction distance dz and the slope is used

to calculate the k, where

$$k = -v\frac{d(\ln[\mathrm{OH}])}{dz}. \tag{53}$$

Exemplary plots of the natural logarithm of [OH] as a function of reaction time are shown in Fig. 3.8 for OH uptake by the different organic substrates.

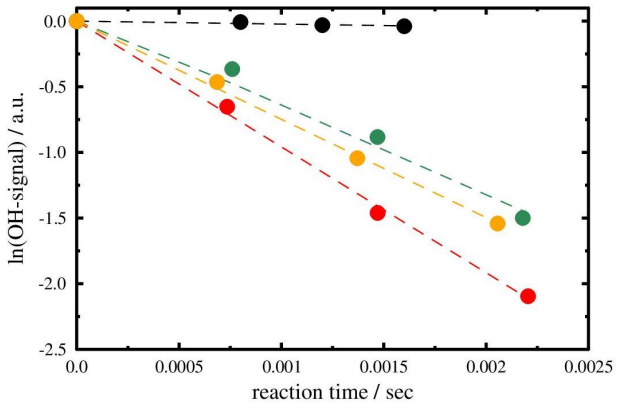

Figure 3.8: Natural logarithm of the observed OH signal as a function of reaction time in the presence of halocarbon wax (black), levoglucosan (red), abietic acid (green), and nitroguaiacol (gold) substrates. Dashed lines represent the corresponding linear fits to the data.

OH radicals react readily with the reactor walls. The fraction of wall collisions that irreversibly remove OH is given by γ. The number of collisions between OH and the walls that result in a loss of OH per unit area is given by gas kinetic theory as $1/4\gamma\omega[\mathrm{OH}]$, where ω is the average molecular speed. Thus the rate of removal of OH by collisions with the wall is given by

$$\frac{d[\mathrm{OH}]}{dt} = \frac{1}{4}\gamma\omega[\mathrm{OH}]\frac{\mathrm{S}}{\mathrm{V}}, \tag{54}$$

where S/V is the surface-to-volume ratio of the cylindrical flow reactor equal to 2/r, where r is the radius of the flow tube. This rate gives the first-order wall loss rate constant k_{w} (s^{-1}) as

$$k_{\mathrm{w}} = \frac{\gamma\omega}{2r}. \tag{55}$$

Thus, γ is determined by re-arranging Eq. 55 to give Eq. 56:

$$\gamma = \frac{2rk_{\mathrm{w}}}{\omega}. \tag{56}$$

3.4.2 Aerosol flow reactor uptakes

Similar to the coated-wall flow tube technique, heterogeneous kinetics can be evaluated using aerosol flow reactors by introducing the reactant gas through a movable injector; however, instead of the gas reacting with the walls, the gas reacts with aerosol particles. The experimental setup consists of an aerosol flow reactor (AFR) coupled to CIMS as shown in Fig. 3.9[13,15]. OH radicals are produced from a microwave discharge of Ar/H_2 in the presence of O_2 using a Beenakker microwave cavity as discussed in Sec. 3.1.2. OH concentrations range from 10^8-10^9 molecule cm^{-3}, which are within an order of magnitude of [OH] measured in fresh biomass burning plumes[63]. OH radicals are introduced to the AFR through a movable glass injector and carried in the AFR by a fast flow of N_2. The AFR temperature is fixed at 293 K using a temperature controlled water jacket. Pressure in the AFR varies between 16 and 30 hPa for the kinetics experiments, ensuring laminar flow. The difference in the OH signal decay in the absence and presence of

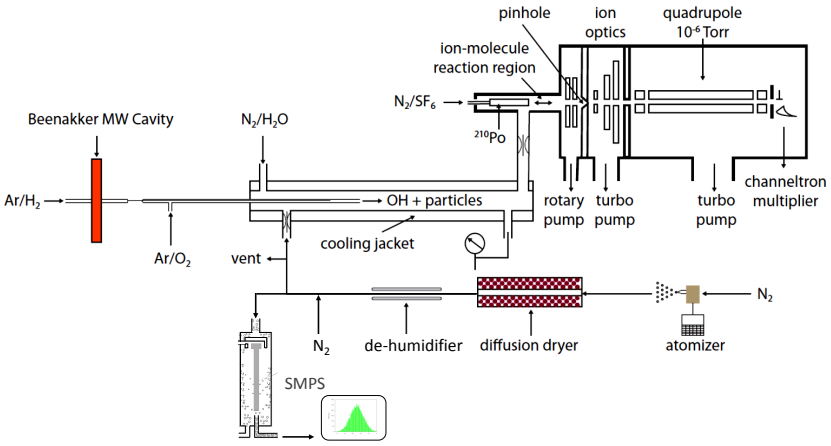

Figure 3.9: Schematic illustration of the aerosol flow reactor (AFR), particle production, OH generation, and OH detection for kinetics experiments.

particles is used in evaluating the observed pseudo first-order loss rate due to OH uptake by the particles, k_1. k_1 is determined from the slope of the natural logarithm of the OH signal decay as a function of reaction time as shown in Fig. 3.10.

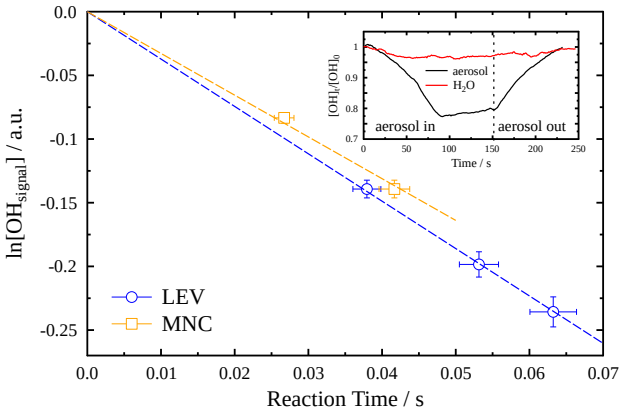

Figure 3.10: Reactive OH loss plotted as the natural logarithm of the observed OH signal as a function of reaction time for a particle surface area density of ∼0.001 cm^{-1} under dry conditions for LEV (blue circles) and MNC (orange squares). The dashed lines represent the corresponding linear fits to the data constrained through the origin. Horizontal and vertical error bars represent ±5% uncertainty in the measured flow rates and OH signal, respectively. An exemplary reactive uptake experiments of OH by LEV particles (black) and the effect of water vapor present only (red) on the OH signal are shown in the inset. The normalized OH signal is presented as a function of experimental time[107].

Typically 5 (up to 15) individual uptake experiments were carried out at each RH. For these experiments, the OH signal was measured in the absence (time = 0) and presence of the particles (time = reaction distance/velocity), accounting for the OH signal losses due to the water vapor and flow reactor wall effects. Since OH diffusional and wall losses can be significant and depend on injector position and thus reaction time making loss estimates difficult, in the majority of cases, k_1 was evaluated over a fixed reaction time thereby keeping OH losses constant. This also ensured a significant decrease in the OH signal attributable to the uptake by the particles. As indicated in Fig. 3.10, when all of the experimental conditions are the same, different

reaction times yield the same k_1. The uncertainty in evaluating k_1 for only one reaction time is reflected in the range of measured γ values.

Figure 3.11 shows the corrected first-order rate constants for OH uptake by LEV and MNC particles, plotted as a function of the particle surface area per unit volume (surface area density, S_a, in units cm^{-1}) at RH=0%. The linear correlations indicate that k_1 depends on S_a, but does not affect γ, in agreement with previous studies[170,194,195].

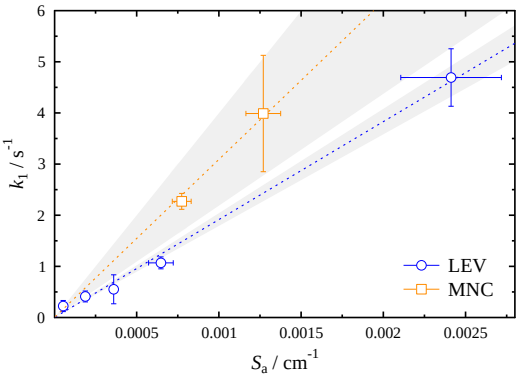

Figure 3.11: First-order loss rates, k_1, for OH uptake by LEV (blue circles) and MNC (orange squares) particles derived at RH=0% as a function of particle surface area density, S_a. The error bars represent 1σ from the mean in k_1 and S_a from three individual uptake measurements conducted under the same experimental conditions at a given S_a. The dotted lines represent the linear fit to the data, constrained through the origin, and shade areas correspond to the 95% confidence intervals.

The observed loss rate of the gas-phase species concentration in the presence of aerosol particles with surface area per unit volume (S_a) can be used to calculate γ as follows.[138]

$$\frac{d[\mathrm{OH}]}{dt} = \frac{\gamma \omega S_a}{4}. \tag{57}$$

Alternatively, the loss of particle-phase species (Org) having radius (r) can be used to calculate γ in Eq. 58.

$$-\frac{d[\mathrm{Org}]}{dt} = \frac{3[\mathrm{OH}]\omega\gamma}{4r}. \tag{58}$$

γ is derived from the following expression:[149]

$$\gamma = \frac{4k_{\mathrm{p}}}{\omega S_{\mathrm{a}}}, \tag{59}$$

where k_{p} is the diffusion-corrected OH loss rate to the particles.

3.5 OH diffusion and correction to experimentally derived γ

The coated-wall flow tube and aerosol flow reactor experiments were conducted at pressures $\leq$30 hPa. The low pressures are necessary to maximize the mean free path of the gas and reduce OH concentration gradients to the flow reactor walls or aerosol particles due to diffusion. However, it is customary to correct γ for gas-phase diffusional losses. In order to correct our observed loss rate k for gas diffusion and obtain the true first-order loss rate to the wall, k_{w} or to the aerosol particles, k_{p} , we apply an algorithm developed by Brown[196], which corrects for changes in the OH concentration profile due to diffusion in the axial and radial direction and uptake, and Fuchs-Sutugin[197], which corrects for changes in the OH concentration profile due to diffusion to the particles, respectively. In order to do so, it is first necessary to determine the diffusion coefficient of OH in the bulk gas flow of the flow reactor. For these experiments, OH was generated in a flow of He or Ar, then mixed with O_2 and transported in a much larger flow of He or N_2. Thus, it is necessary to determine the gas-phase diffusion coefficient of OH in a mixture of He and O_2. To calculate the diffusion coefficient of OH in a mixture of He and O_2 we used the following equation[198]

$$D_{\mathrm{OH}} = \left(\frac{p_{\mathrm{He}}}{D_{\mathrm{OH-He}}} + \frac{p_{\mathrm{O_2}}}{D_{\mathrm{OH-O_2}}}\right)^{-1}, \tag{60}$$

where p_{He} and $p_{\mathrm{O_2}}$ were derived from flow and pressure measurements. The gas-phase diffusion coefficient of OH in He ($D_{\mathrm{OH-He}}$) was taken as 662$\pm$33 Torr cm^2 sec^{-1} at 293 K[199] and corrected for T and p.[200] Measurements of the diffusion coefficient of OH in O_2 are not available. The O_2 concentrations used in this study were typically greater than H_2 to produce both high OH concentrations and mimic atmospheric conditions. Although O_2 concentrations were relatively low during the reactive uptake experiments, $\sim$0.1–10%, it may affect the diffusion of OH in the flow reactor. The estimated diffusion coefficient of OH in O_2, $D_{\mathrm{OH-O_2}}$=180$\pm$18 Torr cm^2 sec^{-1}, is based on

transport properties of its polar analogue, H_2O, in O_2, which has been found to have similar transport properties as OH.[199,201] This value is similar to the measured diffusion coefficient of OH in air of ∼160 Torr cm^2 sec^{-1}.[199]

3.5.1 Diffusion correction to coated-wall flow reactors

For fast reactions, i.e. γ>0.1, flow tube experiments can often be diffusion-limited.[152] For diffusion limitations to occur, the rate of reactive uptake must be faster than the rate of supply of the reactive gas to the reactor walls. The rate of uptake of a trace gas onto the reactive flow tube walls is reduced by the concentration gradient close to the walls surface, resulting in an underestimation of the true loss rate to the wall. For the coated-wall flow tube uptake measurements discussed in this disseration, γ was diffusion-corrected following the approach by Brown[196], a method developed to account for the effects of axial and radial diffusion on the measured first-order rate constant. For simplicity, the gas-phase diffusion effects on measured reaction rates using flow tube reactors is discussed here as outlined in Howard[189].

The gas flow through the flow reactor is considered fully developed viscous flow. A pressure gradient (ΔP/ΔZ) for cylindrical flow tubes as defined in Eq. 61[202] builds as the flow velocity is increased.

$$\frac{\Delta P}{\Delta z} = \frac{0.0059 \eta v}{r^2}, \tag{61}$$

where η is the gas viscosity (g cm^{-1} s^{-1}). This gradient will be larger at higher temperatures since gas viscosity increases with temperatures. The gas maintains a parabolic velocity profile

$$v(r) = 2v(1 - \frac{a^2}{r^2}), \tag{62}$$

where a is the radial parameter. For parabolic flow, the gas velocity is greatest at the center of the tube. The pressure gradient produces velocity and thus gas-phase concentration gradients. These effects can be neglected under the assumption that the pressure is measured near the point of reaction.

Whenever reaction occurs, gas-phase concentration gradients are developed. This is inherent for all flow reactor techniques and is clear in Eq. 63, which shows the change in the reactant concentration as a function of distance down the flow tube.

$$\frac{d[\mathrm{OH}]}{dz} = \frac{-k[\mathrm{OH}]}{v}. \tag{63}$$

Thus axial concentration gradients causes OH to be transported down the tube with an additional velocity component v_{d} given by Fick's first law

$$J = -D\frac{d[\mathrm{OH}]}{dz} = v_{\mathrm{d}}[\mathrm{OH}], \tag{64}$$

where J is the flux (molecule cm^{-2} s^{-1}) and D is the gas-phase diffusion coefficient (cm^2 s^{-1}). Combining Eqs. 63 and 64 gives the additional velocity component v_{d}=Dk/v and the correct transport for the reactant is v+v_{d}. Assuming k_{c} is the corrected rate constant and k is the measured value, the correction for axial diffusion is $(v+v_{\mathrm{d}})/v$, and

$$k_c = k(1 + \frac{kD}{v^2}). \tag{65}$$

Accounting for wall loss rates, the appropriate correction to the observed loss rate due to axial diffusion is given by

$$k_c = k(1 + \frac{(k + 2k_{\mathrm{w}})D}{v^2}). \tag{66}$$

Typically, after correcting for gas-phase diffusion effects, γ was enhanced by a factor of 5-8 using the more sophisticated correction by Brown[196], which in addition to axial diffusion, corrects for radial diffusion. Thus, for the coated-wall flow tube experiments, γ can be very sensitive to the gas-phase diffusion coefficient of OH. When accounting for the uncertainty in the calculated gas-phase diffusion coefficient, the measured γ can vary significantly. To reduce these diffusion effects, the pressure in the flow tube could be reduced further. In doing so, the mean free path, i.e. the average distance that OH travels before colliding with another gas molecule, is lengthened. Also, shortening the distance that OH is required to travel between the source and the reactor walls will reduce the uptake uncertainties due to gas-phase diffusion.

3.5.2 Diffusion correction to aerosol particles

The rate of uptake of a trace gas by aerosol particles can be reduced due to a concentration gradient close to the particle surface, resulting in an underestimation of the true loss rate to the particles, which must be corrected. However, ultrafine particles behave similar to gas molecules and collide due to Brownian motion[43] more frequently than with the walls. The shorter

distance that OH must travel to collide with the particles compared to the cylindrical flow tube walls ensures that gas-to-particle collisions are frequent and OH concentration gradients are minimized.

Equation 59 was corrected for gas-phase diffusion limitations due to gas-phase concentration gradients developed between the particle surface and the surrounding gas applying an approach by Fuchs and Sutugin[197] as shown in Eq. 67.

$$\frac{1}{\gamma} = \frac{1}{\gamma_{\text{exp}}} - \frac{0.75 + 0.286Kn}{Kn(Kn+1)}, \tag{67}$$

where Kn is the Knudsen number and γ_{exp} is the measured γ before diffusion correction. For mono-dispersed particles, Kn is given by

$$Kn = \frac{3D_{\text{OH}}}{\omega r}, \tag{68}$$

where r is the particle radius and D_{OH} is the gas phase diffusion coefficient of OH. The aerosol particles used in this study, however, are polydispersed, so Kn was calculated by

$$Kn = \frac{\Sigma(N_i Kn(i))}{\Sigma N_i} = \frac{3D_{OH}\Sigma(N_i/r_i)}{\omega \Sigma N_i}, \tag{69}$$

where N_i and $Kn(i)$ are the aerosol number concentration and the Knudsen number of the i-th size bin with the radius of r_i, respectively. The diffusion correction using this approach resulted in a small correction to γ of $<0.1\%$ for the aerosol size ranges and pressures applied in the RH-dependent uptake experiments.

4 Results: Heterogeneous OH oxidation of biomass burning organic aerosol surrogate compounds: assessment of volatilisation products and the role of OH concentration on the reactive uptake kinetics

The sections from 4.1 to 4.8 are the reproduction of the publication "Heterogeneous OH oxidation of biomass burning organic aerosol surrogate compounds: assessment of volatilisation products and the role of OH concentration on the reactive uptake kinetics" by Jonathan H. Slade and Daniel A. Knopf published in *Physical Chemistry Chemical Physics*, Vol. 15, 5898–5915, 2013, with permission from the Owner's Society on behalf of the Royal Society of Chemistry. The layout of the article as well as the section figures and table numberings have been adapted to match with the thesis structure. Sections 4.8 covers the supplemental material to the main article covered in sections 4.1 to 4.7.

Heterogeneous OH oxidation of biomass burning organic aerosol surrogate compounds: assessment of volatilisation products and the role of OH concentration on the reactive uptake kinetics

Jonathan H. Slade[1] and Daniel A. Knopf[1*]

[1]Institute for Terrestrial and Planetary Atmospheres/School of Marine and Atmospheric Sciences, Stony Brook University, Stony Brook, NY 11794-5000, USA

[*]To whom correspondence should be addressed. Email:Daniel.Knopf@stonybrook.edu

Published in *Physical Chemistry Chemical Physics*, Vol. 15, 5898–5916, 2013,

4.1 Abstract

The reactive uptake coefficients (γ) of OH by levoglucosan, abietic acid, and nitroguaiacol serving as surrogate compounds for biomass burning aerosol have been determined employing a chemical ionisation mass spectrometer coupled to a rotating-wall flow-tube reactor over a wide range of [OH]$\sim 10^7$–10^{11} molecule cm^{-3}. Volatilisation products of these organic substrates due to heterogeneous oxidation by OH have been determined at 1 atm using a high resolution proton transfer reaction time-of-flight mass spectrometer (HR-PTR-ToF-MS). γ range within 0.05–1 for [OH]=2.6×10^7–3×10^9 molecule cm^{-3} for all investigated organic compounds, but decrease to 0.008–0.034 for [OH]=4.1×10^{10}–6.7×10^{10} molecule cm^{-3}. γ as a function of [OH] can be described by a Langmuir-Hinshelwood model, neglecting bulk processes, suggesting that despite its strong reactivity, OH is mobile on surfaces prior to reaction. The best fit Langmuir-Hinshelwood parameters on average are K_{OH}=3.81×10^{-10} cm^3 molecule^{-1} and k_{s}=9.71×10^{-17} cm^2 molecule^{-1} sec^{-1} for all of the investigated organic compounds. Volatilised products have been identified indicating enhancements over background of 50% up to a factor of 15. Amongst the common volatile organic compounds (VOCs) identified between levoglucosan, abietic acid, and nitroguaiacol were methanol, acetaldehyde, formic acid, and acetic acid. VOCs having the greatest enhancement over background were glucic acid from levoglucosan, glycolic acid from abietic acid, and methanol and nitric acid from nitroguaiacol. Reaction mechanisms leading to the formation of glucic acid, glycolic acid, methanol, and nitric acid are proposed. Estimated lower limits of atmospheric lifetimes of biomass burning aerosol particles, 200 nm in diameter, by heterogeneous OH oxidation under fresh biomass burning plume conditions are $\sim$2 days and up to $\sim$2 weeks for atmospheric background conditions. However, estimated lifetimes depend crucially on [OH] and corresponding γ, emphasising the need to determine γ under relevant conditions.

4.2 Introduction

Aerosol particles are ubiquitous and have a profound influence on visibility, atmospheric chemistry, health, and climate.[3] Aerosol particles can both scatter radiation directly or indirectly by modification and formation of clouds; the latter process being one of the greatest areas of climate uncertainty.[5] Inherent in this uncertainty is the difficulty in quantifying the impact of particle ageing mechanisms.[8] Chemical ageing of aerosol through heterogeneous oxidation by reactive trace gas species such as OH, O_3, and NO_3 can significantly influence aerosol lifetime, composition, and physical properties,[12–14] and thus its climate potential.[16,17]

Numerous laboratory studies have investigated chemical ageing of model organic aerosol,[31,32,36,95,110,166] organic coated salt particles,[203] and ambient particles collected in the field by OH[204] due to its strong reactivity, with uptake coefficients (γ), defined as the fraction of collisions with a surface that result in a reactive loss, typically between 0.1 and 1. Recent studies indicate that certain systems exhibit $\gamma>1$, suggesting secondary loss of OH by additional loss pathways at the surface.[36,205] Less understood are the reaction products and pathways of heterogeneous oxidation, because of the likely dependence on chemical makeup, physical state of the particle, and environmental conditions.[8,12,206,207] Following reaction with OH in the presence of O_2, condensed phase compounds may undergo functionalisation and fragmentation reaction pathways, either forming oxygenated functional groups that stay partitioned to the particle phase or fragmented short-chained compounds that, depending on their vapour pressures, volatilise from the surface, respectively.[12,163] From a gas-phase budget perspective, heterogeneous oxidation by OH is likely not a limiting factor for atmospheric OH since gas-phase loss with e.g. NO_2 is much faster,[31] however sufficient volatilisation may impact the gas-phase budget of volatile organic compounds (VOCs).[37] The effect of OH on lifetimes of organic aerosol, however, can be significant.[32,207] Furthermore, low-volatility compounds can participate in secondary organic aerosol (SOA) formation,[38] not only changing aerosol mass distribution, but also particle number density, potentially impacting the available cloud condensation nuclei (CCN)[39] and ice nuclei (IN)[40–42] for the formation of clouds.

Several studies have identified volatilised products formed by heterogeneous oxidation of condensed-phase organics by OH radicals. Molina *et al.*[32] observed sufficient volatilisation of alkane and aromatic surfaces such as paraffin and pyrene films, respectively, suggesting that volatilisation may

be a major loss pathway for organic aerosol with lifetimes comparable to loss due to wet deposition.[32] McNeill *et al.*[166] showed that oxidation of palmitic acid aerosol particles by OH results in significant production of formic acid (HCOOH). Vlasenko *et al.*[110] identified a suite of volatilised products related to the breakage of a -CH_2- group, resulting in the release of formic acid and formaldehyde from pyrene and n-hexane soot, ethylhexanal from BES (bis(ethylhexyl)sebacate), and a series of carboxylic acids, aldehydic carboxylic acids, and alcohols from stearic acid OH oxidation. The yield of volatilised products were found to be strongly dependent on the partial pressure of O_2, consistent with the formation of alkyl peroxy radicals that subsequently undergo self-reaction (in the absence of NO) to form an alkoxy radical followed by scission.[32] The extent of volatilisation is recognised to depend on the degree of oxygenation of the material, whereby more oxidised species tend to fragment more compared to their chemicallyreduced counterparts.[81,163,208] Furthermore, the size and geometry of the reacting molecule can play a role in the degree of fragmentation.[95]

Imperative for understanding gas-to-particle processing is the ability to model the uptake of reactive gas-phase constituents to different surfaces. In doing so, knowledge of physicochemical processes such as mass transport, chemical reactions at the interface, and the connection between particle surface, bulk, and gas-phase processes, and thus oxidant and particle lifetimes become available.[209–212] Due to its high reactivity with most organic species, it is conceivable that upon collision with a reactive surface, OH radicals undergo a direct reaction, also termed Eley-Rideal kinetics;[210] although this has not been confirmed.[12,138] However, the reactive uptake of O_3 and NO_2 to various organic substrates and black carbon have shown a non-linear dependence on gas-phase concentration, decreasing at larger oxidant concentrations, indicative of oxidants first adsorbing to the surface and then undergoing competing reactions with the surface reactive sites, also termed Langmuir-Hinshelwood (L-H) kinetics.[209] Knopf *et al.*[13] showed that the uptake of NO_3 by biomass burning aerosol surrogate compounds decreased at higher [NO_3]. The change in γ for NO_3 uptake by levoglucosan could only be described by accounting for NO_3 adsorption and surface reaction (L-H type reaction) and diffusion of NO_3 into the bulk and subsequent reaction.[14] Previous studies of the reactive uptake of OH by condensed-phase organics employed [OH]$\sim 10^8$–10^9 molecule cm^{-3}, however volatilisation studies used [OH] up to $\sim 10^{11}$ molecule cm^{-3}.[31,32,95,166] Renbaum and Smith[213] observed relatively lower γ to squalane and 2-octyldodecanoic acid (ODA) at higher [OH]$\sim 10^{11}$ molecule

cm^{-3}. However, these authors assert that observed lower γ employing high [OH] may be an artifact in aerosol flow tube studies in part due to large variations in residence times and adsorption of OH precursor gases such as O_3 to the surface prior to OH mass accommodation. If OH first adsorbs to the surface followed by reaction, the longer surface residence time may alter OH reaction specificity[110,214] at both the surface and potentially in the bulk, and thus influence changes in particle composition. With longer residence times at the surface, more OH is available to participate in aqueous phase reactions resulting in a higher degree of oxygenation of surface-bound species. With respect to volatilisation, longer residence times of OH at the surface may result in a greater degree of fragmentation of surface-bound products, which may lead to a higher flux of volatile species from the surface.

The aim of this study is to both derive γ over a wide range of [OH] ($\sim 10^7$–10^{11} molecule cm^{-3}) to infer the underlying uptake process and to explore potential OH-induced fragmentation pathways by identifying volatilised products of organic compounds specific to biomass burning aerosol (BBA). Biomass burning plumes represent a major source of condensed and gas-phase species to the atmosphere, with particle emission rates comparable to fossil-fuel burning,[73] and represents a majority of primary organic aerosol found in the atmosphere.[20] Within fresh biomass burning plumes OH concentrations up to 1.7×10^7 molecule cm^{-3} have been observed.[63,215] While BBA composition varies depending on vegetation-type,[82] surrogate compounds of BBA consist of cellulose and hemicellulose decomposition products such as levoglucosan (1,6-anhydro-β-glucopyranose, $C_6H_{10}O_5$), resin acids such as abietic acid (1-phenanthrenecarboxylic acid, $C_{20}H_{30}O_2$), and substituted phenols such as 5-nitroguaiacol (2-methoxy-5-nitrophenol, $C_7H_7NO_4$) from lignin decomposition.[90,92] Recently, methyl-nitrocatechols have been identified as a tracer species for biomass burning secondary organic aerosol (SOA).[99] Knopf *et al.*[13] investigated the stability of these BBA surrogate compounds with respect to heterogeneous oxidation by O_3, NO_2, NO_3, and N_2O_5. Although the derived uptake coefficients are lower than those typically involving OH,[95] the oxidative power ($\gamma \times$[oxidant]) was comparable to that of OH. Only two studies thus far have investigated the stability of levoglucosan in wood smoke[83] and pure levoglucosan[83,95] by heterogeneous OH oxidation. Kessler *et al.*[95] derived γ=0.91 and observed volatilisation of levoglucosan, although the focus was on particle mass loss rather than product identification. Although the contribution of BBA volatilisation to the total volatile organic compound (VOC) concentration found in biomass burning plumes is difficult to as-

sess, more than half of the light non-methane hydrocarbons (NMHCs) from biomass burning are C_2–C_4 hydrocarbons, and composed of alcohols, aldehydes, ketones, carboxylic acids, esters, ethers, and furanes.[97] Ageing, and thus the impact on particle composition and potential input of gases to the atmosphere may significantly affect the role of these species in climate and other relevant atmospheric and environmental processes.

Here, we investigate the OH reactivity and identify volatilisation products of levoglucosan, abietic acid, and nitroguaiacol representing typical compounds of BBA. γ as a function of OH concentration is determined using a rotating-wall flow-tube coupled to a chemical ionization mass spectrometer (CIMS). In evaluating the potential for volatilisation, we employ a high resolution proton transfer reaction time-of-flight mass spectrometer (HR-PTR-ToF-MS) coupled to a separate flow tube reactor operated at atmospheric pressure.

4.3 Results and discussion

4.3.1 Kinetics derived from uptake experiments

The reactive uptake coefficients were determined as described in detail previously.[13] In short, γ was determined from the irreversible removal of OH as a function of injector position. From these data the observed pseudo first-order wall loss rate k_{obs} is determined when plotting the change of the natural logarithm of the OH signal as a function of reaction time. This is shown for OH uptake by the species studied here in Fig. 3.8. k_{obs} wasdetermined from the slope of the linear fit to the data. The uptake of OH by surfaces other than the substrate that are coated by halocarbon wax are significantly lower. Thefirst-order wall loss rate, k_{wall}, was calculated from k_{obs} using the Brown[196] formalism to account for changes in the OH concentration due to uptake.[13]

The reactive uptake coefficient, γ, was obtained using the equation[216]

$$\gamma = \frac{2rk_{\text{wall}}}{\omega_{\text{OH}} + rk_{\text{wall}}} , \tag{70}$$

where r is the flow tube radius and ω_{OH} is the molecular velocity of OH.

The gas-phase diffusion coefficient of OH in He ($D_{\text{OH-He}}$) was taken as 662±33 Torr cm^2 sec^{-1} at 293 K[199] and corrected for T and p.[200] Measurements of the diffusion coefficient of OH in O_2 are not available. The O_2

concentrations used in this study were typically greater than H_2 to both produce high OH concentrations and mimic atmospheric conditions. Although O_2 concentrations were relatively low during the reactive uptake experiments, $\sim$0.1–10%, it may affect the diffusion of OH in the flow reactor. The estimated diffusion coefficient of OH in O_2,D_{OH-O_2}=180$\pm$18 Torr cm^2 sec^{-1}, is based on transport properties of its polar analogue, H_2O, in O_2, which has been found to have similar transport properties as OH.[199,201] This value is similar to the measured diffusion coefficient of OH in air of $\sim$160 Torr cm^2 sec^{-1}.[199] To calculate the diffusion coefficient of OH in a mixture of He and O_2 we used the following equation[198]

$$D_{OH} = (\frac{p_{He}}{D_{OH-He}} + \frac{p_{O_2}}{D_{OH-O_2}})^{-1} , \quad (71)$$

where p_{He} and p_{O_2} were derived from flow and pressure measurements.

The diffusion limit of the heterogeneous kinetics can be estimated using $k_{dl} \approx 3.66D/r^2$, where k_{dl} is the diffusion limited rate constant, D is the diffusion coefficient, and r is the radius of the flow tube.[217,218] One OH uptake experiment involving palmitic acid was conducted in the diffusion limit. For the remaining uptake experiments presented in this study diffusion limited conditions were not reached. However, applying the uncertainty in the diffusion coefficients can result in $\gamma \geq 1$, indicative of potential diffusion limitations. The γ values reported in this study are the mean of at least 5 (up to 16) reactive uptake measurements and for each employing freshly prepared organic substrates. Presented γ represent a range due to the uncertainty in the diffusion coefficients of OH in He and OH in O_2 accounting for the range in individually observed γ values.

Table 4.1: Comparison of OH reactive uptake coefficients, γ, with different substrates determined in this study with literature values.

Substrate	Work	γ_{min}	γ_{avg}	γ_{max}
Levoglucosan	This study	0.12	0.52	1
	Kessler *et al.*[95]		0.91 ($\pm$0.08)[a]	
Palmitic acid	This study	0.14	0.71	1
Stearic-palmitic acid	Bertram *et al.*[31]	0.14	0.32	1
Halocarbon wax	This study	2.32×10^{-4}	5.14×10^{-4}	6.62×10^{-4}
	Bertram *et al.*[31]	3×10^{-4}	6×10^{-4}	9×10^{-4}

[a]Reported uncertainty is due to the uncertainty in experimental parameters and does not represent a measurement range.

For validation purposes, we determined γ for the uptake of OH by halocarbon wax, palmitic acid (hexadecanoic acid, $C_{16}H_{32}O_2$), and levoglucosan for comparison with previous works.[31,95] Table 4.1 summarises γ determined at OH concentrations comparable to previous studies ($\sim10^8$–10^9 molecule cm^{-3}). Within uncertainties, γ of OH for all of the investigated surfaces are in agreement with previous literature values. The uncertainty in γ for OH uptake by levoglucosan reported by Kessler *et al.*[95] is due to uncertainties in their experimental parameters and does not represent a range in γ as given in this study. OH uptake by palmitic acid differs slightly from that determined by Bertram *et al.*[31] possibly due to the additional presence of stearic acid (octadecanoic acid, $C_{18}H_{36}O_2$) in their study. The good agreement of γ with previous literature studies for both slow uptakes with halocarbon wax and fast uptakes with levoglucosan and palmitic acid indicates that our technique can determine γ with good accuracy over a wide range of reaction probabilities.

4.3.2 OH dependencey of the reactive uptake coefficient

The reactive uptakes of OH by levoglucosan, abietic acid, and 5-nitroguaiacol were investigated under dry conditions and in the absence of NO_2 for a wide range of OH concentrations ($\sim10^7$–10^{11} molecule cm^{-3}) as shown in Fig. 4.1. The influence of RH on the reactive uptake was not investigated as

atmospherically relevant RH increases the pressure in the flow reactors to a level that slower diffusion may affect heterogeneous kinetics. If RH is sufficiently high to cause deliquesence or a moisture-induced phase transition of the organic substrate, OH uptake is likely enhanced as indicated by previous studies.[33,34,106] For all substrates, within experimental uncertainties γ was greatest (between 0.056 and 1) at relatively lower [OH]$\sim 10^7$–10^9 molecule cm^{-3}, comparable to previous studies.[12] At [OH]$>10^9$ molecule cm^{-3}, γ falls precipitously and continues to decrease reaching a minimum of $\gamma \sim 0.01$ at our maximum detectable OH concentration of $\sim 10^{11}$ molecule cm^{-3}. γ was also comparable between the three different substrates indicating that both a similar uptake process may occur at the surface as well as the unselective reactivity of the OH radical toward organic species containing different chemical functionalities.

Levoglucosan contains three hydroxyl (-OH) functional groups and two ethers. Abietic acid contains conjugated unsaturated bonds, a carboxylic acid, and many tertiary hydrogens, all of which are highly reactive toward the hydroxyl radical.[61] 5-nitroguaiacol is aromatic, but contains a hydroxyl group *ortho* to a methoxy (-OCH_3) functional group and a nitro group (-NO_2) *para* to the methoxy group. Both -OH and -OCH_3 on aromatics are *ortho* and *para* directing electron-donating substituents. The nitro group is *meta* directing, but because of the orientation of the functional groups on 5-nitroguaiacol, presumably all of the functional groups are susceptible to OH attack, which typically results in electrophilic aromatic substitution by OH.[61] More detail regarding the reaction mechanisms of OH with the organic substrates is reserved for the volatilisation section; however, Knopf *et al.*[13] gives a qualitatively similar discussion for the reaction of NO_3 radicals with the same substrates studied here.

We can infer from gas-phase kinetics the similar OH reactivities towards the various functional groups on the compounds studied here. Presumably, OH will abstract the weakest bound hydrogen based on the structure-activity relationship (SAR)[219] or add across a double bond.[61] Both hydrogen abstraction and addition of OH across a double bond have comparable gas-phase reaction rate constants ranging from $\sim 10^{-12}$–10^{-13} cm^3 molecule^{-1} sec^{-1} and typically become more reactive with increasing molecular size.[220] It is not clear if OH-addition adducts form on the organic substrates studied here or affect the rate of OH uptake, although OH-addition adducts have been observed on compounds containing conjugated double bonds[221,222] and in the condensed-phase on dimethyl sulfoxide (DMSO).[223] Adduct formation

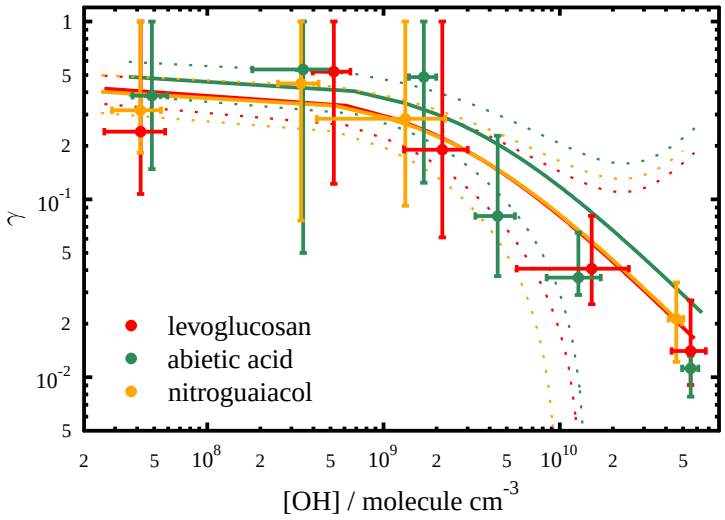

Figure 4.1: Average OH uptake coefficients, γ, for levoglucosan (red), abietic acid (green), and nitroguaiacol (orange) as a function of gas-phase OH concentration. Each data point represents the average γ of at least five separate experiments. Vertical error bars represent the largest range in γ due to the uncertainty in the diffusion coefficient for OH in He and O_2 accounting for the range in γ obtained from individual uptake experiments. Horizontal error bars represent 1σ from the mean in OH concentration. The solid lines are the modeled γ values applying Eq. 72 applying the individually derived γ values and dotted lines are the 95% confidence intervals of the modeled γ for levoglucosan (red), abietic acid (green), and nitroguaiacol (orange).

on levoglucosan in the condensed-phase is unlikely as OH reaction with levoglucosan particles has been shown to proceed via H-atom abstraction and not OH addition.[95]

The decrease in γ with higher OH concentration for the compounds studied and to the extent observed here is unique and suggests that upon collision with the substrate, OH radicals first adsorb to the surface and then react, i.e. the rate of irreversible reactive uptake to the surface is slower than the rate of OH adsorption, indicative of L-H kinetics.[14,209] To our knowledge no other study has explicitly measured γ over this range of OH concentrations

nor observed such a trend in γ as a function of OH concentration. Kessler *et al.*[214] observed strong uptake of OH to highly oxidised single-component aerosol particles composed of 1,2,3,4-butanetetracarboxylic acid (BTA), citric acid, and tartaric acid. Their data suggests that despite the high O:C and low H:C ratios, the strong reactive uptake may be aided by adsorption of OH followed by reaction, resulting in a longer residence time for OH to abstract a hydrogen atom.Vlasenko *et al.*[110] noted similar findings with regard to heterogeneous oxidation of BES by OH. In their study, the production of 2-ethylhexanal from BES is unique to OH attack of the CH_2O moiety of BES and suggests that OH is mobile on the surface of BES prior to reaction. Che *et al.*[224] found that γ of OH on liquid squalane particles decreased from $\sim$0.54 to $\sim$0.31 between different experiments in the presence of $\sim 3\times10^8$ molecule cm^{-3} and $\sim 10^{10}$ molecule cm^{-3} OH, respectively. However, recent work suggests that interferences due to adsorption of OH precursor gases such as O_3 at higher [OH] to the surface may act as a shield to OH uptake,[213] resulting in lower γ at higher OH concentrations that can be misconstrued as a L-H type uptake process by OH. In evaluating the extent to which O_2 may impact uptake of OH, we used a modified L-H mechanism described by Renbaum and Smith[213] to model γ as a function of [O_2] for levoglucosan, abietic acid, and nitroguaiacol. However, no reasonable results based on a fit of this modified L-H mechanism to experimental data could be obtained. γ at the highest [O_2] was generally lower than γ at the lowest [O_2], however insufficient data points were available to conclusively assess the role of O_2 in the OH uptake. Renbaum and Smith[213] found that their trend in γ was fully explained by the presence of co-adsorbate O_3. O_2 is less surface reactive than O_3 and the lack of a clear trend of γ with [O_2] suggests that only OH contributes to the relatively lower γ at higher OH concentrations.The potential formation of other co-adsorbates such as HO_2 and H_2O_2 formed from HO_x reactions in the injector may affect OH uptake to the substrates studied here. However, the HO_2 concentrations were at or below background levels. We have no direct measurements of [H_2O_2]. We estimate that H_2O_2 formation due to OH self-reaction in the gas-phase for the reaction times in the flow reactor of $\sim$1 ms at our highest employed [OH]$\sim 5\times10^{10}$ molecule cm^{-3} and [O_2]$\sim 2\times10^{18}$ molecule cm^{-3} results in maximum [H_2O_2]$\sim 2\times10^6$ molecule cm^{-3}, which is four orders of magnitude less than [OH]. Hence, H_2O_2 has likely a very minor effect on the reactive uptake at higher [OH].

Table 4.2: Langmuir-Hinshelwood model fitting parameters, K_{OH} and k_s, derived using experimentally obtained γ and k_{obs} as a function of OH concentration.

Substrate	K_{OH} / cm^3 molecule^{-1}	k_S / cm^2 molecule^{-1} sec^{-1}
Levoglucosan	4.27 ($\pm$2.71) $\times$ 10^{-10}	8.14 ($\pm$4.30) $\times$ 10^{-17}
	2.74 ($\pm$0.63) $\times$ 10^{-11} [a]	7.96 ($\pm$1.66) $\times$ 10^{-16} [a]
Abietic acid	3.20 ($\pm$2.27) $\times$ 10^{-10}	1.26 ($\pm$0.77) $\times$ 10^{-16}
Nitroguaiacol	3.96 ($\pm$4.40) $\times$ 10^{-10}	8.38 ($\pm$8.44) $\times$ 10^{-17}

[a] Derived using k_{obs} as a function of [OH] from Fig. 4.2.

The data in Fig. 4.1 is modeled based on a non-linear least squares fit applying a L-H mechanism described in Ammann *et al.*[155] given as

$$\gamma = \frac{4k_s[\text{Org}]K_{OH}}{\sigma_{OH}\omega_{OH}(1 + K_{OH}[OH])} , \tag{72}$$

where k_s is the reaction rate constant at the surface of the substrate, [Org] is the surface concentration of the organic taken as 2×10^{14} molecule cm^{-2},[14] K_{OH} is the adsorption/desorption equilibrium constant of OH, and σ_{OH} is the surface area occupied by one adsorbed OH molecule approximated as 1.08×10^{-15} cm^2 molecule^{-1} using the cross-section of H_2O.[211,212] The best fit parameters, k_s and K_{OH} are given in Table 4.2. Within uncertainties, both K_{OH} and k_s derived from equation 3 between levoglucosan, abietic acid, and nitroguaiacol are comparable. To our knowledge, no other studies have determined k_s or the adsorption/desorption equilibrium constant of OH, K_{OH}. Here, on average for all of the organic substrates, K_{OH} is 3.81×10^{-10} cm^3 molecule^{-1}, about four to five orders of magnitude greater than e.g. the adsorption/desorption rate of O_3, K_{O_3}, on 2-ODA particles.[213] k_s on average for all of the organic substrates is 9.71×10^{-17} cm^2 molecule^{-1} sec^{-1}, comparable or slightly larger in magnitude compared to k_s for O_3 uptake.[155,159,225] k_s is also significantly smaller in magnitude compared to NO_3 reaction with levoglucosan and abietic acid substrates.[14] However, a large K_{OH} and a relatively smaller k_s may suggest additional processes unaccounted for in the applied L-H mechanism, e.g. surface regeneration due to volatilisation or OH diffusion and reaction in the bulk.[13,14] Future work investigating the time-dependent kinetics and employing a detailed flux-based heterogeneous

kinetics model will be important for resolving these issues. In summary, the good agreement between modeled γ as a function of [OH] using equation 3 and the experimental data for all investigated organic substrates suggests that OH follows a L-H mechanism, whereby OH first adsorbs to the surface followed by reaction.

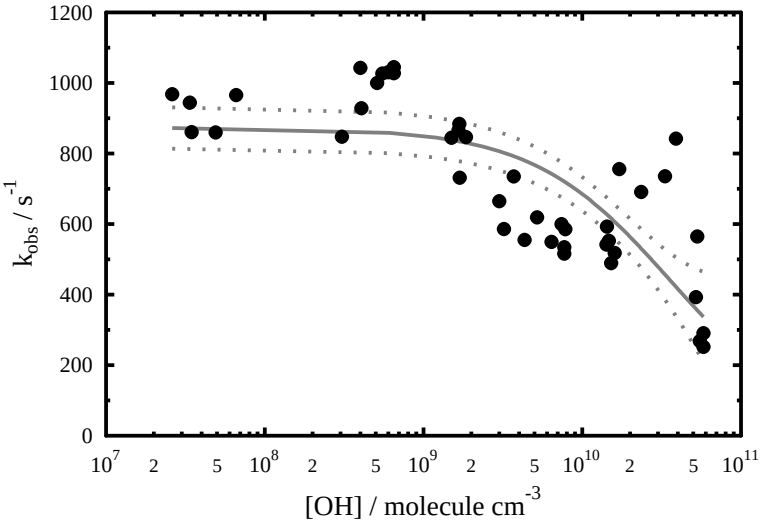

Figure 4.2: k_{obs} as a function of OH concentration for levoglucosan. The solid gray line represents the modeled k_{obs} applying Eq. 73 and dotted lines represent corresponding 95% confidence intervals.

Figure 4.2 shows exemplary the experimentally derived pseudo first-order reaction rate constant of the decay of OH, k_{obs}, as a function of [OH] for levoglucosan. k_{obs} stays nearly constant up to [OH]$\sim 2\times 10^9$ molecule cm^{-3} and then rapidly decreases at higher [OH] similar to the trend in γ as a function of [OH] as shown in Fig. 4.1. This behavior is indicative of slower OH uptake at higher employed [OH] due to the depletion of surface reactive sites, consistent with a Langmuir-type uptake process.[155] Furthermore, k_{obs} as a function of [OH] shown in Fig. 4.2 is fit well by a non-linear least squares fit to a Langmuir isotherm[159] given by

$$k_{\mathrm{obs}} = \frac{k_{\mathrm{s}}[\mathrm{Org}]K_{\mathrm{OH}}[\mathrm{OH}]}{1 + K_{\mathrm{OH}}[\mathrm{OH}]} \frac{[\mathrm{Org}]}{[\mathrm{OH}]_{\mathrm{s}}} \,, \tag{73}$$

where $[OH]_s$ is surface adsorbed concentration of OH molecules given by $[OH]_s$=[OH](V/S) assuming unity OH surface accommodation, and V/S is the volume-to-surface area ratio of the flow tube being 0.440 cm. Since we do not measure the pseudo first-order reaction rate constant of the decay of the organic species, $k_{obs-Org}$, we convert $k_{obs-Org}$ to k_{obs} assuming equilibrium and a bimolecular reaction. The solid line in Fig. 4.2 shows k_{obs} as a function of [OH] applying equation 4 and the dotted lines represent the 95% confidence intervals. The best fit parameters, k_s and K_{OH} using equation 4 are given in Table 4.2 for levoglucosan. k_s and K_{OH} derived from k_{obs} are $7.96(\pm1.66)\times10^{-16}$ cm^2 molecule^{-1} sec^{-1} and $2.74(\pm0.63)\times10^{-11}$, respectively, compared to k_s=$8.14(\pm4.30)\times10^{-17}$ cm^2 molecule^{-1} sec^{-1} and K_{OH}=$4.27(\pm2.71)\times10^{-10}$ cm^3 molecule^{-1} when fitting a L-H isotherm to γ for levoglucosan. These differences are most likely due to applied assumptions deriving the decay of the organic species. For these reasons we recommend to use k_s and K_{OH} derived from equation 3 to describe the underlying heterogeneous kinetics.

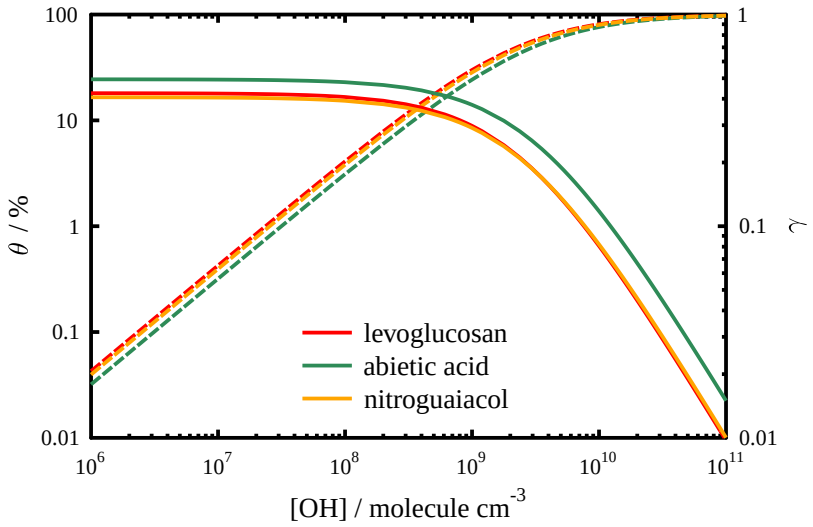

Figure 4.3: Modeled γ and θ applying Eqs. 72 and 74, respectively, for levoglucosan (red), abietic acid (green), and nitroguaiacol (orange). Solid lines refer to γ and dashed lines refer to θ.

The equilibrium OH surface coverage (θ) of the organic substrates studied here can be estimated based on K_{OH} as outlined in Pöschl *et al.*,[159] where

$$\theta = \frac{K_{\mathrm{OH}}[\mathrm{OH}]}{1 + K_{\mathrm{OH}}[\mathrm{OH}]} \ . \tag{74}$$

Figure 4.3 shows θ and γ as a function of [OH] applying experimentally determined K_{OH} and γ for investigated organic substrates given in Table 4.2. θ increases with [OH] and for θ>20%, γ decreases most significantly. At low [OH]$\leq 2\times10^7$ molecule cm^{-3}, equilibrium OH surface coverage can be on the order of 95%.

4.4 Volatilisation products of BBA surrogate compounds exposed to OH

The formation of volatile gas-phase products from heterogeneous oxidation are shown in Figs. 4.4–4.6 for palmitic acid, levoglucosan, abietic acid, and 5-nitroguaiacol, where the HR-PTR-ToF-MS spectra measured in the presence of [OH]$\sim 2\times10^{10}$ molecule cm^{-3} are compared to those measured in the absence of the organic substrates. Palmitic acid was chosen for volatilisation product studies in order to compare with findings from McNeill *et al.*[166] In the presence of OH, the products reached steady-state concentrations up to $\sim$60 scans, with a set scan rate of 1s/scan. This is equivalent to an atmospheric OH exposure of $\sim 5\times10^{-8}$ atm sec or 1 week of exposure to typical background atmospheric [OH]$\sim 2\times10^6$ molecule cm^{-3}. Each spectrum up to m/z=350 Th is an average of three consecutively measured full scans. The most significant peaks above a peak amplitude of $\sim$1 cps occurred between m/z=10–150 Th, so peaks above m/z=150 Th are not shown.

The larger signal intensities in red relative to gray as shown in Figs. 4.4–4.6 indicate that volatile gas-phase products are being formed and then detected downstream of the flow reactor. The background peaks in the presence of OH and no substrates as shown in gray in Figs. 4.4–4.6 may arise from impurities or degassing from the flow tube, or along the inlet leading to the HR-PTR-ToF-MS. In all cases, the presence of O_3 and H_2O had minimal effects on the signal, however when adding H_2O to the system, some of the species shown in gray had greater intensity than application of dry N_2 alone, probably from impurities in the water, although efforts were made to remove these impurities by degassing the denuder in a separate pumping

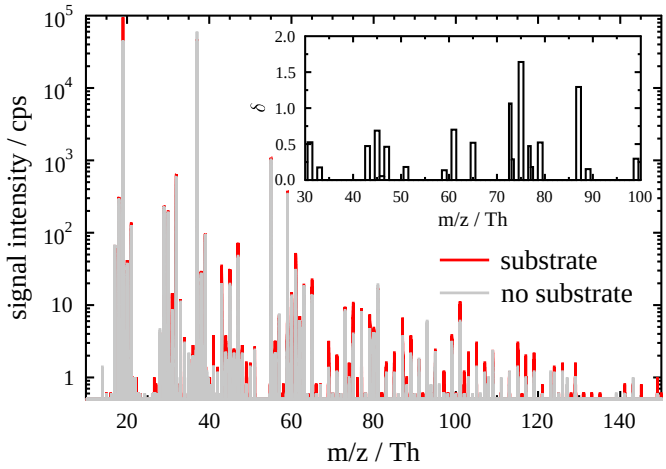

Figure 4.4: Volatilized product spectra for palmitic acid in the presence of OH without substrate (light gray) and in presence of the substrate (red). Inset panel shows the background corrected (i.e. OH + no substrate) relative difference in the H_3O^+ integrated and normalized intensities for some of the major peaks detected upon exposure to OH. See text for details.

system. Regardless, these peaks were considered as a part of the background for both the presence and absence of the organic substrates, and therefore had no impact on the peaks in the presence of OH. Extra care was taken to minimize these effects by first cleaning the flow tubes in an acetone-water rinse cycle followed by baking in an oven at 408 K for at least 24 hours, but the flow tubes were likely impacted by adsorption of low-volatility organics from the background conditioning cycle. However, it is not surprising that some of the background peaks arise at the same masses as those observed in the presence of OH and the substrates since VOC impurities may produce a range of carboxylic acids and carbonyls.[110] We attribute all other changes in the mass spectrum as arising from OH surface oxidation chemistry. A comprehensive list of all of the major peaks detected based on their difference to the background and their corresponding formulas and related isomers are given in Table 4.3.

The largest peaks across all of the spectra were m/z=19, 32, 37, and 55 Th, which correspond to H_3O^+, O_2^+, $H_3O^+{\cdot}H_2O$, and $H_3O^+{\cdot}(H_2O)_2$, re-

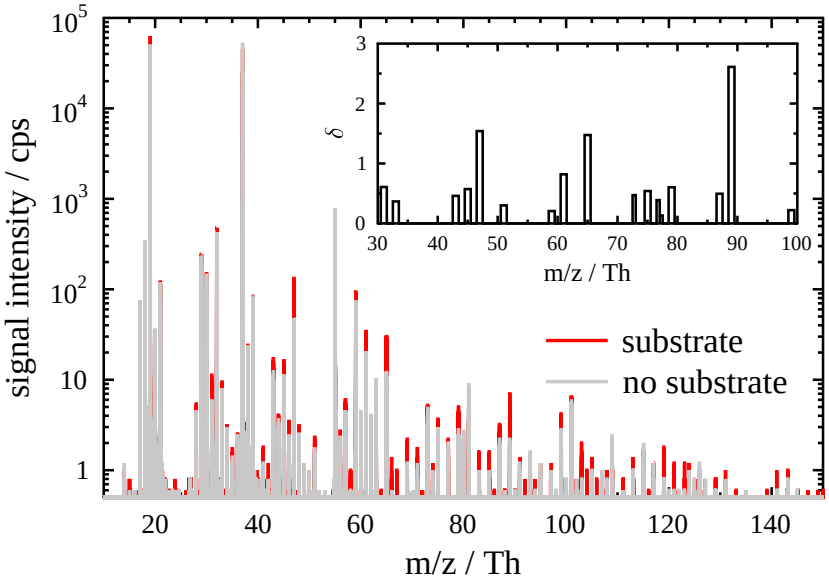

Figure 4.5: Volatilized product spectra for levoglucosan in the presence of OH without substrate (light gray) and in presence of the substrate (red). Inset panel shows the background corrected (i.e. OH + no substrate) relative difference in the H_3O^+ integrated and normalized intensities for some of the major peaks detected upon exposure to OH. See text for details.

spectively. The intensities of these peaks did not significantly change in the presence and absence of the substrates + OH. As discussed above, we encountered significant clustering of H_2O with H_3O^+ due to the high RH (∼60%) used for producing OH, which can result in additional proton transfer between the VOC and cluster ion.[179] This may skew interpretation of the absolute VOC concentration and product yield. RH can impact the detection sensitivity of formaldehyde (CH_2O) by a favourable back reaction of protonated HCHO with water.[180] The presence of 60% RH likely does not lead to deliquescence or a moisture-induced phase transition of the applied organic substrates or affect the uptake kinetics.[33,34,106] However, it cannot be ruled out that adsorption of water on the organic substrate surfaces may affect the kinetics by blocking reactive sites and suppress volatilisation due to the

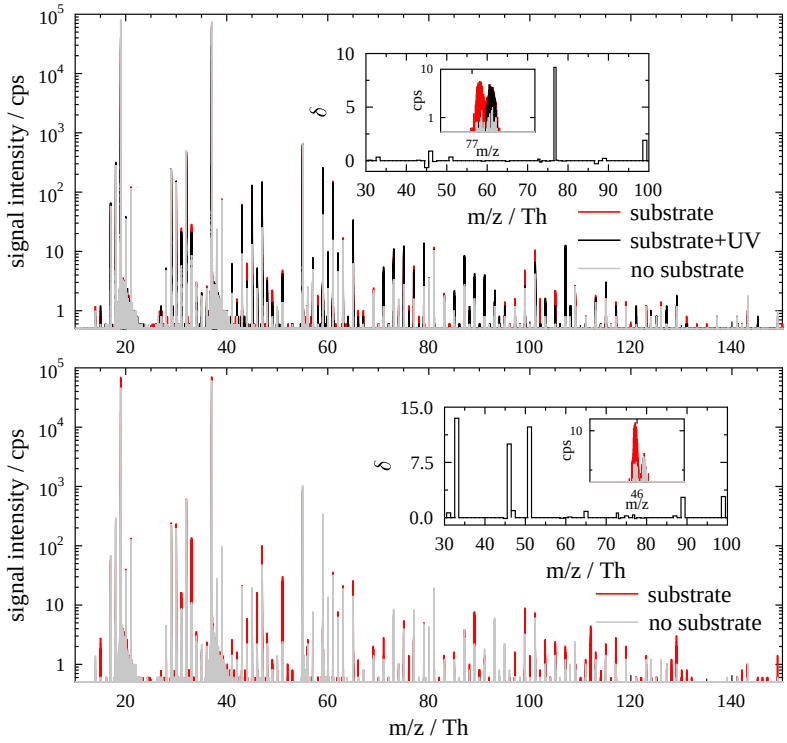

Figure 4.6: Volatilized product spectra for abietic acid (top) and 5-nitroguaiacol (bottom) in the presence of OH without substrate (light gray) and in presence of the substrate (red), and UV + substrate (black). Inset panel shows the background corrected (i.e. OH + no substrate or UV + substrate) relative difference in the H_3O^+ integrated and normalized intensities for some of the major peaks detected upon exposure to OH. The insets in the panels for abietic acid and nitroguaiacol show the mass-corrected intensities at m/z=77.022 Th and m/z=45.992 Th, respectively. See text for details.

presence of a water layer. Due to these influences as well as the possibility of fragmentation of some of the parent species and not having individual gas standards for the VOCs discussed here, we do not report on product concentration yields. Instead, We interpret VOC yields based on their relative change in intensities accounting for the background, δ, as shown in the inset

panels of Figs. 4.4–4.6 and concomitantly in Fig. 4.7 and defined as:

$$\delta = \frac{I_{\text{substrate+OH}} - I_{\text{OH}}}{I_{\text{OH}}} \,, \tag{75}$$

where $I_{\text{substrate+OH}}$ is the VOC signal intensity in the presence of OH and substrate and I_{OH} is the VOC signal intensity in the absence of the substrate. Prior to background correction for the calculation for δ, the signals for each experiment were normalized to the reagent ion (H_3O^+) intensity (defined as the signal at $H_3^{18}O^+$ multiplied by 500 based on its isotopic abundance to $H_3^{16}O^+$). See supplementary material for further information regarding the HR-PTR-ToF-MS sampling protocol and signal analysis.

For validation purposes, Fig. 4.4 shows for palmitic acid that some of the major peaks correspond to protonated aldehydes, carbonyls, carboxylic acids, aldehydic carboxylic acids, and alcohols that differ in structure by a CH_2 group. This is qualitatively similar to the results in Vlasenko *et al.*,[110] which observed a sequence of peaks related to these protonated species from heterogeneous oxidation of stearic acid by OH. Specifically, peaks consistent with either protonated aldehydes or carbonyls are centered around m/z=31, 45, 59, 73, 87 Th, etc. A discrete sequence also arises from protonated carboxylic acids, aldehydic carboxylic acids, or alcohols, at m/z=33, 47, 61, 75, 89 Th, etc. Some of the significant differences in peak intensities occured at m/z=47.013, 73.023, 75.046, and 87.042 Th corresponding to CH_2O_2 (formic acid), $C_3H_4O_2$, $C_2H_4O_3$, and $C_4H_6O_2$, respectively. McNeill *et al.*[166] also observed formic acid from the heterogeneous oxidation of palmitic acid by OH. However, in their study, formic acid was produced in the greatest quantities compared to other species, but this was likely due to a lower sensitivity of their reagent ion, I^-, with aldehydes and ketones.[166]

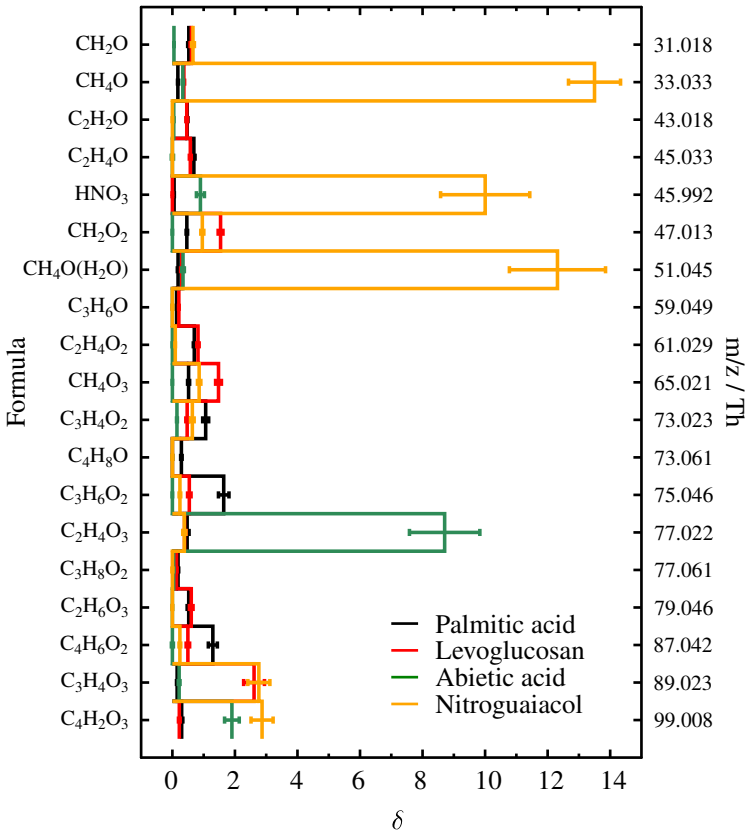

Figure 4.7: Relative difference to background for the major peaks detected upon exposure to OH for palmitic acid (black) levoglucosan (red), abietic acid (green), and nitroguaiacol (orange). The vertical error bars represent 1σ from the mean in the integrated intensities for each protonated mass. Suggested formulas for the detected peaks and corresponding protonated m/z are shown on the y-axes.

Table 4.3: Volatilised product distribution as measured by HR-PTR-ToF-MS for palmitic acid, levoglucosan, abietic acid, and nitroguaiacol + OH reaction. Values are background corrected relative abundances normalized to $H_3O^+ \times 10^{-3}$. Values in parentheses represent the change in relative abundances of each compound relative to background and normalized to H_3O^+, as defined in the text.

m/z / Th	Formula ($C_xH_yO_z$)	Name	Parent Compound			
			$C_{16}H_{32}O_2$	$C_6H_{10}O_5$	$C_{20}H_{30}O_2$	$C_7H_7NO_4$
31.018	CH_2O	Formaldehyde	0.090 (0.53)	0.072 (0.61)	0.019 (0.05)	0.113 (0.66)
33.033	CH_4O	Methanol	0.031 (0.18)	0.053 (0.37)	0.144 (0.33)	2.38 (13.5)
43.018	C_2H_2O	Acetic acid fragment Ethenone Ethynol Oxirene Acetaldehyde 1 or 2-propanol	0.181 (0.47)	0.109 (0.46)	0.056 (0.04)	-0.004 (-0.01)
45.033	C_2H_4O	Acetaldehyde Ethylene oxide	0.254 (0.69)	0.117 (0.57)	-1.99 (-0.65)	-0.042 (-0.11)
45.992	NO_2^+	Nitric acid parasitic NO_2^+	0.002 (0.05)	0 (0)	0.015 (0.90)	0.291 (10.0)
47.013	CH_2O_2	Formic acid	0.500 (0.46)	1.91 (1.54)	-0.283 (-0.08)	1.03 (0.96)
51.045	$CH_4O(H_2O)$	Methanol(H_2O)	0.007 (0.18)	0.008 (0.30)	0.026 (0.34)	0.484 (12.3)
59.049	C_3H_6O	Acetone Propanal	1.07 (0.14)	0.398 (0.21)	-0.301 (-0.04)	-0.620 (-0.08)
61.029	$C_2H_4O_2$	Acetic acid Methyl formate 1,2-dioxetane Hydroxy-acetaldehyde	0.485 (0.70)	0.384 (0.82)	-0.003 (0)	0.064 (0.09)
65.020	CH_4O_3	HO_2CH_2OH	0.144 (0.52)	0.413 (1.48)	-0.051 (-0.07)	0.238 (0.86)

			Methanetriol			
73.023	$C_3H_4O_2$	Methyl glyoxal	3.76 (1.06)	0.045 (0.47)	0.026 (0.15)	2.25 (0.64)
		Propanedial				
		3-Oxetanone				
		2-propenoic acid				
73.060	C_4H_8O	Butanal	0.064 (0.29)	-0.003 (-0.02)	-0.045 (-0.13)	-0.026 (-0.12)
		2-methyl-propanal				
		Ethoxy-ethene				
		2-butanone				
		Methoxy-propene				
		Butenol (isomers)				
75.046	$C_3H_6O_2$	Propanoic acid	0.129 (1.64)	0.028 (0.54)	-0.013 (-0.05)	0.019 (0.24)
		Ethyl formate				
		2-hydroxy-propanal				
		Methoxy-acetaldehyde				
		Methyl acetate				
		1-hydroxy-2-propanone				
77.022	$C_2H_4O_3$	Glycolic acid	0.024 (0.47)	0.012 (0.39)	0.126 (8.71)	0.019 (0.38)
		Peracetic acid				
		Hydroxy-acetic acid				
		Trioxolane (isomers)				
77.060	$C_3H_8O_2$	2-methoxy-ethanol	0.031 (0.18)	0.005 (0.13)	0.004 (0.04)	-0.021 (-0.12)
		Dimethoxymethane				
		Propanediol				
		1-methylethyl-hydroperoxide				
		Ethoxy-methanol				
		Propylene glycol				
	$C_3H_6O(H_2O)$	Acetone(H_2O)				
		Propanol(H_2O)				
79.046	$C_2H_6O_3$	$HOCH_2CH_2OOH$	0.061 (0.52)	0.039 (0.60)	-0.013 (-0.03)	-0.006 (-0.05)
		Orthoacetic acid				
87.042	$C_4H_6O_2$	2,3-butanedione	0.080 (1.29)	0.025 (0.50)	-0.063 (-0.28)	0.015 (0.24)

		Butyrolactone Acetic acid ethenyl ester 2-propenoic acid, methyl ester 2-methyl-2-propenoic acid Butenoic acid (isomers) Crotonic acid Formic acid, 2-propenyl ester 1-Propen-2-ol, formate				
89.023	$C_3H_4O_3$	Pyruvic acid Glucic acid Acetic acid, oxo-,methyl ester	0.007 (0.15)	0.096 (2.61)	0.008 (0.22)	0.119 (2.77)
99.008	$C_4H_2O_3$	Maleic anhydride	0.018 (-0.30)	0.014 (0.22)	0.068 (1.90)	0.171 (2.87)

4.4.1 Volatilisation products of levoglucosan

The heterogeneous oxidation of levoglucosan by OH resulted in the production of several volatilised species as shown in Fig. 4.5. A similar protonated m/z sequence arises as in palmitic acid suggesting that breakage of the 7-membered ring of levoglucosan by decomposition and further oxidation results in the production of aldehydes and carboxylic acids. Volatilisation of pure levoglucosan aerosol particles has been observed before.[95] In that study, OH oxidation of levoglucosan resulted in ∼23% yield of volatilised products based on particle mass loss; however, these products (with the exception of CO_2) were not identified. In this study, we attempt to bridge that gap by identifying volatilised products to better infer the volatilisation mechanism. The most significant peaks (almost a doubling in intensity) observed relative to the background due to OH oxidation of levoglucosan were m/z=47.013, 65.020, and 89.023 Th corresponding to CH_2O_2, CH_4O_3, and $C_3H_4O_3$, respectively. The increase in m/z=89.023 Th is most significant and unique to levoglucosan compared to the other species (with the exception of 5-nitroguaiacol) as shown in Table 4.3.

4.4.2 Volatilisation products of abietic acid

Abietic acid significantly degraded in the presence of UV radiation resulting in a number of volatile species having the same mass as in the presence of both OH and UV as shown in the black and red spectra in Fig. 4.6, respectively. We define the product yield with respect to the background as,

$$\delta = \frac{I_{\text{substrate+OH}} - I_{\text{substrate+UV}}}{I_{\text{substrate+UV}}} \,, \tag{76}$$

accounting for the strong UV effects on the volatilised product spectrum, where $I_{\text{substrate+UV}}$ is the signal intensity in the presence of UV radiation and substrate in the absence of OH. Due to the similarities in the change in VOC intensities and product distribution in the presence of OH and UV, δ in the case for abietic acid is negative for some of the major peaks, which suggests that upon exposure to OH some of the UV-induced products may have been consumed. Although abietic acid is a terpenoid, there were no noticeable differences in signal intensities to the background in the presence of O_3/O_2 alone. However, it is likely that O_3 may have an impact on the surface-bound species during the background conditioning cycle even so OH tends

to react with unsaturated hydrocarbons at a relatively higher rate.[61] Resin acids are also known to decompose photolytically in surface waters forming lighter hydrocarbons.[226] The formation pathways and identification of the smaller volatile compounds, however, is not known. In the presence of OH, the most dominant species formed that was not influenced by UV radiation was $C_2H_4O_3$ (m/z=77.022 Th), accounting for an increase of a factor of 8. In comparison, the increase in this signal with respect to palmitic acid, levoglucosan, and 5-nitroguaiacol was 0.47, 0.39, and 0.38, respectively as shown in the inset panels of Figs. 4.4–4.6 and concomitantly in Fig. 4.7. Because of the influence of UV light on the volatilised product spectrum of abietic acid in the presence of OH, we caution extrapolation to atmospheric conditions.

4.4.3 Volatilisation products of nitroguaiacol

Heterogeneous oxidation of 5-nitroguaiacol by OH radicals produced significant amounts of methanol (m/z=33.033 Th), its cluster with water (m/z=51.045 Th), and NO_2^+ (m/z=45.992 Th) by factors of 13.5, 12.3, and 10, respectively, as shown in Fig. 4.6. Many other volatilised products were formed, in particular $C_3H_4O_3$ (m/z=89.023 Th) by a factor of 3, suggesting that addition of OH to the aromatic ring may result in ring cleavage. The formation of methanol and NO_2^+ is likely related to favourable attack of their positions on the aromatic ring by OH. The signal at m/z=45.992 Th is unique to 5-nitroguaiacol, however PTR-ToF-MS in general is not sensitive to NO_2 unless it is charged or the charged species is formed by an independent process. This signal is attributed to proton transfer with nitric acid (HNO_3) by:[227]

$$HNO_3 + H^+ \rightarrow NO_2^+ + H_2O \qquad \text{R8}$$

indicative of HNO_3 formation prior to protonation by the reaction between volatilised NO_2 and OH.

4.5 Volatilisation reaction mechanisms

In this section, we suggest likely OH oxidation pathways that lead to degradation of the parent compounds and subsequent production of species with higher volatilities. We do this for levoglucosan, abietic acid, and 5-nitroguaiacol and the likely pathways leading to formation of volatilised products that had the greatest increase with respect to the background. We use, to the best

of our knowledge, the SAR framework[219] in determining the position of the initial OH attack, which is the limiting step in the formation of the products observed here. We interpret further mechanistic changes based on the general gas-phase mechanisms of OH with hydrocarbons[12] in the absence of NO_2. The general mechanism is as follows: first, OH attacks the weakest bound hydrogen of R-H resulting in the formation of an alkyl radical (R·). In the presence of O_2, this alkyl radical will convert to an alkyl peroxy radical (ROO·). In general, there are three pathways that an alkyl peroxy radical can take: (1) in the presence of HO_2 will form an organic hydroperoxide (ROOH) (2) self-reaction leading to the formation of an alcohol (ROH) and carbonyl (R'R"C=O), and (3) self-reaction leading to the formation of two alkoxy radicals (2RO·). Pathway 2 in the solution phase appears to be most important for primary and secondary radicals.[228] For tertiary radicals, pathway 3 is most important.[228,229] In certain conditions, depending on the size and orientation of hydrogens, the alkoxy radical may isomerize resulting in alcohol formation (2ROH). In the presence of O_2, the alkoxy radical can form a carbonyl and HO_2. The alkoxy radical may also decompose forming products of greater volatility, such as an aldehyde (R'CHO) and another smaller alkyl radical. It is important to note that depending on the residence time of OH on the surface of these substrates, higher degrees of oxygenation may occur. Because of the high OH concentrations used in the volatilisation experiments, it is possible that more OH molecules reside on the surface that are available for reaction compared to atmospheric conditions, which may result in a greater yield of volatilised products than would normally be observed in the atmosphere.

4.5.1 Levoglucosan volatilisation mechanism

The mechanism leading to the formation of glucic acid (hydroxypropanedial, $C_3H_4O_3$) from heterogeneous oxidation of levoglucosan by OH is shown in Fig. 4.8. The limiting step in this reaction is the initial OH attack. The only conceivable pathway in the production of glucic acid is attack of the tertiary hydrogen of the carbon on the ether (i.e. H-C-O-R). This pathway is in contrast to the one proposed by Kessler *et al.*,[95] which suggests OH will attack either the hydrogen bound to the carbon on the -COH group or the hydrogen bound to the hydroxyl group on the -COH group, the latter leading to decomposition. This also differs from the interpretation by Knopf *et al.*[13] in the case of NO_3 radical oxidation of levoglucosan. This may be

the case for alcohols, but levoglucosan also contains two ethers, which are found to have lower threshold energies of H atom abstraction by OH than tertiary hydrogens on an H-C-OH group as in isopropyl tert butyl ether compared to isopropyl alcohol.[230] This may be the case here, in which the decomposition pathway will produce a carbonyl on the ether and scission of the nearby -COH group. In the presence of O_2 the resulting ·COH rapidly forms a second carbonyl. Assuming enough OH is present to form secondary generation decomposition products, which is likely the case here, OH attack of the second tertiary hydrogen attached to the carbon on the remaining ether may result in a similar decomposition pathway. This may lead to cleavage of the nearby -COH group and subsequent formation of another carbonyl. The resulting volatilised product corresponding to m/z=89.023 Th is glucic acid. An examination of the vapour pressure of glucic acid, estimated to be ∼0.4 hPa at 298 K suggests that enough glucic acid may exist in the gas-phase for detection. To our knowledge, no other estimates of its vapour pressure have been made. For comparison, hydroxyacetaldehyde ($C_2H_4O_2$), having a similar configuration as glucic acid, has a vapour pressure ≤5 hPa at 298 K,[231] consistent with its relatively smaller size. Note that the fraction of glucic acid remaining in the condensed-phase is not known and clearly surface analysis techniques must be employed to differentiate its contribution to both phases.

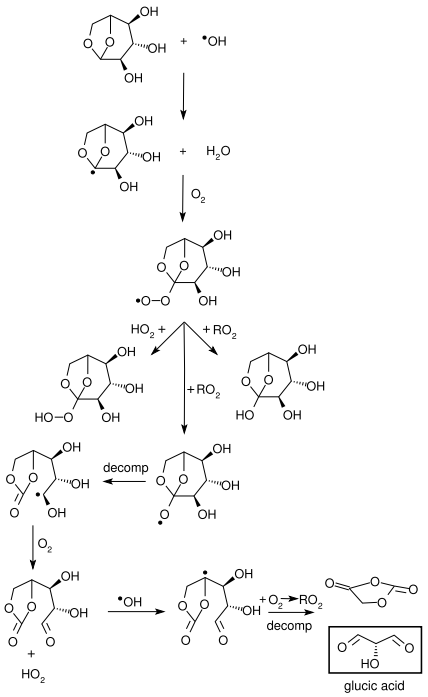

Figure 4.8: Suggested OH-initiated reaction mechanism for levoglucosan leading to the formation of glucic acid ($C_3H_4O_3$). See text for more detail.

4.5.2 Abietic acid volatilisation mechanism

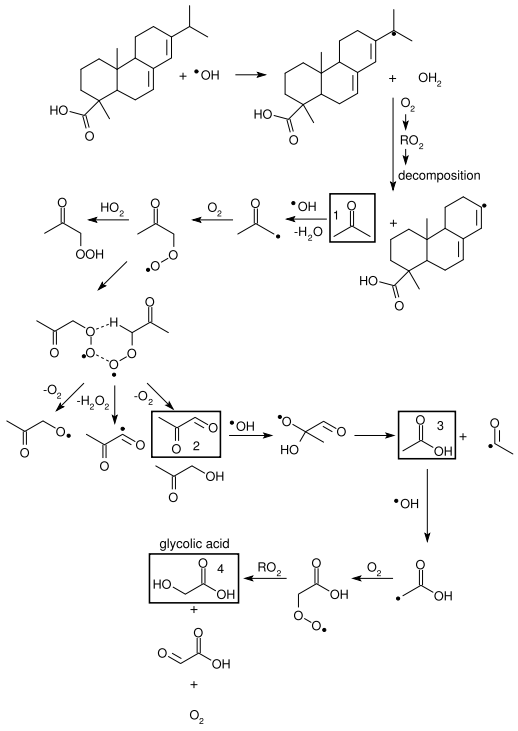

Figure 4.9: Suggested OH-initiated reaction mechanism for abietic acid leading to the formation of glycolic acid ($C_2H_4O_3$). The mechanisms leading to the formation of acetic acid (3) from pyruvic acid (2) and pyruvic acid (2) from acetone (1) are adapted from Schaefer *et al.*[232] The mechanism leading to the formation of glycolic acid (4) from acetic acid (3) is adapted from Tan *et al.*[233]

The mechanism leading to the formation of glycolic acid (m/z=77.022 Th, $C_2H_4O_3$) from heterogeneous OH oxidation of abietic acid is shown in Fig. 4.9. The impact of species formed by UV exposure on the formation of glycolic acid is not known. Because the signal at m/z=77.022 Th increased only when OH was present, we attribute its production to OH oxidation of

abietic acid and not as a result of UV radiation. There are many reactive sites on abietic acid, in particular the unsaturated bonds, which are susceptible to OH addition[234] as well as other weakly bound hydrogens, particularly on the isopropyl functional group. The low production of volatile species in the presence of OH after subtracting the influences due to UV radiation suggests that several generations of oxidation are needed in order to form volatilised products upon OH attack of the double bond. The limiting step in the production of glycolic acid, however, may be attributed to OH attack of the isopropyl functional group due to its weakly bound tertiary hydrogen. OH attack at this position results in hydrogen abstraction forming an isopropyl radical and H_2O. In the presence of O_2, an isopropyl peroxy radical is formed. Assuming the self-reaction leads to formation of an isopropyl-oxy radical and decomposition, the likely formed species is acetone. The fate of acetone at this stage is not certain; if it evaporates from the substrate surface we should have observed an increase in the signal for acetone (m/z=59.049 Th), but that was not the case. On the other hand if acetone resides on the surface or in the aqueous phase it may oxidise further in the presence of OH, which is more consistent to what is observed here. The heterogeneous oxidation of aqueous phase acetone by OH has been shown to result in the formation of pyruvic acid followed by acetic acid through a similar decomposition process.[232] Work by Tan *et al.*[233] has shown that heterogeneous oxidation of acetic acid in the aqueous phase by OH can result in the formation of glycolic acid. Presumably a similar mechanism will occur in the gas phase since acetic acid has a vapour pressure comparable to that of glycolic acid ∼14 hPa at 293 K. However, we do not observe a significant increase in acetic acid as part of the volatilised spectrum, suggesting that if acetic acid were to evaporate from the surface, it is rapidly converted to products such as glycolic acid in the presence of OH and O_2. This interpretation is also contingent on the presence of an aqueous phase, but the physical nature of the organic substrate surface is not well characterized here. Abietic acid is mostly water-insoluble and has similar physical characterisitics as glassy substances.[235] However, diffusion of water through glasses may be important since the estimated diffusion length is ∼300 nm for applied experimental timescales (∼15 min) and temperature (∼303 K) and assuming a diffusion coefficient, D_{H_2O} =10^{-16} m^2 s^{-1} at 300 K.[105] It is also possible that monolayers of water build up along the surface, acting as a separate interface for aqueous-phase chemistry. More than two monolayers of water were shown to form on halocarbon wax after 15 min exposure to 60% RH,[236] which may be the case here as well. Clearly, analysis of the

surface-bound species is needed to verify this interpretation.

4.5.3 Nitroguaiacol volatilisation mechanism

5-nitroguaiacol has a unique arrangement of its various functional groups. As described in previous sections, both the -OCH_3 and -OH groups are *ortho* and *para* directing electron-donating substituents on aromatics favoring electrophilic substitution of the OH radical at those positions. In addition, the -NO_2 is electron-withdrawing and strongly deactivating and *meta* directing. The -NO_2 group is *para* to -OCH_3 and -OH is both *meta* to -NO_2 and *ortho* to -OCH_3. The most abundant products formed suggests that OH preferentially attacks both -OCH_3 and -NO_2 resulting in the production of methanol (CH_3OH) and NO_2, respectively as shown in Fig. 4.10. The release of -NO_2 by electrophilic substitution by OH has been observed in the case of 4-nitrophenol[237] and nitrobenzene.[238] The production of methanol by OH substitution of the -OCH_3 group has been observed in the case of methoxylated phenols.[239] Other volatilised products were observed as well suggesting that decomposition of the aromatic ring may be a major pathway.

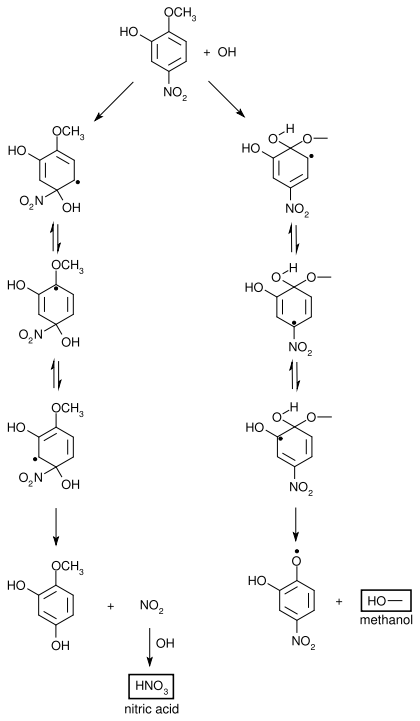

Figure 4.10: Suggested OH-initiated reaction mechanism for 5-nitroguaiacol leading to the formation of nitric acid (HNO_3) and methanol (CH_4O). See text for more detail.

4.6 Atmospheric implications

In assessing the impact of γ with changing [OH] we can consider the atmospheric lifetime of the first monolayer, τ_{ML}, of the particle surface as:[13,31]

$$\tau_{\mathrm{ML}} = \frac{4N_{\mathrm{tot}}}{\gamma\omega_{\mathrm{OH}}[\mathrm{OH}]_{\mathrm{atm}}} \ , \tag{77}$$

where N_{tot} represents the surface concentration, ω_{OH} is the mean thermal velocity of OH, and $[\mathrm{OH}]_{\mathrm{atm}}$ is the concentration of OH in the atmosphere. We

assume N_{tot} =1.8×10^{14} molecule cm^{-2} based on the average number of surface reactive sites.[14] For the uptakes at lower OH concentrations (∼10^{7}–10^{9} molecule cm^{-3}), we assume γ=0.48 based on the largest modeled γ in Fig. 4.1, representing a lower limit of τ_{ML}, and for the uptakes at the highest OH concentrations an average γ=0.01, representing an upper limit of τ_{ML}. For the larger uptakes, the lifetime of one monolayer coverage yields τ_{ML} ∼3.5 hr for background [OH]$_{\mathrm{atm}}$ =2×10^{6} molecule cm^{-3} and τ_{ML} ∼24 min for [OH]$_{\mathrm{atm}}$ =1.7×10^{7} molecule cm^{-3} representative of biomass burning plume conditions. Not surprisingly, for the smaller uptakes at higher OH concentrations (above ∼10^{10} molecule cm^{-3}) the lifetimes are significantly longer, ∼1 week for background conditions and ∼19.5 hrs for biomass burning plume conditions.

The lifetime of an aerosol particle, τ_{part}, assuming spherical geometry, with a radius, R=100 nm, containing 60:2:1 wt% levoglucosan, abietic acid, and nitroguaiacol, respectively[13] and an average molecular weight, M=105 g mol^{-1} and density, ρ ∼1.05 g cm^{-3} can be estimated following the approach by George *et al.*[36] and references therein:

$$\tau_{\mathrm{part}} = \frac{4}{3} R \frac{\rho N_{\mathrm{a}}}{\gamma \omega_{\mathrm{OH}} [\mathrm{OH}]_{\mathrm{atm}} \mathrm{M}} \ , \tag{78}$$

where N_{a} is Avagadro's number. For background conditions, assuming γ=0.48 modeled at lower OH concentrations,lower limit particle lifetimes τ_{part}∼2 weeks are derived. Applying γ=0.01 yields upper limit particle lifetimes τ_{part}∼2 years. Under conditions of fresh biomass burning plumes, in which [OH]∼1.7×10^{7} molecule cm^{-3}, lower limit τ_{part}∼2 days are derived assuming γ=0.48 and upper limit τ_{part}∼90 days are derived assuming γ=0.01, suggesting that BBA particle lifetimes with respect to OH oxidation can be on the order of atmospherically relevant timescales, but can vary significantly depending on which γ value is applied. While these idealised results, not accounting for diffusion and bulk effects,[14] suggest that heterogeneous oxidation by OH is important on atmospheric timescales, the differences in lifetimes with regard to applied γ emphasises the importance of accurately determining γ at ambient OH concentrations. At higher OH concentrations, lifetimes can be significantly overestimated. However, our results also indicate that γ reaches a maximum at [OH]≤∼10^{9} molecule cm^{-3}, a typical range used in previous literature studies.[31,32,36,95,110] These simplified lifetime estimates can be improved by incorporation of our data in kinetic flux models[14,211] and particle resolved[211] models, allowing to derive more real-

istic γ and τ for implementation in large scale models, which is, however, beyond the scope of this paper. Clearly, our results indicate that biomarkers levoglucosan, abietic acid, and nitroguaiacol are not photochemically inert and thus care should be taken when applying these species in aerosol source apportionment models.

The mobility of OH on surfaces may potentially play an important role in heterogeneous OH oxidation of aerosol particles. Our observations imply that OH resides at the surface prior to reaction suggesting that longer OH residence times on the surface renders surface-bound species more susceptible to OH attack, thus potentially leading to a greater degree of oxygenation and OH specificity.[95,110,138] Longer OH residence time on particle surfaces will likely result in the loss of hydroxyl groups in favour of the formation of less hygroscopic carbonyl functionalities,[240] thus impacting the efficiency of the particle to act as CCN. This is consistent with our mass spectra, showing a suite of volatilised aldehydes, ketones, and carboxylic acids that presumably form on the particle from relatively lower volatility first-generation OH oxidation products containing carbonyl functionalities. Aged biomass burning aerosol particles have been shown to be deficient in hydroxyl groups with an increase in carbonyl functionalities.[241] We also observed production of acetaldehyde (CH_3OH) and formic acid (HCOOH), consistent with observations by Hennigan *et al.*[83] in OH impacted biomass burning smoke. Although not quantified, accounting for volatilisation of these species from BBA may result in better agreement between measured and predicted ambient VOC concentrations.[37]

Atmospherically relevant OH surface coverages can be estimated from K_{OH}. Background atmospheric [OH] are typically $\leq 2\times10^6$ molecule cm^{-3} [61] and results in $\sim$0.1% surface coverage as shown in Fig. 4.3. In a biomass burning plume where [OH] can be greater than 10^7 molecule cm^{-3},[63,215] OH coverage can approach 1%. For longer atmospheric exposure times, which may be represented by our highest employed [OH], equilibrium OH surface coverage may increase significantly leading to a reduction of γ by an order of magnitude.

HNO_3 production by OH oxidation of substituted-guaiacols such as nitroguaiacol in BBA may explain the enhanced acidity and production of nitrates observed in aged biomass burning plumes.[76] Recent work by Knopf *et al.*[13] observed strong uptake of NO_3 radicals in an atmospherically relevant mixture of levoglucosan, abietic acid, and 5-nitroguaiacol with γ as high as that of NO_3 uptake to 5-nitroguaiacol alone, suggesting that nitroguaiacol

preferentially resides at the surface. While substituted-guaiacols account for nearly 1% by weight of typical mixed BBA particles,[92] the heterogeneous production of NO_2 and gas-phase HNO_3 by this pathway may be important. To a first-approximation, assuming [OH] under young biomass burning plume conditions, we estimate that HNO_3 production may contribute up to ∼33% of the HNO_3 concentration measured in young biomass burning plumes,[242] which becomes more significant depending on the composition or size of the particle and age of the plume. Revolatilised NO_2 may lead to the formation of organic nitrates via the alkoxy radical + NO_x pathway.[32] NO production from photolysed NO_2 will likely accelerate the removal of peroxy radicals in favour of alkoxy radical formation, which may lead to more decomposition and production of species with higher volatility.

4.7 Conclusions

The reactive uptake coefficients for major compounds of biomass burning aerosol levoglucosan, abietic acid, and nitroguaiacol with OH have been determined over a range of OH concentrations. For all of the species studied here, the uptakes of OH range from ∼0.01–1 at higher and lower [OH], accounting for the uncertainties in the diffusion coefficients. The weaker uptake of OH at relatively higher [OH] is indicative of a surface adsorption process by which OH first adsorbs to the surface followed by reaction with surface reactive sites, also termed Langmuir-Hinshelwood kinetics. A L-H model[155] shows good agreement with the trend in observed γ as a function of [OH] suggesting that OH follows a L-H uptake mechanism and allowing for the first time derivation of the OH adsorption/desorption equilibrium constant, K_{OH} and the OH surface reaction rate constant, k_s. The best fit parameters on average are K_{OH}=3.81×10^{-10} cm^3 molecule^{-1} and k_s=9.71×10^{-17} cm^2 molecule^{-1} sec^{-1} for all of the investigated organic compounds. It is not clear the extent to which O_2 used as the precursor to OH in this study affects the reactive uptake of OH since the modified L-H model could not describe corresponding [O_2] dependencies. Based on the range of γ determined in this study, BBA particle lifetime estimates can vary ∼1–2 orders of magnitude indicating the importance to investigate heterogeneous oxidation kinetics at atmospherically relevant conditions.

In this study we showed that organic substrates representative of biomass burning organic aerosol react efficiently with OH radicals. Our observations imply that heterogeneous OH oxidation produces sufficiently volatile prod-

ucts to partition to the gas phase. These results are consistent with previous findings.[32,95,110] In particular, we provide insight into the possible volatilised products and reaction pathways resulting from heterogeneous OH oxidation of levoglucosan, a substantial component of BBA and typically employed as a biomolecular marker. While we could not provide VOC concentration yields, we do observe increases in some of the volatile species by factors of 2–15 relative to the background, with the most significant increases attributed to glucic acid from levoglucosan, glycolic acid from abietic acid, and methanol and nitric acid from 5-nitroguaiacol, indicative of potential ring cleavage and formation of species with higher volatility. The production of nitric acid from nitroguaiacol in the presence of OH suggests that OH substitution at the -nitro position releases NO_2, which promptly reacts with OH in the gas-phase to form nitric acid. While it is possible that the slower uptakes observed at higher OH concentrations are unique to the compounds studied here, it also indicates that estimations of VOC yields that assume unity uptake under enhanced OH concentrations[32,110] may be underestimated since it is possible that a smaller fraction of the reactive collisions between OH and the organic species are responsible for the observed volatilised products. Volatilisation not only impacts atmospheric lifetime of organic aerosol, but indicates that heterogeneous OH oxidation may affect particle composition and hygroscopicity of organic aerosol and thus its CCN[16] and potentially IN[88] efficiency. Our study strongly suggests that these major biomarkers for biomass burning aerosol are not photochemically inert and this should be considered when apportioning aerosol sources.

4.8 Supplemental material

4.8.1 Box model description

OH concentrations applied in the atmospheric pressure flow reactor were quantified using a photochemical box model based on 24 O_x and HO_x cycling/self reactions[176] and the photolysis of O_3 and H_2O_2 as shown in table 4.4. This model includes heterogeneous loss to halocarbon wax for several of the reactive species including OH, O, and HO_2. The output of this model is shown in Fig. 4.11. We measured the uptake of OH by halocarbon wax at similar [OH] ($\sim 10^{10}$ molecule cm^{-3}) as applied in the atmospheric pressure flow reactor ([OH]$\sim 2\times 10^{10}$ molecule cm^{-3}) and observed an average $\gamma = 8\times 10^{-4}$. The reactive uptake of O and HO_2 by halocarbon wax as far as we know has not been reported in the literature. We assume that γ for O and HO_2 are similar to γ for OH uptake by halocarbon wax. γ for O_3 uptake by halocarbon wax was at or below our detection limit of $\gamma \leq 10^{-6}$, so we apply γ for O_3 uptake by halocarbon wax as 10^{-6}. The photolysis rate of O_3 using the UV lamp was estimated based on loss measurements of $[O_3]$ under O_3/O_2 flow using an ozone monitor. Based on these loss measurements over a range of $[O_3]$ we determined an average photolysis rate of ~ 0.042 s^{-1}.

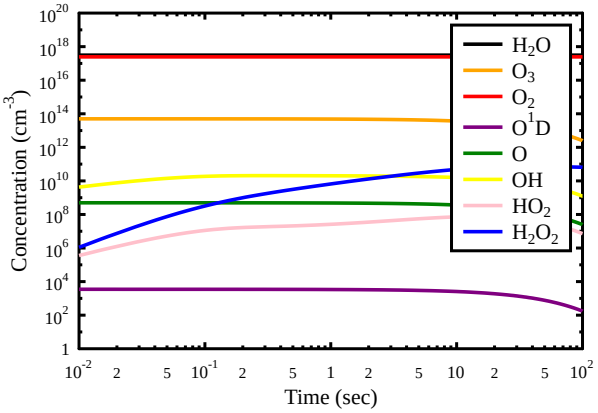

Figure 4.11: Atmospheric pressure flow reactor box model of gas-phase concentrations due to the production of OH from O_3 photolysis in the presence of O_2 and H_2O.

The box model shows the evolution of the different oxidants potentially forming during the production of OH. The largest concentrations are that of H_2O (black), held near 60% RH, and O_2 (red), and do not change significantly over time. For all of the other species in Fig. 4.11, steady-state is reached on the order of milliseconds except for H_2O_2 and HO_2 that continue to build-up over time. OH (yellow) reaches steady-state at about 0.1 seconds, but begins to decrease due to gas-phase reactions with other species as well as heterogeneous loss to the halocarbon wax-coated walls of the flow reactor. O_3 concentrations were maintained near 12 ppm during volatilization measurements resulting in ∼0.8 ppb OH according to the box model. In a set of separate experiments, a known trace quantity of isoprene was added to the flow and based on the reaction rate of isoprene with OH (1×10^{-10} cm^3 molec^{-1} sec^{-1})[176] [OH] was determined over a range of initial [O_3] (∼500 ppb - 15 ppm) as shown in Fig. 4.12. Within experimental uncertainties based on the error in the reaction rate constant of isoprene and OH, our photochemical box model is in good agreement with the measured values over a range of initial [O_3].

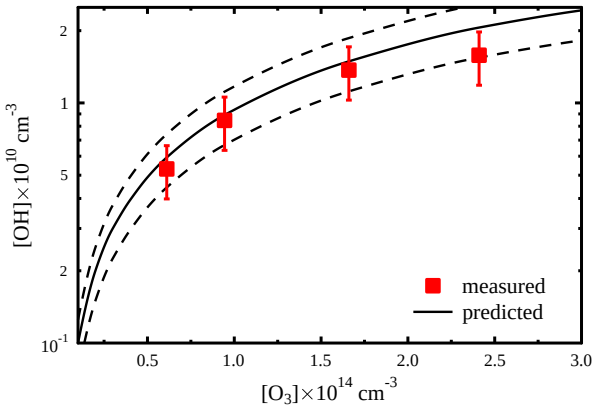

Figure 4.12: OH predicted by the photochemical box model (line) compared to measured [OH] derived from isoprene + OH loss experiments (squares). Error bars and dashed lines represent ±25% uncertainty in the rate constant of OH and isoprene[15].

Table 4.4: Photochemical box model reactions for evaluating gas-phase OH radical concentrations at atmospheric pressure in a flow reactor

R1	+	R2	→	P1	+	P2	k
O_3	+	$h\nu$		O^1D	+	O_2	j = 0.042 or 0.008 s^{-1}
O^1D	+	M		O	+	M	2E-11 cm^3 $molec^{-1}$ sec^{-1}
O^1D	+	H_2O		OH	+	OH	2.2E-10 cm^3 $molec^{-1}$ sec^{-1}
O^1D	+	H_2		OH	+	H	1.1E-10 cm^3 $molec^{-1}$ sec^{-1}
O	+	OH		O_2	+	H	2.4E-11$e^{(\frac{110}{T})}$ cm^3 $molec^{-1}$ sec^{-1}
H	+	O_2		HO_2			5.4E-32 cm^6 $molec^{-2}$ sec^{-1}
H	+	HO_2		2OH			8E-11 cm^3 $molec^{-1}$ sec^{-1}
H	+	HO_2		H_2	+	O_2	5.6E-12 cm^3 $molec^{-1}$ sec^{-1}
H	+	HO_2		H_2O	+	O	2.4E-12 cm^3 $molec^{-1}$ sec^{-1}
O	+	HO_2		OH	+	O_2	2.7E-11$e^{(\frac{224}{T})}$ cm^3 $molec^{-1}$ sec^{-1}
OH	+	OH		H_2O	+	O	6.2E-14$(\frac{T}{298})^{2.6}e^{(\frac{945}{T})}$ cm^3 $molec^{-1}$ sec^{-1}
OH	+	OH		H_2O_2			6.9E-31$(\frac{T}{300})^{-0.8}$ cm^6 $molec^{-2}$ sec^{-1}
O^1D	+	O_3		O_2	+	O	2.4E-10 cm^3 $molec^{-1}$ sec^{-1}
H	+	O_3		OH	+	O_2	2.9E-11 cm^3 $molec^{-1}$ sec^{-1}
OH	+	O_3		HO_2	+	O_2	1.7E-12$e^{(\frac{-940}{T})}$ cm^3 $molec^{-1}$ sec^{-1}
OH	+	HO_2		H_2O	+	O_2	4.8E-11$e^{(\frac{250}{T})}$ cm^3 $molec^{-1}$ sec^{-1}
HO_2	+	O_3		OH	+	$2O_2$	2.03E-16$(\frac{T}{300})^{4.57}e^{(\frac{693}{T})}$ cm^3 $molec^{-1}$ sec^{-1}
HO_2	+	HO_2		H_2O_2	+	O_2	2.2E-13$e^{(\frac{600}{T})}$ cm^3 $molec^{-1}$ sec^{-1}
OH	+	H_2O_2		H_2O	+	HO_2	2.9E-12$e^{(\frac{-160}{T})}$ cm^3 $molec^{-1}$ sec^{-1}
O	+	H_2O_2		OH	+	HO_2	1.4E-12$e^{(\frac{-2000}{T})}$ cm^3 $molec^{-1}$ sec^{-1}
O	+	O_3		$2O_2$			8E-12$e^{(\frac{-2060}{T})}$ cm^3 $molec^{-1}$ sec^{-1}
O^1D	+	O_2		O	+	O_2	3.2E-11$e^{(\frac{67}{T})}$ cm^3 $molec^{-1}$ sec^{-1}
OH	+	wall		loss			γ = 8E-4
O	+	wall		loss			$\gamma \approx$ 8E-4
HO_2	+	wall		loss			$\gamma \approx$ 8E-4
O_3	+	wall		loss			$\gamma \approx$ 1E-6
OH	+	H_2		H_2O	+	H	7.7E-12$e^{(\frac{-2100}{T})}$ cm^3 $molec^{-1}$ sec^{-1}
O	+	O_2		O_3			5.6E-34$(\frac{T}{300})^{-2.6}$ cm^6 $molec^{-2}$ sec^{-1}
H_2O_2	+	$h\nu$		2OH			j ≈1E-5 s^{-1}

4.8.2 HR-PTR-ToF-MS sampling protocol and signal analysis

The HR-PTR-ToF-MS experiments were run for 600 sec resulting in 600 scans per experiment. In the case of OH impacted experiments, the background signal (in the presence of both H_2O vapor and O_3) was recorded for ∼250 scans at which point the UV lamp was switched on to allow for OH production. We continued to record the signal in the presence of OH for an additional 950 scans, where the last experimental run period of 600 scans (600 sec) was taken as the average signal in the presence of OH. Prior to switching on the UV lamps, the impacts of background (N_2/O_2 alone, $N_2/O_2/H_2O$, N_2/H_2O, O_3/O_2, and $N_2/O_2/H_2O$/UV) both in the presence and absence of the organic substrate were assessed using the same sampling protocol. Because the HR-PTR-ToF-MS has a high sampling rate and mass resolution, the peaks were first quantified by integrating over a pre-defined mass-corrected protonated m/z range, based on well defined signal at $H_3^{18}O^+$ (m/z=21.0221 Th), NO^+ (m/z=29.9979 Th), and acetone(H^+) (m/z=59.049 Th), using the PTR-MS ToF viewer 1.4 software. Mass calibration was done prior to sampling as well, so there was little mass shift correction post sampling. The pre-defined mass ranges used for integration of the major peakes discussed here were held constant between background experiments in the presence of the organic substrate and OH as to not artificially increase or decrease the integrated intensities between the two experiments.

Here ends the publication:

Heterogeneous OH oxidation of biomass burning organic aerosol surrogate compounds: assessment of volatilisation products and the role of OH concentration on the reactive uptake kinetics

Jonathan H. Slade[1] and Daniel A. Knopf[1*]

[1]Institute for Terrestrial and Planetary Atmospheres/School of Marine and Atmospheric Sciences, Stony Brook University, Stony Brook, NY 11794-5000, USA

*To whom correspondence should be addressed. Email:Daniel.Knopf@stonybrook.edu

Published in *Physical Chemistry Chemical Physics*, Vol. 15, 5898–5916, 2013,

4.9 Modeling the multiphase OH oxidation kinetics of BBA surrogate compounds

This section describes key results that aimed to develop a more thorough understanding of the physical and chemical processes governing the reactive uptake of OH by BBA surrogate-substrates discussed in the previous sections of this chapter. The results summarized here are adapted from a recently submitted publication, currently under review at *Journal of Physical Chemistry A.*, entitled "Multiphase chemical kinetics of OH radical uptake by molecular organic markers of biomass burning aerosols: Humidity and temperature dependence, surface reaction, and bulk diffusion" by Andrea Arangio, Jonathan H. Slade, Thomas Berkemeier, Ulrich Pöschl, Daniel A. Knopf, and Manabu Shiraiwa[35].

4.9.1 OH exposures and model fits

KM-GAP was applied to model the temporal evolution and dependence of γ on [OH] using the experimental results of the reactive uptake of OH by levoglucosan and abietic acid substrates, representing biomolecular markers of BBA. Levoglucosan and abietic acid substrates were exposed under dry conditions to OH in the presence of O_2 using a coated-wall flow tube reactor

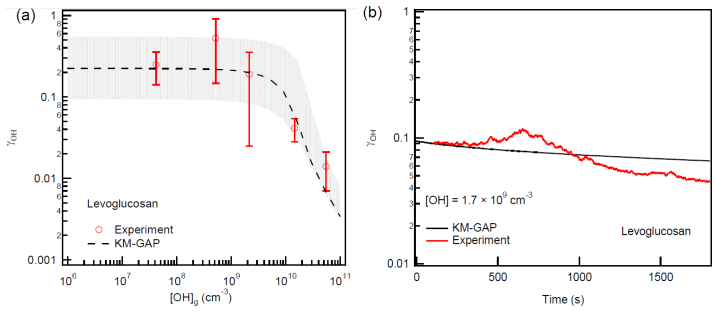

Figure 4.13: OH uptake coefficient, γ, for levoglucosan measured (red), taken from Slade and Knopf[15] and modeled (black) by KM-GAP: (a) γ as a function of gas-phase OH concentration. The shaded area represents model simulations with range of kinetic parameters listed in Table 4.5. (b) Temporal evolution of γ with gas-phase OH concentration of 1.7×10^9 molecule cm^{-3}. Figure adapted from Arangio *et al.*[35].

coupled to CIMS. The substrates were exposed to OH for ∼40 min at a pressure of 5.5 hPa and [OH]=1.7×10^{9} molecule cm^{-3}. The residence time of OH over the exposed substrates ranged from 0.08-1.25 ms.

Figures 4.13a and 4.13b show the measured (red) and KM-GAP modeled (black) dependence of γ on [OH] and the temporal evolution of γ in the presence of levoglucosan substrates, respectively. As indicated in Fig. 4.13a, below [OH]=10^{9} molecule cm^{-3}, measured γ is relatively constant at ∼0.3, then decreases significantly as [OH] increases. As indicated in Fig. 4.13b, γ decreases slightly from ∼0.1 to 0.06 over the course of the exposure. Both the dependence of γ on [OH] and the temporal evolution of γ are well-reproduced by KM-GAP. The temporal evolution and dependence of γ on [OH] for OH uptake by abietic acid substrates is similar to the results for levoglucosan, so for simplicity only the levoglucosan exposures will be discussed. Based on these fits, physicochemical parameters of the OH uptake are derived. Table 4.5 shows the different parameters and their magnitudes used in fitting the experimental data. D_{OH} ∼10^{-10} cm^2 s^{-1} in levoglucosan and abietic acid

Table 4.5: Kinetic parameters for multiphase chemical reactions of OH with levoglucosan used in the KM-GAP model. Adapted from Arangio *et al.*[35].

Parameter	Levoglucosan
$\alpha_{s,0}$	1
τ_d(s)	(1.5-7)$\times10^{-6}$
k_{SLR}(cm^2 s^{-1})	(2-5)$\times10^{-10}$
k_{BR}(cm^3 s^{-1})	1.8×10^{-12}
$K_{\mathrm{sol,cc}}$(mol cm^{-3} atm^{-1})	3×10^{-3}
D_{OH}(cm^2 s^{-1})	3×10^{-10}
D_{org}(cm^2 s^{-1})	(2-8)$\times10^{-16}$

is consistent with the bulk diffusivity of water in levoglucosan, D_{w} ≈10^{-10} cm^2 s^{-1}, which is reasonable given that OH and H_2O have similar molecular and transport properties[243]. The surface reaction rate constant, k_{SLR} ∼10^{-10} cm^2 s^{-1} is similar to the reported values for NO_3 surface reaction with levoglucosan and abietic acid in Shiraiwa *et al.*[14]. The bulk reaction rates, k_{BR}, represent intermediate values of measured k_{BR} for OH and levoglucosan in the literature, which ranges between 3.1×10^{-13}-1.1×10^{-11} cm^3 molecule^{-1} s^{-1} [83,123,244,245].

The results presented in the previous section indicate that OH radical uptake by organic BBA surrogate substrates does not follow an Eley-Rideal uptake mechanism. To a first approximation, it was demonstrated that OH uptake follows a L-H uptake mechanism whereby OH first adsorbs to the organic substrate surface, then undergoes reaction. However, the KM-GAP model results indicate OH uptake is not as straightforward as the L-H uptake approximation[15]. A steady decrease in γ for OH uptake by levoglucosan implies that the surface may be saturated with OH with increasing [OH] due to slow diffusion of adsorbed OH into the the particle bulk. At the surface, OH is removed due to reaction with levoglucosan, which for unsaturated organic molecules occurs via H-atom abstraction[32]. OH reaction with levoglucosan is thought to occur via H-atom abstraction of the α-C attached to the alcohol (i.e. -OH) functionalities or H-atom abstraction of the alcohol functionalities themselves[95]. Based on the LEV volatilization product distribution measured in Slade and Knopf[15], H-atom abstraction likely occurs also via the ether functionalities. The reaction products of LEV are slightly less reactive (γ=0.56) towards OH than pure LEV (γ=0.91)[95]. Even in the presence of highly oxidized organic particles, OH uptake can be efficient[214]. With increasing OH exposure time, the reactive uptake decreases only slightly implying that OH remains highly reactive towards LEV and/or its oxidation products.

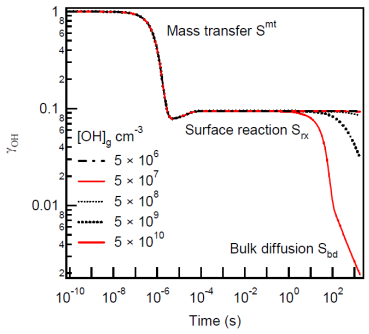

Figure 4.14: Temporal evolution of γ for OH uptake by levoglucosan at different OH concentrations. OH uptake is initially limited by mass transfer (S^{mt}) of OH until $\sim 10^{-6}$ s, then limited by surface reaction (S_{rx}) and the bulk-to-surface transport of levoglucosan (S_{bd}) depending on OH gas-phase concentration. Figure adapted from Arangio *et al.*[35].

To determine if diffusion of OH from the surface to the particle bulk of LEV or the diffusion of LEV from the bulk to surface can explain the dependency of the OH uptake coefficient on [OH], the fitting parameters determined by the KM-GAP simulations were applied to determine the kinetic regimes and limiting cases. Figure 4.14 shows the temporal evolution of γ applying five different OH concentrations (5×10^6-5×10^{10} molecule cm^{-3}) and allows to determine the limiting cases for OH uptake at the different [OH]. Initially, OH uptake is limited by mass transfer of OH until $\sim10^{-6}$ s due to rapid uptake. For all the different applied [OH], after 10^{-6} s and up to $\sim$1 s, OH uptake is limited by surface reaction. In other words, OH does not diffuse through the particle over this timescale and is instead lost by reaction to LEV at the surface or LEV is not replenished. The concentration of LEV is sufficiently high to remove OH even at the highest applied [OH]. However, depending on the applied OH concentration, above $\sim$1 s, OH uptake can be limited by bulk diffusion of the organic moving from the bulk to the surface. After 100 s of OH exposure to levoglucosan substrates, OH uptake at [OH]$>10^9$ molecule cm^{-3} is bulk diffusion limited. This is due to the rapid depletion of levoglucosan with increasing [OH], for which after $\sim$10 s of exposure, a strong concentration gradient of levoglucosan in the bulk develops. After $\sim$100 s of exposure, levoglucosan is depleted at the surface, volatilization products are lost to the gas-phase. These results indicate that OH uptake by LEV is limited by surface-bulk exchange.

4.9.2 Conclusion

The results reported in Arangio *et al.*[35] demonstrate that the dependence of OH uptake on both gas-phase [OH] and time can be reproduced applying KM-GAP. The decrease in γ with increasing [OH], as first reported in Slade and Knopf[15], is likely a result of LEV bulk-to-surface diffusion limitations. Below [OH]$\sim10^9$ molecule cm^{-3}, OH uptake is limited by its surface reaction with LEV. OH uptake by LEV substrates depends on the degree of saturation and mass transport of OH from the surface to the bulk and LEV from the bulk to the surface, which depends strongly on the applied OH concentration. These results implicate that gas uptake by glassy or semisolid aerosol depends strongly on ambient conditions, including the gas-phase oxidant concentration, which can vary widely in the atmosphere depending on location or proximity to different pollutant sources. For example, under pristine atmospheric conditions, i.e. low NO_x and O_3, OH concentrations can

be lower than 0.1 ppt[43]. However, in highly polluted conditions, such as a biomass burning plume, OH concentrations can be higher than 1 ppt[63,64]. The results indicate that the degraded fraction of LEV depends strongly on [OH], suggesting that LEV lifetimes can also vary with [OH][15,35,107]. The particle's bulk diffusivity plays an important role in LEV lifetime; the bulk diffusivity can change in response to temperature or RH, which positively feeds back to oxidant diffusivity, thus higher temperatures or greater RH promotes LEV and OH mobility in the condensed-phase and thus enhanced degradation of LEV[35,107].

5 Results: Multiphase OH oxidation kinetics of organic aerosol: The role of particle phase state and relative humidity

The sections from 5.1 to 5.6 are the reproduction of the publication "Multiphase OH oxidation kinetics of organic aerosol: The role of particle phase state and relative humidity" by Jonathan H. Slade and Daniel A. Knopf published in *Geophysical Research Letters*, Vol. 41, 5297–5306, 2014, with permission from John Wiley and Sons on behalf of the American Geophysical Union. The layout of the article as well as the section figures and table numberings have been adapted to match with the thesis structure. Section 5.6 covers the supplemental material to the main article covered in sections 5.1 to 5.5.

Multiphase OH oxidation kinetics of organic aerosol: The role of particle phase state and relative humidity

Jonathan H. Slade[1] and Daniel A. Knopf[1*]

[1]Institute for Terrestrial and Planetary Atmospheres/School of Marine and Atmospheric Sciences, Stony Brook University, Stony Brook, NY 11794-5000, USA

[*]To whom correspondence should be addressed. Email:Daniel.Knopf@stonybrook.edu

Published in *Geophysical Research Letters*, Vol. 14, 5297–5306, 2014, with permission from Wiley and Sons, Inc. on behalf of the American Geophysical Union, copyright 2014.

5.1 Abstract

Organic aerosol can exhibit different phase states in response to changes in relative humidity (RH), thereby influencing heterogeneous reaction rates with trace gas species. OH radical uptake by laboratory generated levoglucosan and methyl-nitrocatechol particles, serving as surrogates for biomass burning aerosol, is determined as a function of RH. Increasing RH lowers the viscosity of amorphous levoglucosan aerosol particles enabling enhanced OH uptake. Conversely, OH uptake by methyl-nitrocatechol aerosol particles is suppressed at higher RH as a result of competitive co-adsorption of H_2O that occupies reactive sites. This is shown to have substantial impacts on organic aerosol lifetimes with respect to OH oxidation. The results emphasize the importance of organic aerosol phase state to accurately describe the multiphase chemical kinetics and thus chemical aging process in atmospheric models to better represent the evolution of organic aerosol and its role in air quality and climate.

5.2 Introduction

Organic aerosol particles are ubiquitous in the atmosphere[51], affecting climate and air quality[246]. Aerosols impact climate directly through their light scattering properties and indirectly by influencing cloud radiative properties[6]. Characterizing aerosol impacts on current and future climates depends critically on our ability to determine and quantify aerosol sources and strengths[247–249] and understand the chemical modifications of organic aerosol particles during atmospheric transport, also termed chemical aging[8,9,12]. Ultimately, the rates at which these modifications proceed depends on particle chemical and physical properties such as composition and phase state and conditions of the reacting environment such as relative humidity (RH) and temperature (T)[33,138,250].

Biomass burning represents a major source of gases and particles to the atmosphere[73] and can significantly affect air quality, human health, cloud formation, and the radiative budget, and thus climate[122,251]. Globally it constitutes the largest source of primary organic aerosol (POA) and black carbon[252], and can yield a significant amount of secondary organic aerosol (SOA)[253]. Organic species representative of biomass burning aerosol (BBA) can exhibit different morphologies and amorphous phase states that range from solid to semi-solid and liquid particles, which change in response to the

ambient RH and T[105]. Only recently, gas uptake by amorphous material was shown to depend on the condensed phase viscosity[33]. Water is expected to influence particle reactivity because it acts as a plasticizer for water soluble and hygroscopic organic material, promoting the mobility of the reactants in the particulate phase[33,106,143]. However, water can also participate in chemical reactions such as hydrolysis[170,195,254], provide a medium for ion dissociation and promote ion-molecule reactions[34,255], and act as a barrier to gas uptake by blocking surface reactive sites[159,255,256]. Studying the influence of water vapor on particle phase state and heterogeneous reactivity of organic aerosol is thus crucial for understanding its impact on climate forcing and air quality.

Here we investigate the influence of RH on the OH radical reactive uptake efficiency by laboratory generated aerosol particles representative of BBA. Levoglucosan (LEV, 1,6-anhydro-β-glycopyranose, $C_6H_{10}O_5$), a common tracer species of BBA POA, and methyl-nitrocatechol (MNC, 4-methyl-5-nitrocatechol, $C_7H_7NO_4$), a proposed tracer species for biomass burning SOA (BBSOA)[99], serve as BBA particle proxies that represent different classes of organic species with different molecular functionalities, phase states, and water solubility. Heterogeneous OH oxidation of LEV has been investigated because of its assumed atmospheric stability[15,83,95,123,245,257,258]. The reactive uptake coefficients, γ, defined as the fraction of gas-to-particle collisions that lead to reaction, range from 0.1 to unity, yielding estimated atmospheric oxidation lifetimes on the order of weeks for RH$\leq$30%[15,95], but only a couple of days for OH oxidation of bulk aqueous LEV solutions and solution droplets[123,244,258]. However, the underlying mechanism for its enhanced degradation in the aqueous phase, how OH reactivity changes in response to RH, and what implications this may have for aerosol chemical aging is yet unknown. To our knowledge there have been no studies investigating the stability of methyl-nitrocatechols in the presence of OH radicals under dry and humid conditions. This study determines systematically γ for RH from 0-40% employing a low pressure aerosol flow reactor (AFR) coupled to a chemical ionization mass spectrometer (CIMS). We present strong evidence that the organic particle phase state, governed by ambient RH, controls OH reactive uptake.

5.3 Results and Discussion

The reactive uptakes of OH by LEV and MNC aerosol particles were investigated under dry conditions and over a range of atmospherically relevant RH (0%≤RH≤40%). At higher RH, the initial OH signal intensity, in the absence of particles, was at or near background levels due to significant water clustering with SF_6^- and thus resulted in the loss of OH detection sensitivity[34]. Therefore, OH uptake by the particles could not be assessed accurately above RH≈40%. Figure 5.1 shows the variation in γ for OH uptake by LEV and MNC particles for different RH. Under dry conditions, OH uptake by both particle types are of the same order (γ_{LEV}=0.21±0.18 and γ_{MNC}=0.22±0.08) and comparable to measurements of OH uptake by LEV and 5-nitroguaiacol (NG) films, the latter being an isomer of MNC[15] as given in Table 1. At RH>0%, OH uptake by LEV particles is enhanced by a factor of 3 yielding γ=0.65(±0.17) at RH=40%. In contrast, OH uptake by MNC particles is suppressed by a factor of 4 at 15%≤RH≤30% resulting in γ=0.06±0.02, which is near the detection limit of γ and thus may be regarded as an upper limit. For comparison with previous studies, heterogeneous second-order rate coefficients, k_2, were derived from γ applying[95]

$$k_2 = \frac{3\gamma\omega M}{2D_0\rho N_{\mathrm{A}}}, \tag{79}$$

where D_0 is the surface area-weighted mean particle diameter, ρ is the density of the organic compound, N_{A} is Avogadro's number, and M is the molecular weight of the organic compound. Our derived k_2 ranges from $1.38(\pm1.26)\times10^{-13}$-$4.25(\pm1.08)\times10^{-13}$ cm^3 molec^{-1} s^{-1} for OH uptake by LEV particles over the measured RH range. As given in Table 1, k_2 is in agreement with previous literature studies within experimental uncertainty. Under dry conditions, k_2 for OH uptake by LEV is in agreement with the study by Bai *et al.*[257], which derived k_2 from quantum chemical calculations using Rice-Ramsperger-Kassel-Marcus (RRKM) theory. The measured k_2 at RH=30% is also in agreement with the study by Kessler *et al.*[95]. Other studies have measured larger k_2, on the order of 10^{-12} cm^3 molecule^{-1} s^{-1}, however employing bulk aqueous LEV solution droplets[258], 45 μM bulk aqueous LEV solutions[123], bulk 1 mM aqueous LEV solutions[244], and LEV substrates[245].

While these studies suggest water can promote the degradation of LEV, except the study by Lai *et al.*[245] that shows the opposite trend, which may

Table 5.1: Uptake coefficients, γ, and second-order rate constants, k_2, for OH uptake by levoglucosan (LEV) and 4-methyl-5-nitrocatechol (MNC).

Organic	Source	RH	γ	$k_2 \cdot 10^{-13}$ / cm^3 $molecule^{-1}$ s^{-1}
LEV	This study[a]	0%	0.21(±0.18)	1.38(±1.26)
		15%	0.33(±0.08)	2.21(±0.51)
		30%	0.46(±0.12)	2.81(±0.60)
		40%	0.65(±0.17)	4.25(±1.08)
	Slade and Knopf[15b]	0%	0.19(±0.17)	
	Bai *et al.*[257c]			2.21
	Kessler *et al.*[95a]	30%	0.91(±0.08)	3.09(±0.18)
	Lai *et al.*[245b]	40%		91.7(±11.6)
MNC	This study[a]	0%	0.22(±0.08)	1.57(±0.56)
		7%	0.11(±0.05)	0.86(±0.39)
		17%	0.06(±0.02)	0.44(±0.18)
		26%	0.07(±0.02)	0.58(±0.15)
NG (isomer)	Slade and Knopf[15b]	0%	0.30(±0.21)	

[a]Employed aerosol particles. [b]Employed substrates. [c]Second order rate coefficient is derived based on RRKM theory with no reported uncertainty.

be due to application of substrates instead of particles, a unique mechanistic understanding for the observed enhancement in reactivity in the presence of water is lacking.

One possible mechanism for the enhancement in γ with increasing RH is that the particle's liquid water content controls particle phase state and the rate of OH loss. Previous studies indicate that LEV constitutes a highly viscous (glassy) solid or semisolid amorphous phase state under dry conditions[106,260]. However, LEV aerosol particles undergo a humidity-induced phase transformation to less viscous, i.e. semi-solid or liquid-like, particles at RH=30-60%[106]. This differs from inorganic species such as NaCl, which exhibits clear deliquescence and efflorescence points separating the liquid and crystalline phases. Under dry conditions, gas uptake is likely dominated by a surface reaction. Thus, the reduced translational motions of reactants in the particulate phase may retard chemical degradation, resulting in the relatively smaller γ at lower RH. However, higher RH can lower particle viscosity[105], likely resulting in a greater degree of diffusive mixing of H_2O and the reactants OH and LEV. This is expected to enhance gas uptake since OH can

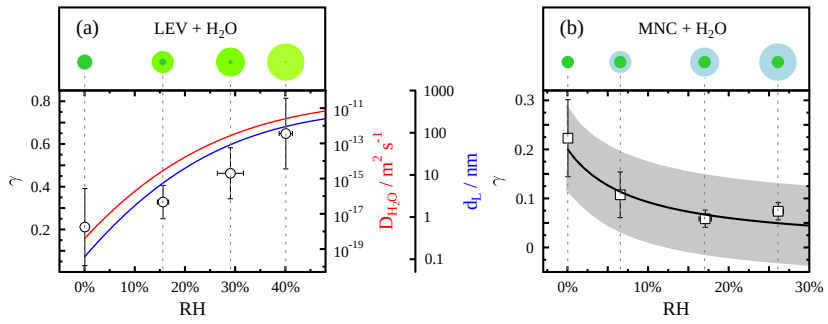

Figure 5.1: Mean OH uptake coefficients, γ, for LEV (a) and MNC (b) aerosol particles as a function of RH. Error bars represent 1σ from the mean in γ and RH. (a) The red and blue lines correspond to D_{H_2O} in LEV[259] and the diffuso-reactive length, d_L, respectively. (b) The solid black line represents a Langmuir-Hinshelwood model that accounts for co-adsorption of H_2O[159] and the shaded region corresponds to the 95% confidence interval. Particle illustrations (not to scale) indicate that (a) LEV takes up water and gradually deliquesces with increasing RH and (b) water continuously adsorbs on MNC particles with increasing RH.

more easily diffuse into the particle and unreacted LEV can be transported to the particle surface. While not investigated for OH, a theoretical study by Shiraiwa *et al.*[14] estimated the diffusion coefficient of NO_3 in amorphous solid organic matrices and showed that LEV is well conserved in the bulk of solid BBA particles under dry conditions, but undergoes rapid degradation upon deliquescence/liquefaction at higher RH. Similar observations of increased reactivity between amorphous organic material and longer-lived trace oxidants such as O_3 and HO_2 at higher RH have been made[33,194,261]. For example, O_3 uptake by an amorphous protein film was shown to be kinetically limited by bulk diffusion under dry conditions, but enhanced in the presence of water vapor[33]. This was attributed to water uptake followed by the physical transformation of the film from a glassy organic matrix to a semi-solid one at higher RH, thereby enhancing the reactivity of the organic. Another study by Lee *et al.*[262] showed that O_3 uptake by maleic and arachidonic acid particles reacted more efficiently when the particles were in a liquid state compared to a solid state. O_3 uptake by benzo[a]pyrene-ammonium sulfate particles was also shown to increase at higher RH only when coated with amorphous

α-pinene SOA[261]. These authors suggest that water uptake lowers the viscosity of the SOA, promoting mass transfer of the reactants in the particle phase, thus enhancing uptake. Furthermore, HO_2 uptake by LEV particles was observed to increase at higher RH[194]. A very recent study by Lai *et al.*[245] suggests that OH-initiated oxidation of LEV is supressed at higher RH, in disagreement with our results. However, their study differs from ours in that they employ LEV bulk samples, which don't exhibit significant water uptake until RH$\geq$80%[106,245,263]. These authors suggest that the decrease in reactivity may be a consequence of adsorbed monolayers of water blocking surface reactive sites. Lastly, a very recent study found that OH oxidation of aqueous succinic acid aerosol exhibited pronounced enhancements in the liquid phase compared to solid phase[264].

To determine the extent that water diffuses in LEV particles over the investigated RH range, the temperature dependent diffusion coefficient of H_2O (D_{H_2O}) in LEV particles was calculated and plotted as a function of RH as shown in Fig. 5.1(a), using the parameterization for diffusion of H_2O in LEV as given by Price *et al.*[259]. Over the investigated RH range, D_{H_2O} increases by over seven orders of magnitude from $\sim 10^{-18}$ to 10^{-11} m^2 s^{-1}. The derived D_{H_2O} indicates LEV particles transition from a highly viscous semi-solid state to a liquid one over the measured RH range[105]. As a consequence, a self-accelerating process is initiated whereby greater water diffusivity lowers particle viscosity, promoting greater diffusion of water and the reactant species OH and LEV in the particulate phase. As a first approximation, we assume the diffusivity of OH (D_{OH}) is equivalent to D_{H_2O} since OH and H_2O possess similar transport properties[243]. The large increase in D_{H_2O} accompanied by a smaller change in γ with increasing RH is partially due to the reacto-diffusive flux term in the calculation of γ, which scales with $\sqrt{D_{OH}}$ for spherical particles[111]. Moreover, particle sizes equivalent to the range applied here, exhibit less change in the rate of uptake even if the bulk diffusion coefficient changes by orders of magnitude because of particle surface curvature effects and smaller characteristic mixing times[33,170,265]. From D_{OH}, the OH diffuso-reactive length, d_L, defined as a measure of the distance a molecule can diffuse before reacting, and thus an estimate of its concentration gradient in the aerosol particle, is derived from[266]

$$d_L = \sqrt{\frac{D_{OH}}{k_1}}. \tag{80}$$

Figure 5.1(a) shows d_L as a function of RH. As discussed in more detail in

the supplemental material and shown in Fig. 5.3, we approximate k_1 to be linear as a function of RH. Under dry conditions d_L is <1 nm, suggesting OH reactive uptake is confined near the particle surface. However, as RH increases to 40%, d_L is enhanced by over two orders of magnitude, up to 100 nm. For a number-weighted particle diameter of 100 nm, typical of BBA[267], our results imply the entire particle volume can undergo reaction with OH under humidified conditions and thus OH oxidation may not only occur along the surface of LEV particles, but also within the particle bulk at higher RH. Similar observations were made for OH oxidation of liquid and solid succinic acid particles such that the characteristic mixing time for OH diffusion in solid succinic acid particles was orders of magnitude longer compared to the liquid particles[264]. Furthermore, oxidation of LEV can result in the formation of carboxylic and aldehydic species[15,257] that have low acid dissociation constants, possibly enhancing the reactive uptake of OH since their conjugate bases weaken their α-C-H bonds, promoting H-atom abstraction and more efficient radical-ion reactions[34].

While there have been no previous studies regarding OH reactivity with MNC, our measured γ=0.22($\pm$0.08), i.e. k_2=1.57($\pm$0.56)$\times10^{-13}$ cm^3 molecule^{-1} s^{-1} under dry conditions, is in agreement with work by Slade and Knopf[15], who measured OH uptake by NG films, an isomer of MNC. Gas-phase rate constants measured for OH radical reaction with methyl-2-nitrophenols are between 2.70×10^{-12}-6.72×10^{-12} cm^3 molecule^{-1} s^{-1} and those with nitrophenols are 9×10^{-13} cm^3 molecule^{-1} s^{-1} [268]. While our estimated second order rate constants for OH reaction with MNC aerosol particles are within one order of magnitude as those measured for gas-phase reactions of nitrophenols, the differences are likely due to the different phases involved.

One possible mechanism for the decrease in γ with increasing RH is that the low solubility of MNC in water (5.28 g L^{-1}) enables water layers to accumulate on the surface, which suppress reactive uptake by limiting OH radical transfer to the reactive hydrophobic core. While not measured directly for OH, atmospheric chemistry model simulations involving hydrophobic soot particles, which include detailed multiphase kinetics, indicate that O_3, NO_2, NO_3, and OH uptake is significantly decreased when RH increases due to competitive co-adsorption of H_2O for reactive sites[211,212]. Furthermore, Pöschl *et al.*[159] attributed a decrease in γ with increasing RH for O_3 uptake by benzo[a]pyrene to surface saturation by water molecules. The non-linear decrease in γ with increasing RH is suggestive of partial inhibition of OH reactive uptake by adsorbed H_2O. The data in Fig. 5.1(b) is modeled

based on a Langmuir-Hinshelwood function that allows for the inhibition of reaction due to the presence of a co-adsorbate such as water[159] (see AM for more details). The best fit Langmuir adsorption equilibrium constant, K_{H_2O}, describing the kinetic data is $2.01(\pm 1.07)\times 10^{-17}$ cm^3 molecule^{-1}, in accordance with the value derived in Pöschl *et al.*[159] of $2.1(\pm 0.4)\times 10^{-17}$ cm^3 molecule^{-1} for water adsorption on benzo[a]pyrene coated soot particles. Assuming complete H_2O surface saturation and inhibition of OH uptake by MNC, OH uptake by water alone would proceed with γ=0.0035[192]. Since γ measured above RH of 15% was at or near our detection limit in γ, the precise RH at which complete H_2O surface saturation occurred could not be determined.

OH reactivity with substituted nitrophenols can also depend on the position of the functionalities along the aromatic ring[15]. Due to the strong electron-donating resonance effect of the lone electron pairs on the oxygen of the -OH groups, which can activate the ring toward electrophilic aromatic substitution, ultimately the position of the -OH groups will determine where OH radical addition occurs. In MNC, both -OH groups are *ortho* to one another and -NO_2 and -CH_3 are *para* to the two -OH groups, resulting in preferred OH radical addition at those positions. However, if water complexes with the catechol -OH groups[269], then the increased steric hindrance of the R-C-OH groups could impede electrophilic OH radical addition and thus further supress OH radical uptake at higher RH.

5.4 Atmospheric Implications

In assessing the impact of γ with changing RH we can consider its affect on the atmospheric e-folding lifetime, τ (τ=$1/k_2$[OH]), of LEV (τ_{LEV}) and MNC (τ_{MNC}) as shown in Fig. 5.2. Based on the derived second-order rate coefficients and assuming an average daytime OH concentration of 2×10^6 molecule cm^{-3} ($\sim$0.1 ppt), under dry conditions, τ_{LEV} and τ_{MNC} are $\sim$27 days. However, at higher RH, τ_{LEV} is reduced to $\sim$13 days at RH=40% and τ_{MNC} is extended to $\sim$115 days at 15%$\leq$RH$\leq$30%. For higher OH concentrations of $\sim 2\times 10^7$ molecule cm^{-3} ($\sim$1 ppt) as observed in biomass burning plumes[63], τ_{LEV} is reduced from $\sim$3 days under dry conditions to $\sim$1 day at RH=40% and τ_{MNC} increases from $\sim$3 days under dry conditions to 9-10 days at 15%$\leq$RH$\leq$30%. The shaded region in Fig. 5.2(a) indicates the likely range of LEV oxidation lifetimes assuming a lower limit of τ_{LEV} applying k_2 measured for OH oxidation of aqueous LEV solutions[123,244,258]. In this case,

τ_{LEV} is on the order of 2 days when [OH]=0.1 ppt and <4 hrs. when [OH]=1 ppt, well within the timeframe of removal by wet deposition of about a week.

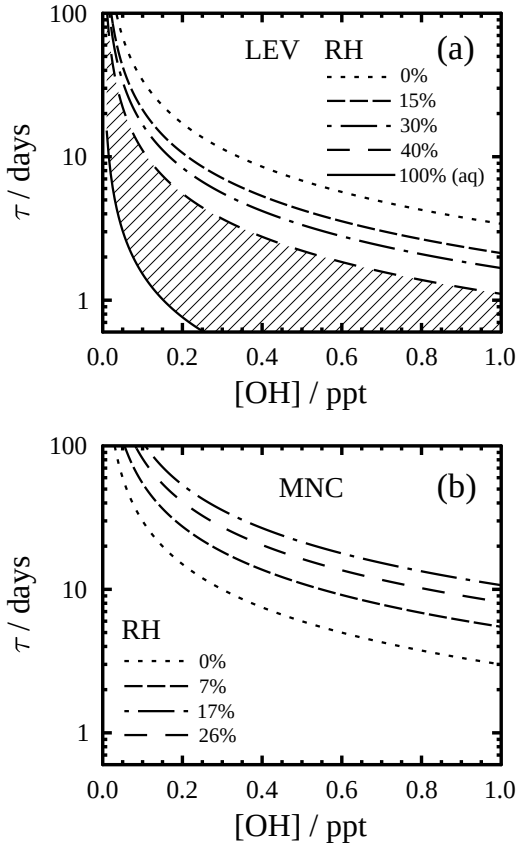

Figure 5.2: Chemical lifetimes, τ, of LEV (a) and MNC (b) as a function of gas-phase OH concentration for different RH as indicated in legends.

Our results imply that degradation of water-soluble organic aerosol can proceed more efficiently in humid environments, but depends crucially on particle phase state. When amorphous organic aerosol particles such as LEV transition to liquid particles, the lower viscosity allows for enhanced diffusive mixing of OH and LEV in the particulate phase, resulting in enhanced gas uptake and particle degradation. Thus, it is expected that organic aerosol reactivity and lifetimes are governed by ambient RH, which in turn varies considerably contingent on region, altitude, and season[270]. In general, RH is

higher in the lower section of the atmospheric column near the surface, thus it is expected that OH oxidation of amorphous organic aerosol is enhanced near the ground. At higher altitudes, e.g. above the boundary layer, where RH is relatively low and ambient T can be near the glass transition point of amorphous organic aerosol[42,105,260], particle oxidation is expected to be less efficient as a result of reduced translational motions of reactant species yielding longer particle lifetimes. OH uptake by aqueous LEV solutions is likely representative of cloud-processing conditions when LEV particles activate and become highly diluted water droplets. In this case, gas uptake and particle degradation can be enhanced due to the lower viscosity of the droplet. BBA particles are a complex mixture of organic and inorganic compounds that likely exhibit complex mixing and various phase states[72,271]. If the presence of other compounds reduce OH uptake and diffusivity and/or shield LEV, the derived reaction kinetics should be regarded as upper limits.

Furthermore, based on our derived H_2O adsorption/desorption rate, water covers a significant surface area of MNC particles, which in turn reduces the reactive uptake of OH by up to a factor of 4 when RH approaches 15%-30%. At higher RH, OH uptake is likely further supressed, extending the lifetime of MNC in SOA, in line with the understanding that nitrophenols exhibit good atmospheric stability[272]. In addition, nitrophenolic species are considered phytotoxic, contributing to forest decline and are readily found in aqueous and SOA media[272]. Our results suggest that its phytotoxicity could be enhanced in humid environments due to little degradation by OH, likely having deleterious effects on public health and air quality. These results may be applicable to other aerosol particle systems having low water-solubility such as PAHs and soot.

Our results indicate that biomarkers such as levoglucosan are not photochemically inert and that their lifetime depends on particle phase state, which changes in response to RH and T. These effects should be taken into account in source apportionment studies that assume biomarker tracers are stable during transport in the atmosphere[91,249]. If not taken into account, LEV concentrations and source strengths can be underestimated. In contrast, MNC is likely a suitable biomarker for BBSOA since oxidation lifetimes are sufficiently long to prevent significant degradation under typical atmospheric transport timescales. Furthermore, parameterizations of atmospheric conditions such as RH and T into chemical transport models that incorporate heterogeneous chemistry could improve regional and global gas-phase budget estimates of HO_x[273,274], since HO_x loss, in part, is dictated by particle phase

state and thus reactivity of organic aerosol.

5.5 Conclusions

The reactive uptake coefficients for OH radical uptake by LEV and MNC serving as BBA and BBSOA surrogate particles have been systematically determined as a function of RH. At RH=0%, $\gamma \sim 0.2$ for OH uptake by both species. However, an increase in RH up to 40% results in a factor of 3 increase in γ for OH uptake by LEV particles and a factor of 4 decrease in γ for OH uptake by MNC particles. We conclude that the increase in γ is attributed to enhanced diffusive mixing of OH and LEV as a result of lower particle viscosity initiated by enhanced diffusion of H_2O in the particle with increasing RH. Derived H_2O diffusivity and OH diffuso-reactive lengths in LEV were enhanced by seven orders in magnitude and two orders in magnitude, respectively, with increasing RH. This suggests OH can react not only on the surface of amorphous LEV particles, but also within the particle bulk at higher RH. LEV represents just one of many types of amorphous organic material, which also include carbohydrates, proteins, carboxylic acids, SOA, and HULIS[33,42,106,260,275]. Thus, consideration of OH reactivity with other amorphous organic substances will further improve our understanding of its influence on chemical aging and thus atmospheric chemistry and climate.

The decrease in OH uptake by MNC particles with increasing RH is attributed to the accumulation of water on MNC particles having low water-solubility, resulting in partial hindrance of reaction. Using a Langmuir-Hinshelwood uptake model that accounts for co-adsorption of H_2O, the trend in γ as a function of RH is well reproduced, and the derived K_{H_2O} is consistent with previously determined K_{H_2O} for water adsorption on hydrophobic organic surfaces.

This study demonstrates that organic aerosol reactivity with OH radicals strongly depends on environmental conditions such as RH, significantly affecting particle chemical lifetimes. Since organic aerosol particle phase state also depends strongly on T, thereby impacting diffusion and viscosity, and a great part of the atmosphere exhibits low temperatures, organic aerosol particle reactivity may also vary strongly with T and thus altitude; likely exhibiting decreased reactivity with decreasing T. Clearly, more systematic studies on the RH and T dependence of organic aerosol multiphase kinetics are needed. Incorporation of our data into chemical transport and particle-resolved aerosol models will improve their accuracy, leading to better pre-

diction of the chemical evolution of organic aerosol and its effects on aerosol lifetime, air quality and climate.

5.6 Supplemental material

5.6.1 Observed loss rate (k_1) dependence on relative humidity

As shown in Eq. 80, d_{L} depends on both the diffusion coefficient of OH, D_{OH}, in levoglucosan, and k_1, which both vary as a function of RH. Therefore, to plot a smooth d_{L} as a function of RH as shown in Fig. 5.1a requires a parameterization for k_1 as a function of RH. Figure 5.3 shows derived k_1 as a function of RH. Based on the scatter in the data, we assume that k_1 depends

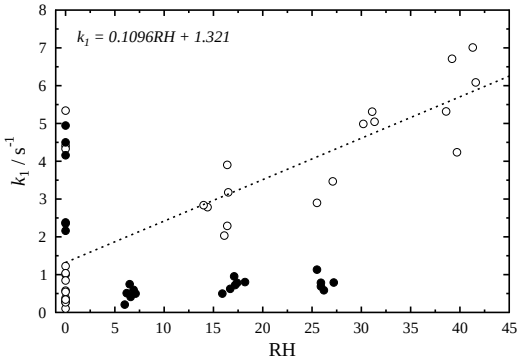

Figure 5.3: k_1 as a funtion of RH for OH uptake by LEV (white circles) and MNC (black circles). The dotted line represents the best fit to the LEV data based on a linear equation.

linearly on RH with $k_1 = 0.1096RH + 1.321$. Note, however, that k_1 also varies with particle surface area density, S_{a}, as shown in Fig. 3.11, and thus the linear function does not account for changes in k_1 due to changes in S_{a}. For example, the large scatter in k_1 at RH = 0% as shown in Fig. 5.3 is due to the wide range in applied S_{a}. A sensitivity analysis on the dependence of k_1 as a function of RH at fixed S_{a} may resolve this bias, but is beyond the scope of this study.

5.6.2 Langmuir-Hinshelwood description accounting for co-adsorption of H_2O

The modeled γ as shown in Fig. 5.1b assumed OH undergoes a Langmuir-Hinshelwood reactive uptake mechanism with MNC and that H_2O partially inhibits reactive uptake of OH by MNC by competing for surface reactive sites and is based on the following equation[159]

$$\gamma = \frac{4k_s[\text{Org}]K_{\text{OH}}}{\sigma_{\text{OH}}\omega_{\text{OH}}(1 + K_{\text{OH}}[\text{OH}] + K_{\text{H}_2\text{O}}[\text{H}_2\text{O}])}, \tag{81}$$

where k_s is the surface reaction rate constant between OH and the organic, [Org] is the surface concentration of the organic, i.e. MNC, estimated to be 2×10^{14} molecule cm^{-2}[15], K_{OH} is the Langmuir adsorption constant of OH taken as 3.96×10^{-10} cm^3 molecule^{-1} as derived from OH adsorption of nitroguaiacol, an isomer of MNC[15], σ_{OH} is the surface area occupied by one adsorbed OH molecule approximated as 1.08×10^{-15} cm^2 molecule^{-1}[15], and [OH] and [H_2O] are the gas-phase concentrations of OH and H_2O, respectively. [H_2O] was determined from the RH measurements in the flow reactor and the vapor pressure of water at 293 K. Both k_s and $K_{\text{H}_2\text{O}}$ are free fitting parameters, which were determined by fitting the data in Fig. 5.1b to the above equation applying a non-linear least sqares fit using a Levenberg-Marquardt algorithm. The best fit parameters to k_s and $K_{\text{H}_2\text{O}}$ are $4.29(\pm0.70)\times10^{-17}$ cm^2 molecule^{-1} s^{-1} and $2.01(\pm1.07)\times10^{-17}$ cm^3 molecule^{-1}, respectively. The derived k_s of $8.38(\pm8.44)\times10^{-17}$ cm^2 molecules^{-1} s^{-1} derived from the OH surface reaction with nitroguaiacol[15]. Excluded in this function are the possible influences of other co-adsorbates that may suppress OH reactive uptake. For example, recombination of OH to H_2O_2 in the adsorbed water later[192] may limit OH reactive uptake by the organic. Increasing RH would result in more monolayers of water on the surface of the particle, thus extending the time for OH to diffuse through the water layers to react with the organic, enabling greater production of H_2O_2. Since H_2O_2 is less reactive than OH with organics[245], less of the organic is degraded and the additional presence of H_2O_2 may compete as well with OH for surface reactive sites. Clearly, more systematic studies are needed to properly assess the roles of other possible co-adsorbates that may also limit the reactive uptake of OH.

Here ends the publication:

Multiphase OH oxidation kinetics of organic aerosol: The role of particle phase state and relative humidity

Jonathan H. Slade[1] and Daniel A. Knopf[1*]

[1]Institute for Terrestrial and Planetary Atmospheres/School of Marine and Atmospheric Sciences, Stony Brook University, Stony Brook, NY 11794-5000, USA

[*]To whom correspondence should be addressed. Email:Daniel.Knopf@stonybrook.edu

Published in *Geophysical Research Letters*, Vol. 14, 5297–5306, 2014, with permission from Wiley and Sons, Inc. on behalf of the American Geophysical Union, copyright 2014.

5.7 Estimation of the OH reacto-diffusive length in levoglucosan particles using the pseudo-first order loss rate of OH in the particle bulk

The following is a summary of the corrections to Fig. 5.1a in section 5.3 and Fig. 5.3 in section 5.6.1. The diffuso-reactive length, d_{L}, calculated from Eq. 80 and plotted as a function of RH in Fig. 5.1a (blue line) erroneously uses the pseudo-first order loss rate of gas-phase OH. The correct pseudo-first order loss rate is $k_1{=}k_2[\mathrm{LEV}]_{\mathrm{B}}$ [138], where k_2 is the second order rate constant derived from γ at a specific RH (see table 5.1), and $[\mathrm{LEV}]_{\mathrm{B}}$ is the bulk concentration of levoglucosan, approximated as $6.27{\times}10^{21}$ molecule cm^{-3}, which assumes a densely packed system formed exclusively by LEV molecules (molecular volume of $1.59{\times}10^{-22}$ cm^3) [35].

In this study, k_2 and subsequently k_1 for OH uptake by LEV particles increases with increasing RH. Figure 5.4 shows the corrected k_1 plotted as a function of RH.

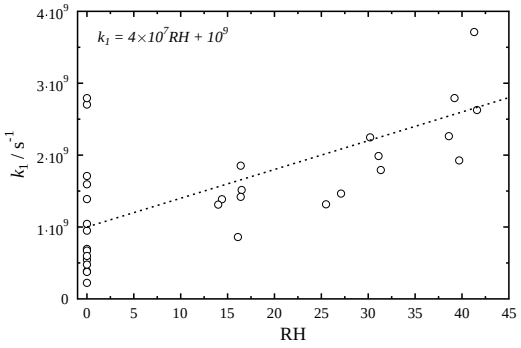

Figure 5.4: k_1 as a funtion of RH for OH uptake by LEV. The dotted line represents the best fit to the LEV data based on a linear equation.

Allowing k_1 to adjust with RH using the linear equation $k_1{=}4{\times}10^7 RH{+}10^9$, Fig. 5.5 shows the corrected d_{L} plotted as a function of RH.

d_{L} increases from approximately 10^{-4} nm at RH=0% to about 0.1 nm at RH=40%. This suggests OH is rapidly removed near the surface of LEV, in agreement with the modeled OH concentration gradients in LEV as reported in Arangio *et al.* [35].

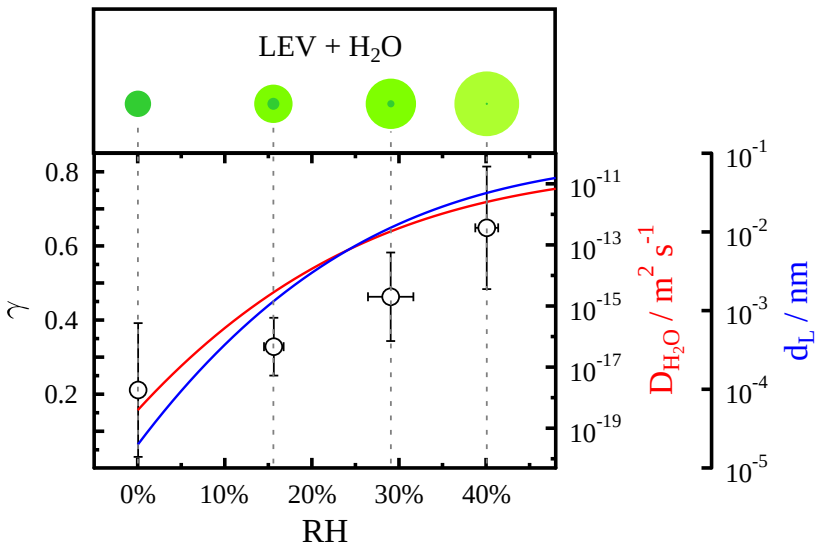

Figure 5.5: Mean OH uptake coefficients, γ, for LEV aerosol particles as a function of RH. Error bars represent 1σ from the mean in γ and RH. The red and blue lines correspond to $D_{\mathrm{H_2O}}$ in LEV[259] and the diffuso-reactive length, d_{L}, respectively. Particle illustrations (not to scale) indicate that LEV takes up water and gradually deliquesces with increasing RH.

6 Results: Chemical aging of single and multicomponent biomass burning aerosol surrogate-particles by OH: Implications for cloud condensation nucleus activity

The sections from 6.1 to 6.4 are the reproduction of the manuscript entitled "Chemical aging of biomass burning aerosol surrogate-particles by OH: Implications for cloud condensation nuclei" by Jonathan H. Slade, Ryan Thalman, Jian Wang, and Daniel A. Knopf in preparation for submission to *Atmospheric Chemistry and Physics Discussions*. The layout of the article as well as the section figures and table numberings have been adapted to match with the thesis structure.

6.1 Abstract

Multiphase OH and O_3 oxidation reactions with atmospheric organic aerosol (OA) can influence particle physicochemical properties including composition, morphology and lifetime. Chemical aging of initially insoluble or low soluble single-component OA by OH and O_3 can increase their water-solubility and hygroscopicity, making them more active as cloud condensation nuclei (CCN) and susceptible to wet deposition. However, an outstanding problem is whether the effects of chemical aging on their CCN activity is preserved when mixed with other organic or inorganic compounds exhibiting greater water-solubility. In this work, the CCN activity of laboratory-generated biomass burning aerosol (BBA) surrogate-particles exposed to OH and O_3 is evaluated by determining the hygroscopicity parameter, κ, as a function of particle type, mixing state, and OH/O_3 exposure applying a CCN counter (CCNc) coupled to an aerosol flow reactor (AFR). Levoglucosan (LEV), 4-methyl-5-nitrocatechol (MNC), and potassium sulfate (KS) serve as representative BBA compounds that exhibit different hygroscopicity, water solubility, chemical functionalities, and reactivity with OH radicals, and thus exemplify the complexity of mixed inorganic/organic aerosol in the atmosphere. The CCN activities of all of the particles were unaffected by O_3 exposure. Following exposure to OH, κ of MNC was enhanced by an order of magnitude, from 0.01 to $\sim$0.1 , indicating that chemically-aged MNC particles are better CCN and more prone to wet deposition than pure MNC particles. No significant enhancement in κ was observed for pure LEV particles following OH exposure. κ of the internally-mixed particles was not affected by OH oxidation. Furthermore, the CCN activity of OH exposed MNC-coated KS particles is similar to the OH unexposed atomized 1:1 by mass MNC:KS binary-component particles. Our results strongly suggest that when OA is dominated by water-soluble organic carbon (WSOC) or inorganic ions, chemical aging has no significant impact on OA hygroscopicity. The organic compounds having low solubility behave as if they are infinitely soluble when mixed with a sufficient amount of water-soluble compounds. At and beyond this point, the particles' CCN activity is governed entirely by the water-soluble fraction and not influenced by the oxidized organic fraction. Our results have important implications for heterogeneous oxidation and its impact on cloud formation given that atmospheric aerosol is a complex mixture of organic and inorganic compounds exhibiting a wide-range of solubilities.

6.2 Introduction

The extent that aerosol-cloud interactions impact the atmospheric radiative budget and climate change is significant, but remains highly uncertain[6]. Attributed to this uncertainty is the difficulty to quantify the effects of chemical aging during atmospheric particle transport by heterogeneous or multiphase chemical reactions between organic aerosol particles and trace gas-phase oxidants and radicals[8,9,12,138]. Heterogeneous oxidation reactions between organic aerosol particles and OH, O_3, or NO_3 can impact the particles' physical and chemical properties[7,8,12,209,276], and has been shown to impact particle hygroscopicity and cloud condensation nuclei (CCN) activity[9,16,17,112,113] and ice nucleation (IN)[88,277].

Cloud nucleation efficiency depends on the particle's solubility in water and hygroscopicity[27,146], and particle size[24]. The majority of submicron aerosol particles are comprised of organic material[18,51], which possess a wide range of hygroscopicity (κ ~0.01-0.5)[27]. A significant portion of atmospheric organic aerosol (OA) is derived from biomass burning (BB) emissions[20,21,122,278]. BB plays an important role both regionally and globally[66], accounting for an estimated 2.5 Pg C yr^{-1} ? . Reflectance data from satellite retrievals indicate that BB accounts for a global footprint of 464 Mha yr^{-1} or roughly ~36% of cropland on earth[68]. Biomass burning aerosol (BBA) constitutes a significant fraction of primary organic aerosol (POA)[20] and secondary organic aerosol (SOA), derived from oxidative aging of volatile and semi-volatile organic vapors emitted from biomass burning plumes[51,84,279]. Molecular markers of BB POA include pyrolyzed forms of glucose such as levoglucosan (LEV, 1-6-anydro-β-glucopyranose)[94] and potassium containing salts such as potassium sulfate (KS, K_2SO_4)[280]. The photo-oxidation of *m*-cresol, which is emitted at high levels from biomass burning[90], in the presence of NO_x, generates 4-methyl-5-nitrocatechol (MNC), which has recently been recognized as a potentially important tracer for biomass burning SOA[99]. With the exception of MNC, the CCN activity and hygroscopicity of LEV and KS, among other select BBA compounds and smoke particles, have been determined[84,182]. Dusek *et al.*[281] measured κ values of 0.2 for the water-soluble organic content (WSOC) in particles produced from controlled laboratory burns. Carrico *et al.*[84] determined a mean κ of 0.1 for carbonaceous particles sampled from open combustion of several biomass fuels. Hygroscopic growth factors of levoglucosan and other biomass burning derived organics range from 1.27-1.29 at RH=90%[106,140]. In-situ field mea-

surements of the CCN efficiency (ratio of CCN to the available condensation nuclei, CN) of biomass burning smoke particles is on the order of 50% at 1% supersaturation[21]. While inorganic ions have only a minor importance as an atmospheric tracer for biomass burning, they can significantly influence the CCN activity of BBA, even if their fractions are significantly less than the organic fraction[92,282]

Heterogeneous OH oxidation of organic aerosol can initiate reactions that result in the production of oxidized polar functional groups that can reduce the particle's surface tension[17] and increase water-solubility[283], enabling greater water uptake and CCN activity. For example, Broekhuizen *et al.*[112] demonstrated that unsaturated fatty acid aerosol particles comprised of oleic acid became more CCN active in the presence of high exposures to O_3. In a follow-up study, Shilling *et al.*[113] corroborated this finding, attributing the enhancement in CCN activity to a combination of an increase in water-soluble material and decrease in surface tension of the aqueous droplet during activation. Petters *et al.*[16] demonstrated that the CCN activity of model saturated and unsaturated OA compounds is enhanced following oxidation by OH and NO_3. George *et al.*[17] showed that the hygroscopicity of a model OA, bis-ethyl-sebacate (BES) and stearic acid, was enhanced following oxidative aging by OH radicals, and attributed this to the formation of highly water-soluble oxygenated functional groups. The hygroscopicity of OH-impacted ambient biogenic SOA was shown to increase at higher OH exposures with increasing oxygen-to-carbon (O:C) ratio[114].

In an effort to better understand the influence of chemical aging on the CCN activity of BBA, recent studies have investigated the influence of oxidative aging on particle hygroscopicity of either particles generated in the laboratory from a specific emission source[125,284,285] or particles collected in the field[286,287], which may include multiple emission sources. While field-collected particle studies of hygroscopic growth and cloud formation are advantageous because they capture the chemical and physical complexity of ambient aerosol, they lack the specificity and control of laboratory studies in order to fully understand the fundamental physico-chemical processes that govern cloud formation. Martin *et al.*[125] investigated the impact of photo-oxidation on the hygroscopicity of wood burning particles and found that after several hours of aging in a smog chamber there is a general enhancement in κ; however, this was attributed to sequential condensation of oxidized organic or inorganic matter and oxidation of the particulate matter itself. However, the effects of OH-initiated oxidation on the hygroscopicity of

BBA particles have yet not been examined systematically. In this work, we investigate the effects of heterogeneous OH oxidation of laboratory-generated BBA surrogate-particles on the particles' hygroscopicity. Here, κ is evaluated for several pure-component and multicomponent aerosol particles containing both sparingly soluble and highly water-soluble compounds, representing the range and complexity of atmospheric aerosol in regards to hygroscopicity and chemical composition. κ is evaluated as a function of OH exposure (i.e. [OH]×time) and O_3 exposure using a custom-built AFR coupled to CCNc. The effects of chemical aging on the CCN activity of internally mixed and organic-coated inorganic particles are presented.

6.3 Results and Discussion

6.3.1 CCN activity of BBA surrogate particles

Exemplary activated fractions, i.e. fraction of initial dry particle sizes activated to CCN, for LEV, MNC, KS, and the ternary particle mixtures at a chamber supersaturation of 0.425% are shown in Fig. 6.1. The activated fraction curves were fit to a cumulative Gaussian distribution function as described previously in detail[182]

$$f(x) = \frac{1}{2}\mathrm{erfc}(\frac{x}{\sqrt{2}}), \tag{82}$$

where $x = (\mathrm{D_d}\text{-}\mathrm{D_{d,50}})/\sigma_\mathrm{D}$. In the fitting procedure, $\mathrm{D_d}$ is the dependent variable and $\mathrm{D_{d,50}}$ and σ_D are adjustable parameters to minimize the root mean square error between *f(x)* and the data. $\mathrm{D_{d,50}}$ is the dry diameter interpreted as where 50% of the dry particles have activated into cloud droplets, also referred to as the critical particle diameter, $\mathrm{D_{p,c}}$.

KS particles exhibit the smallest particle activation diameter of ∼50 nm, followed by LEV particles at ∼75 nm, and MNC particles at ∼210 nm at S=0.425%. The critical diameter of levoglucosan is in good agreement with the critical diameters of levoglucosan measured by Petters and Kreidenweis[27] at the same S. The MNC activation diameter is similar to that of NO_3 oxidized oleic acid particles at the same S[16], consistent with the presence of relatively hydrophobic unsaturated bonds and organo-nitrogen species. In this study, κ is derived from Eq. 2, where S evaluated at 0.2, 0.27, 0.35, and 0.425% is used in place of S_c and D_d is the determined $D_\mathrm{p,c}$. At lower S, the activated fraction curves are shifted to larger sizes since the smaller particles do not activate at lower S.

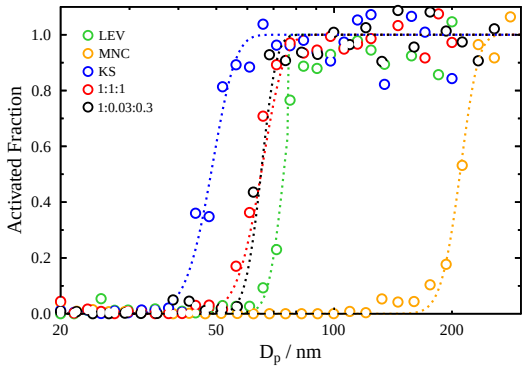

Figure 6.1: Exemplary activated fractions, i.e. fraction of the initial dry particle sizes activated to CCN as a function of the initial dry particle diameter, for LEV (green), MNC (orange), KS (blue), 1:1:1 (red) and 1:0.03:0.3 (black) particles at a S=0.425%. The dotted lines correspond to the fits applying Eq. 8.

Table 6.1 lists the derived κ values for all of the particle types employed in this study in comparison to literature values. The reported uncertainties in κ are $\pm 1\sigma$ from the mean κ measured at all S. The measured κ values for LEV and KS are consistent with κ for LEV and KS given in the literature. κ=0.169 for LEV is close to the humidified tandem-DMA (HT-DMA) derived κ=0.165[84]. Within experimental uncertainty, κ for KS is in agreement with the value derived in Carrico *et al.*[84]. To our knowledge, no previous hygroscopicity measurements of MNC have been made. For comparison, HULIS, which is known to contain nitrocatechols[89], exhibits a κ value of 0.05[84]. In addition, κ for NO_3 oxidized oleic acid particles, comprising similar chemical functionalities as MNC (i.e. nitrogen oxides and conjugated double bonds) is $\sim$0.01[16].

κ of the binary and ternary mixed particles, on average range from 0.131 ($\pm$0.014) to 0.355 ($\pm$0.042). The mixed particles containing a significant fraction of MNC (i.e. 1:1:0, 0:1:1, 1:1:1) exhibit relatively lower κ values than the 1:0:1 mixture. This is expected since MNC alone has significantly lower κ than either LEV or KS. The 1:0.03:0.3 ternary-component particles exhibit a slightly lower κ compared to the other particle mixtures, due to the relatively low KS content. As listed in table 2, the measured κ values are

Table 6.1: Tabulated hygroscopicity parameters, κ, for the various particle types investigated in this study.

Compound	κ^1	κ^2	κ^3	References
LEV	0.169 ($\pm$0.013)	0.188	0.165	Carrico *et al.*[84]
			0.208 ($\pm$0.015)	Petters and Kreidenweis[27]
KS	0.55 ($\pm$0.08)	0.55	0.52	Carrico *et al.*[84]
MNC	0.01 ($\pm$0.004)	0.16		
LEV:MNC:KS	κ^1	κ^2	κ^4	
1:1:0	0.131 ($\pm$0.014)	0.173	0.085	
1:0:1	0.355 ($\pm$0.042)	0.329	0.318	
0:1:1	0.301 ($\pm$0.047)	0.300	0.204	
1:1:1	0.261 ($\pm$0.012)	0.256	0.188	
1:0.03:0.3	0.227 ($\pm$0.016)	0.241	0.221	

[1]This study. Reported uncertainties are $\pm 1\sigma$ from the mean in the measured κ. [2]Predicted values applying the volume mixing rule without solubility limitations. [3]Literature reported values. [4]Predicted values applying the volume mixing rule and experimentally derived single-component κ (i.e. with solubility limitations).

reasonably predicted applying the volume mixing rule[27]:

$$\kappa = \kappa_{\mathrm{Org}} \cdot \varepsilon_{\mathrm{Org}} + \kappa_{\mathrm{Inorg}}(1 - \varepsilon_{\mathrm{Org}}), \tag{83}$$

where κ_{Org} and κ_{Inorg} are the κ values of the organic and inorganic particles, respectively, and $\varepsilon_{\mathrm{Org}}$ is the organic volume fraction of the particles. However, the quality of the estimate depends on whether the effects of solubility are to be included. For example, applying the experimentally-derived κ of MNC particles in the volume mixing rule results in a significant underprediction of κ for the 1:1:0, 0:1:1, and 1:1:1 particle mixtures. This deviation in κ suggests water uptake by the pure-component particles is mechanistically different than water uptake by the mixed particles that contain significant amounts of MNC. The volume mixing rule is applicable over a range of mixtures and hygroscopicity; however, when the particles contain both soluble and sparingly soluble compounds, predicted κ can deviate significantly from measured κ values[146]. MNC is significantly less soluble in water compared to pure LEV and KS. During CCN activation, the most water-soluble material dissolves first and enhances the solute effect in the Köhler equation. More water-soluble particles retain a larger content of liquid water and consequently, the

less water-soluble material can more easily dissolve in the presence of hygroscopic and water-soluble substances during water uptake[146,288–290]. This solubility constraint in the volume mixing rule is described in more detail in Petters and Kreidenweis[146]. As a result, depending on the volume fraction of the sparingly soluble compounds, the peak of the Köhler curve may occur at a sufficiently large droplet size when all compounds, including the sparingly soluble compounds, are completely dissolved. The same can be applied here for the mixtures containing appreciable amounts of MNC. The solubility of MNC in water is C=0.004 and falls in the sparingly water-soluble category[146]. To verify whether MNC behaves as if it is infinitely soluble in a solution containing KS, Fig. 6.2 shows derived Köhler curves of pure MNC and mixtures containing variable amounts of KS, and the MNC dissolved fraction, x_{MNC}. According to Fig. 6.2, the critical supersaturation,

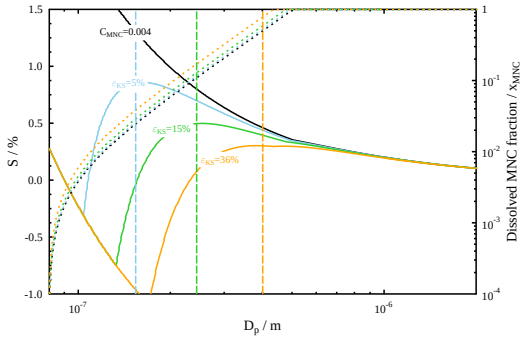

Figure 6.2: Example Köhler curves (solid lines) calculated from Eq. 1 for pure MNC (black), MNC mixed with 5% (blue), 15% (green), and 36% (orange) by volume KS. The dotted lines are the dissolved fractions of MNC, x_{MNC}, calculated from Eq. 7, corresponding to the different Köhler curves. Where x_{MNC} corresponds to the maximum in the Köhler curves is given by the vertical dashed lines. CCN activation is not limited by the solubility of MNC when the maximum in the Köhler curve corresponds to x_{MNC}=1.

i.e. maximum in the Köhler curve, decreases with increasing KS volume fraction. Accordingly, the dissolved fraction of MNC increases with increasing KS volume fraction. At a KS volume fraction of ∼36% (MNC volume fraction of ∼64%) indicated by the orange curves in Fig. 6.2, the maximum in the Köhler curve corresponds to x_{MNC} ≈1, implying that CCN activation is not limited by MNC solubility. This MNC volume fraction corresponds to

the 1:1 by mass MNC:KS particles, which suggests that for this particular mixture, MNC behaves as if there are no solubility limitations (i.e. infinitely soluble) during CCN activation and κ of MNC can be predicted using Eq. 14. This result is consistent for both the 1:1 by mass LEV:MNC and 1:1:1 by mass LEV:MNC:KS particles. Figure 6.3 shows the predicted κ values including solubility contraints (open circles) and excluding solubility limitations (closed circles) plotted against the measured κ values for all of the particle mixtures applied in this study.

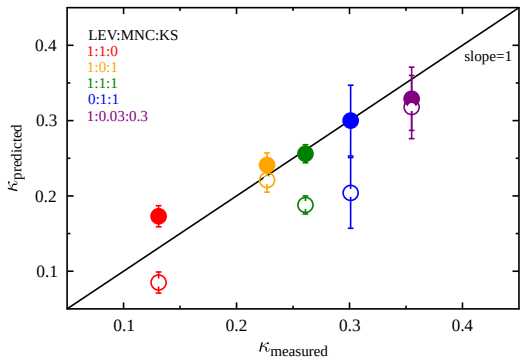

Figure 6.3: Measured κ values for the binary and ternary particle mixtures of LEV, MNC, and KS, shown as a function of predicted κ applying the volume mixing rule including solubility limitations (open circles) and excluding solubility limitations (closed circles). The black line represents a slope of 1 in the measured versus predicted κ. The LEV:MNC:KS mass ratios are indicated in the legend for 1:1:0 (red), 1:0:1 (orange), 1:1:1 (green), 0:1:1 (blue), and 1:0.03:0.3 (purple). See text for more details.

The measured κ for the 1:1 by mass MNC:KS is 0.301 ($\pm$0.047). When including MNC solubility limitations, i.e. applying the experimentally derived κ of pure MNC in the volume mixing rule, the predicted κ of the mixture is significantly less at 0.204 (open blue circles in Fig. 6.3). However, when excluding the effects of solubility, predicted κ=0.300 (closed blue circles in Fig. 6.3), is in excellent agreement with the measured κ. Except for the 1:0.03:0.3 by mass LEV:MNC:KS particles (open purple circles in Fig. 6.3), the predicted κ values applying the volume mixing rule of 1:1 by mass LEV:MNC (open red circles) and 1:1:1 by mass LEV:MNC:KS (open green circles) particles are significantly lower than the experimentally derived κ.

However, when excluding their solubility limitations, the predicted κ values are in much better agreement with the measurements. The volume content of MNC in the 1:0.03:0.3 by mass LEV:MNC:KS particles was too low to impact the measured κ values.

6.3.2 CCN activity of single-component BBA surrogate-particles exposed to OH and O_3

Surrogate single-component BBA particles were oxidized in the presence of O_3 (mixing ratio, χ_{O_3}=0.76-20 ppm) and in the presence of OH radicals (0.2×10^{10}-2×10^{10} molecule cm^{-3}), corresponding to <1 day up to $\sim$ 1 week of a 12-hr daytime OH exposure at [OH] = 2×10^6 molecule cm^{-3} and <1 hr up to 10 hrs of O_3 exposure at a background χ_{O_3}=20 ppb[291]. The hygroscopicity of the particles was determined as a function of OH and O_3 exposure. The results for the single-component organic particles LEV and MNC are shown in Fig. 6.4.

The reactive uptake, condensed-phase reaction products, and volatilized reaction products resulting from heterogeneous OH oxidation of LEV is well-documented[15,95,107,123,244,257]. However, there are no direct measurements of its CCN activity following OH oxidation. Kessler *et al.*[95] showed that following OH exposure, particle volatilization accounts for a $\sim$20% by mass loss of LEV. This suggests that the majority of the reaction products, which include carboxylic and aldehydic species[244,257], remain in the condensed-phase. Although volatilization due to high OH exposures has been linked to an increase in the critical supersaturation and thus suppression in the CCN activity of oxidized squalane particles[30], the results here suggest regardless of volatilization, the condensed-phase reaction products are just as or somewhat more active CCN than pure LEV. On average, there is a slight increase in κ for LEV particles with increasing OH exposure as indicated by the positive slope in the linear fit to the data (κ=$9\times10^{-15}\cdot$[OH]$_{\text{exp}}$+0.17); however, this apparent enhancement in κ is not significant since the average κ values for each OH exposure fall well within the range of measured κ. Such an incremental enhancement in κ may be a result of similar κ between LEV and its oxidation products. The hygroscopicity of several carboxylic acids that may represent OH oxidation products, including malonic, glutaric, glutamic, succinic, and adipic acid exhibit κ values between 0.088-0.248[27], similar to κ of oxidized and pure LEV. Furthermore, the hygroscopicity of organic compounds containing hydroxyl functionalities (like LEV) or carboxylic groups are nearly

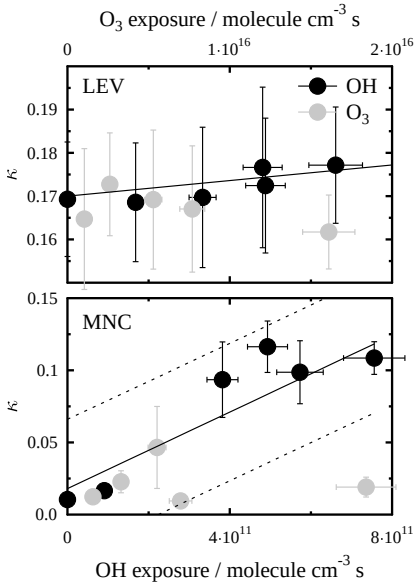

Figure 6.4: Derived κ for LEV and MNC particles are shown as a function of OH and O_3 exposure. The black circles correspond to κ due to chemical aging by OH and the gray circles correspond to κ due to chemical aging by O_3. The vertical error bars represent $\pm 1\sigma$ from the mean of the data acquired at a given OH or O_3 exposure. Horizontal error bars of the κ values correspond to the uncertainty in the OH exposure based on a $\pm 5\%$ drift in RH over the sampling period. Horizontal error bars of the κ for the O_3 exposures correspond to the uncertainty in the O_3 exposure based on a drift in the measured $[O_3]$ of $\pm 10\%$. The solid black lines show the best linear fit to the OH exposure data and the dashed lines in the lower panel show the 95% confidence intervals of the fit.

equivalent[283]. We also cannot rule out that volatilization, while reducing particle mass, also removes newly formed reaction products from the aerosol phase, leaving the parent organic (i.e. LEV), and thus κ unchanged. No significant changes in LEV hygroscopicity were observed following exposure to O_3. This result is not surprising since O_3 is generally unreactive with aliphatic compounds and LEV is alicyclic[13,43]. However, as shown in Fig. 6.4 at higher OH exposures, there is a greater separation in measured κ between purely O_3-oxidized and OH-oxidized LEV particles, indicative of the role of

particle oxidation in enhancing particle hygroscopicity with increasing OH exposure.

O_3 exposure does not have a quantifiable impact on the hygroscopicity of MNC, even so MNC is aromatic and thus susceptible to O_3 addition forming a primary ozonide followed by rapid decomposition to aldehydic species[43]. This may be a result of water adsorption on the surface of MNC at the RH employed, likely inhibiting O_3 uptake by MNC[107,159,211,212]. The CCN activity of MNC aerosol particles increases with OH exposure as shown in the bottom panel of Fig. 6.4. MNC becomes more CCN active with increasing OH exposure and κ transitions from 0.01 in absence of OH to $\sim$0.1 for OH exposures equivalent to a few days in the atmosphere. The data can be represented by a fit to a linear function with the form κ=10^{-13}·$[OH]_{exp}$+0.018. Further exposure ($\geq$4·10^{11} molecules cm^{-3} s) does not significantly enhance κ of MNC, which suggests MNC (or the particle surface[107]) is fully oxidized and that the reaction products reach a maximum in κ. Similar enhancements in κ and subsequent constant κ values with increasing OH exposure have been observed for organic aerosol with initially low hygroscopicity[17,29]. For example, George *et al.*[17] observed that κ of BES increased from $\sim$0.008 to $\sim$0.08 for an OH exposure of $\sim$1.5·10^{12} molecule cm^{-3} s and κ of stearic acid increased from $\sim$0.004 to $\sim$0.04 due to OH exposure of $\sim$7.5·10^{11} molecule cm^{-3} s.

The enhancement in κ of MNC following OH exposure may be linked to the formation of more hydrophilic chemical functionalities. Strongly linked to enhancements in OA hygroscopicity are larger O:C ratios[29,39,181,283,292]. Neglecting the oxygens in the -nitro functionality of MNC[283], the O:C ratio of pure MNC is $\sim$0.29, close to the lower end in O:C where transitions from low κ to high κ typically occurs[283]. The presence of -methyl, unsaturated, and -nitro functionalities are also linked to low hygroscopicity[283]. As proposed in Slade and Knopf[107] and observed for other nitro-phenolic species, OH oxidation of MNC can favor removal of the -nitro functionality by electrophilic substitution of OH[15,237,293]. OH substitution at the -methyl position and addition to the double bonds is also possible[294]. OH addition to the -nitro or -methyl functionality would increase O:C to $\sim$0.43 or $\sim$0.5, respectively. OH substitution at both positions would enhance O:C to $\sim$0.67. Suda *et al.*[283] showed that hydroxyl-dominated OA with an O:C of less than $\sim$0.3 has an apparent κ of $\leq 10^{-3}$. However, an increase in O:C to 0.4 or 0.6 due to the addition of hydroxyl, aldehydic, or carboxylic functionalities results in an enhanced κ of $\sim$0.1. Thus, small changes in O:C can signif-

icantly affect κ. Pure MNC is also sparingly soluble in water and thus κ is strongly dependent on its actual solubility, which can change depending on the oxidation level and the presence of other compounds having different solubility[146]. Consequently, the conversion from low to high κ following OH oxidation is consistent with the addition of more hydrophilic functionalities and a molecular transition from sparingly soluble to sufficiently water-soluble compounds.

6.3.3 CCN activity of binary-component BBA surrogate-particles exposed to OH and O_3

Binary-component particles consisting of LEV:MNC, LEV:KS, and MNC:KS in 1:1 mass ratios were exposed to OH and O_3 and analyzed for their CCN activity as a function of OH and O_3 exposure. The approach here is to determine if the presence of more than one component can influence the CCN activity of another following OH and O_3 oxidation, i.e. are the observed changes in hygroscopicity of the pure component particles following OH oxidation retained when mixed? Figure 6.5 shows κ as a function of OH and O_3 exposure for the different binary aerosol mixtures. The solid and dashed black lines in Fig. 6.5 display the modeled κ as a function of OH exposure using the volume mixing rule including and excluding MNC solubility limitations, respectively, based on the linear fits of κ as a function of OH exposure for pure LEV and MNC particles (Fig. 6.4). Modeled κ as a function of OH exposure excluding MNC solubility limitations (i.e. dashed lines in Fig. 6.5) assumes κ for MNC of the mixed particles is 0.16.

There are two important points to be made of the results from Fig. 6.5. (1) Hygroscopicity of the mixed particles is virtually unchanged as a function of OH exposure, i.e. while OH exposure significantly impacts MNC hygroscopicity alone, it does not significantly influence κ for the binary component particles containing MNC; and (2) κ and the trend in κ with OH exposure is significantly underpredicted assuming MNC solubility limitations are applicable in the volume mixing rule (solid lines in Fig. 6.5). Similar to the single-component particles, exposure to O_3 did not impact κ of the binary component particles. As discussed previously and demonstrated in Fig. 6.2, the presence of either KS or LEV influences the impact MNC solubility has on particle activation. We have shown that MNC exhibits no solubility limitations for the volume fractions applied here. Larger volume fractions of MNC would be expected to have a greater influence on κ following OH ex-

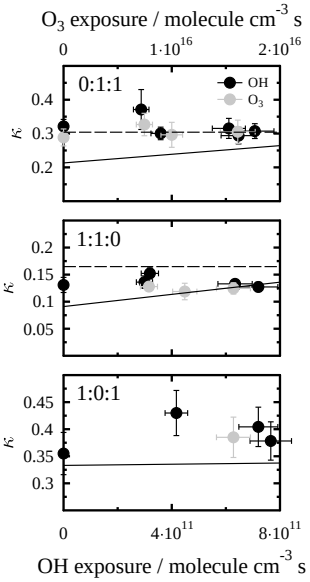

Figure 6.5: Derived κ for the binary component particles of LEV:MNC:KS mass ratios 0:1:1 (top), 1:1:0 (middle), and 1:0:1 (bottom) are shown as a function of OH and O_3 exposure. The black circles correspond to κ due to chemical aging by OH and the gray circles correspond to κ due to chemical aging by O_3. Error bars correspond to error bars given in Fig. 6.4 The solid black lines are modeled κ using the volume mixing rule as a function of OH exposure including MNC solubility limitations and applying the linear fit to the measured κ of pure MNC as a function of OH exposure (Fig. 6.4). The dashed lines are modeled κ using the volume mixing rule as a function of OH exposure excluding MNC solubility limitations.

posure. The organic content of BBA was shown to dominate hygroscopic growth, in particular the water soluble organic content (WSOC), which is largely levoglucosan[281]. Other studies have indicated that sparingly soluble organic compounds have limited importance in CCN activity of atmospheric aerosol[295–298], although they are, besides completely insoluble organic material, the most likely class of compounds susceptible to hygroscopic changes following oxidation due to their low water-solubility. In other words, there is more room for an enhancement in the solute effect of sparingly soluble organic particles compared to more water-soluble particles. Our results show that oxidative aging impacts on the hygroscopicity of pure component particles can be vastly different if the particles are internally mixed with substances having different water-solubilities. Futher highlighting this point as shown in Fig. 6.5, are the similar κ values measured in the absence (O_3 only) and presence of OH at the highest OH exposures for the particles containing MNC.

6.3.4 CCN activity of ternary-component BBA surrogate-particles exposed to OH and O_3

Here we investigate the CCN activity of internally mixed LEV, MNC, and KS particles with 1:1:1 and with an atmospherically relevant mass ratio of 1:0.03:0.3 (LEV:MNC:KS) following exposure to OH and O_3. The results are shown in Fig. 6.6.

Within the uncertainty of the measured κ values for the 1:1:1 and 1:0.03:0.3 ternary component particles, their hygroscopicities are virtually unaffected by exposure to OH, similar to the binary mixtures; however, on average the 1:1:1 particle mixture exhibits a slight enhancement in hygroscopicity. The predicted κ values for the 1:1:1 mixture, which include MNC solubility limitations (black line), significantly underestimates κ, and only after removing these limitations (dashed line) do the predicted values agree with measured κ. This is not surprising, given that the more water-soluble components, LEV and KS are present at equal mass to MNC, and thus MNC behaves as if it is infinitely soluble during CCN activation. At the highest OH exposures, κ in the presence of OH is on average larger than κ of the particles exposed to only O_3, which suggests that OH oxidation may enhance the hygroscopicity of mixed BBA particles containing sparingly soluble material, albeit at large volume fractions. One possible explanation for the slight enhancement in κ with OH exposure, which differs from the binary mixed particles, is the pres-

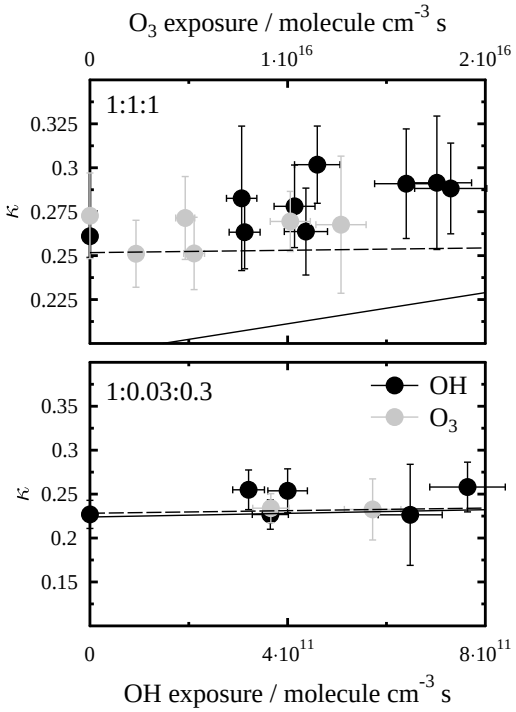

Figure 6.6: Derived κ for the ternary component particles with LEV:MNC:KS mass ratios 1:1:1 (top) and 1:0.03:0.3 (bottom) are shown as a function of OH and O_3 exposure. The black circles correspond to κ due to chemical aging by OH and the gray circles correspond to κ due to chemical aging by O_3. Error bars correspond to error bars given in Fig. 6.4 and dashed lines are the same as in Fig. 6.5.

ence of both MNC and LEV, which both exhibit enhancements in κ following OH oxidation. However, the range in measured κ at a given OH exposure is sufficiently large that within experimental uncertainty, there is no significant trend in κ with OH exposure.

The WSOC, mostly LEV, is known to dominate the volume fraction of BBA[281]. MNC constitutes $\leq$5% by mass of the organic fraction of BBA as shown in both field and lab chamber studies[89,99]. The remaining fraction can be largely composed of inorganic salts, including KS[72,299]. To simulate atmospheric BBA, we atomized a mixed aqueous solution of LEV, MNC, and KS in a mass ratio of 1:0.03:0.3 and measured its CCN activity unexposed and after exposure to OH and O_3. The resulting κ of this mixture as a function of OH and O_3 exposure is displayed in the bottom panel of Fig. 6.6. As anticipated, since pure LEV shows little enhancement in CCN activity with OH exposure (Fig. 6.4) and dominates the volume fraction of this mixture, and KS is unreactive to OH, there were no measured enhancements in κ following OH exposure. A similar observation was made from laboratory-controlled burns, whereby following several hours of photo-oxidation, there were very slight enhancements in κ of the particles[125]. Larger enhancements in κ were observed only for the SOA particles generated from oxidative aging of gas phase volatiles emitted during the controlled burns, in the absence of seed particles[125]. This implies that photo-oxidative aging of BBA contributes little to changes in its hygroscopicity, unless the entire aerosol population is comprised of SOA material (e.g. MNC). Furthermore, both predicted κ including solubility limitations and without solubility limitations are in agreement with the measured values. This is due to the low mass fraction of MNC present, which has sufficiently low impact on both the solubility and level of oxidation of the mixed aerosol particles.

6.3.5 Mixing state effects on κ

Internally mixed organic-inorganic atmospheric aerosol particles can exhibit phase separations, i.e. core-shell structure, which often contains an insoluble or solid inorganic core with a more viscous organic outter layer[300–302]. The presence of an organic coating has been shown to impact CCN activity and water uptake[289,300,303], ice nucleation efficiency[304–306], and heterogeneous chemistry[307–310]. Because MNC originates from gas-phase chemical reactions, and has been measured in BBA particles, MNC must partition from the gas to the particulate phase. In this section, we investigate if the mixing state

of mixed MNC and KS particles has any effect on its CCN activity following OH exposure by the application of atomized MNC:KS binary component particles and MNC-coated KS particles. For example, Abbatt *et al.*[289] observed a complete deactiviation in the CCN activity of ammonium sulfate particles when thickly coated with stearic acid.

The CCN activity of KS particles coated with MNC was measured as a function of the organic volume fraction ($V_{f,org}$) of MNC, and before and after OH exposure as shown in Fig. 6.7A. Figure 6.7A displays a colormap of the dry KS particle size distribution evolution following exposure to MNC, where time=0 min is the point at which KS particle growth occured by MNC condensation. The $50th$ percentile of the number-weighted particle size distribution evolved from D_p=40 nm to D_p=60 nm as indicated by the black line in Fig. 6.7A, corresponding to an enhancement in the MNC $V_{f,org}$ from 0% at time=0 min to ∼70% shortly after, close to the $V_{f,org}$ of the atomized MNC:KS binary component particles of 64%. The similar $V_{f,org}$ between the atomized and coated MNC/KS particles enables a direct intercomparison of the CCN activity, since relatively larger MNC $V_{f,org}$ would bias towards lower κ and vice versa.

The particles' hygroscopicity was analyzed throughout the period of condensational growth as demonstrated in Fig. 6.7B and shown as the black circles. The black line in Fig. 6.7B displays the steps in S over the course of the experiment. The first two κ values are of pure KS particles evaluated at S=0.2%. Subsequent κ values are of MNC-coated KS particles, which increase in $V_{f,org}$ with time. The change in $V_{f,org}$ with time is indicated by the blue circles. $V_{f,org}$ allows to compare measured κ with that predicted using the volume mixing rule. As previously discussed, the solubility limitations of pure MNC can be neglected when predicting κ of the atomized 1:1 mass ratio MNC:KS binary component particles. To determine if the solubility of MNC impacts the MNC-coated KS particles similarly to the atomized mixture, κ is predicted using the volume mixing rule and applying a pure MNC κ of 0.01($\pm$0.004) (i.e. measured pure MNC κ, which includes solubility limitations) as shown by the dotted line in Fig. 6.7B, and compared to predicted κ applying a pure MNC κ of 0.16 (i.e. pure MNC κ in the absence of solubility limitations calculated from Eq. 6) as indicated in the dashed line in Fig. 6.7B. The predicted κ with increasing $V_{f,org}$ generally captures the measured trend in κ with increasing $V_{f,org}$, however, similar to the atomized MNC:KS binary component particles, assuming MNC CCN activity is limited by its solubility, the volume mixing rule underpredicts measured κ.

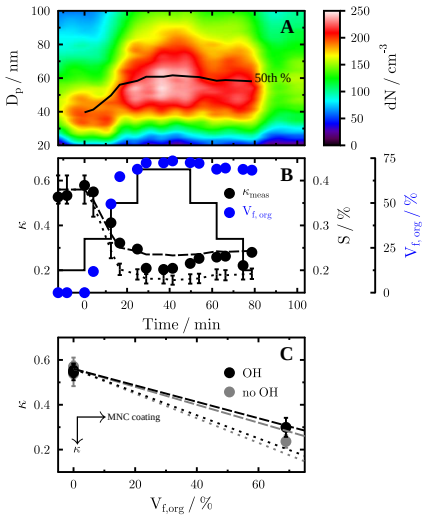

Figure 6.7: OH exposure effects on the CCN activity of MNC-coated KS particles. Panel A shows a color map of the number-weighted particle size disribution (dN) of KS and MNC-coated KS particles plotted as a function of MNC-coating. Panel B shows the change in particle hygroscopicity (black circles) and MNC volume fraction ($V_{f,org}$, blue circles) with time as a function of S given as black solid line. The dotted line shows the predicted κ using the volume mixing rule corresponding to the $V_{f,org}$ at a given time and assuming the CCN activity of MNC is limited by its solubility (i.e. MNC κ=0.01($\pm$0.004)). The dashed line shows the predicted κ using the volume mixing rule corresponding to the $V_{f,org}$ at a given time and assuming the CCN activity of MNC is not limited by its solubility (i.e. MNC κ=0.16 calculated from Eq. 6). Panel C shows the change in κ for the MNC-coated KS particles as a function of $V_{f,org}$ and OH exposure. OH unexposed particles are plotted as gray circles. Particles exposed to OH at 3.3×10^{11} molecule cm^{-3} s are indicated by the black circles. The error bars represent 1σ from the mean in κ. The dotted lines show predicted κ using the volume mixing rule assuming the CCN activity of MNC is limited by its solubility for the unexposed (gray) and OH exposed (black) particles. The dashed lines show predicted κ using the volume mixing rule assuming the CCN activity of MNC is not limited by its solubility for the unexposed (gray) and OH exposed (black) particles.

When applying a pure MNC κ=0.16 in the absence of solubility limitations, the volume mixing rule is in slightly better agreement with the measured κ values. However, there are notable deviations between measured κ and predicted κ in both cases, which depend on S. For example, in Fig. 6.7B, the predicted κ including MNC solubility limitations (dotted line) is in better agreement with the measured κ at S=0.425% than at lower S. At higher S, the particles that activate first are smaller in diameter than the particles that activate first at lower S. Assuming different sized KS particles were exposed to an equal quantity of gas-phase MNC, the larger particles, having relatively larger surface area than the smaller KS particles, would acquire a thinner organic coating, and thus relatively smaller $V_{f,org}$. As a result, the particles that activate at S=0.425% possess a larger $V_{f,org}$ compared to the particles that activate at e.g. S=0.2%. This corresponds to a decrease in measured κ at S=0.425% (i.e. better agreement with predicted κ including MNC solubility limitations) relative to other S as indicated in Fig. 6.7B. While this experimental limitation is a source of uncertainty in the CCN activity analysis of the MNC-coated KS particles, it is included in the reported averaged κ values, since the averaged κ includes κ measured at different S. However, the generally better agreement in the predicted κ excluding MNC solubility limitations with the measured κ indicates that MNC is sufficiently water-soluble not deactivating KS, in contrast to the particle systems studied by Abbatt *et al.*[289].

The effects of OH exposure on the CCN activity of MNC-coated KS particles as a function of $V_{f,org}$ is given in Fig. 6.7C. κ is plotted as a function of MNC $V_{f,org}$. The κ values impacted by an OH exposure of 3.3×10^{11} molecule cm^{-3} s are given by the black circles. Gray circles correspond to κ in the absence of OH. At $V_{f,org}$=0% κ is $\sim$0.55 and independent of OH exposure. κ decreases to $\sim$0.24 at $V_{f,org}$ $\approx$70%, but undergoes a slight enhancement to $\sim$0.3 following exposure to OH. The dotted gray line indicates the modeled change in unexposed κ as a function of $V_{f,org}$ applying the volume mixing rule and assuming MNC κ=0.01 (i.e. including MNC solubility limitations). The modeled κ slightly underpredicts measured κ, which suggests in the presence of KS at this $V_{f,org}$ $\approx$70%, MNC may not be limited by its solubility, similar to the atomized 1:1 mass ratio MNC:KS binary component particles. However, the dashed gray line shows the modeled κ as a function of $V_{f,org}$ applying the volume mixing rule and assuming MNC is not limited by its solubility, i.e. MNC κ=0.16, which slightly over predicts the measured κ. A reasonable explanation for this is that $V_{f,org}$ $\approx$70% is sufficiently large such that MNC

solubility limitations on the CCN activity of MNC-coated KS particles are partially exhibited. The dashed black line in Fig. 6.7C shows the modeled change in κ as a function of $V_{f,org}$ for the OH exposed particles excluding MNC solubility limitations and applying the volume mixing rule assuming κ of MNC has adjusted to the applied OH exposure based on the linear fit to κ of MNC as a function of OH exposure (Fig. 6.4). The modeled κ is in good agreement with the measured κ for the OH exposed particles, which suggests it is reasonable to assume MNC is not significantly limited by its solubility at $V_{f,org}$ $\approx$70% for the MNC-coated KS particles. While OH exposure has a significant impact on the CCN activity of pure MNC, its impact on the CCN activity of MNC-coated KS particles is significantly less, and the higher water-solubility of KS governs hygroscopic growth, similar to the atomized MNC:KS binary component particles.

6.4 Conclusions

To our knowledge, there are no studies that have explicitly investigated the influence of OH-initiated oxidative aging on the hygroscopicity of organic and mixed organic-inorganic BBA particles. Biomass burning can greatly influence cloud formation and microphysical properties by increasing the available CCN in the atmosphere[21]. However, the efficiency at which aerosol particles act as CCN depends on their water solubility, hygroscopicity, and size, which can be altered by multiphase chemical reactions with gas-phase oxidants. While it is recognized that a significant fraction of BBA are comprised of organic material[82], most of which are water-soluble[281,311], water uptake can be sensitive to the inorganic mass fraction[312,313]. In this study we investigated how sensitive the CCN activity of single-component and mixed water-soluble/insoluble compounds associated with BBA are to OH oxidation. The important findings relevant to the atmosphere include (i) the hygroscopicity of water-soluble organic compounds is unaffected by chemical aging, (ii) The hygroscopicity of single-component water-insoluble organic compounds is affected by chemical aging as anticipated from previous studies[16,17,29,112–114], and (iii) if considering mixtures of water-soluble and insoluble materials, the effects of chemical aging by OH are more complicated and single-component derived κ and changes to κ as a function of OH exposure do not translate directly to mixtures.

WSOC constitutes a significant fraction of biomass burning OA[78,82,281,311,314] and atmospheric OA in general[315,316]. Water-soluble OA is an effective CCN

because it enhances the solute term in the Köhler equation. Chemical aging is known to promote the solubility of initially insoluble and sparingly soluble OA by yielding more water-soluble and multifunctional reaction products[16,17,317]. The question of atmospheric relevance depends on the concentration or potency of a particular molecule in the atmosphere. MNC, while contributing little to the mass fraction of BBA particles, is toxic to forests[272] and recognized as an important biomass burning SOA molecular marker[99]. An OH exposure equivalent to only a few days of atmospheric exposure leads to an order of magnitude enhancement in MNC hygroscopicity. This implies that aged MNC is more susceptible to wet depositional losses over atmospherically relevant particle transport timescales, e.g. through cloud formation, compared to fresh MNC. Calculations from Petters *et al.*[16] indicate that substantial wet depositional losses can occur when κ>0.01. The question of the utility of MNC as a molecular marker for source apportionment is raised since molecular markers are assumed to be inert over the course of its lifetime in the atmosphere. Clearly, OH oxidation of MNC influences its chemical composition, but in doing so also decreases its atmospheric lifetime by enhancing its CCN activity. However, our results strongly suggest if the OA is WSOC-dominated, e.g. by LEV, the reaction products likely have similar CCN activity to the parent WSOC, and thus particle oxidation plays a very minor role in enhancing the CCN activity of WSOC. Indeed, very little enhancements to the hygroscopicity of BBA produced from controlled wood burning resulted from several hours of photo-oxidation, likely a result of the high WSOC content of BBA[125].

Much less is known of the effects of chemical aging on the CCN activity of internally mixed water-soluble and insoluble organic-inorganic particles. While oxidative aging can enhance the hygroscopicity of single-component particles with initally low water-solubility, atmospheric aerosol particles are not often pure and consist of both organic and inorganic compounds[318–320]. Organic compounds alone can influence the hygroscopicity of inorganic aerosol particles[321–324] and moderate amounts of water-soluble inorganics can render low-solubility organics infinitely water-soluble[146,288–290]. When mixed with LEV or KS (or both) in significant mass fractions, the effects of OH oxidative aging on the hygroscopicity of single-compnent MNC are not revealed in the measured κ for the binary or ternary-component particles. Furthermore, a thick coating of MNC on KS particles had similar impacts on the CCN activity behavior with increasing OH exposure as the atomized binary-component MNC:KS particles. The water-soluble fraction (i.e. KS) was sufficiently large

that MNC became infinitely soluble. Our results indicate that it is the fraction of the water-soluble component of internally mixed water-soluble and insoluble organic-inorganic particles that dictates whether chemical aging will enhance the particles' CCN activity. Chemical aging has no major impact on the CCN activity of mixed water-soluble and insoluble compounds beyond the point that the insoluble component becomes infinitely soluble. Below this point, chemical aging can influence the CCN activity of the insoluble component.

7 Results: The role of particle phase in the OH oxidative aging and cloud condensation nucleus activity of organic aerosol

7.1 Abstract

Particle phase (solid, semisolid, liquid) is an important physical characteristic of atmospheric aerosol, dictating multiphase organic aerosol (OA) oxidation kinetics. Recent work has demonstrated that particle phase, driven by changes in relative humidity (RH) or temperature, can effect the reactive uptake of OH radicals and O_3 by OA. However, whether particle phase and OH oxidation can influence the oxidation state of OA and its role in larger scale atmospheric processes such as cloud formation is unknown. In this work, the cloud condensation nucleus (CCN) activity of Suwanee River Fulvic Acid (SRFA), a surrogate compound for humic-like substances (HULIS) in biomass burning aerosol (BBA) is determined as a function of OH exposure and temperature. Particle phase is altered by varying the temperature of SRFA above and below its glass transition temperature (T_g). Our results demonstrate that the CCN activity of SRFA is sensitive to changes in particle phase following exposure to OH. At all temperatures, an increase in OH exposure resulted in an increase in the hygroscopicity parameter, κ. However, the most significant enhancements in κ following OH exposure occured when temperatures were below T_g. At higher temperatures, OH oxidation had less impact on SRFA CCN activity. The degree of particle oxidation and change in CCN activity following OH exposure at different temperatures is likely related to changes in bulk diffusivity and volatility. Below T_g, OH uptake may be limited by diffusion of SRFA from the bulk to the particle surface, thus with increasing OH exposure, the SRFA surface is becoming more oxidized and CCN active. Above T_g, the effects of surface oxidation on the particles' CCN activity may be suppressed due to greater diffusion and mixing of unoxidized SRFA transported from the bulk to the surface. In addition, volatilization of SRFA oxidation products may act as a sink for gas-phase OH, reducing OH concentrations and thus oxidation at the surface. The results presented here demonstrate that multiphase oxidation reactions can enhance the CCN activity of OA, a process which is dependent on particle phase and favored at lower temperatures.

7.2 Introduction

Multiphase oxidative aging of atmospheric aerosol is an important, but poorly understood process, influencing aerosol particle lifetime and role in air quality and climate[8,9,12]. Multiphase chemical reactions between atmospheric aerosol particles and trace gases including OH, O_3 and NO_3 can impact aerosol optical properties[124,325], the generation and budget of volatile organic compounds (VOCs) in the atmosphere[15,37,110], and the particle's cloud condensation nucleus (CCN) activity[16,17,28,114,145]. Key processes driving multiphase reactions include, among others, molecular diffusion of the adsorbed gas molecules and condensed-phase material, and reaction.[12,33,111,138,148,150–152,209] Aerosol particles are largely organic[18,51] and exhibit many phase states, i.e. solid, semisolid, and liquid phases, classified by viscosity or molecular diffusivity[105,139]. Temperature and RH-induced changes in particle viscosity can affect the translational motions of condensed-phase molecules and thus potential that adsorbed gases interact with the bulk material. Particle phase is known to affect the onset of ice nucleation[42,105], aqueous-phase chemistry[326,327], gas uptake and thus particle lifetimes[33,35,107,261,262,264,328]. However, a link has not yet been drawn between particle phase, oxidation, and CCN activity.

Unlike inorganic particles that can possess a rigid or crystal-like structure, OA is often characteristic of glassy or semisolid (amorphous) phases[105,139]. The phase state of amorphous aerosol particles is strongly influenced by changes in temperature and RH[33,35,105]. For example, the diffusion of water in amorphous levoglucosan (LEV) particles, a major biomarker for biomass burning aerosol (BBA)[94,329], is enhanced by several orders of magnitude over modest increases in RH (from 0% to 40%).[107,259] Over this RH range, LEV physically transforms from a glass to a less-viscous semisolid and the reactive uptake of OH is enhanced by a factor of three[107]. Previous studies have observed similar RH dependencies for OH uptake by glutaric acid[34], O_3 uptake by an amorphous protein[33], maleic and arachidonic acid[262], and α-pinene secondary organic aerosol (SOA) particles[261]. HO_2 uptake by LEV was also found to depend on RH[194] and thus particle phase. In all cases, gas uptake was enhanced with increasing RH. A decrease in LEV lifetime, which is affected by particle phase[107], due to OH oxidation brings into question its suitability as a tracer compound for BBA source apportionment. Similarly, temperature is expected to influence particle phase; higher temperature promotes diffusion of the bulk organic material and adsorbed gas molecules,

and thus the probability that the molecules react with one another. Arangio *et al.*[35] demonstrated that a rise in temperature from <0°C to 25°C can decrease the lifetime of LEV following reaction with OH from several years to <1 day, respectively, due to a temperature-induced increase in LEV bulk diffusivity and OH diffusion in the bulk. A similar change in LEV lifetime due to differences in particle phase onset by changes in RH was presented in Slade and Knopf[107]. While temperature impacts particle phase and diffusivity, temperature can also affect the particle's vapor pressure, promoting the evaporation of the particle and its reaction products at higher temperature. On the other hand, lower temperatures increase particle viscosity and may limit reactive gas uptake to near the particle surface, as well as lowering the particle's vapor pressure.

Multiphase oxidation of OA can alter the particle's CCN activity due to the formation of surface active organic molecules or oxygenated functional groups that tend to reduce the particle's surface tension or increase the particle's oxidation state, polarity, and thus water-solubility, respectively.[16,17,28,30,114,130] A decrease in the CCN activity of OA following OH oxidation can occur due to a decrease in particle size and mass through volatilization (molecular fragmentation) reaction pathways[30].

HULIS, which include fulvic acids, such as SRFA, represent large molecular weight organics that are commonly found in soil and aquatic environments that become aerosolized during biomass burning and represent a significant fraction of BBA[330–333]. Like other amorphous organic substances, HULIS does not exhibit a clear deliquescence RH, instead hygroscopic growth and thus changes to the particle's phase state is gradual[334–336]. The growth factors of several different HULIS range from 1.05-1.17 at RH=85%[334]. Atmospheric HULIS are CCN active with a hygroscopicity, defined as κ, that ranges from 0.04-0.1[337]. SRFA has a known κ between 0.025 and 0.077[86,182,323], at maximum about half that of other water-soluble organics[27], and exhibits a hygroscopic growth factor of 1.05 at RH=85%[323]. The glass transition temperature of SRFA, T_g, defined as the temperature at which a particle transitions between a liquid/semi-solid state to a solid (glassy) state,[105,139,143] is estimated to be ∼309 K at RH=0%[336]. At higher RH, T_g is lowered (i.e. SRFA is less viscous) due to the plasticizing effect of water[42]. Consequently, SRFA presents a unique and atmospherically relevant class of OA that following changes of its phase and reaction with OH may impact its oxidation state and CCN activity. This work aims to bridge the gap between multiphase oxidation, particle phase, and cloud formation. Here, particle phase

effects on the OH oxidative aging and CCN activity of SRFA is investigated using a temperature-controlled aerosol flow reactor (AFR) coupled to a CCN counter.

7.3 Results and discussion

SRFA particles were exposed to a range of [OH] at different temperatures (286 K $\leq$ T $\leq$ 317 K) and similar residence time, resulting in a wide range of OH exposures, from $\sim 0.7\times10^{11}$ to 7×10^{11} molecule cm^{-3} s, which translates to <1 day up to $\sim$8 days of OH exposure in the atmosphere at [OH]=2×10^{6} molecule cm^{-3}. Figure 7.1 demonstrates the dependence of SRFA T_{g} on RH and the dotted lines show the T_{g} range of all the different measurements accounting for the range of applied RH. The measured κ of OH unexposed

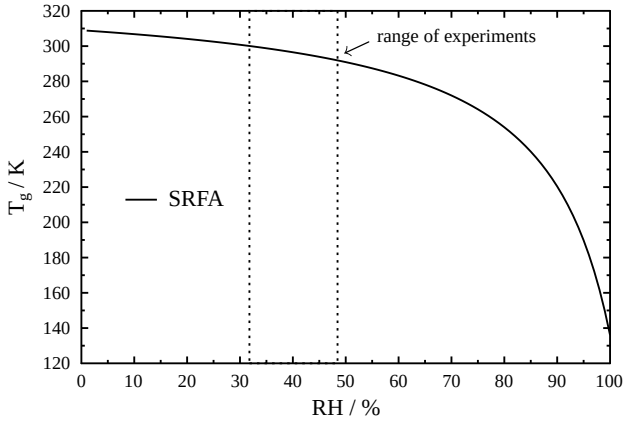

Figure 7.1: Glass transition, T_{g}, as a function of RH for Suwannee River fulvic acid. The dotted lines show the range of T_{g} over the RH ranges applied in this study. This parameterization is discussed in more detail in Wang *et al.*[42]

SRFA is 0.047, in agreement with the range of κ for SRFA reported in previous studies[182]. Furthermore, for the OH unexposed particles, temperature does not siginificantly influence the measured κ values. Figure 7.2 shows κ plotted against OH exposure, where the different colors represent the temperatures at which the particles were exposed to OH in the AFR, as indicated in the legend. For all of the investigated temperatures, κ for SRFA particles

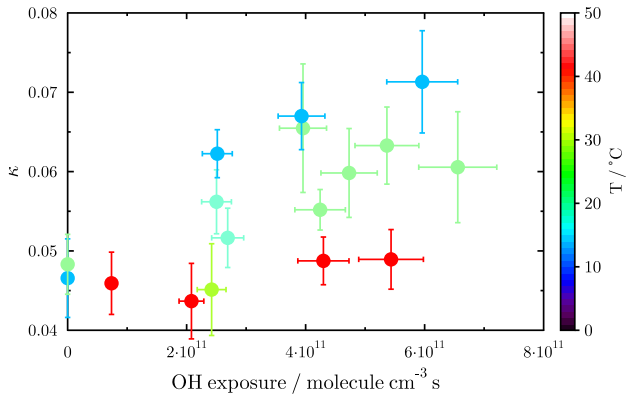

Figure 7.2: The hygroscopicity parameter, κ, is shown as a function of OH exposure at different flow reactor temperatures. The vertical error bars represent 1σ from the mean in κ and the horizontal error bars represent an uncertainty in the OH exposure of $\pm 10\%$ due to a drift in RH of 5% over the course of a measurement as discussed in the main text. Temperatures are shown in the color scale.

is enhanced with increasing OH exposure. The enhancement in κ measured at the lowest temperatures is more pronounced than at higher temperatures. For example, at $\sim 12^o$C, as indicated by the blue circles in Fig. 7.2, κ is enhanced from 0.047 to $\sim$0.07 under no OH exposure to an OH exposure of $\sim 6 \times 10^{11}$ molecules cm^{-3} s, respectively. However, near room temperature, $\sim 20^o$C, indicated by the teal circles in Fig. 7.2, κ is enhanced with increasing OH exposure from $<$0.05 up to $\sim$0.06-0.065. On average, κ undergoes only a very slight enhancement with increasing OH exposure when T$\sim 40^o$C as indicated by the red circles in Fig. 7.2.

Similar enhancements in κ following OH and O_3 oxidation were measured for OA having initially low hygroscopicity and low water-solubility[16,17,112,145]. In a recent study by Slade *et al.*[145], the CCN activity of methyl nitrocatechol (MNC), a surrogate BBA compound serving as a molecular marker for biomass burning secondary organic aerosol[99], was enhanced by an order of magnitude with increasing OH exposure equivalent to a few days of atmospheric OH exposure. Given that MNC is sparingly soluble in water, this enhancement in κ is consistent with an enhancement in its water-solubility, due to the generation of more polar and oxygenated functional groups at

the particle surface. Similarly, the enhancement in κ for SRFA with increasing OH exposure may be attributed to the generation of oxidized and polar functional groups that possess greater CCN activity. Due to limited analytical capabilities, no detailed chemical composition analysis of SRFA or its reaction products were obtained. However, for comparison, it is speculated that OH oxidation of MNC results in electrophilic OH substitution of the -methyl and -nitro functionalities, and OH addition to the aromatic ring, resulting in an increase in the oxygen-to-carbon (O:C) ratio, which strongly influences κ[29,39,114,283]. While the exact molecular weight and composition of SRFA is unknown, fulvic acids, like humic substances, are large molecular weight species comprised of phenols, ketones, and carboxylic acid functionalities. Thus, it is expected that similar reaction pathways following OH oxidation increases the oxidation state and thus CCN activity of SRFA. However, because SRFA is more complex and significantly larger than e.g. MNC, likely several generations of oxidation are needed to completely oxidize SRFA. Hence, even though the SRFA particles were exposed to [OH] over similar magnitudes to that of MNC in Slade *et al.*[145], the enhancment in κ is relatively smaller. Previous works have demonstrated that further exposure of the particles to OH does not necessarily enhance κ[17,29,145], implying that the particles are completely oxidized. The κ values plotted in Fig. 7.2 continue to increase with OH exposure, thus further enhancements in κ are expected at even greater OH exposures.

An alternative representation of the data from Fig. 7.2 is plotted in Fig. 7.3, which shows κ as a function of temperature in the AFR, where the different shades in the data points indicate the level of OH exposure. Here, the effects of varying temperature on the extent of OH oxidation and CCN activity of SRFA at similar OH exposures is clearly recognized. At all levels of OH exposure, κ decreases with increasing temperature in the AFR. The pink shaded region in Fig. 7.3 shows the range in SRFA T_g accounting for the effects of RH in the flow reactor. At 0% RH, SRFA T_g=309 K[336]; however, increasing RH lowers T_g due to the plasticizing effects of water[42]. Based on the experimental range in RH=32%-45%, SRFA T_g is reduced from 309 K at RH=0% to 300 K at 32% and 296 K at RH=45%. However, the experiments were carried out at temperatures well below and above the range in T_g. Below T_g, the measured κ values at all OH exposures are significantly greater than the measured κ above T_g, demonstrating that the effects of OH oxidation on the CCN activity of SRFA particles are more pronounced when the particles acquire a solid (glassy) phase state compared to a less viscous

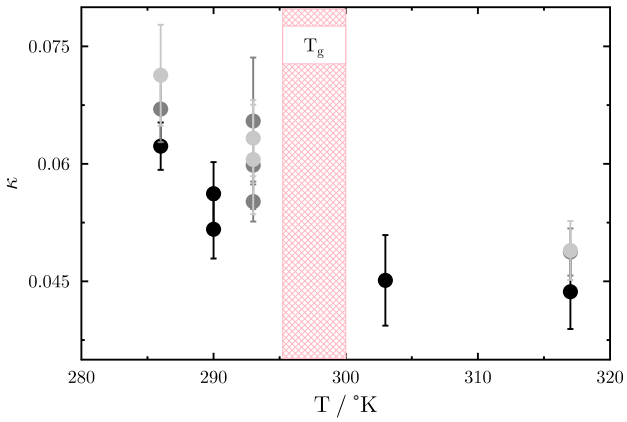

Figure 7.3: The hygroscopicity parameter, κ, is shown as a function of flow reactor temperature for different OH exposures. Shaded circles correspond to different OH exposures: $\sim 2.5\times10^{11}$ molecule cm^{-3} s (black symbols), $\sim 5\times10^{11}$ molecule cm^{-3} s (dark gray symbols), and $\sim 6\times10^{11}$ molecule cm^{-3} s (light gray symbols). The vertical error bars represent 1σ from the mean in κ. The pink shaded region shows the range in glass transition temperature, T_{g}, for the experiments accounting for the influence of RH.

semisolid/liquid phase state.

Only a few studies have demonstrated the influence of OA particle phase on gas uptake of trace gas-phase oxidants[14,33,35,107,244]. All conclude that an increase in RH or temperature can increase oxidant and organic molecular diffusion in the bulk, resulting in greater gas uptake. The results here indicate that OA at lower temperatures and thus higher viscosity are more CCN active following OH oxidation. There are two possible mechanisms to explain this: (i) The changes in particle viscosity with temperature affects the level of surface oxidation, i.e. the surface of SRFA is more oxidized in a highly viscous solid (glassy) phase state compared to a less-viscous semisolid phase state, since unoxidized LEV from the particle bulk cannot significantly diffuse and mix with oxidized LEV near the particle surface. (ii) Changes in SRFA volatility and the volatility of the reaction products with temperature affects [OH] near the particle surface and thus particle oxidation and CCN activity.

The greater bulk diffusivity at higher temperature promotes the movement of bulk unoxidized SRFA to the surface, further lowering the CCN activity of OH exposed SRFA. Below T_{g}, it is expected that the surface of

SRFA is also oxidized to a greater extent due to a decrease in the transport of OH radicals from the surface to the particle bulk. Recent work has shown that NO_3 uptake and reaction with BBA-type compounds, including LEV, are limited to the surface, but bulk uptake and reaction becomes more important following water uptake and liquefaction at higher RH[14]. A very recent study by Arangio *et al.*[35] demonstrated the OH reactive uptake by LEV is limited by surface-bulk exchange. However, upon increasing temperature LEV becomes less viscous, allowing OH to more easily diffuse into and react with LEV, thus resulting in greater LEV degradation[35]. In addition, as LEV rapidly depletes at the surface due to reaction with OH, the generation of volatile reaction products[15,95] may provide an additional gas-phase OH sink. This implies gas uptake and thus level of particle oxidation depends strongly on the interplay of particle phase and chemical reaction. Similar to LEV, SRFA oxidation at lower temperatures may be limited by the transport of SRFA from the particle bulk to the surface. In addition, assuming the reactions between OH and SRFA can lead to volatilization, and volatility increases with temperature, the oxidized material, which is likely responsible for the enhanced CCN activity at temperatures below T_g, may be removed due to evaporation at higher temperatures, a process that may also decrease near-surface gas-phase [OH], and thus the level of particle oxidation. A very rough estimation of the effects of temperature on the volatility and subsequent oxidation of SRFA based on a single experiment, whereby SRFA particle mass was measured at 318 K and directly after at 288 K, indicates that the difference in total particle mass between the two different temperatures is ∼26%, implying that 26% of the particle mass measured at 288 K, which includes oxidized and unoxidized SRFA, may have evaporated to the gas-phase at 318 K. This additional mass of material in the gas-phase may significantly reduce gas-phase [OH], and thus the fraction of oxidized SRFA. However, more controlled experiments and the application of a detailed model of gas uptake that accounts for the mass transport of volatilized reaction products are needed to verify this.

7.4 Atmospheric Implication

The CCN activity of aerosol particles depends on the droplet surface tension, the particle's water-solubility, and particle size during activation[27]. Chemical aging can enhance CCN activity by generating surface-active organic compounds that lower droplet surface tension or by producing more water-soluble

compounds. OH oxidation reactions that lead to particle volatilization can reduce CCN activity by reducing particle size[30]. Alternatively, oxidation followed by oligomerization can increase particle size and enhance CCN activity[338–340]. In this study, κ is enhanced by a maximum of about a factor of 3 following OH oxidation at temperatures below the particle's T_g. Above T_g, there is less enhancement in SRFA CCN activity. This implies that aged HULIS in BBA can promote the particle's CCN activity, a process which is favored at lower temperatures. This is important to the atmosphere since the majority of atmospheric temperatures are well below the T_g of SRFA, particularly at and above cloud level. In general, at all levels of the atmosphere, temperatures can be below the T_g of SRFA. Furthermore, BBA has been found in the upper troposphere (UT)-lower stratosphere (LS)[126,127], where temperatures never reach above the T_g of SRFA, thus BBA in the UT-LS may more efficiently oxidize and become more CCN active than BBA near Earth's surface, where temperatures are generally higher. Assuming a typical particle transport time in the atmosphere of up to two weeks and a 12 hr daytime atmospheric [OH]$\sim 2\times10^6$ molecule cm^{-3}, atmospheric OH exposures can be $\sim 10^{12}$ molecule cm^{-3} s, implying that κ and thus cloud formation potential can be enhanced by more than a factor of three. The importance of phase in governing the extent that other amorphous particles are oxidized and act as CCN has not been evaluated; however, a large fraction of atmospheric organic aerosol is considered amorphous[33,105,133,139]. Amorphous phase states influence gas-to-particle partitioning, gas uptake, and ice nucleation, which is sensitive to changes in temperature and RH[33,42,105–107,133]. The results presented here suggests chemical aging of amorphous particles and particle phase can have significant implications in the particle's ability to form clouds.

7.5 Conclusion

In this study, the CCN activity of SRFA, a representative HULIS found in BBA particles, was investigated as a function of OH exposure and temperature. At temperatures below the T_g of SRFA, OH oxidative aging leads to more enhanced CCN activity. At temperatures above T_g, OH oxidative aging played no significant role in the CCN activity of SRFA. We conclude that the the CCN activity dependence on particle phase and oxidation may be due to temperature-induced changes in the particle's viscosity and volatility. At temperatures below T_g, SRFA acquires a more viscous phase state

and lower vapor pressure, and reaction is likely limited to the surface. In contrast, at temperatures above T_g, SRFA is less viscous and has a higher vapor pressure. This can reduce the oxidation state of SRFA and its CCN activity in two ways: (i) The lower particle viscosity promotes the movement of unoxidized SRFA from the bulk to the particle surface, which dampens the effects of OH oxidation on the CCN activity of SRFA. (ii) while more tests are needeed to verify, higher vapor pressure implies that the oxygenated reaction products that likely enhance the CCN activity of SRFA are short-lived on the surface and evaporate. This may reduce the OH concentration near the particle surface by providing an additional gas-phase OH sink, thus reducing particle oxidation.

SRFA represents only one class of amorphous organic material. The impacts of particle phase on the extent of OH oxidation and CCN activity as demonstrated here likely plays an important role in the chemical aging and CCN activity of other amorphous organic aerosol. Clearly, more studies corroborating this work are needed in addition to a detailed model of gas uptake[14,35,161,211,212], which can account for mass transport and volatilization in order to obtain a better understanding of the underlying physical and chemical processes governing the results discussed here and their implications to the atmosphere.

8 Conclusions and Outlook

The main focus of the research presented in this thesis is on the investigation of the chemical aging process of BBA by OH. In particular, the determination of the OH reactive uptake kinetics, and the impact of multiphase OH oxidation on the formation of volatilized reaction products and CCN activity. OH uptake was assessed as a function of RH and oxidant concentration and the particles' CCN activity was determined as a function of both temperature and OH exposure. Reactive uptake experiments were carried out using CIMS coupled to various types of flow reactors. OH reactive uptake coefficients were determined for several BBA surrogate-substrates as a function of OH concentration. Volatilized reaction products and their magnitudes were measured using HR-PTR-ToF-MS. The application of KM-GAP provided a detailed analysis of the physical and chemical processes governing OH uptake by BBA substrates, the temporal evolution of OH uptake, and its dependence on OH concentration. An RH and temperature-controlled AFR coupled to CIMS was used to evaluate how variations in particle phase influence the rate of OH uptake by BBA surrogate-particles. The CCN activity of single and mixed-component organic and inorganic BBA surrogate-particles was investigated before and after exposure to OH using an AFR coupled to a CCNc. Furthermore, temperature-dependent measurements of the CCN activity of SRFA particles as a function of OH exposure provided the first insight of the link between OA particle phase and CCN activity following OH oxidation. The main conclusions are summarized below.

8.1 Conclusions

OH reactive uptake as a function of OH concentration and volatilization products

This study investigated the effects of varying OH concentration on the reactive uptake of OH by BBA surrogate-substrates and the resulting volatilized reaction products. OH uptake coefficients, γ, were derived by coated-wall flow reactor-based kinetics, whereby OH loss was measured by CIMS as a function of exposed substrate surface area over a wide range of OH concentrations. This approach not only allowed for an examination of the effects of OH concentration on measured γ, but also provided insight of the governing OH uptake mechanisms. γ ranged from 0.056-1 for all applied BBA surrogate-

substrates. However, γ decreases significantly when [OH] is adjusted above [OH]$\sim 10^9$ molecule cm^{-3}. This decrease in γ with increasing [OH] was fit to a Langmuir-Hinshelwood uptake model, which assumes OH first adsorbs to the substrate then undergoes reaction. The initial adsorption step prior to reaction implies the number of available surface reactive sites decreases with increasing [OH]. The degree of OH saturation and competition for surface reactive sites also increases with increasing [OH], thus reducing the number of OH molecules reacted away relative to the number of OH collisions with the surface. The derived physicochemical parameters, which include the surface reaction rate constant, k_s, and adsorption/desorption equilibrium constant of OH, K_{OH}, enabled an estimation of OH surface coverage, θ, which could be determined as a function of gas-phase OH concentrations. Over atmospherically relevant OH concentration ranges, OH surface coverage is minimal (<10%) and reactive uptake is fast. With increasing OH concentration up to $\sim 10^{11}$ molecule cm^{-3}, the entire surface can become saturated with OH, which slows the loss rate of OH at the substrate surface.

Follow-up work, which aimed to develop a more thorough understanding of the physical and chemical processes governing the reactive uptake of OH by levoglucosan and abietic acid substrates, determined that OH uptake is limited by bulk-to-surface exchange. In this work, the kinetic multi-layer model of gas-particle interaction in aerosols and clouds (KM-GAP) was applied to the [OH]-dependent kinetic study and to measurements of γ as a function of OH exposure to the reactive surface. The decrease in γ with increasing [OH] is related to diffusion limitations of the condensed-phase organic penetrating the bulk surface. At lower, more atmospherically relevant [OH], OH uptake is limited by surface reaction with the organic species.

Several volatilized reaction products were detected following OH oxidation of levoglucosan, abietic acid, and nitroguaiacol. Their relative enhancements over the background indicate that BBA volatilization may attribute to the atmospheric budget of VOCs. Product analysis enabled an examination of possible volatilization reaction pathways. These findings indicate that the lifetimes of levoglucosan, abietic acid, and nitroguaiacol, and likely other organic molecular markers, can be reduced following oxidation by OH. Furthermore, lifetime estimates and reaction product yields can depend on the applied γ, and thus [OH].

The effect of particle phase on the reactive uptake of OH by BBA surrogate-particles

This study investigated the effect of changes in organic particle phase in response to varying ambient RH on the OH reactive uptake by laboratory-generated LEV and MNC particles, representing key molecular markers of BBA. OH reactive uptakes were evaluated over a range of RH from 0%-40% employing an aerosol flow reactor coupled to CIMS. γ of $\sim$0.2 was measured for both LEV and MNC under dry conditions (i.e. RH=0%), in agreement with previously measured γ applying LEV and nitroguaiacol (which is a MNC isomer) substrates. However, an increase in RH from 0%-40% resulted in a factor of 3 increase in γ yielding 0.65 for LEV. This enhancement in γ with increasing RH was attributed to an increase in the bulk diffusivity of OH and LEV since LEV is known to undergo a moisture-induced phase transformation from a glassy/solid state to a semisolid/liquid phase state over this change in RH. In contrast, OH reactive uptake by MNC decreases significantly to γ=0.06 as RH increases from 0% to 17%. This decrease in γ with increasing RH was modeled applying a Langmuir-Hinshelwood type function that accounts for the competitive adsorption of both OH and water vapor. This concept indicates that adsorbed water vapor may decrease OH permeability to the surface of MNC. This work demonstrated that the interplay of atmospheric water vapor and reactive trace gas species can dictate the lifetime of LEV and MNC. At RH=40%, the e-folding lifetime of LEV decreases to less than a week. With increasing RH, near 100%, which is relevant to cloud conditions, LEV is short-lived with a lifetime less than a day due to reaction with OH. The results emphasize that changes to particle phase state can significantly alter the chemical aging process and lifetime of OA and thus may affect its role in air quality and climate

OH oxidative aging impacts on the CCN activities of single and mixed-component BBA surrogate-particles

Previous studies have demonstrated that initially unoxidized single-component organic aerosol particles can undergo a hydrophobic-to-hydrophilic transition following oxidation by OH or O_3. In this work, we investigate if OH oxidative aging of single-component BBA-surrogate particles can impact the particles' CCN activity and whether its effect is retained when the particles are mixed with organic and inorganic components. The particles' CCN activity is measured applying a CCNc and the particles are exposed to OH in a custom-built AFR. OH oxidation leads to an order of magnitude

enhancement in κ of MNC particles, which suggests chemically-aged MNC is more susceptible to wet depositional losses than fresh MNC. However, when MNC is mixed with either LEV or KS, the greater water-solubility of both LEV and KS overshadow the chemical aging effects of MNC, and thus chemical aging does not necessarily play a significant role in the CCN activity of mixed water-soluble and low-soluble components. A similar result was obtained for the MNC-coated KS particles, which suggests the mixing state of BBA may not significantly influence the particles' CCN activity following OH oxidation. The results emphasize that the CCN activity of mixed-component particles depends strongly on the water-soluble fraction. When OA is dominated by WSOC or inorganic ions, chemical aging has no significant impact on OA hygroscopicity.

Particle phase impacts on the extent of OH oxidative aging and CCN activity of BBA surrogate-particles

Based on our earlier understanding that particle phase can influence the reactive uptake of OH by amorphous OA, we employed SRFA as a representative HULIS material of BBA and measure its CCN activity following OH exposure at different temperatures in the flow reactor. Here, SRFA particles were subjected to a range of OH exposures (0-6$\times10^{11}$ molecule cm^{-3} s) and the particles' CCN activity was evaluated at several temperatures ranging from 286 K to 317 K. At temperatures below the glass transition temperature of SRFA, i.e. SRFA is in a solid (glassy) phase state, OH exposure can significantly enhance the CCN activity of SRFA particles, increasing κ from $\sim$0.04 to $\sim$0.08. Conversely, when the temperature is above the glass transition temperature of SRFA, i.e. SRFA is in a less-viscous, semisolid state, OH exposure does not significantly enhance the CCN activity of SRFA particles. The results are consistent with both temperature-induced particle volatility effects and temperature-induced phase changes. On one hand, temperature will impact the vapor pressure of both SRFA particles and the products that form due to reaction with OH. At higher temperatures, the organics evaporate to a greater extent and thus act as an additional gas phase OH sink, which reduces the amount of OH that is taken up by SRFA particles. On the other hand, a phase transition from a solid (glassy) state to semisolid phase state with increasing temperature enhances the diffusivity of both OH and SRFA particles, suggesting that the relatively constant κ with increasing OH exposure measured at high temperatures may result from enhanced bulk-

to-surface diffusion of unoxidized SRFA. Thus, greater mixing of unoxidized and oxidized SRFA at higher temperatures may suppress the enhancement in CCN activity that is normally observed when the particles are oxidized by OH at lower temperatures. This work demonstrates for the first time that the chemical aging effects on cloud formation may be strongly linked to particle phase.

8.2 Outlook

A link between BBA particle phase, OH concentration, particle reactivity, reaction products, and CCN activity has been presented in this thesis. Despite the novel results presented here, significant work is still needed to provide a more complete understanding of the underlying mechanisms driving the chemical aging of OA and its impact on important atmospheric processes such as cloud formation. The results presented here raise a number of outstanding questions and points as detailed below that should be addressed in future research.

- *What role does particle phase play in the extent of particle oxidation and volatilization?* We demonstrate that particle phase can influence the reactivity of organic particles with OH; however, it is not clear if phase can significantly influence the oxidation state of OA, a key characteristic to better understanding its role in cloud formation. For example, while gas uptake can be enhanced following reaction with less-viscous OA, gas uptake by highly viscous OA can lead to more efficient oxidation of the particle surface[35]. The cloud formation potential of OA depends on the particle's hygroscopicity, which can depend strongly on the particle's oxidation state[283]. Less is known if phase can influence particle volatilization following reaction with OH. Renbaum and Smith[328] demonstrated that Cl radical oxidation of solid brassidic acid particles generated more multiply-oxidized and lower molecular weight species (compounds that are normally volatilized) in the condensed phase than in liquid brassidic acid particles. This suggests that slower diffusion of the oxidation products in solid particles confines them to the surface or near surface where they continue to react with Cl, producing more highly oxygenated compounds that degrade rapidly. Other works have demonstrated that a higher degree of particle oxidation leads to more efficient volatilization[208,341].

- *What is the role of volatilization on new particle formation?* Volatilized reaction products contribute to the overall VOC burden in polluted environments[37]. However, it is not known if volatilization and the recondensation of volatilized organic material produced from the same particle source can contribute significantly to SOA formation. An interesting future study may focus on the role OH-initiated oxidation and volatilization of OA plays in the formation and growth of new and pre-existing particles, respectively. Such experiments remain challenging in order to segragate the two phases, particularly for mixed organic particle systems that are reactive to OH; however, an initial experiment may make use of unreactive poly-styrene latex (PSL) beads of a known size that when oxidized in the presence of organic aerosol of a different size, an increase in PSL size would indicate that volatilization can lead to particle growth.

- *What other areas of research can benefit from kinetic flux models like KM-GAP?* Multiphase kinetic modeling of experimental gas uptake measurements will facilitate a more complete understanding of the processes that govern gas uptake and chemical aging. Models such as KM-GAP have proven to be useful in this regard as it allows for determining e.g. limiting cases for gas uptake. In addition, KM-GAP can be implemented to better understand the chemical and physical processes and timescales of cloud formation. Utilizing KM-GAP to describe the effects of competitive gas uptake of multiple species on the uptake kinetics and incorporation into particle-resolved transport models[211,212] would help better constrain the role chemical aging plays in air quality, source apportionment, and climate.

- *How does temperature affect gas uptake kinetics?* The temperature profile of Earth's atmosphere varies widely, however the majority of it is well below room temperature, where gas uptake experiments are typically carried out. Lower temperatures are known to slow gas-phase reaction kinetics and increase particle viscosity. However, there are very few studies that have measured gas uptake at lower temperatures. Thus, a complete treatment of the effects of temperature on particle phase and reaction kinetics is important to assess its importance in the atmosphere.

- *What effect does the formation of reactive intermediates have on gas uptake?* OH reactive uptake was shown to be limited by OH concentration and in one case hindered in the presence of water vapor. However, we lack a detailed understanding of the surface chemistry of the substrates and particles. It is likely that other components, e.g. H_2O_2 and reactive intermediates, such as oxidized organics, can impact OH uptake. For example, the formation of reactive oxygen intermediates (ROIs) was shown to slow O_3 uptake by OA due to competitive surface reaction[342]. Thus, better knowledge of the particles' surface properties is needed to obtain a more complete understanding of gas uptake and mass transport.

- *How does multiphase oxidation influence the CCN activity of mixed water-soluble and insoluble compounds of different mixing state in atmospheric aerosol?* Future studies investigating the CCN activity of aged aerosol particles should also consider the impacts of aging when the particles are mixed with different components possessing a range in water-solubility. We demonstrate that chemical aging does not affect the CCN activity of mixed sparingly water-soluble and completely water-soluble material. However, it is not known if chemical aging of mixed insoluble and water-soluble components or its mixing state can impact the particles' CCN activity. For example, Abbatt *et al.*[289] demonstrated that the CCN activity of ammonium sulfate is completely deactivated when thickly coated with succinic acid. Whether multiphase OH oxidation can enhance the CCN activity of succinic acid and thus permit activation of succinic acid-coated ammonium sulfate particles is unknown. BBA can consist of mixed insoluble soot encased in a less-viscous organic coating[72]. The role that soot plays in the multiphase OH oxidation kinetics and CCN activation of BBA is unknown. Future work should focus on the impacts of chemical aging on similar particle systems comprised of mixed insoluble and water-soluble species.

- *What experimental improvements could be made to develop a more comprehensive picture of OA chemical aging?* The results presented in this study were obtained using custom-built instrumentation and applying novel experimental designs. We demonstrate, for the first time, that CIMS can be applied to measure OH reactive uptake by laboratory-

generated aerosol particles at low pressure. In addition, HR-PTR-ToF-MS enabled a detailed analysis of the gas-phase VOC composition. However, without analysis of the condensed-phase composition during uptake, only a part of the story is uncovered. If used in parallel with techniques such as aerosol mass spectrometry, a comprehensive data set of in-situ OH, VOCs, and particle composition could be obtained, which would permit a better understanding of the chemical aging process and its impact on gas and condensed-phase composition.

References

[1] R. J. Charlson, S. E. Schwartz, J. M. Hales, R. D. Cess, J. A. Coakley, J. E. Hansen and D. J. Hofmann, *Science*, 1992, **255**, 423–430.

[2] M. O. Andreae and P. J. Crutzen, *Science*, 1997, **276**, 1052–1058.

[3] V. Ramanathan, P. J. Crutzen, J. T. Kiehl and D. Rosenfeld, *Science*, 2001, **294**, 2119–2124.

[4] S. Twomey, *Atmos. Environ.*, 1974, **8**, 1251–1256.

[5] P. Forster, V. Ramaswamy, P. Artaxo, T. Berntsen, R. Betts, D. W. Fahey, J. Haywood, J. Lean, D. C. Lowe, G. Myhre, J. Nganga, R. Prinn, G. Raga, M. Schulz and R. Van Dorland, in *Climate Change 2007: The Physical Science Basis. Contribution of Working Group I to the Fourth Assessment Report of the Intergovernmental Panel on Climate Change*, Cambridge University Press, Cambridge, United Kingdom and New York, NY, USA, 2007, ch. 2. Changes in Atmospheric Constituents and in Radiative Forcing, pp. 131–234.

[6] T. F. Stocker, D. Qin, G. K. Plattner, M. Tignor, S. K. Allen, J. Boschung, A. Nauels, Y. Xia, V. Bex and P. M. Midgley, *Climate Change 2013: The Physical Science Basis. Contribution of Working Group I to the Fifth Assessment Report of the Intergovernmental Panel on Climate Change*, Cambridge University Press, 2013.

[7] Y. Rudich, *Chem. Rev.*, 2003, **103**, 5097–5124.

[8] Y. Rudich, N. M. Donahue and T. F. Mentel, *Annu. Rev. Phys. Chem.*, 2007, **58**, 321–352.

[9] U. Pöschl, *Atmos. Res.*, 2011, **101**, 562–573.

[10] M. Kanakidou, J. H. Seinfeld, S. N. Pandis, I. Barnes, F. J. Dentener, M. C. Facchini, R. Van Dingenen, B. Ervens, A. Nenes, C. J. Nielsen, E. Swietlicki, J. P. Putaud, Y. Balkanski, S. Fuzzi, J. Horth, G. K. Moortgat, R. Winterhalter, C. E. L. Myhre, K. Tsigaridis, E. Vignati, E. G. Stephanou and J. Wilson, *Atmos. Chem. Phys.*, 2005, **5**, 1053–1123.

[11] J. L. Jimenez, M. R. Canagaratna, N. M. Donahue, A. S. H. Prévôt, Q. Zhang, J. H. Kroll, P. F. DeCarlo, J. D. Allan, H. Coe, N. L. Ng, A. C. Aiken, K. S. Docherty, I. M. Ulbrich, A. P. Grieshop, A. L. Robinson, J. Duplissy, J. D. Smith, K. R. Wilson, V. A. Lanz, C. Hueglin, Y. L. Sun, J. Tian, A. Laaksonen, T. Raatikainen, J. Rautiainen, P. Vaattovaara, M. Ehn, M. Kulmala, J. M. Tomlinson, D. r. Collins, M. J. Cubison, E. J. Dunlea, J. A. Hufman, T. B. Onasch, M. R. Alfarra, P. I. Williams, K. Bower, Y. Kondo, J. Schneider, F. Drewnick, S. Borrmann, S. Weimer, K. Demerjian, D. Salcedo, L. Cottrell, R. Griffin, A. Takami, T. Miyoshi, S. Hatakeyama, A. Shimono, J. Y. Sun, Y. M. Zhang, K. Dzepina, J. R. Kimmel, D. Sueper, J. T. Jayne, S. C. Herndon, A. M. Trimborn, L. R. Williams, E. C. Wood, A. M. Middlebrook, C. E. Kolb, U. Baltensperger and D. R. Wornsop, *Science*, 2009, **326**, 1525–1529.

[12] I. J. George and J. P. D. Abbatt, *Nat. Chem.*, 2010, **2**, 713–722.

[13] D. Knopf, S. Forrester and J. Slade, *Phys. Chem. Chem. Phys.*, 2011, **13**, 21050–21062.

[14] M. Shiraiwa, U. Pöschl and D. A. Knopf, *Environ. Sci. Technol.*, 2012, **46**, 6630–6636.

[15] J. H. Slade and D. A. Knopf, *Phys. Chem. Chem. Phys.*, 2013, **15**, 5898–5915.

[16] M. D. Petters, A. J. Prenni, S. M. Kreidenweis, P. J. DeMott, A. Matsunaga, Y. B. Lim and P. J. Ziemann, *Geophys. Res. Lett.*, 2006, **33**, 1107–1118.

[17] I. J. George, R. Y.-W. Chang, V. Danov, A. Vlasenko and J. P. D. Abbatt, *Atmos. Environ.*, 2009, **43**, 5038–5045.

[18] Q. Zhang, J. L. Jimenez, M. R. Canagaratna, J. D. Allan, H. Coe, I. Ulbrich, M. R. Alfarra, A. Takami, A. M. Middlebrook, Y. L. Sun, K. Dzepina, E. Dunlea, K. Docherty, P. F. DeCarlo, D. Salcedo, T. Onasch, J. T. Jayne, T. Miyoshi, A. Shimono, S. Hatakeyama, N. Takegawa, Y. Kondo, J. Schneider, F. Drewnick, S. Borrmann, S. Weimer, K. Demerjian, P. Williams, K. Bower, R. Bahreini, L. Cottrell, R. J. Griffin, J. Rautiainen, J. Y. Sun, Y. M. Zhang and D. R. Worsnop, *Geophys. Res. Lett.*, 2007, **34**, L13801.

[19] C. L. Heald, H. Coe, J. L. Jimenez, R. J. Weber, R. Bahreini, A. M. Middlebrook, L. M. Russell, M. Jolleys, T.-M. Fu, J. D. Allan, K. N. Bower, G. Capes, J. Crosier, W. T. Morgan, N. H. Robinson, P. I. Williams, M. J. Cubison, P. F. DeCarlo and E. J. Dunlea, *Atmos. Chem. Phys.*, 2011, **11**, 12673–12696.

[20] T. C. Bond, D. G. Streets, K. F. Yarber, S. M. Nelson, J.-H. Woo and Z. Klimont, *J. Geophys. Res.*, 2004, **109**, D14203.

[21] M. O. Andreae, D. Rosenfeld, P. Artaxo, A. A. Costa, G. P. Frank, K. M. Longo and M. A. F. Silva-Dias, *Science*, 2004, **303**, 1337–1342.

[22] C. N. Cruz and S. N. Pandis, *Atmos. Environ.*, 1997, **31**, 2205–2214.

[23] D. A. Hegg, S. Gao, W. Hoppel, G. Frick, P. Caffrey, W. R. Leaitch, N. Shantz, J. Ambrusko and T. Albrechcinski, *Atmos. Res.*, 2001, **58**, 155–166.

[24] U. Dusek, G. P. Frank, L. Hildebrandt, J. Curtius, J. Schneider, S. Walter, D. Chand, F. Drewnick, S. Hings, D. Jung, S. Borrmann and M. O. Andreae, *Science*, 2006, **312**, 1375–1378.

[25] S. M. Kreidenweis, L. A. Remer, R. Bruintjes and O. Dubovik, *J. Geophys. Res.*, 2001, **106**, 4831–4844.

[26] J. Duplissy, P. F. DeCarlo, J. Dommen, M. R. Alfarra, A. Metzger, I. Barmpadimos, A. S. H. Prévôt, E. Weingartner, T. Tritscher, M. Gysel, A. C. Aiken, J. L. Jimenez, M. R. Canagaratna, D. R. Worsnop, D. R. Collins, J. Tomlinson and U. Baltensperger, *Atmos. Chem. Phys.*, 2011, **11**, 1155–1165.

[27] M. D. Petters and S. M. Kreidenweis, *Atmos. Chem. Phys.*, 2007, **7**, 1961–1971.

[28] A. T. Lambe, A. T. Ahern, L. R. Williams, J. G. Slowik, J. P. S. Wong, J. P. D. Abbatt, W. H. Brune, N. L. Ng, J. P. Wright, D. R. Croasdale, D. R. Worsnop, P. Davidovits and T. B. Onasch, *Atmos. Meas. Tech.*, 2011, **4**, 445–461.

[29] A. T. Lambe, T. B. Onasch, P. Massoli, D. R. Croasdale, J. P. Wright, A. T. Ahern, L. R. Williams, D. R. Worsnop, W. H. Brune and P. Davidovits, *Atmos. Chem. Phys.*, 2011, **11**, 8913–8928.

[30] C. W. Harmon, C. R. Ruehl, C. D. Cappa and K. R. Wilson, *Phys. Chem. Chem. Phys.*, 2013, **15**, 9679–9693.

[31] A. K. Bertram, 2001.

[32] M. J. Molina, A. V. Ivanov, S. Trakhtenberg and L. T. Molina, *Geophys. Res. Lett.*, 2004, **31**, .

[33] M. Shiraiwa, M. Ammann, T. Koop and U. Pöschl, *Proc. Natl. Acad. Sci.*, 2011, **108**, 11003–11008.

[34] J.-H. Park, A. V. Ivanov and M. J. Molina, *J. Phys. Chem. A*, 2008, **web-release**, .

[35] A. Arangio, J. H. Slade, T. Berkemeier, U. Pöschl, D. A. Knopf and M. Shiraiwa, *J. Phys. Chem. A.*, 2014.

[36] I. J. George, A. Vlasenko, J. G. Slowik, K. Broekhuizen and J. P. D. Abbatt, *Atmos. Chem. Phys.*, 2007, **7**, 4187–4201.

[37] A. J. Kwan, J. D. Crounse, A. D. Clarke, Y. Shinozuka, B. E. Anderson, J. H. Crawford, M. A. Avery, C. S. McNaughton, W. H. Brune, H. B. Singh and P. O. WEnnberg, *Geophys. Res. Lett.*, 2006, **33**, L15815.

[38] J. H. Kroll and J. H. Seinfeld, *Atmos. Environ.*, 2008, **42**, 3593–3624.

[39] P. Massoli, A. T. Lambe, A. T. Ahern, L. R. Williams, M. Ehn, J. Mikkilä, M. R. Canagaratna, W. H. Brune, T. B. Onasch, J. T. Jayne, T. Petäjä, M. Kulmala, A. Laaksonen, C. E. Kolb, P. Davidovits and D. R. Worsnop, *Geophys. Res. Lett.*, 2010, **37**, L24801.

[40] D. A. Knopf, B. Wang, A. Laskin, R. C. Moffet and M. K. Gilles, *J. Geophys. Res.*, 2010, **37**, L11803.

[41] B. Wang, A. T. Lambe, P. Massoli, T. B. Onasch, P. Davidovits, D. R. Worsnop and D. A. Knopf, *J. Geophys. Res.*, 2012, **117**, D16209.

[42] B. Wang, A. Laskin, T. Roedel, M. K. Gilles, R. C. Moffet, A. Tivanski and D. A. Knopf, *J. Geophys. Res.*, 2012, **117**, D00V19.

[43] J. H. Seinfeld and S. N. Pandis, *Atmospheric Chemistry and Physics*, John Wiley & Sons, New York, 1998.

[44] I. S. A. Isaksen, C. Granier, G. Myhre, T. K. Berntsen, S. B. Dalsoren, M. Gauss, Z. Klimont, R. Benestad, P. Bousquet, W. Collins, T. Cox, V. Eyring, D. Fowler, S. Fuzzi, P. Jockel, P. Laj, U. Lohmann, M. Maione, P. Monks, a. S. H. Prevot, F. Raes, A. Richter, B. Rognerud, M. Schulz, D. Shindell, D. S. Stevenson, T. Storelvmo, W.-C. Wang, M. van Weele, M. Wild and D. Wuebbles, *Atmos. Environ.*, 2009, **43**, 5138–5192.

[45] A. Peters, H. E. Wichmann, T. Tuch, J. Heinrich and J. Heyder, *Am. J. Resp. Crit. Care*, 1997, **155**, 1376–1383.

[46] M. Shiraiwa, K. Selzle and U. Poschl, *Free Rad. Res.*, 2012, **46**, 927–939.

[47] V. Ramanathan and Y. Feng, *Atmos. Environ.*, 2009, **43**, 37–50.

[48] V. Ramanathan and G. Carmichael, *Nat. Geo.*, 2008, **1**, 221–227.

[49] A. H. Goldstein and I. E. Galbally, *Environ. Sci. Technol.*, 2007, **41**, 1514–1521.

[50] C. D. O'Dowd, B. Langmann, S. Varghese, C. Scannell, D. Ceburnis and M. C. Facchini, *Geophys. Res. Lett.*, 2008, **35**, 2657–2665.

[51] M. Hallquist, J. C. Wenger, U. Baltensperger, Y. Rudich, D. Simpson, M. Claeys, J. Dommen, N. M. Donahue, C. George, A. H. Goldstein, J. F. Hamilton, H. Herrmann, T. Hoffmann, Y. Iinuma, M. Jang, M. E. Jenkin, J. L. Jimenes, A. Kiendler-Scharr, W. Maenhaut, G. McFiggans, T. F. Mentel, A. Monod, A. S. H. Prévôt, J. H. Seinfeld, J. D. Surratt, R. Szmigielski and J. Wildt, *Atmos. Chem. Phys.*, 2009, **9**, 5155–5236.

[52] J. Z. Yu, D. R. Cocker, R. J. Griffin, R. C. Flagan and J. H. Seinfeld, *J. Atmos. Chem.*, 1999, **34**, 207–258.

[53] R. J. Griffin, D. R. Cocker, J. H. Seinfeld and D. Dabdub, *Geophys. Res. Lett.*, 1999, **26**, 2721–2724.

[54] N. L. Ng, A. J. Kwan, J. D. Surratt, A. W. H. Chan, P. S. Chhabra, A. Sorooshian, H. O. T. Pye, J. D. Crounse, P. O. Wennberg, R. C. Flagan and J. H. Seinfeld, *Atmos. Chem. Phys.*, 2008, **8**, 4117–4140.

[55] N. L. Ng, P. S. Chhabra, A. W. H. Chan, J. D. Surratt, J. H. Kroll, A. J. Kwan, D. C. McCabe, P. O. Wennberg, A. Sorooshian, S. M. Murphy, N. F. Dalleska, R. C. Flagan and J. H. Seinfeld, *Atmos. Chem. Phys.*, 2007, **7**, 5159–5174.

[56] Y. B. Lim and P. J. Ziemann, *Environ. Sci. Technol.*, 2009, **43**, 2328–2334.

[57] C. L. Heald, D. J. Jacob, R. J. Park, L. M. Russell, B. J. Huebert, J. H. Seinfeld, H. Liao and R. J. Weber, *Geophys. Res. Lett.*, 2005, **32**, .

[58] R. Volkamer, F. S. Martini, L. T. Molina, D. Salcedo, J. L. Jimenez and M. J. Moline, *Geophys. Res. Lett.*, 2007, **34**, .

[59] J. D. Surratt, A. W. H. Chan, N. C. Eddingsaas, M. N. Chan, C. L. Loza, A. J. Kwan, S. P. Hersey, R. C. Flagan, P. O. Wennberg and J. H. Seinfeld, *Proc. Nat. Acad. Sci.*, 2010, **107**, 6640–6645.

[60] A. L. Robinson, N. M. Donahue, M. K. Shrivastava, E. A. Weitkamp, A. M. Sage, A. P. Grieshop, T. E. Lane, J. R. Pierce and S. N. Pandis, *Science*, 2007, **315**, 1259–1262.

[61] B. Finlayson-Pitts and N. Pitts, *Chemistry of the Upper and Lower Atmosphere*, Academic Press, San Diego, California, 2000.

[62] M. Z. Jacobson, *J. Geophys. Res.-Atmos.*, 1998, **103**, 10593–10604.

[63] R. J. Yokelson, J. D. Crounse, P. F. DeCarlo, T. Karl, S. Urbanski, E. Atlas, T. Campos, Y. Shinozuka, V. Kapustin, A. Clarke, A. Weinheimer, D. J. Knapp, D. D. Montzka, J. Holloway, P. Weibring, F. Flocke, W. Zheng, D. Toohey, P. O. WEnnberg, C. Wiedinmyer, L. Mauldin, A. Fried, D. Richter, J. Walega, J. L. Jimenez, K. Adachi, P. R. Buseck, S. R. Hall and R. Shetter, *Atmos. Chem. Phys.*, 2009, **9**, 5785–5812.

[64] R. J. Yokelson, S. P. Urbanski, E. L. Atlas, D. W. Toohey, E. C. Alvarado, J. D. Crounse, P. O. Wennberg, M. E. Fisher, C. E. Wold, T. L. Campos, K. Adachi, P. R. Buseck and W. M. Hao, *Atmos. Chem. Phys.*, 2007, **7**, 5569–5584.

[65] D. M. J. S. Bowman, J. K. Balch, P. Artaxo, W. J. Bond, J. M. Carlson, M. A. Cochrane, C. M. D'Antonio, R. S. DeFries, J. C. Doyle, S. P. Harrison, F. H. Johnston, J. E. Keeley, M. A. Krawchuk, C. A. Kull, J. B. Marston, M. A. Moritz, I. C. Prentice, C. I. Roos, A. C. Scott, T. W. Swetnam, G. R. van der Werf and S. J. Pyne, *Science*, 2009, **324**, 481–484.

[66] S.-C. Park, D. K. Burden and G. M. Nathanson, *J. Phys. Chem. A*, 2007.

[67] G. R. van der Werf, J. T. Randerson, L. Giglio, G. J. Collatz, P. S. Kasibhatla and A. F. Arellano, *Atmos. Chem. Phys.*, 2006, **6**, 3423–3441.

[68] J. T. Randerson, Y. Chen, G. R. van der Werf, B. M. Rogers and D. C. Morton, *J. Geophys. Res.-Biogeo.*, 2012, **117**, G04012.

[69] D. F. Nygaard, *World population projections, 2020*, United nations technical report, 1994.

[70] J. S. Levine, W. R. Cofer III, D. R. Cahoon JR and E. L. Winstead, *Environ. Sci. Technol*, 1995, **29**, 120–125.

[71] M. Keywood, M. Kanakidou, A. Stohl, F. Dentener, G. Grassi, C. P. Meyer, K. Torseth, D. Edwards, A. M. Thompson, U. Lohmann and J. Burrows, *Crit. Rev. Environ. Sci. Technol.*, 2013, **43**, 40–83.

[72] M. Posfai, R. Simonics, J. Li, P. V. Hobbs and P. R. Buseck, *J. Geophys. Res.-Atmos.*, 2003, **108**, 231–240.

[73] P. J. Crutzen and M. O. Andreae, *Science*, 1990, **250**, 1669–1678.

[74] M. T. Latif, N. Y. Anuwar, T. Srithawirat, I. S. Razak and N. A. Ramli, *Aerosol Air Qual. Res.*, 2011, **11**, 837–845.

[75] G. Wang, C. Chen, J. Li, B. Zhou, M. Xie, S. Hu, K. Kawamura and Y. Chen, *Atmos. Environ.*, 2011, **45**, 2473–2479.

[76] K. A. Pratt, S. M. Murphy, R. Subramanian, P. J. DeMott, G. L. Kok, T. Campos, D. C. Rogers, A. J. Prenni, A. J. Heymsfield, J. H. Seinfeld and K. A. Prather, *Atmos. Chem. Phys.*, 2011, **11**, 12549–12565.

[77] E. J. T. Levin, G. R. McMeeking, C. M. Carrico, L. E. Mack, S. M. Kreidenweis, C. E. Wold, H. Moosmueller, W. P. Arnott, W. M. Hao, J. L. Collett and W. C. Malm, *J. Geophys. Res. Atmos.*, 2010, **115**, D18210.

[78] K. Saarnio, M. Aurela, H. Timonen, S. Saarikoski, K. Teinilä, T. Mäkelä, M. Sofiev, J. Koskinen, P. P. Aalto, M. Kulmala, J. Kukkonen and R. Hillamo, *Sci. Total Environ.*, 2010, **408**, 2527–2542.

[79] S. T. Martin, M. O. Andreae, P. Artaxo, D. Baumgardner, Q. Chen, A. H. Goldstein, A. Guenther, C. L. Heald, O. L. Mayol-Bracero, P. H. McMurry, T. Pauliquevis, U. Pöschl, K. A. Prather, G. C. Roberts, S. R. Saleska, M. A. Silva Dias, D. V. Spracklen, E. Swietlicki and I. Trebs, *Rev. Geophys.*, 2010, **48**, RG2002.

[80] S. Kundu, K. Kawamura, T. W. Andreae, A. Hoffer and M. O. Andreae, *Atmos. Chem. Phys.*, 2010, **10**, 2209–2225.

[81] J. S. Smith, A. Laskin and J. Laskin, *Anal. Chem.*, 2009, **81**, 1512–1521.

[82] J. S. Reid, T. F. Eck, S. A. Christopher, R. Koppmann, O. Dubovik, D. P. Eleuterio, B. N. Holben, E. A. Reid and J. Zhang, *Atmos. Chem. Phys.*, 2005, **5**, 827–849.

[83] C. J. Hennigan, A. P. Sullivan, J. L. Collett and A. L. Robinson, *Geophys. Res. Lett.*, 2010, **37**, L09806.

[84] C. M. Carrico, M. D. Petters, S. M. Kreidenweis, A. P. Sullivan, G. R. McMeeking, E. J. T. Levin, G. Engling, W. C. Malm and J. L. Collett Jr., *Atmos. Chem. Phys.*, 2010, **10**, 5165–5178.

[85] S. Fuzzi, S. Decesari, M. C. Facchini, E. Matta, M. Mircea and E. Tagliavini, *Geophys. Res. Lett.*, 2001, **28**, 4079–4082.

[86] E. Dinar, I. Taraniuk, E. R. Graber, S. Katsman, T. Moise, T. Anttila, T. F. Mentel and Y. Rudich, *Atmos. Chem. Phys.*, 2006, **6**, 2465–2481.

[87] E. R. Graber and Y. Rudich, *Atmos. Chem. Phys.*, 2006, **6**, 729–753.

[88] B. Wang and D. A. Knopf, *J. Geophys. Res.*, 2011, **116**, D03205.

[89] M. Claeys, R. Vermeylen, F. Yasmeen, Y. Gómez-Gonzáles, X. Chi, W. Maenhaut, T. Mészáros and I. Salma, *Environ. Chem.*, 2012, **9**, 273–284.

[90] J. J. Schauer, M. J. Kleeman, G. R. Cass and B. R. T. Simoneit, *Environ. Sci. Technol.*, 2001, **35**, 1716–1728.

[91] B. R. T. Simoneit, *Appl. Geochem.*, 2002, **17**, 129–162.

[92] Y. Iinuma, E. Brüggemann, T. Gnauk, K. Müller, M. O. Andreae, G. Helas, R. Parmar and H. Herrmann, *J. Geophys. Res.*, 2007, **112**, D08209.

[93] G. Engling, J. J. Lee, Y.-W. Tsai, S.-C. C. Lung, C. C.-K. Chou, C. Chan and C.-Y. Chan, *Aerosol Sci. Technol.*, 2009, **43**, 662–672.

[94] B. R. T. Simoneit, *Environ. Sci. Pollut. Res.*, 1999, **6**, 159–169.

[95] S. H. Kessler, J. D. Smith, D. L. Che, D. R. Worsnop, K. R. Wilson and J. H. Kroll, *Environ. Sci. Technol.*, 2010, **44**, 7005–7010.

[96] P. M. Lemieux, C. C. Lutes and D. A. Santoianni, *Prog. Energy Combust. Sci.*, 2004, **30**, 1–32.

[97] R. Koppmann, K. von Czapiewski and J. S. Reid, *Atmos. Chem. PHys. Discuss.*, 2005, **5**, 10455–10516.

[98] C. R. Ruehl, T. Nah, G. Isaacman, D. R. Worton, A. W. H. Chan, K. R. Kolesar, C. D. Cappa, A. H. Goldstein and K. R. Wilson, *J. Phys. Chem. A*, 2013, **117**, 3990–4000.

[99] Y. Iinuma, O. Boge, R. Grafe and H. Herrmann, *Environ. Sci. Technol*, 2010, **44**, 8453–8459.

[100] L. D. Yee, K. E. Kautzman, C. L. Loza, K. A. Schilling, M. M. Coggon, P. S. Chhabra, M. N. Chan, A. W. H. Chan, S. P. Hersey, J. D. Crounse, P. O. Wennberg, R. C. Flagan and J. H. Seinfeld, *Atmos. Chem. Phys. Discusss.*, 2013, **13**, 3485–3532.

[101] *http://elte.prompt.hu*.

[102] J. J. Schauer, W. F. Rogge, L. M. Hildemann, M. A. Mazurek and G. R. Cass, *Atmos. Environ.*, 1996, **30**, 3837–3855.

[103] L. M. Hildemann, W. F. Rogge, G. R. Cass, M. A. Mazurek and B. R. T. Simoneit, *J. Geophys. Res.*, 1996, **101**, 19541–19549.

[104] C. G. Nolte, J. J. Schauer, G. R. Cass and B. R. T. Simoneit, *Environ. Sci. Technol.*, 2001, **35**, 1912–1919.

[105] T. Koop, J. Bookhold, M. Shiraiwa and Pöschl, *Phys. Chem. Chem. Phys.*, 2011, **13**, 19238–19255.

[106] E. Mikhailov, S. Vlasenko, S. T. Martin, T. Koop and U. Pöschl, *Atmos. Chem. Phys.*, 2009, **9**, 9491–9522.

[107] J. Slade and D. Knopf, *Geophys. Res. Lett.*, 2014, **41**, .

[108] M. J. Evans and D. J. Jacob, *Geophys. Res. Lett.*, 2005, **32**, 10004–10012.

[109] M. J. Molina, T. L. Tso, L. T. Molina and F. C. Y. Wang, *Science*, 1987, **238**, 1253–1257.

[110] A. Vlasenko, I. J. George and J. P. D. Abbatt, *J. Phys. Chem. A*, 2008, **112**, 1552–1560.

[111] U. Pöschl, Y. Rudich and M. Ammann, *Atmos. Chem. Phys.*, 2007, **7**, 5989–6023.

[112] K. E. Broekhuizen, T. Thornberry, P. P. Kumar and J. P. D. Abbatt, *J. Geophys. Res.*, 2004, **109**, S524–S537.

[113] J. E. Shilling, S. M. King, M. Mochida, D. R. Worsnop and S. T. Martin, *J. Phys. Chem. A*, 2007, **111**, 3358–3368.

[114] J. P. S. Wong, A. K. Y. Lee, J. G. Slowik, D. J. Cziczo, W. R. Leaitch, A. Macdonald and J. P. D. Abbatt, *Geophys. Res. Lett.*, 2011, **38**, L22805.

[115] R. Kotzick and R. Niessner, *Atmos. Environ.*, 1999, **33**, 2669–2677.

[116] J. R. Marlon, P. J. Bartlein, C. Carcaillet, D. G. Gavin, S. P. Harrison, P. E. Higuera, F. Joos, M. J. Power and I. C. Prentice, *Nat. Geosci.*, 2008, **1**, 697–702.

[117] J. E. Penner, R. E. Dickinson and C. A. O'Neill, *Science*, 2001, **256**, 1432–1434.

[118] M. O. Andreae and P. Merlet, *Glob. Biogeochem. Cycle*, 2001, **15**, 955–966.

[119] S. Marshall, J. A. Taylor, R. J. Oglesby, J. W. Larson and D. J. Erickson, *Environ. Soft.*, 1996, **11**, 53–58.

[120] S. J. Abel, J. M. Haywood, E. J. Highwood, J. Li and P. R. Buseck, *Geophys. Res. Lett.*, 2003, **30**, 1783.

[121] S. Gao, D. A. Hegg, P. V. Hobbs, T. W. Kirchstetter, B. I. Magi and M. Sadilek, *J. Geophys. Res.*, 2003, **108**, S524–S537.

[122] P. S. Monks, C. Granier, S. Fuzzi, A. Stohl, M. L. Williams, H. Akimoto, M. Amann, A. Baklanov, U. Baltensperger, I. Bey, N. Blake, R. S. Blake, K. Carslaw, O. R. Cooper, F. Dentener, D. Fowler, E. Fragkou, G. J. Frost, S. Generoso, P. Ginoux, V. Grewe, A. Guenther, H. C. Hansson, S. Henne, J. Hjorth, A. Hofzumahaus, H. Huntrieser, I. S. A. Isaksen, M. E. Jenkin, J. Kaiser, M. Kanakidou, Z. Klimont, M. Kulmala, P. Laj, M. G. Lawrence, J. D. Lee, C. Liousse, M. Maione, G. McFiggans, A. Metzger, A. Mieville, N. Moussiopoulos, J. J. Orlando, C. D. O'Dowd, P. I. Palmer, D. D. Parrish, A. Petzold, U. Platt, U. Pöschl, R. C. E. Prévôt, A. S. H., S. Reimann, Y. Rudich, K. Sellegri, R. Steinbrecher, D. Simpson, H. ten Brink, J. Theloke, G. R. van der Werf, R. Vautard, V. Vestreng, C. Vlachokostas and R. von Glasow, *Atmos. Environ.*, 2009, **43**, 5268–5350.

[123] D. Hoffmann, A. Tilgner, Y. Iinuma and H. Herrmann, *Environ. Sci. Technol.*, 2010, **44**, 694–699.

[124] G. Adler, J. M. Flores, A. Abo Riziq, S. Borrmann and Y. Rudich, *Atmos. Chem. Phys.*, 2011, **11**, 1491–1503.

[125] M. Martin, T. Tritscher, Z. Jurányi, M. F. Heringa, B. Sierau, E. Weingartner, R. Chirico, M. Gysel, A. S. H. Preévôt, U. Baltensperger and U. Lohmann, *J. Aerosol. Sci.*, 2013, **56**, 15–29.

[126] M. Fromm, J. Alfred, K. Hoppel, J. Hornstein, R. Bevilacqua, E. Shettle, R. Servranckx, Z. Q. Li and B. Stocks, *Geophys. Res. Lett.*, 2000, **27**, 1407–1410.

[127] M. Fromm, R. Bevilacqua, R. Servranckx, J. Rosen, J. P. Thayer, J. Herman and D. Larko, *J. Geophys. Res.*, 2005, **110**, D08205.

[128] G. Wotawa and M. Trainer, *Science*, 2000, **288**, 324–328.

[129] J. S. Reid, P. V. Hobbs, R. J. Ferek, D. R. Blake, J. V. Martins, M. R. Dunlap and C. Liousse, *J. Geophys. Res.-Atmos.*, 1998, **103**, 32059–32080.

[130] C. D. Cappa, D. L. Che, S. H. Kessler, J. H. Kroll and K. R. Wilson, *J. Geophys. Res. Atmos.*, 2011, **116**, .

[131] D. M. Murphy and T. Koop, *Q. J. R. Meteorol. Soc.*, 2005, **131**, 1539–1565.

[132] R. Pruppacher, H. and J. D. Klett, *Microphysics of Clouds and Precipitation*, Kluwer Academic Publishers, Netherlands, 1997.

[133] A. Virtanen, J. Joutsensaari, T. Koop, J. Kannosto, P. Yli-Pirilä, J. Leskinen, J. M. Mäkelä, J. K. Holopainen, U. Pöschl, M. Kulmala, D. R. Worsnop and A. Laaksonen, *Nature*, 2010, **467**, 824–827.

[134] A. Virtanen, J. Kannosto, H. Kuuluvainen, A. Arffman, J. Joutsensaari, E. Saukko, L. Hao, P. Yli-Pirila, P. Tiitta, J. K. Holopainen, J. Keskinen, D. R. Worsnop, J. N. Smith and A. Laaksonen, *Atmos. Chem. Phys.*, 2011, **11**, 8759–8766.

[135] E. Saukko, A. T. Lambe, P. Massoli, T. Koop, J. P. Wright, D. R. Croasdale, D. A. Pedernera, T. B. Onasch, A. Laaksonen, P. Davidovits, D. R. Worsnop and A. Virtanen, *Atmos. Chem. Phys.*, 2012, **12**, 7517–7529.

[136] D. M. Lienhard, D. L. Bones, A. Zuend, U. K. Krieger, J. P. Reid and T. Peter, *J. Phys. Chem. A.*, 2012, **116**, 9954–9968.

[137] P. Kumar, *Proc. Natl. Acad. Sci. USA.*, 2006, **103**, 12955–12956.

[138] J. P. D. Abbatt, A. K. Y. Lee and J. A. Thornton, *Chem. Soc. Rev.*, 2012, **41**, 6555–6581.

[139] B. Zobrist, C. Marcolli, T. Peter and T. Koop, *J. Phys. Chem. A*, 2008, **112**, 3965–3975.

[140] M. N. Chan, M. Y. Choi, N. L. Ng and C. K. Chan, *Environ. Sci. Technol.*, 2005, **39**, 1555–1562.

[141] S. M. Kreidenweis, K. Koehler, P. J. DeMott, A. J. Prenni, C. Carrico and B. Ervens, *Atmos. Chem. Phys.*, 2005, **5**, 1357–1370.

[142] B. Zobrist, C. Marcolli, T. Peter and T. Koop, *J. Phys. Chem. A*, 2008, **112**, 3965–3975.

[143] B. Zobrist, V. Soonsin, B. P. Luo, U. K. Krieger, C. Marcolli, T. Peter and T. Koop, *Phys. Chem. Chem. Phys.*, 2011, **13**, 3514–3526.

[144] P. G. Debenedetti and F. H. Stillinger, *Nature*, 2001, **410**, 259–267.

[145] J. H. Slade, R. Thalman, J. Wang and D. A. Knopf, 2014.

[146] M. Petters and S. Kreidenweis, *Atmos. Chem. Phys.*, 2008, **8**, 6273–6279.

[147] S. Solomon, M. Mills, L. E. Heidt, W. H. Pllock and A. F. Tuck, *J. Geophys. Res.-Atmos.*, 1992, **97**, 825–842.

[148] S. E. Schwartz and J. E. Freiberg, *Atmos. Environ.*, 1981, **15**, 1129–1144.

[149] C. E. Kolb, R. A. Cox, J. P. D. Abbatt, M. Ammann, E. J. Davis, D. J. Donaldson, B. C. Garrett, C. George, P. T. Griffiths, D. R. Hanson, M. Kulmala, G. McFiggans, U. Pöschl, I. Riipinen, M. J. Rossi, Y. Rudich, P. E. Wagner, P. M. Winkler, D. R. Worsnop and C. D. O'Dowd, *Atmos. Chem. Phys.*, 2010, **10**, 10561–10605.

[150] P. Davidovits, J. H. Hu, D. R. Worsnop, M. S. Zahniser and C. E. Kolb, *Fraday Discuss.*, 1995, **100**, 65–82.

[151] S. E. Schwartz, *Mass-transport considerations pertinent to aqueous phase reactions of gases in liquid-water clouds*, Brookhaven national lab technical report, 1986.

[152] P. Davidovits, C. E. Kolb, L. R. Williams, J. T. Jayne and D. R. Worsnop, *Chemical Reviews*, 2006, **106**, 1323–1354.

[153] D. D. Eley and E. K. Rideal, *Nature*, 1940, 401–402.

[154] I. Langmuir, *Trans. Faraday Soc.*, 1922, **17**, 0621–0654.

[155] M. Ammann, U. Pöschl and Y. Rudich, *Phys. Chem. Chem. Phys.*, 2003, **5**, 351–356.

[156] M. Ammann and U. Pöschl, *Atmos. Chem. Phys.*, 2007, **7**, 6025–6045.

[157] W. Wang, S. Wang, X. Ma and J. Gong, *Chem. Soc. Rev.*, 2011, **40**, 3703–3727.

[158] U. Pöschl, *Angew. Chem.-Int. Edit.*, 2005, **44**, 7520–7540.

[159] U. Pöschl, T. Letzel, C. Schauer and R. Niessner, *J. Phys. Chem. A*, 2001, **105**, 4029–4041.

[160] K. R. Kolesar, G. Buffaloe, K. R. Wilson and C. D. Cappa, *Environ. Sci. Technol.*, 2014, **48**, 3196–3202.

[161] M. Shiraiwa, C. Pfrang, T. Koop and U. Pöschl, *Atmos. Chem. Phys.*, 2012, **12**, 2777–2794.

[162] M. Shiraiwa, A. Zuend, A. K. Bertram and J. H. Seinfeld, *Phys. Chem. Chem. Phys.*, 2013, **15**, 11441–11453.

[163] J. H. Kroll, J. D. Smith, D. L. Che, S. H. Kessler, D. R. Worsnop and K. R. Wilson, *Phys. Chem. Chem. Phys.*, 2009, **11**, 8005–8014.

[164] M. Shiraiwa, T. Berkemeier, K. A. Schilling-Fahnestock, J. H. Seinfeld and U. Pöschl, *Atmos. Chem. Phys.*, 2014, **14**, 8323–8341.

[165] G. Isaacman, A. W. H. Chan, T. Nah, D. R. Worton, C. R. Ruehl, K. R. Wilson and A. H. Godstein, *Environ. Sci. Technol.*, 2012, **46**, 10632–10640.

[166] V. F. McNeill, R. L. N. Yatavelli, J. A. Thornton, C. B. Stipe and O. Landgrebe, *Atmos. Chem. Phys.*, 2008, **8**, 5465–5476.

[167] A. W. Birdsall and M. J. Elrod, *J. Phys. Chem. A*, 2011, **115**, 5397–5407.

[168] C. I. M. Beenakker, *Spectrochim. Acta, Part B*, 1976, **31**, 483–486.

[169] C. I. M. Beenakker, *Spectrochim. Acta, Part B*, 1977, **32**, 173–187.

[170] D. R. Hanson and E. R. Lovejoy, 1994.

[171] E. R. Lovejoy, T. P. Murrells, A. R. Ravishankara and C. J. Howard, *The Journal of Physical Chemistry*, 1990, **94**, 2386–2393.

[172] L. G. Huey, D. R. Hanson and C. J. Howard, *J. Phys. Chem.*, 1995, **99**, 5001–5008.

[173] M. Elrod, R. Meads, J. Lipson, J. Seeley and M. Molina, *J. Phys. Chem.*, 1996, **100**, 5808.

[174] P. P. Wickramanayake, G. J. Gardner, K. W. Michael Siu and S. S. Berman, *Int. J. Mass Sectrom. Ion Proc.*, 1986, **69**, 39.

[175] A. T. Lambe, J. Y. Zhang, A. M. Sage and N. M. Donahue, *Environ. Sci. Technol.*, 2007, **41**, year.

[176] R. Atkinson, D. L. Baulch, R. A. Cox, J. N. Crowley, R. F. Hampson, R. G. Hynes, M. E. Jenkin, M. J. Rossi and J. Troe, *Atmos. Chem. Phys.*, 2004, **4**, 1461–1738.

[177] A. Jordan, S. Haidacher, G. Hanel, E. Hartungen, L. Märk, H. Seehauser, R. Schottkowsky, P. Sulzer and T. D. Märk, *Int. J. Mass Spectrom.*, 2009, **286**, 122–128.

[178] W. Lindinger, A. Hansel and A. Jordan, *Chem. Soc. Rev.*, 1998, **27**, 347–354.

[179] R. Taipale, T. Ruuskanen, J. Rinne, M. Kajos, H. Hakola, T. Pohja and M. Kulmala, *Atmos. Chem. Phys.*, 2008, **8**, 6681–6698.

[180] A. Vlasenko, A. Macdonald, S. Sjostedt and J. Abbatt, *Atmos. Meas. Tech.*, 2010, **3**, 1055–1062.

[181] F. Mei, P. L. Hayes, A. Ortega, J. W. Taylor, J. D. Allan, J. Gilman, W. Kuster, J. de Gouw, J. L. Jimenez and J. Wang, *J. Geophys. Res.-Atmos*, 2013, **118**, 2903–2917.

[182] M. Petters, C. Carrico, S. Kreidenweis, A. Prenni, P. DeMott, J. Collett Jr. and H. Moosmüller, *J. Geophys. Res.*, 2009, **114**, D22205.

[183] G. C. Roberts and A. Nenes, *Aerosol Sci. Technol.*, 2005, **39**, 206–221.

[184] S. Lance, J. Medina, J. N. Smith and A. Nenes, *Aerosol Sci. Technol.*, 2006, **40**, 242–254.

[185] D. Rose, S. S. Gunthe, E. Mikhailov, G. P. Frank, U. Dusek, M. O. Andreae and U. Pöschl, *Atmos. Chem. Phys.*, 2008, **8**, 1153–1179.

[186] D. R. Collins, R. C. Flagan and J. H. Seinfeld, *Aerosol Sci. Technol.*, 2002, **36**, 1–9.

[187] E. R. Lovejoy, L. G. Huey and D. R. Hanson, *J. Geophys. Res.*, 1995, **100**, 18775–18780.

[188] T. Thornberry and J. P. D. Abbatt, *Phys. Chem. Chem. Phys.*, 2004, **6**, 84–93.

[189] C. J. Howard, *J. Phys. Chem.*, 1979, **83**, 3–9.

[190] R. Atkinson, W. P. L. Carter, C. N. Plum, A. M. Winer and J. N. Pitts, *Int. J. Chem. Kin.*, 1984, **16**, 887–898.

[191] D. R. Hanson and K. Mauersberger, *J. Phys. Chem.*, 1990, **94**, 4700–4705.

[192] D. R. Hanson and A. R. Ravishankara, *J. Phys. Chem.*, 1992, **96**, 2682–2691.

[193] J. V. Seeley, J. T. Jayne and M. J. Molina, *Chem. Kin.*, 1993, **25**, 571–594.

[194] F. Taketani and Y. Kanaya, *J. Phys. Chem. Lett.*, 2010, **1**, 1701–1704.

[195] J. A. Thornton, C. F. Braban and J. P. D. Abbatt, *Phys. Chem. Chem. Phys.*, 2003, **5**, 4593–4603.

[196] R. L. Brown, *J. Res. Natl. Bur. Stand. U. S.*, 1978, **83**, 1–8.

[197] N. A. Fuchs and A. G. Sutugin, *Highly Dispersed Aerosols*, *Ann Arbor Sci.*, 2nd edn, 1970.

[198] D. R. Hanson and A. R. Ravishankara, *J. Geophys. Res.*, 1991, **96**, 5081–5090.

[199] A. Ivanov, S. Trakhtenberg, A. Bertram, Y. Gershenson and M. Molina, *J. Phys. Chem. A*, 2006, **111**, 1632–1637.

[200] E. N. Fuller, S. D. and J. C. Giddings, *Indust. Eng. Chem.*, 1966, **58**, 19–27.

[201] W. Massman, *Atmos. Environ.*, 1998, **32**, 1111–1127.

[202] F. Kaufman, *Prog. React. Kinet.*, 1961, **1**, 3–39.

[203] P. L. Cooper and J. P. D. Abbatt, *J. Phys. Chem.*, 1996, **100**, 2249–2254.

[204] I. J. George, J. Slowik and J. P. D. Abbatt, *Geophys. Res. Lett.*, 2008, **35**, L13811.

[205] J. D. Hearn and G. D. Smith, *Geophys. Res. Lett.*, 2006, **33**, L17805.

[206] J. Jimenez, M. Canagaratna, N. Donahue, A. Prevot, Q. Zhang, J. Kroll, P. DeCarlo, J. Allan, H. Coe, N. Ng, A. Aiken, K. Docherty, I. Ulbrich, A. Grieshop, A. Robinson, J. Duplissy, J. Smith, K. Wilson, V. Lanz, C. Hueglin, Y. Sun, J. Tian, A. Laaksonen, T. Raatikainen, J. Rautiainen, P. Vaattovaara, M. Ehn, M. Kulmala, J. Tomlisnon, D. Collins, M. Cubison, E. Dunlea, J. Hufman, T. Onasch, M. Alfarra, P. Williams, K. Bower, Y. Kondo, J. Schneider, F. Drewnick, S. Borrmann, S. Weimer, K. Demerjian, D. Salcedo, L. Cottrell, R. Griffin, A. Takami, T. Miyoshi, S. Hatakeyama, A. Shimono, J. Sun, Y. Zhang, K. Dzepina, J. Kimmel, D. Sueper, J. Jayne, S. Herndon, A. Trimborn, L. Williams, E. Wood, A. Middlebrook, C. Kolb, U. Baltensperger and D. Worsnop, *Science*, 2009, **326**, 1525–1529.

[207] N. Donahue, K. Henry, T. Mentel, A. Kiendler-Scharr, C. Spindler, B. Bohn, T. Brauers, H. Dorn, H. Fuchs, R. Tillmann, A. Wahner,

H. Saathoff, K.-H. Naumann, O. Mohler, T. Leisner, L. Muller, M.-C. Reinnig, T. Hoffmann, K. Salo, M. Hallquist, M. Frosch, M. Bilde, T. Tritscher, P. Barmet, A. Praplan, P. DeCarlo, J. Dommen, A. Prevot and U. Baltensperger, *Proc. Nat. Acad. Sci.*, 2012, **109**, 13503–13508.

[208] E. Mysak, J. Smith, P. Ashby, J. Newberg, K. Wilson and H. Bluhm, *Phys. Chem. Chem. Phys.*, 2011, **13**, 7554–7564.

[209] U. Pöschl, Y. Rudich and M. Ammann, *Atmos. Chem. Phys. Discuss.*, 2005, **5**, 2111–2191.

[210] M. Shiraiwa, R. Garland and U. Pöschl, *Atmos. Chem. Phys.*, 2009, **9**, 9571–9586.

[211] M. Springmann, D. A. Knopf and N. Riemer, *Atmos. Chem. Phys.*, 2009, **9**, 7461–7479.

[212] J. C. Kaiser, N. Riemer and D. A. Knopf, *Atmos. Chem. Phys.*, 2011, **11**, 4505–4520.

[213] L. H. Renbaum and G. D. Smith, *Atmos. Chem. Phys.*, 2011, **11**, 6881–6893.

[214] S. H. Kessler, T. Nah, K. E. Daumit, J. D. Smith, S. R. Leone, C. E. Kolb, D. R. Worsnop, K. R. Wilson and J. H. Kroll, *J. Phys. Chem. A*, 2012, **116**, 6358–6365.

[215] P. V. Hobbs, P. Sinha, R. J. Yokelson, T. J. Christian, D. R. Blake, S. Gao, T. W. Kirchstetter, T. Novakov and P. Pilewskie, *J. Geophys. Res.*, 2003, **108**, 676–680.

[216] H. Motz and H. Wise, *J. Chem. Phys.*, 1960, **32**, 1893–1894.

[217] D. Murphy and D. Fahey, *Anal. Chem.*, 1987, **69**, 2753–2759.

[218] Y. M. Gershenzon, V. M. Grigorieva, A. V. Ivanov and R. G. Remorov, *Faraday Discuss.*, 1995, 83–100.

[219] L. Vereecken and J. Peeters, *Chem. Phys. Lett.*, 2001, **333**, 162–168.

[220] W. DeMore, S. Sander, D. Golden, R. Hampson, M. Kurylo, C. Howard, A. Ravishankara, C. Kolb and M. Molina, *Chemical kinetics and photochemical data for use in stratospheric modeling*, National Aeronautics and Space Administration, Jet Propulsion Laboratory, California Institute of Technology, Pasadena, California, 1997.

[221] R. Y. Zhang, I. Suh, W. Lei, A. d. Clinkenbeard and S. W. North, *J. Geophys. Res. Atmos.*, 2000, **105**, 24627–24635.

[222] R. Knispel, R. Koch, M. Siese and C. Zetzch, *Ber. Bunsenges. Phys. Chem.*, 1990, **94**, 1375–1379.

[223] V. Dookwah-Roberts, *Spectroscopy and kinetics of weakly bound gas phase adducts of atmospheric interest*, 2008, http://search.proquest.com/docview/304644786?accountid=14172.

[224] D. L. Che, J. D. Smith, S. R. Leone, M. Ahmed and K. R. Wilson, *Phys. Chem. Chem. Phys.*, 2009, **11**, 7885–7895.

[225] V. F. McNeill, G. M. Wolfe and J. A. Thornton, *J. Phys. Chem. A*, 2007, **111**, 1073–1083.

[226] N. S. Corin, P. H. Backlund and M. A. M. Kulovaara, *Environ. Sci. Technol.*, 2000, **34**, 2231–2236.

[227] Y. Ishikawa and R. Binning Jr., *Chem. Phys. Lett.*, 2001, **343**, 597–603.

[228] G. A. Russell, *J. Am. Chem. Soc.*, 1957, **79**, 2977–2978.

[229] R. Atkinson, D. L. Baulch, R. A. Cox, R. F. Hampson, J. A. Kerr, M. J. Rossi and J. Troe, *J. Phys. Chem. Ref. Data*, 1997, **26**, 1329–1499.

[230] T. Ogura, A. Miyoshi and M. Koshi, *Phys. Chem. Chem. Phys.*, 2007, **9**, 5133–5142.

[231] M. Petitjean, E. Reyès-Pérez, D. Pérez, P. Mirabel and S. Le Calvé, *J. Chem. Eng. Data*, 2010, **55**, 852–855.

[232] T. Schaefer, J. Schindelka, D. Hoffmann and H. Herrmann, *J. Phys. Chem. A.*, 2012, **116**, 6317–6326.

[233] Y. Tan, Y. Lim, K. Altieri, S. Seitzinger and B. Turpin, *Atmos. Chem. Phys.*, 2012, **12**, 801–813.

[234] S. Moussa and B. Finlayson-Pitts, *Phys. Chem. Chem. Phys.*, 2010, **12**, 9419–9428.

[235] M. Williams, R. Landel and J. Ferry, *J. Am. Chem. Soc.*, 1955, **77**, 3701–3707.

[236] A. L. Sumner, E. J. Menke, Y. Dubowski, J. T. Newberg, R. M. Penner, J. C. Hemminger, L. M. Wingen, T. Brauers and B. J. Finlayson-Pitts, *Physical Chemistry Chemical Physics*, 2004, **6**, 604–613.

[237] A. Di Paola, V. Augugliaro, L. Palmisano, G. Pantaleo and E. Savinov, *J. Photoch. Photobio. A*, 2003, **155**, 207–214.

[238] B. Chen, C. Yang and N. Goh, *J. Environ. Sci.*, 2006, **18**, 1061–1064.

[239] S. Steenken and P. O'Neill, *J. Phys. Chem.*, 1977, **81**, 505–508.

[240] B. Hemming and J. Seinfeld, *Ind. Eng. Chem. Res.*, 2001, **40**, 4162–4171.

[241] L. N. Hawkins and L. M. Russell, *Adv. Meteorol.*, 2010, **2010**, 612132.

[242] M. Andreae, E. Browell, M. Garstang, G. Gregory, R. Harriss, G. Hill, D. Jacob, M. Pereira, G. Sachse, A. Setzer, P. Silva-Dias, R. Talbot, A. Torres and S. Wofsy, *J. Geophys. Res.*, 1988, **93**, 1509–1527.

[243] A. V. Ivanov, S. Trakhtenberg, A. K. Bertram, Y. M. Gershenzon and M. J. Molina, *J. Phys. Chem. A*, 2007, **111**, 1632–1637.

[244] R. Zhao, E. L. Mungall, A. K. Y. Lee, D. Aljawhary and J. P. D. Abbatt, *Atmos. Chem. Phys. Discuss.*, 2014, **14**, 8819–8850.

[245] C. Lai, Y. Liu, J. Ma, Q. Ma and H. He, *Atmos. Environ.*, 2014, **91**, 32–39.

[246] S. J. Smith and T. C. Bond, *Atmos. Chem. Phys.*, 2014, **14**, 537–549.

[247] J. J. Schauer, W. F. Rogge, L. M. Hildemann, M. A. Mazurek, G. R. Cass and B. T. Simoneit, *Atmos. Environ.*, 2007, **30**, 3837–3855.

[248] M. K. Shrivastava, R. Subramanian, W. F. Rogge and A. L. Robinson, *Atmos. Environ.*, 2007, **41**, 9353–9369.

[249] A. L. Robinson, R. Subramanian, N. M. Donahue, A. Bernardo-Bricker and W. F. Rogge, *Environ. Sci. Technol.*, 2006, **40**, 7811–7819.

[250] P. J. Gallimore, P. Achakulwisut, F. D. Pope, J. F. Davies, D. R. Spring and M. Kalberer, *Atmos. Chem. Phys.*, 2011, **11**, 12181–12195.

[251] J. E. Penner, R. E. Dickinson and C. A. O'Neill, *Science*, 1992, **256**, 1432–1434.

[252] T. C. Bond, S. J. Doherty, D. W. Fahey, P. M. Forster, T. Berntsen, B. J. DeAngelo, M. G. Flanner, S. Ghan, B. Karcher, D. Koch, S. Kinne, Y. Kondo, P. K. Quinn, M. C. Sarofim, M. G. Schultz, M. Schulz, C. Venkataraman, H. Zhang, S. Zhang, N. Bellouin, S. K. Guttikunda, P. K. Hopke, M. Z. Jacobson, J. W. Kaiser, Z. Klimont, U. Lohmann, J. P. Schwarz, D. Shindell, T. Storelvmo, S. G. Warren and C. S. Zender, *J. Geophys. Res.*, 2013, **118**, 5380–5552.

[253] M. J. Cubison, A. M. Ortega, P. L. Hayes, D. K. Farmer, D. Day, M. J. Lechner, W. H. Brune, E. Apel, G. S. Diskin, J. A. Fisher, H. E. Fuelberg, A. Hecobian, D. J. Knapp, T. Mikoviny, D. Riemer, G. W. Sachse, W. Sessions, R. J. Weber, A. J. Weinheimer, A. Wisthaler and J. L. Jimenez, *Atmos. Chem. Phys.*, 2011, **11**, 12049–12064.

[254] E. N. Escorcia, S. J. Sjostedt and J. P. D. Abbatt, *J. Phys. Chem. A*, 2010, **114**, 13113–13121.

[255] G. Rubasinghege and V. H. Grassian, *Chem. Commun.*, 2013, **49**, 3071–3094.

[256] Y. Zhao, Z. Chen, X. Shen and D. Huang, *Atmos. Environ.*, 2013, **67**, 63–72.

[257] J. Bai, X. Sun, C. Zhang, Y. Xu and C. Qi, *Chemosphere*, 2013, **93**, 2004–2010.

[258] D. M. N. Yang, L. M. and L. E. Yu, *Geochim. Cosmochim. Ac.*, 2009, **73**, A1477.

[259] H. C. Price, B. J. Murray, J. Mattsson, D. O'Sullivan, T. W. Wilson, K. J. Baustian and L. G. Benning, *Atmos. Chem. Phys.*, 2014, **14**, 3817–3830.

[260] B. Zobrist, C. Marcolli, D. A. Pedernera and T. Koop, *Atmos. Chem. Phys.*, 2008, **8**, 5221–5244.

[261] S. Zhou, M. Shiraiwa, R. D. McWhinney, U. Pöschl and J. P. D. Abbatt, *Fraday Discuss.*, 2013, **165**, 391–406.

[262] J. W. L. Lee, V. Carrascón, P. J. Gallimore, S. J. Fuller, A. Björkegren, D. R. Spring, F. D. Pope and M. Kalberer, *Phys. Chem. Chem. Phys.*, 2012, **14**, 8023–8031.

[263] M. Mochida and K. Kawamura, *J. Geophys. Res.*, 2004, **109**, S524–S537.

[264] M. N. Chan, H. Zhang, A. H. Goldstein and K. R. Wilson, *J. Phy. Chem. C*, 2014.

[265] G. D. Smith, E. Woods, T. Baer and R. E. Miller, *J. Phys. Chem. A*, 2003, **107**, 9582–9587.

[266] A. R. R. Hanson, D. R. and S. Solomon, *J. Geophys. Res.*, 1994, **99**, 3615–3629.

[267] M. O. Andreae, D. Rosenfeld, P. Artaxo, A. A. Costa, G. P. Frank, K. M. Longo and M. A. F. Silva-Dias, *Science*, 2004, **303**, 1337–1342.

[268] I. Bejan, I. Barnes, R. Olariu, S. Zhous, P. Wiesen and T. Benter, *Physical Chemistry Chemical Physics*, 2007, **9**, 5686–5692.

[269] T. J. Barnum, N. Medeiros and R. Z. Hinrichs, *Atmos. Environ.*, 2012, **55**, 98–106.

[270] J. P. Peixoto and A. H. Oort, *J. Climate*, 1996, **9**, 3443–3463.

[271] R. J. Hopkins, K. Lewis, Y. Desyaterik, Z. Wang, A. V. Tivanski, W. P. Arnott, A. Laskin and M. K. Gilles, *Geophys. Res. Lett.*, 2007, **34**, L18806.

[272] M. A. J. Harrison, S. Barra, D. Borghesi, D. Vione, C. Arsene and R. I. Olariu, *Atmos. Environ.*, 2005, **39**, 231–248.

[273] R. V. Martin, D. J. Jacob and R. M. Yantosca, *J. Geophys. Res.*, 2003, **108**, 4097.

[274] J. Mao, D. J. Jacob, M. J. Evans, J. R. Olson, X. Ren, W. H. Brune, J. M. St. Clair, J. D. Crounse, K. M. Spencer, M. R. Beaver, P. O. Wennberg, M. J. Cubison, J. L. Jimenez, A. Fried, P. Weibring, J. G. Walega, S. R. Hall, A. J. Weinheimer, R. C. Cohen, G. Chen, J. H. Crawford, C. McNaughton, A. D. Clarke, L. Jaeglé, J. A. Fisher, R. M. Yantosca, P. Le Sager and C. Carouge, *Atmos. Chem. Phys.*, 2010, **10**, 5823–5838.

[275] B. J. Murray, *Atmos. Chem. Phys.*, 2008, **8**, 5423–5433.

[276] G. B. Ellison, A. F. Tuck and V. Vaida, *J. Geophys. Res.-Atmos.*, 1999, **104**, 11633–11641.

[277] S. D. Brooks, K. Suter and L. Olivarez, *J. Phys. Chem. A.*, 2014, **118**, 10036–10047.

[278] M. D. Hays, P. M. Fine, C. D. Geron, M. J. Kleeman and B. K. Gullett, *Atmos. Environ.*, 2005, **39**, 6747–6764.

[279] S. H. Jathar, T. D. Gordon, C. J. Hennigan, H. O. T. Pye, G. Pouliot, P. J. Adams, N. M. Donahue and A. L. Robinson, *Proc. Nat. Acad. Sci.*, 2014, **111**, 10473–10478.

[280] A. E. Sheffield, G. E. Gordon, L. A. Currie and G. E. Riederer, *Atmos. Environ.*, 1994, **28**, 1371–1384.

[281] U. Dusek, G. P. Frank, A. Massling, K. Zeromskiene, Y. Iinuma, O. Schmid, G. Helas, T. Hennig, A. Wiedensohler and M. O. Andreae, *Atmos. Chem. Phys.*, 2011, **11**, 9519–9532.

[282] G. Roberts, P. Artaxo, J. Zhou, E. Swietlicki and M. O. Andreae, *J. Geophys. Res.*, 2002, **107**, 8070.

[283] S. Suda, M. Petters, G. Yeh, C. Strollo, A. Matsunaga, A. Faulhaber, P. Ziemann, A. Prenni, C. Carrico, R. Sullivan and S. Kreidenweis, *Environ. Sci. Technol*, 2014, **48**, 10182–10190.

[284] A. P. Grieshop, J. M. Logue, N. M. Donahue and A. L. Robinson, *Atmos. Chem. Phys.*, 2009, **9**, 1263–11277.

[285] T. Novakov and C. E. Corrigan, *Geophys. Res. Lett.*, 1996, **23**, 2141–2144.

[286] D. Rose, A. Nowak, P. Achtert, A. Wiedensohler, M. Hu, M. Shao, Y. Zhang, M. O. Andreae and U. Pöschl, *Atmos. Chem. Phys.*, 2010, **10**, 3365–3383.

[287] S. S. Gunthe, S. M. King, D. Rose, Q. Chen, P. Roldin, D. K. Farmer, J. L. Jimenez, P. Artaxo, M. O. Andreae, S. T. Martin and U. Pöschl, *Atmos. Chem. Phys.*, 2009, **9**, 7551–7575.

[288] M. Bilde and B. Svenningsson, *Tellus*, 2004, **56B**, 128–134.

[289] J. P. D. Abbatt, K. Broekhuizen and P. P. Kumal, *Atmos. Environ.*, 2005, **39**, 4767–4778.

[290] N. C. Shantz, W. R. Leaitch, L. Phinney, M. Mozurkewich and D. Toom-Sauntry, *Atmos. Chem. Phys.*, 2008, **8**, 5869–5887.

[291] R. Vingarzan, *Atmos. Environ.*, 2004, **38**, 3431–3442.

[292] F. Mei, A. Setyan, Q. Zhang and J. Wang, *Atmos. Chem. Phys.*, 2013, **13**, 12155–12169.

[293] L. Chen, H. Moosmuller, W. Arnott, J. Chow, J. Watson, R. Susott, R. Babbitt, C. Wold, E. Lincoln, W. Hao, H. Moosmuller, W. P. Arnott, J. C. Chow, J. G. Watson, R. A. Susott, R. E. Babbitt, C. E. Wold, E. N. Lincoln and W. M. Hao, *Environ. Sci. Technol.*, 2007, **41**, 4317–4325.

[294] M. Anbar, D. Meyerstein and P. Neta, *J. Phys. Chem.*, 1966, **70**, 2660–2662.

[295] U. Dusek, D. S. Covert, A. Wiedensohler, C. Neususs, D. Weise and W. Cantrell, *Tellus B.*, 2003, **55**, 35–53.

[296] R. Gasparini, R. J. Li, D. R. Collins, R. A. Ferrare and V. G. Brackett, *J. Geophys. Res.-Atmos.*, 2006, **111**, D05S12.

[297] B. Ervens, G. Feingold and S. M. Kreidenweis, *J. Geophys. Res.-Atmos.*, 2005, **110**, D18211.

[298] M. O. Andreae and D. Rosenfeld, *Earth-Sci. Rev.*, 2008, **89**, 13–41.

[299] J. Rissler, A. Vestin, E. Swietlicki, G. Fisch, J. Zhou, P. Artaxo and M. O. Andreae, *Atmos. Chem. Phys.*, 2006, **6**, 471–491.

[300] C. N. Cruz and S. N. Pandis, *J. Geophys. Res.-Atmos.*, 1998, **103**, 13111–13123.

[301] M. Pósfai, H. F. Xu, J. R. Anderson and P. R. Buseck, *Geophys. Res. Lett.*, 1998, **25**, 1907–1910.

[302] L. M. Russell, S. F. Maria and S. C. B. Myneni, *Geophys. Res. Lett.*, 2002, **29**, 26–1–26–4.

[303] R. M. Garland, M. E. Wise, M. R. Beaver, H. L. DeWitt, A. C. Aiken, J. L. Jimenez and M. A. Tolbert, *Atmos. Chem. Phys.*, 2005, **5**, 1951–1961.

[304] K. J. Baustian, D. J. Cziczo, M. E. Wise, K. A. Pratt, G. Kulkarni, A. G. Hallar and M. A. Tolbert, *J. Geophys. Res.-Atmos*, 2012, **117**, D06217.

[305] O. Möhler, S. Benz, H. Saathoff, M. Schnaiter, R. Wagner, J. Schneider, S. Walter, V. Ebert and S. Wagner, *Environ. Res. Lett.*, 2008, **3**, .

[306] B. Friedman, G. Kulkarni, J. Beránek, A. Zelenyuk, J. A. Thornton and D. J. Cziczo, *J. Geophys. Res.*, 2011, **116**, D17203.

[307] Y. Katrib, S. T. Martin, H. M. Hung, Y. Rudich, H. Z. Zhang, J. G. Slowik, P. Davidovits, J. T. Jayne and D. R. Worsnop, *J. Phys. Chem. A*, 2004, **108**, 6686–6695.

[308] K. M. Gierlus, O. Laskina, T. L. Abernathy and V. H. Grassian, *Atmos. Environ.*, 2012, **46**, 125–130.

[309] D. A. Knopf, *J. Phys. Chem. A*, 2007, **111**, 1376–1377.

[310] L. M. Cosman, D. A. Knopf and A. K. Bertram, *J. Phys. Chem. A.*, 2008, **112**, 2386–2396.

[311] B. Graham, O. L. Mayol-Bracero, P. Guyon, G. C. Roberts, S. Decesari, M. C. Facchini, P. Artaxo, W. Maenhaut, P. Koll and M. O. Andreae, *J. Geophys. Res.-Atmos*, 2002, **107**, 8047.

[312] T. A. Semeniuk, M. E. Wise, S. T. Martin, L. M. Russell and P. R. Buseck, *J. Atmos. Chem.*, 2007, **56**, 259–273.

[313] C. R. Ruehl, P. Y. Chuang, A. Nenes, C. D. Cappa, K. R. Kolesar and A. H. Goldstein, *Geophys. Res. Lett.*, 2012, **39**, L23801.

[314] S. Saarikoski, M. Sillanpaa, M. Sofiev, H. Timonen, K. Saarnio, K. Teinela, A. Karppinen, J. Kukkonen and R. Hillamo, *Atmos. Environ.*, 2007, **41**, 3577–3589.

[315] P. Saxena and L. M. Hildemann, *J. Atmos. Chem.*, 1996, **24**, 57–109.

[316] H. Timonen, S. Carbone, M. Aurela, K. Saarnio, S. Saarikoski, N. L. Ng, M. R. Canagaratna, M. Kulmala, V. M. Kerminen, D. R. Worsnop and R. Hillamo, *J. Aero. Sci.*, 2013, **56**, 61–77.

[317] S. Decesari, M. C. Facchini, E. Matta, M. Mircea, S. Fuzzi, A. R. Chughtai and D. M. Smith, *Atmos. Environ.*, 2002, **36**, 1827–1832.

[318] D. M. Murphy and D. S. Thomson, *J. Geophys. Res.-Atmos*, 1997, **102**, 6353–6368.

[319] D. M. Murphy, D. J. Cziczo, K. D. Froyd, P. K. Hudson, B. M. Matthew, A. M. Middlebrook, R. E. Peltier, A. Sullivan, D. S. Thomson and R. J. Weber, *J. Geophys. Res.*, 2006, **111**, D23S32.

[320] A. M. Middlebrook, D. M. Murphy and D. S. Thomson, *J. Geophys. Res.*, 1998, **103**, 16475–16483.

[321] C. Marcolli, B. P. Luo and T. Peter, *J. Phys. Chem. A*, 2004, **108**, 2216–2224.

[322] M. Y. Choi and C. K. Chan, *Environ. Sci. Technol*, 2002, **36**, 2422–2428.

[323] B. Svenningsson, J. Rissler, E. Swietlicki, M. Mircea, M. Bilde, M. C. Facchini, S. Decesari, S. Fuzzi, J. Zhou, J. Monster and T. Rosenorn, *Atmos. Chem. Phys.*, 2006, **6**, 1937–1952.

[324] J. Wang, Y.-N. Lee, P. H. Daum, J. Jayne and M. L. Alexander, *Atmos. Chem. Phys.*, 2008, **8**, 6325–6339.

[325] A. T. Lambe, C. D. Cappa, P. Massoli, T. B. Onasch, S. D. Forestieri, A. T. Martin, M. J. Cummings, D. R. Croasdale, W. H. Brune, D. R. Worsnop and P. Davidovits, *Environ. Sci. Technol.*, 2013, **47**, 6349–6357.

[326] C. Pfrang, M. Shiraiwa and U. Poschl, *Atmos. Chem. Phys.*, 2011, **11**, 7343–7354.

[327] M. Kuwata and S. T. Martin, *Proc. Nat. Acad. Sci.*, 2012, **109**, 17354–17359.

[328] L. H. Renbaum and G. D. Smith, *Phys. Chem. Chem. Phys.*, 2009, **11**, 2441–2451.

[329] M. P. Fraser and K. Lakshmanan, *Environ. Sci. Technol.*, 2000, **34**, 4560–4564.

[330] J. A. Gonzalez-Perez, F. J. Gonzalez-Vila, G. Almendros and H. Knicker, *Environ. Int.*, 2004, **30**, 855–870.

[331] O. L. Mayol-Bracero, P. Guyon, B. Graham, G. Roberts, M. O. Andreae, S. Decesari, M. C. Facchini, S. Fuzzi and P. Artaxo, *J. Geophys. Res.-Atmos.*, 2002, **107**, 189–195.

[332] I. Salma, R. Ocskay and G. G. Lang, *Atmos. Chem. Phys.*, 2008, **8**, 2243–2254.

[333] E. A. Stone, C. J. Hedman, R. J. Sheesley, M. M. Shafer and J. J. Schauer, *Atmos. Environ.*, 2009, **43**, 4205–4213.

[334] C. L. Badger, I. George, P. T. Griffiths, C. F. Braban, R. A. Cox and J. P. D. Abbatt, *Atmos. Chem. Phys.*, 2006, **6**, 755–768.

[335] M. Gysel, E. Weingartner, S. Nyeki, D. Paulsen, U. Baltensperger, I. Galambos and G. Kiss, *Atmos. Chem. Phys.*, 2004, **4**, 35–50.

[336] K. Young and E. Leboeuf, *Environ. Sci. Technol.*, 2000, **34**, 4549–4553.

[337] T. B. Kristensen, H. Wex, B. Nekat, J. K. Nojgaard, D. van Pinxteren, D. H. Lowenthal, L. R. Mazzoleni, K. Dieckmann, C. B. Koch, T. F. Mentel, H. Herrmann, A. G. Hallar, F. Stratmann and M. Bilde, *J. Geophys. Res. Atmos.*, 2012, **117**, .

[338] T. M. VanReken, N. L. Ng, R. C. Flagan and J. H. Seinfeld, *J. Geophys. Res.*, 2005, **110**, 4441–4446.

[339] S. M. King, T. Rosenoern, J. E. Shilling, Q. Chen, Z. Wang, G. Biskos, K. A. McKinney, U. Poschl and S. T. Martin, *Atmos. Chem. Phys.*, 2010, **10**, 3953–3964.

[340] M. Kuwata, Q. Chen and S. T. Martin, *Phys. Chem. Chem. Phys.*, 2011, **13**, 14571–4583.

[341] T. Nah, S. H. Kessler, K. E. Daumit, J. H. Kroll, S. R. Leone and K. R. Wilson, *Phys. Chem. Chem. Phys.*, 2013, **15**, 18649–18663.

[342] M. Shiraiwa, Y. Sosedova, A. Rouviére, H. Yang, Y. Zhang, J. P. D. Abbatt, M. Ammann and U. Pöschl, *Nat. Chem.*, 2011, **3**, 291–295.